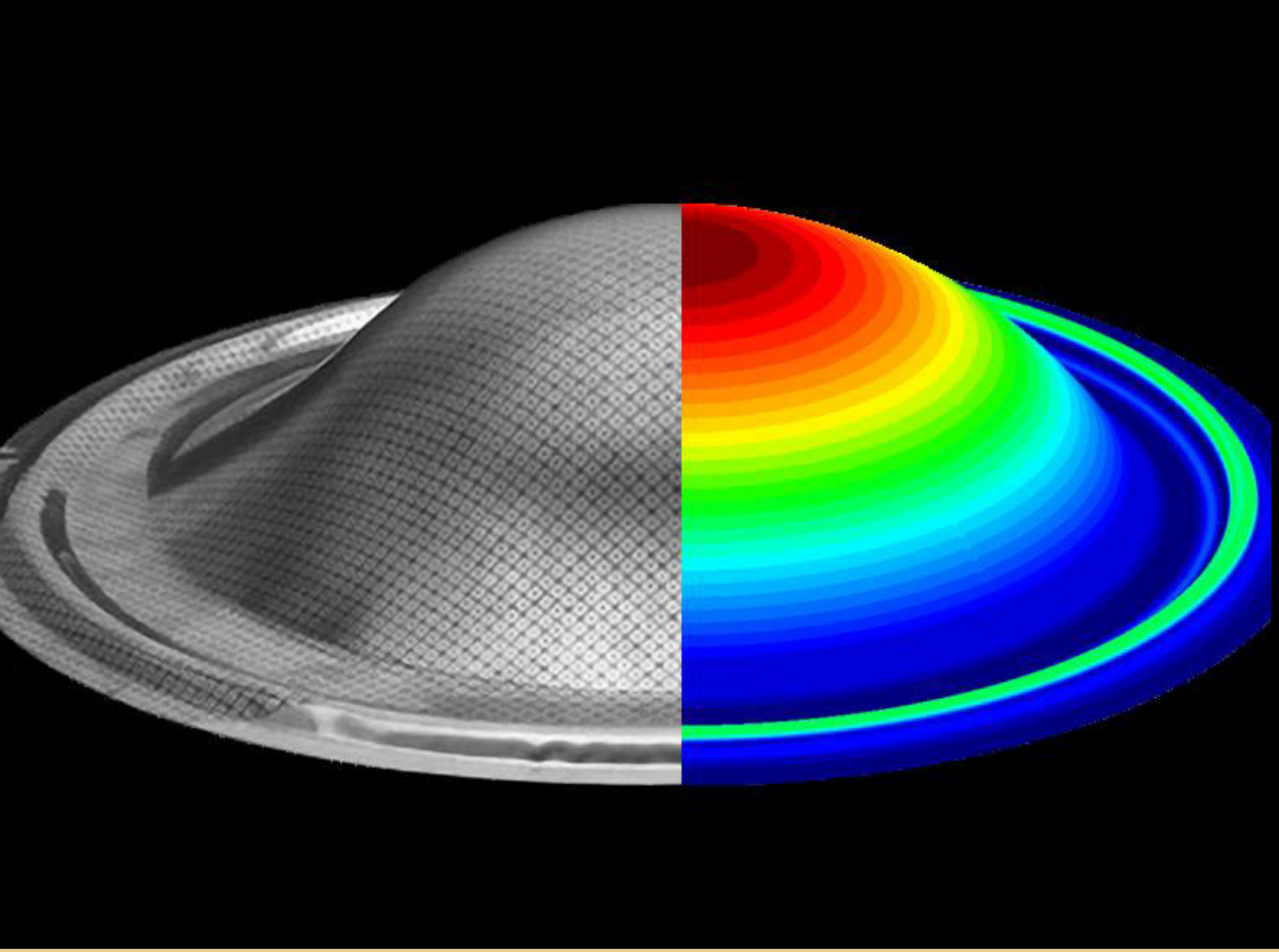

Luís Carlos Duarte dos Reis

CONSTITUTIVE PARAMETERS IDENTIFICATION OF METAL SHEETS USING CIRCULAR BULGE TESTS

Doctoral Thesis in Mechanical Engineering, specialization in Production Technologies, supervised by Professor José Valdemar Bidarra Fernandes and Professor Abel Dias dos Santos, submitted to the Department of Mechanical Engineering, Faculty of Sciences and Technology of the University of Coimbra

September 2015

· U C ·

UNIVERSIDADE DE COIMBRA

Constitutive Parameters Identification of Metal Sheets using Circular Bulge Tests

A dissertation submitted to the Department of Mechanical Engineering of the University of Coimbra in partial fulfilment to the requirements for degree of Doctor of Philosophy in Mechanical Engineering

Luís Carlos Duarte dos Reis

Scientific advisers:

Prof. **José Valdemar Bidarra Fernandes**, University of Coimbra, Portugal

Prof. **Abel Dias dos Santos**, University of Porto, Portugal

Department of Mechanical Engineering
Faculty of Sciences and Technology
University of Coimbra

Coimbra, September 2015

To my *family*

"*I do not like to state an opinion on a matter unless I know the precise facts.*"

Albert Einstein

Acknowledgements

The work presented in this PhD thesis has been carried out in the last four years at the Department of Mechanical Engineering of the University of Coimbra. These years of research were a very productive period in my engineering education, as well as in my personal development. Freedom of investigation and guidance of my scientific advisors allowed me to improve the knowledge in the field of the bulge test and characterization of plastic behaviour of metal sheets.

I particularly wish to express my sincere gratitude to my scientific advisors, Professor José Valdemar Fernandes and Professor Abel Dias dos Santos, for the valuable guidance, support and clarifications provided during my PhD thesis. Their high scientific competences and critical analysis have guided me throughout all the difficulties and contributed to the achievement of this thesis. I also want to express my appreciation for the effort expended in this work and for the critical and suggestive reading of the text.

I would like to thank Professor Marta Oliveira for the availability, the precious teachings, for her support and good humour, and in particular by the pride and rigour imposed in her work.

I am grateful for the excellent support provided within the Centre for Mechanical Engineering of the University of Coimbra (CEMUC) and the opportunity given to me for developing my research work. I also wish to thank all current and former colleagues of CEMUC for the encouragement, friendship and good mood communicated to me.

I like to thank my family and Luísa for the love and support they gave me, for their encouragement, personal sacrifice and understanding through all the years. Without them, it would have not been possible to finish this work. To them, words are not enough to express my appreciation.

Finally, I wish to thank all my friends and colleagues of the course, those of which I do not enumerate fearing of forgetting someone, for their patience, for their support and encouragement and especially for all the moments of joyful fellowship.

Coimbra, September 2015

The financial support of this work has been provided by the Portuguese Foundation for Science and Technology (FCT) via the project Pest-C/EME/UI0285/2013 and by FEDER funds through the program COMPETE – Programa Operacional Factores de Competitividade. Both supports are gratefully acknowledged.

Abstract

The hydraulic bulge test remains nowadays an important tool for characterizing the behaviour of sheet materials submitted to large plastic deformation. Data from this test, not only provides additional information to the tensile stress *vs*. strain curve, but also plays an important role as input information for identifying the parameters of the current most advanced yield criteria.

The circular hydraulic bulge test is studied by means of finite element simulations, using the in-house code DD3IMP. This work aims to contribute to the easy and accurate evaluation of stress *vs*. strain curve of sheet metals in biaxial tension. Variables of the test, such as pressure evolution during the test, geometry of the cap, including radius of curvature and sheet thickness, strain and stress paths at the pole of the cap, were analysed. This allows to make recommendations in order to improve the traditional experimental procedure for determining the stress *vs*. strain curve, but also to develop new direct and inverse methodologies for simplifying its evaluation.

The traditional procedure for obtaining the stress *vs*. strain curve from the circular bulge test does not takes into account the anisotropy of the material. The detailed analysis of issues such as the geometry of the spherical cap and the stress and strain paths at the pole, allowed to understand the relationships between such variables of the test, the sheet anisotropy and the different hardening behaviours of the material. The in-depth understanding of these relationships has repercussions on the experimental evaluation of the stress *vs*. strain curve of materials when using the bulge test, for which recommendations are made.

Analytical models for the radius of curvature and the sheet thickness evolutions with the pole bulge height were proposed. These models are based in an extensive analysis of material

behaviours, i.e. different values of yield stress, hardening coefficient, anisotropy, and also different values of initial sheet thickness and geometry of the circular bulge test. The analysed geometric variables include the bulge die radius and the fillet radius of the die. The validation of the proposed analytical models is performed both by numerically generated results and experimental results; in the latter case, results were considered not only from literature, having various die geometries, but also from an experimental equipment in the framework of this thesis, having a specific die geometry. This formulation shows to be appropriate for simplifying the experimental assessment of the hardening curve from the hydraulic bulge test. Namely, it is possible to avoid the complex experimental procedure to determine the stress and strain values during the test, which requires specific devices for evaluating the radius of curvature and the sheet thickness at the pole of the cap.

Finally, the current results also showed that it is possible to overlap the curves concerning the evolution of the pressure with the pole height, and this insight was explored in order to build an inverse strategy for identifying the parameters of the Swift hardening law, from the bulge test. The overlapping of these curves can be accomplished by using multiplying factors for the pressure and the pole height, which in case of materials with the same hardening coefficient it is independent of the remaining parameters of the Swift law, anisotropy and initial thickness of the sheet. Moreover, the analysis of the pressure evolution during the test has shown that corresponding values of these factors are sensitive to the parameters of Swift law and the initial sheet thickness, being only slightly dependent of the anisotropy of the material. The proposed methodology consisted on choosing the best overlap between the experimental and reference results, which were numerically obtained for isotropic materials with various values of the hardening coefficient. Validation was performed using numerical generated results and experimental results. The methodology allows simplifying the experimental procedure and in addition is not exposed to experimental errors related to the experimental evaluation of strain at the pole and the use of membrane theory approach, for assessment of the stress from the radius of curvature, which is usually the major source of error.

Keywords: Hardening law, Hydraulic bulge test, Isotropic and anisotropic metal sheets, Modelling, Inverse analysis, Membrane theory, Numerical simulation.

Resumo

O ensaio de expansão biaxial sob pressão hidráulica continua a ser hoje em dia uma ferramenta importante de caracterização do comportamento plástico de chapas metálicas quando sujeitas a grandes deformações plásticas. A informação retirada deste ensaio não só faculta dados adicionais aos da curva tensão-deformação em tração, mas também desempenha um papel importante como informação necessária para identificação de parâmetros dos critérios de plasticidade mais avançados.

Este trabalho foi realizado recorrendo a simulações numéricas do ensaio de expansão biaxial em matriz circular, com recurso ao programa DD3IMP. Tem como objetivo contribuir para a determinação da curva tensão *vs*. deformação de chapas metálicas em tração biaxial, de modo simples e preciso. Durante o ensaio foram analisadas variáveis relacionadas com a geometria da chapa, tais como o raio de curvatura e a espessura da chapa, e outras como a evolução de pressão e as trajetórias de tensão e de deformação no pólo da calote. Isto permitiu delinear algumas recomendações, de modo a melhorar o procedimento tradicional experimental de determinação da curva tensão *vs*. deformação, e desenvolver novos métodos diretos e inversos com o intuito de simplificar a sua avaliação.

O procedimento tradicional de obtenção da curva tensão *vs*. deformação do ensaio de expansão biaxial em matriz circular não toma em consideração a anisotropia do material. Neste estudo detalhado analisam-se em pormenor alguns aspetos, tais como a geometria da calote esférica e as trajetórias de tensão e de deformação no pólo, de modo a compreender as relações entre as diferentes variáveis do ensaio em função da anisotropia do material e para diferentes comportamentos de encruamento. Isto permitiu uma compreensão

aprofundada destas relações, com impacto na determinação experimental da curva tensão *vs*. deformação do material, para o que são feitas recomendações.

Foram propostos modelos analíticos que descrevem a evolução do raio de curvatura e da espessura de chapa em função da altura de pólo. Estes modelos são baseados numa ampla análise de comportamentos de materiais, ou seja, para diferentes valores de tensão limite de elasticidade, coeficiente de encruamento, anisotropia, e também para diferentes valores de espessura inicial da chapa e geometrias circulares de matriz. As variáveis analisadas, respeitantes à geometria da matriz, são o raio da matriz e o raio de concordância da matriz. A validação dos modelos analíticos propostos foi realizada com resultados gerados numericamente e experimentalmente; neste último caso, foram utilizados os existentes na literatura, para várias geometrias de matriz, e os obtidos no âmbito da presente tese, com uma geometria de matriz específica. A formulação desenvolvida mostra-se adequada para simplificar a determinação experimental da curva de encruamento recorrendo ao ensaio de expansão biaxial sob pressão hidráulica. Nomeadamente, é possível evitar o procedimento experimental complexo para determinar os valores de tensão e de deformação durante o ensaio, o qual requer dispositivos específicos para a análise do raio de curvatura e da espessura da chapa no pólo da calote.

Por fim, os resultados apresentados também indicaram a possibilidade de sobrepor as curvas da evolução da pressão em função da altura de pólo e este conhecimento foi fundamental para conceber uma estratégia de análise inversa para identificar os parâmetros da lei encruamento de Swift, baseada no ensaio de expansão biaxial. Foi possível obter a sobreposição das curvas de pressão em função da altura de pólo utilizando fatores de multiplicação para a pressão e para a altura de pólo, no caso de materiais com o mesmo coeficiente de encruamento, independentemente dos restantes parâmetros da lei de encruamento de Swift, da anisotropia do material e da espessura inicial da chapa. Além disso, a análise da evolução da pressão durante o ensaio mostrou que os valores desses fatores são sensíveis aos parâmetros da lei de Swift e à espessura inicial da chapa, sendo apenas ligeiramente dependentes da anisotropia do material. A metodologia proposta consiste em definir a melhor sobreposição entre os resultados experimentais e os de referência, obtidos numericamente para materiais isotrópicos com diferentes valores de coeficiente de encruamento. Esta metodologia foi validada utilizando resultados gerados numericamente e resultados experimentais. Desta forma, com os desenvolvimentos realizados é possível

simplificar o procedimento experimental, sem se estar exposto a erros relacionados com a determinação experimental da deformação no pólo da calote e a utilização da teoria de membrana na avaliação da tensão a partir da análise do raio de curvatura, fatores que correspondem normalmente às principais fontes de erro.

Palavras-chave: Lei de encruamento, Ensaio de expansão biaxial sob pressão hidráulica, Chapas metálicas isotrópicas e anisotrópicas, Modelação, Análise inversa, Teoria da membrana, Simulação numérica.

[Page intentionally left blank]

Contents

List of Figures

[Page intentionally left blank]

List of Tables

[Page intentionally left blank]

Acronyms and Symbology

Acronyms

CEMUC	Centre for Mechanical Engineering of the University of Coimbra
DD3IMP	Deep-Drawing 3D IMPlicit code
DIC	Digital Image Correlation
Drucker+L	Drucker yield criterion with linear transformation **L**
FE	Finite Element
FEA	Finite Element Analysis
FLC	Forming Limit Curve
Hill'48	Hill 1948 yield criterion
INEGI	Institute of Science and Innovation in Mechanical and Industrial Engineering
NXT	Software package used to evaluate the curvature of the surface
RD	Rolling Direction of the metal sheet
TD	Transverse Direction of the metal sheet
ND	Normal Direction to the sheet plane

Symbology

α	Angle subtended by the centre of the test, the centre of curvature of the concordance zone of the die and the pole of the cap
β	Stress path
$\bar{\varepsilon}$	Equivalent plastic strain
$\bar{\varepsilon}_{aniso}$	Equivalent plastic strain under anisotropy conditions
ε_0	Parameter of Swift hardening law
$\varepsilon_x \left(= \varepsilon_1\right)$	Principal strain in the rolling direction
ε_{1mid}	Principal strain at the middle plane in the rolling direction
$\varepsilon_y \left(= \varepsilon_2\right)$	Principal strain in the transverse direction
ε_{2mid}	Principal strain at the middle plane in the transverse direction
$\varepsilon_z \left(= \varepsilon_3\right)$	Principal strain in the sheet thickness
ε_3^{pl}	Principal plastic strain in the sheet thickness
ε_{3mid}	Principal strain at the middle plane in the sheet thickness
ε_1^e	Principal elastic strain in the rolling direction of the sheet plane
ε_2^e	Principal elastic strain in the transverse direction of the sheet plane
ε_b	Bending strain
η	Normalized measuring distance
ρ	Radius of curvature at the middle plane
$\rho_x \left(= \rho_1\right)$	Radius of curvature along the rolling direction
$\rho_y \left(= \rho_2\right)$	Radius of curvature along the transverse direction
ρ_{ext}	Radius of curvature of the external surface of the cap
$\bar{\sigma}$	Equivalent stress
$\bar{\sigma}_{aniso}$	Equivalent stress under anisotropy conditions

σ_B	Biaxial true stress
$\sigma_0 (= Y_0)$	Initial yield stress
$\sigma_x (= \sigma_1)$	Principal stress in the rolling direction
$\sigma_y (= \sigma_2)$	Principal stress in the transverse direction
$\sigma_z (= \sigma_3)$	Principal stress normal to the sheet plane
σ_{sat}	Parameter of Voce hardening law
ν	Poisson coefficient
ζ	Defines the original location of a finite element
a	Element dimension according to O*x* direction
a_1 to a_6	Parameters of the equation for the evolution of the radius of curvature
b	Element dimension according to O*y* direction
b_1 to b_6	Parameters of the equation for the evolution of the sheet thickness
c	Parameter of the Drucker+L yield criterion
C_0	Initial length of the region used for determining the radius of curvature
c_1 to c_8	Parameters of the equation for the evolution of the sheet thickness
C_1 to C_6	Parameters of the Drucker+L yield criterion
c_y	Exponent parameter of Voce hardening law
d	Distance to the pole of the cap
$d\varepsilon_1$	Increment of plastic deformation in the O1 direction
$d\varepsilon_2$	Increment of plastic deformation in the O2 direction
$d\lambda$	Incremental scalar factor of proportionality
D_{CV}	Diameter between the spherometers
d_M	Diameter of the die
D_{st0}	Initial diameter of the bulge expansion for determination of the strain value in the sheet plane
D_{st}	Diameter of the bulge expansion for determination of the strain value in the sheet plane
E	Young's Modulus
F	Parameter of the Hill'48 yield criterion
G	Parameter of the Hill'48 yield criterion

H	Parameter of the Hill'48 yield criterion
h	Pole height
h_{CV}	Height difference between the pole and the three positions of the spherometers
K	Parameter of Swift hardening law
L	Parameter of the Hill'48 yield criterion
M	Parameter of the Hill'48 yield criterion
N	Parameter of the Hill'48 yield criterion
n	Hardening coefficient of Swift law
p	Hydraulic Pressure
R^2	Correlation coefficient
R_1	Die profile radius
R_D	Drawbead radius
R_M	Die radius
R_S	Initial sheet radius
R_{sat}	Parameter of Voce hardening law
$\overline{r}$	Normal anisotropy coefficient
r_0	Anisotropy coefficient in uniaxial tension along the RD
r_{45}	Anisotropy coefficient in uniaxial tension at 45° with the RD
r_{90}	Anisotropy coefficient in uniaxial tension along the TD
t	Sheet thickness
t_0	Initial sheet thickness
V	Volume of fluid accumulated inside the cap
Y	Flow stress

Chapter 1.

General Introduction

This chapter introduces the framework of the study in the current area of research, related to the characterization of the plastic behaviour of metal sheets and particularly by using the hydraulic bulge test. The objectives and achievements of the developed research under this thesis are presented, comprising the studies and proposed methodologies up to the direct and inverse analysis of circular bulge test.

Also, a global overview of the document is presented by describing its structure and defining the covered topics in each chapter.

[Page intentionally left blank]

1.1. Background and Motivation

Currently, products manufactured from metal sheets are used in many industrial applications, from general machinery to automobile and aircraft components and even consumer goods. The main reason for using these products from sheet metal is related to the high productivity rate, as well as the increased ease of manufacturing and automation.

The analysis by the Finite Element Method (FEM) is currently unavoidable in the design of metal forming processes. On the other hand, the modelling of plastic behaviour of metal sheets, used in forming processes, is an important issue for the numerical simulation [1–3]. For this reason, the development of models with the objective to improving the description of the yield locus [4–8] and its evolution during deformation [9-13] is of fundamental importance, if accuracy of numerical results is to be improved. The introduction of new materials in this area of engineering has also encouraged the development of numerical modelling topics; as examples of these materials, one shall mention the high-strength steels, aluminium alloys or magnesium alloys, which are being increasingly used in the automotive industry. These materials present different and characteristic behaviours, such as higher springback and a lower formability, when compared with traditional materials (e.g. mild steels). The sheet metal processing of these non-traditional materials is thus a challenge, both experimentally and for the numerical simulation, because the existing models reveal not always the needed suppleness to adequately describe all aspects of their behaviour. Moreover, the results of numerical simulation of metal forming processes are influenced not only by the selected constitutive model but also by the values of corresponding parameters. In fact, the convenient description of mechanical behaviour of metal sheets depends largely on the parameter identification strategies [14,15].

Up to now, the strategies for identification of the constitutive parameters generally consist on an optimization problem, where an objective function is used to minimize the gap between the experimental and computed results [3,16–20]. When different types of experimental data are available to be used, each term in the objective function is multiplied by a weight coefficient, which states the relative importance for each type of data or mechanical test. Generally, the weight coefficients are chosen by the user, and there is no

established procedure, being suitable to define the best values for these coefficients. These methodologies lead to results for the constitutive model parameters that depend on the type and number of mechanical tests and respective available data, the weight coefficients and even the optimization algorithm or objective function.

Several tests, such as simple tension, at different angles with the rolling direction, shear and biaxial stress (cruciform tests or circular bulge test) are generally used for identification of the constitutive parameters [21,22]. However, only occasionally all these tests are simultaneously considered. Moreover, the strain paths associated with these tests do not entirely correspond to those observed in deep-drawing components: simple tension rarely occurs, and shear only occurs in the blank flange (volume within the blank holder). In fact, most of the strain paths in these components are in the range between simple tension and balanced biaxial tension. In case of biaxial stress paths (balanced or unbalanced), the bulge test allows to obtain relatively high strain values before necking, when compared to, e.g. cruciform tests, [23,24] and so the definition of the equivalent stress *vs*. strain curves can be performed up to large strain values, for several strain paths that mainly depend on the geometry of the die (circular or elliptical).

At present, the access to computational methods enables the simulation of metal forming processes, in an increasingly sophisticated and realistic way and the use of these numerical codes allows fast resolution of plasticity problems. The numerical simulation results presented in this thesis were obtained using the finite element code DD3IMP, which was developed and continuously updated in Experimental Technology Group and Computational, in Mechanical Engineering Centre at the University of Coimbra – CEMUC. This code is particularly devoted to three-dimensional numerical simulation of metal forming processes, including sheet metal forming processes [25,26]. The available facilities in Institute of Science and Innovation in Mechanical and Industrial Engineering – INEGI were also used to carry experimental bulge tests.

1.2. Objectives and Achievements

The purpose of this thesis is to analyse the circular bulge test, in order to establish methodologies that can improve the accuracy and simplification of the experimental procedures to obtaining the stress *vs.* strain curves in biaxial strain paths. This presumes analysing variables of bulge test, such as the principal strains and stresses in the sheet plane, curvature and sheet thickness at the pole of the cap, pressure and pole height evolutions, by resorting to numerical simulation capabilities. Based on this analysis, the objectives also include obtaining simplified and accurate procedures, which will give the assessment of sheet metal behaviour in biaxial strain and stress paths, those which can be found from bulge test. In fact, the current experimental procedures require the use of relatively complex devices that generate data with time consuming analysis, also revealing calibration and accuracy issues not always adequately solved. Moreover, in case of materials with planar anisotropy, the stress and strain paths are hardly experimentally defined, which prevents a proper analysis.

In order to study particular features of this test, systematic numerical analyses on materials with isotropic and anisotropic behaviour was carried out, concerning the geometry of the cap and the stress and strain distributions at the pole, and also the evolutions of the radius of curvature and sheet thickness during the test.

This analysis will take advantage in the development of methods to explore the experimental results, according to its procedures, as well as defining equations for the evolutions of the sheet thickness and the curvature radius during the test, which allows the assessment of the biaxial flow stress curve. The main target is to simplify the experimental procedure, thus avoiding the experimental complexity for determining the stress and strain values at different moments of the test, which requires specific devices for assessing the curvature radius and the sheet thickness at the pole of the cap. The proposed equations were tested using numerical generated results of the bulge test as well as experimental data.

In addition, the possibility to achieve a unified description of the pressure evolution with the pole height, was explored. This gives the understanding that it is possible the overlapping of the curves pressure *vs.* pole height of different metal sheets, provided that the hardening

parameter of the Swift law has the same value, whatever the values of the remaining hardening and anisotropy parameters of the material, and sheet thickness. To succeed obtaining the overlapping of the curves, one needs that the values of the pressure and the pole height shall be multiplied by factors which depend on the ratio between the yield stresses of the materials, and the anisotropy and thicknesses ratio of the sheets. This strategy allowed the development of a simplified inverse analysis strategy for determining all parameters of the Swift law, from the results of pressure *vs.* pole height. This methodology provides an efficient and easy to implement alternative, which was also tested using numerical generated bulge test results as well as the experimental data.

1.3. Thesis Outline

In order to facilitate the reading and understanding of this thesis, the current section presents the structure as well as a brief summary of the topics covered in each chapter. The content of the thesis is organized into four chapters; this first chapter defines the framework of the work in the area to which it belongs, i.e. the characterization of the plastic behaviour of metal sheet, and sets the objectives and achievements of this work.

Chapter 2 presents the literature review of the bulge test, by referring to the membrane theory and methodologies for assessing the hydraulic pressure and radius of curvature, stress, strain, and sheet thickness at the pole. Direct and inverse methodologies for assessing the hardening law are described. Reference is made to the standard ISO 16808:2014 for the bulge test.

Chapter 3 is composed of three papers that consist on the innovative research conducted within the framework of this thesis; the first paper concerns "*Anisotropy and plastic flow in circular bulge test*"; the second paper discusses "O*n the determination of the work hardening curve using the bulge test*"; and the last paper is related to "*Inverse Identification of Swift law parameters using the bulge test*".

Chapter 4 summarizes the main issues addressed in the thesis, emphasising the main contributions of the present work. At the end of this chapter, some recommendations for future work are provided.

References

[1] Choi Y, Han C-S, Lee JK, Wagoner RH. Modeling multi-axial deformation of planar anisotropic elasto-plastic materials, part I: Theory. Int J Plast 2006; 22: 1745–64. Doi:10.1016/j.ijplas.2006.02.002.

[2] Choi Y, Han C-S, Lee JK, Wagoner RH. Modeling multi-axial deformation of planar anisotropic elasto-plastic materials, part II: Applications. Int J Plast 2006; 22: 1765–83. Doi:10.1016/j.ijplas.2006.02.003.

[3] Flores P, Duchene L, Bouffioux C, Lelotte T, Henrard C, Pernin N, et al. Model identification and FE simulations: Effect of different yield loci and hardening laws in sheet forming. Int J Plast 2007; 23: 420–49. Doi:10.1016/j.ijplas.2006.05.006.

[4] Barlat F, Lege DJ, Brem JC. A six-component yield function for anisotropic materials. Int J Plast 1991; 7: 693–712. Doi:10.1016/0749-6419(91)90052-Z.

[5] Cazacu O, Barlat F. Generalization of Drucker's Yield Criterion to Orthotropy. Math Mech Solids 2001; 6: 613–30. Doi:10.1177/108128650100600603.

[6] Bron F, Besson J. A yield function for anisotropic materials Application to aluminum alloys. Int J Plast 2004; 20: 937–63. Doi:10.1016/j.ijplas.2003.06.001.

[7] Barlat F, Aretz H, Yoon JW, Karabin ME, Brem JC, Dick RE. Linear 7ransformation-based anisotropic yield functions. Int J Plast 2005; 21: 1009–39. Doi:10.1016/j.ijplas.2004.06.004.

[8] Hu W. An orthotropic yield criterion in a 3-D general stress state. Int J Plast 2005; 21: 1771–96. Doi:10.1016/j.ijplas.2004.11.004.

[9] Chaboche JL. Constitutive equations for cyclic plasticity and cyclic viscoplasticity. Int J Plast 1989; 5: 247–302. Doi:10.1016/0749-6419(89)90015-6.

[10] Chun BK, Jinn JT, Lee JK. Modeling the Bauschinger effect for sheet metals, part I: theory. Int J Plast 2002; 18: 571–95. Doi:10.1016/S0749-6419(01)00046-8.

[11] Chun BK, Kim HY, Lee JK. Modeling the Bauschinger effect for sheet metals, part II: applications. Int J Plast 2002; 18: 597–616. Doi:10.1016/S0749-6419(01)00047-X.

[12] Lee M-G, Kim D, Kim C, Wenner ML, Wagoner RH, Chung K. Spring-back evaluation of automotive sheets based on isotropic-kinematic hardening laws and non-quadratic anisotropic yield functions. Int J Plast 2005; 21: 883–914. Doi:10.1016/j.ijplas.2004.05.015.

[13] Lee M-G, Kim D, Kim C, Wenner ML, Chung K. Spring-back evaluation of automotive sheets based on isotropic–kinematic hardening laws and non-quadratic anisotropic yield functions, part III: applications. Int J Plast 2005; 21: 915–53. Doi:10.1016/j.ijplas.2004.05.014.

[14] Alves JL. Simulação numérica do processo de estampagem de chapas metálicas: Modelação mecânica e métodos numéricos. PhD Thesis. University of Minho, 2003.

[15] Chaparro BM. Comportamento plástico de materiais metálicos: identificação e optimização de parâmetros. PhD Thesis. University of Coimbra, 2006.

[16] Rabahallah M, Balan T, Bouvier S, Bacroix B, Barlat F, Chung K, et al. Parameter identification of advanced plastic strain rate potentials and impact on plastic anisotropy prediction. Int J Plast 2009; 25: 491–512. Doi:10.1016/j.ijplas.2008.03.006.

[17] Stoughton TB, Yoon JW. Anisotropic hardening and non-associated flow in proportional loading of sheet metals. Int J Plast 2009; 25: 1777–817. Doi:10.1016/j.ijplas.2009.02.003.

[18] Chaparro BM, Alves JL, Menezes LF, Fernandes J V. Optimization of the Phenomenological Constitutive Models Parameters Using Genetic Algorithms. Adv. Methods Mater. Form. SE – 3, Springer Berlin Heidelberg; 2007, p. 35–54. Doi:10.1007/3-540-69845-0_3.

[19] Chaparro BM, Thuillier S, Menezes LF, Manach PY, Fernandes J V. Material parameters identification: Gradient-based, genetic and hybrid optimization algorithms. Comput Mater Sci 2008; 44: 339–46. Doi:10.1016/j.commatsci.2008.03.028.

[20] Bouvier S, Gardey B, Haddadi H, Teodosiu C. Characterization of the strain-induced plastic anisotropy of rolled sheets by using sequences of simple shear and uniaxial tensile tests. J Mater Process Technol 2006; 174: 115–26. Doi:10.1016/j.jmatprotec.2005.04.086.

[21] Koç M, Billur E, Cora ÖN. An experimental study on the comparative assessment of hydraulic bulge test analysis methods. Mater Des 2011; 32: 272–81. Doi:10.1016/j.matdes.2010.05.057.

[22] Zang SL, Thuillier S, Le Port A, Manach PY. Prediction of anisotropy and hardening for metallic sheets in tension, simple shear and biaxial tension. Int J Mech Sci 2011; 53: 338–47. Doi:10.1016/j.ijmecsci.2011.02.003.

[23] Santos AD, Teixeira P, Barata da Rocha A, Barlat F, On the Determination of Flow Stress Using Bulge Test and Mechanical Measurement. In: Barlat F, Moon YH, Lee MG, editors. 10th Int. Conf. NUMIFORM, Pohang, Republic of Korea: American Institute of Physics; 2010, p. 845–52. Doi:10.1063/1.3457644.

[24] Santos AD, Teixeira P, Barlat F. Flow stress determination using hydraulic bulge test and a mechanical measurement system. Int. Deep Draw. Res. Gr. Conf. IDDRG, Bilbao, Spain: IDDRG; 2011, p. 91–100.

[25] Menezes LF, Teodosiu C. Three-dimensional numerical simulation of the deep-drawing process using solid finite elements. J Mater Process Technol 2000; 97: 100–6. Doi:10.1016/S0924-0136(99)00345-3.

[26] Oliveira MC, Alves JL, Menezes LF. Algorithms and Strategies for Treatment of Large Deformation Frictional Contact in the Numerical Simulation of Deep Drawing Process. Arch Comput Methods Eng 2008; 15: 113–62. Doi:10.1007/s11831-008-9018-x.

[Page intentionally left blank]

Chapter 2.

Literature Review

This chapter provides a literature review on the bulge test, which includes the definition of the membrane theory and the existing methodologies to evaluate the hydraulic pressure, the radius of curvature, the sheet thickness, the strain and the stress at the pole of the cap. Direct approaches and inverse analysis methodologies for determining the hardening curve are also described. A brief reference and description of the International Standard ISO 16808:2014, for determination of the biaxial stress *vs*. strain curve of metallic sheet by the bulge test, is additionally presented.

[Page intentionally left blank]

2.1. Hydraulic Bulge Test

The hydraulic bulge test has started to be studied since the mid-twentieth century and has become an increasingly common test to examine the plastic behaviour of metal sheets under biaxial tension. In the 1980s and 1990s, further developments and confirmations have been carried out, for example evolving comparison of analytical with experimental solutions, as by Shang *et al*. [1]. This test has stimulated the interest of researchers for determining the stress *vs*. strain curves up to significantly high levels of deformation (up to about 70%, depending on the hardening coefficient of the material), as compared to those achieved in uniaxial tensile tests, where the uniform deformation is limited by the necking. Therefore, the bulge test can give supplementary description of the plastic behaviour of metal sheets during the forming processes [2], when compared to other tests. Additionally, when combined with other tests, the biaxial test gains importance, since it allows the analysis of the anisotropy of the material by comparing the respective biaxial stress *vs*. strain curves with those obtained from uniaxial tensile tests and other tests under different strain paths [3].

In this test, the periphery of a metal sheet is immobilized using, for example, a circular drawbead, which prevents this region of the sheet to move in the radial direction. Then a pumping hydraulic fluid (mostly used) [4], a viscous material (to prevent leakage) [5,6] or a pneumatic gas (most utilized at elevated temperature levels) [7], is used as a pressure medium and applied in the central area on one side of the sheet, deforming it into approximately spherical or ellipsoidal shape, depending on the geometry of the die, being circular or elliptical. The deformation of the sheet is promoted by the applied hydraulic pressure, which minimizes the problems associated with the characterization of frictional contact. The test conditions promote the biaxial strain path at the pole of the cap, which in the case of a circular die, is approximately spherical in the region of the pole and along a circle of constant latitude [8,9].

The circular bulge test has been the subject of growing interest in the characterization of the hardening law and the determination of the yield surface at room [10] and warm [11] temperatures. However, the analysis of the test shows some complexities, since the evaluation of the hardening law is performed using the membrane theory [12], which

requires the evaluation of the radius of curvature, the sheet thickness at the pole and the hydraulic pressure during the test. Alternatively, the determination of the sheet thickness at a given moment of the test can be performed based on various mathematical models, which take into account the geometry of the test [2,13] or the strain value at the pole. Moreover, the analysis of the test generally assumes isotropy and equibiaxial stress and strain [14], although the metal sheets are usually anisotropic [15]. The results of Yoshida [16] show that for orthotropic sheet metals, the stress state at the top of the cap deviate by 1-5% from the equibiaxial stress state, although his results only concern materials with relatively low anisotropy in the sheet plane.

This test can also be used to obtain the strain limits defining the points of the Forming Limit Curve (FLC), with a typical example represented in Figure 2.1. Usually, the FLC is determined using experimental tests, between uniaxial tension and biaxial stretching (such as bulge test with circular and elliptical dies geometries to obtain various strain paths), with monotonic loading paths, meaning that it is only valid for processes in which the loading path is linear. However, non-linear strain paths play an important role in forming of complex shapes, when changes of direction occur for metal flow.

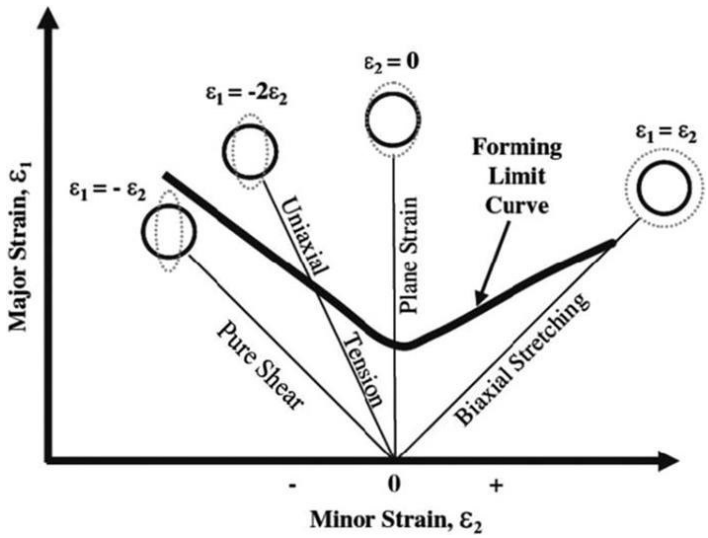

Figure 2.1. Schematic representation of Forming Limit Curve [17].

Measurement devices used in experimental tests have been developed over the last years. They can be grouped into mechanical and optical systems.

Young *et al*. [18] describes mechanical systems for direct measurement of the radius of curvature and strain at the pole of the cap using a three point spherometer and an extensometer, respectively. These measurement systems, similar to those used in INEGI (see Figure 2.2), involve mechanical contact with the sheet to be tested. The spherometer evaluates, during the test, the height difference between the pole and three positions at a fixed radius. The radius of curvature of the sphere at the pole of the cap follows a simple geometrical equation that is presented later in the respective subchapter. The extensometer allows determining the strain value in the sheet plane, in a region near the pole of the cap, during the test in one material orientation. The data recorded during the test are the pressure, the height between the pole and the three points spherometer, as well as the distance between the extensometer tips. The positions of the three points for the spherometers and the initial diameter for the extensometer was optimized by Santos [19], through the use of numerical simulations.

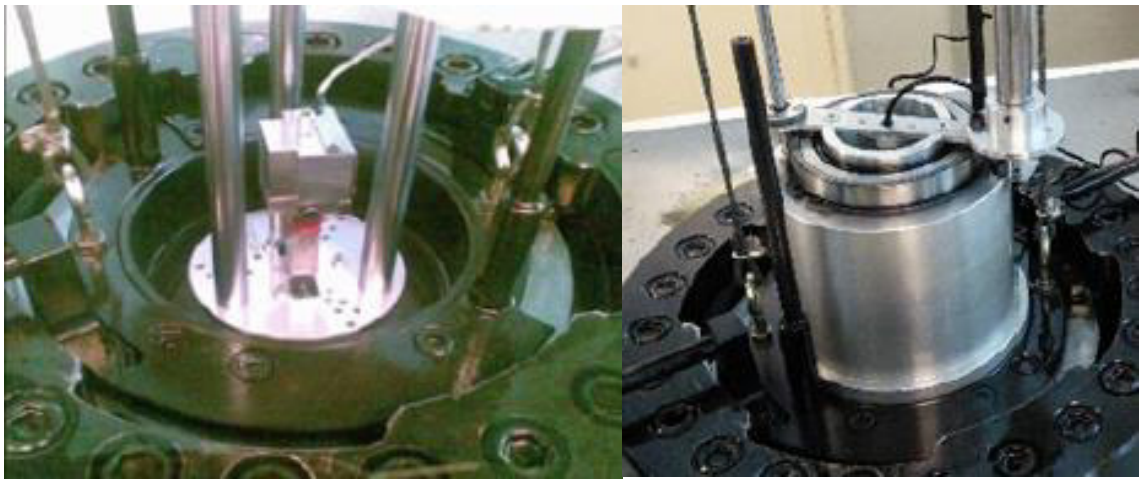

Figure 2.2. Experimental bulge test device used in INEGI [20].

The use of mechanical measurement systems requires the assumption that an equibiaxial strain state exists at the pole of the cap (which is not the general case of anisotropic materials [21]), since they only allow determining the strain along in one direction.

Optical measuring systems are alternative to determine the strain state in anisotropic materials [22]. Mutrux *et al*. [23] and Keller *et al*. [24] describe 3D optical systems that consist of two cameras and a laser. The lasers sensors can measure the shape of the cap based on the spatial coordinates of points previously marked on the surface of the sheet. The

camera system uses a previously filed grid on the surface blank to evaluate the principal strains, ε_1 and ε_2, in the sheet plane. The sheet thickness is determined based on the principal strains in the sheet plane, while the radius of curvature is usually obtained by fitting a spherical function to points near the pole of the cap. Mulder *et al*. [25] evaluated the profile of the bulge by fitting spherical, paraboloid and ellipsoid shapes functions using the least squares method. These authors [25] reach the same conclusion as Güner *et al*. [26], that is the radius of curvature can be accurately derived by any of those shape functions, but the ellipsoidal function allows a wider range of data points to be considered without loss of accuracy.

In the next subsections it is presented an overview of the methodologies for determining the radius of curvature, the sheet thickness and the strains and stress, at the pole of the cap during the bulge test. These variables are used for determining the biaxial stress *vs*. strain curve. Inverse analysis methodologies for identifying the parameters of the hardening law from the bulge test results are also described. In order to standardize determination of the biaxial stress *vs*. strain curve from this test, the German group's IDDRG (International Deep Drawing Research Group) made a proposal to ISO standards in July 2007 for the bulge test under hydraulic pressure [24,27]. Recently, this International Standard has been published as an ISO 16808:2014 [28] and at the end of this chapter, a brief summary of the ISO standard is presented.

2.2. Membrane Theory

During the bulge test, the inner surface of the sheet is submitted to pressure, so that its shape at the top of the cap is approximately spherical or ellipsoidal (depending on the die geometry used). Thus, the surface geometry at the pole can display one or two radii of curvature, respectively.

The analysis of the installed stresses in the sheet during the bulge test is performed using the membrane theory [12], which is valid for a small ratio between the sheet thickness and the bulge die diameter, typically values lower than 1/50 are recommended for circular die [29,30]. Under these conditions, the bending stresses can be neglected and it can be assumed that the thickness stress is zero.

Let us consider a small surface element at the pole of the cap, to which is associated the O*xyz* axis system, coincident with the axes of anisotropy of the sheet, as shown in Figure 2.3. The main geometrical characteristics of the element are also presented in the figure.

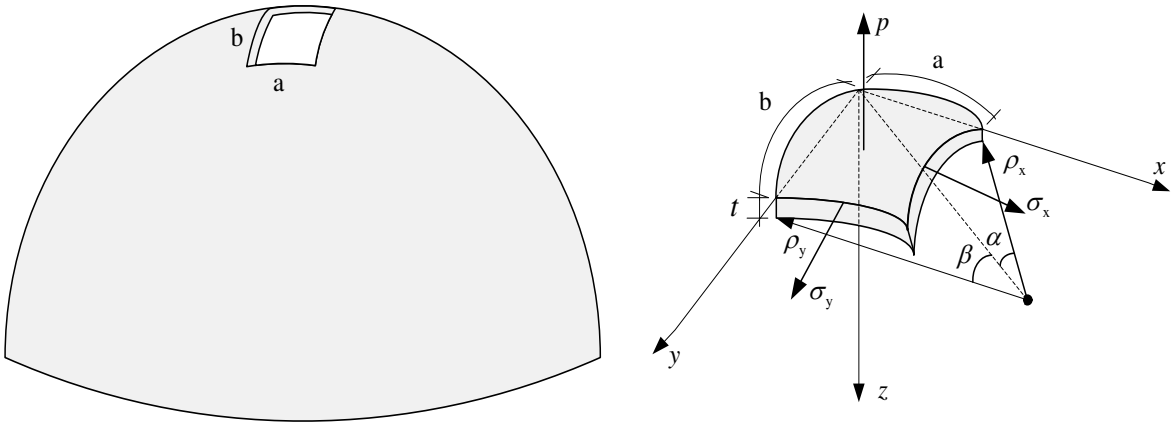

Figure 2.3. Small element at the pole of the cap (adapted from [31]).

Figure 2.4 shows the forces acting on the element, showing details of its geometry, where t is the sheet thickness, ρ_x and ρ_y are the radii of curvature in the O*xz* and O*yz* planes, a and b are respectively the element dimensions according to Ox and Oy directions, and σ_x and σ_y are the stresses in the sheet plane.

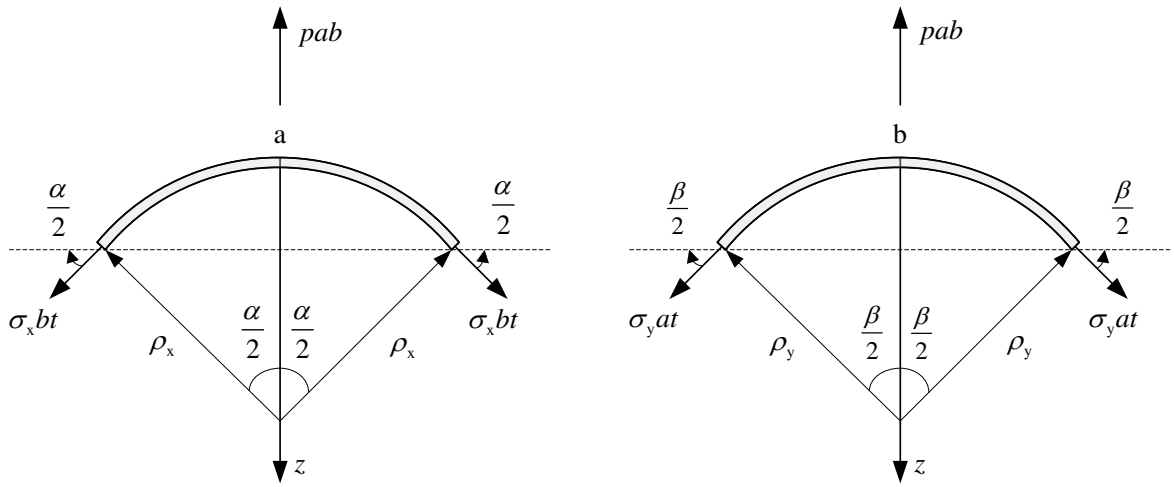

Figure 2.4. Geometry of the pole of the cap in the O*xz* (left) and O*yz* (right) plans. The stresses promoting the balance of forces, at each moment of the test, are also shown (adapted from [31]).

The balance of forces in the Oz direction allows obtaining the following equation:

$$2\sigma_x bt \sin\left(\frac{\alpha}{2}\right) + 2\sigma_y at \sin\left(\frac{\beta}{2}\right) = pab\,, \tag{2.1}$$

Considering that the size of the element tends to zero and so the angles α and β are also small, one can write:

$$\sin\alpha \cong \alpha = \frac{a}{\rho_x} \text{ and}$$
$$\sin\beta \cong \beta = \frac{b}{\rho_y}\,. \tag{2.2}$$

and replacing into equation (2.1), the following can be obtained:

$$\frac{\sigma_x}{\rho_x} + \frac{\sigma_y}{\rho_y} = \frac{p}{t}\,. \tag{2.3}$$

This equation is called membrane theory equation or Laplace's Equation. For the case of in-plane isotropic materials, using a circular die, it can be simplified as examined in the following section.

2.3. Analysis of the test

To perform the analysis of the bulge test, i.e. to determine σ_x and σ_y in order to establish the stress *vs*. strain curve of the material, it is necessary to know the value of each variable of the membrane theory (equation (2.3)) at various test steps. That is, to experimentally determine the stress *vs*. strain curve it is required the determination of the evolution of pressure, p, the radii of curvature, ρ_x and ρ_y, and the sheet thickness at the pole, t, during the test. The radius of curvature and sheet thickness at the pole of the cap can be determined using different procedures, referred in the literature, which are described and analysed in the following subsections.

2.3.1. Hydraulic pressure

During the bulge test, the pressure is imposed by a hydraulic pump and is uniformly distributed on one side of the sheet, which deforms with the approximate shape of a spherical or ellipsoidal surface, depending on the die used and the sheet properties. The pressure is recorded during the test.

2.3.2. Radius of curvature

The determination of the stress *vs*. strain curve with the membrane theory requires the knowledge of the radius of curvature of half thickness at pole of the cap, which can be obtained by different procedures. Some of these procedures are now described.

Some authors [16,25,30] consider that the radius of curvature shall be measured in the two principal directions of the circular bulge specimen. However, the analysis performed by other authors, using computer generated results, indicates that the radii of curvature are equal in principal directions, even in anisotropic materials [32]. The radius of curvature is experimentally determined during the test on the outer surface of the cap, ρ_{ext}, using either contact or contactless equipment. The radius of curvature at half thickness, ρ, of the sheet to be considered in equation (2.3) can be determined based on the following equations [33,34], respectively:

$$\rho = \rho_{ext} - \frac{t}{2} \tag{2.4}$$

$$\rho = \rho_{ext} - 0.6t \tag{2.5}$$

where t is the actual sheet thickness at the pole of the cap.

Equation (2.4) is generally the most used experimentally. Equation (2.5) tries to balance the fact that the centres of curvature do not coincide, for the outer surface and at half thickness, because the sheet thickness increases from the pole towards the periphery (see Figure 2.5). Figure 2.5 shows the difference between the radius of curvature at half thickness of the sheet considering non-homogeneous thinning ρ and homogeneous thinning ρ^*.

In case of non-homogeneous thinning at the top of the cap it is shown that ρ is smaller than ρ^*.

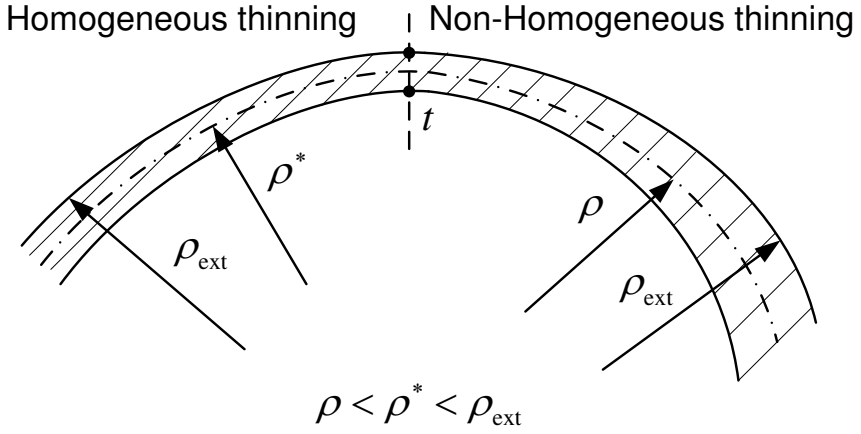

Figure 2.5. Difference between homogeneous and non-homogeneous thinning (adapted from [33]).

In the experimental test, the determination of the radius of curvature can be evaluated using optical systems [26], by fitting a suitable function to the measured points, or using three points spherometers [35], as shown in Figure 2.6. In case of spherometers, the experimental evaluation of the radius of curvature can be performed based on the diameter between the spherometers, D_{CV}, and the height difference, h_{CV}, between the pole and the three positions of the spherometers, based on the following equation [34,36]:

$$\rho_{ext} = \frac{\left(D_{CV}/2\right)^2 + {h_{CV}}^2}{2h_{CV}}. \tag{2.6}$$

Another procedure for determining the radius of curvature at the pole of the cap is the use of models [29,37,38] involving some geometric parameters of the cap, at each moment of the test, as shown in Figure 2.7. The initial thickness of the sheet is t_0, ρ_{ext} is the radius of curvature of the outer surface of the sheet at the pole, R_M is the die radius, R_1 is the die profile radius, h is the pole height at each moment of the test, C_0 is the initial length of the region used for determining the radius, ρ_{ext}, and α is the angle subtended by the centre of the test (O), the centre of curvature of the concordance zone of the die (Q) and the pole of the cap (P). Table 2.1 shows examples of models proposed for determining the radius of curvature at the pole of the cap, which avoid the use of spherometer or optical systems.

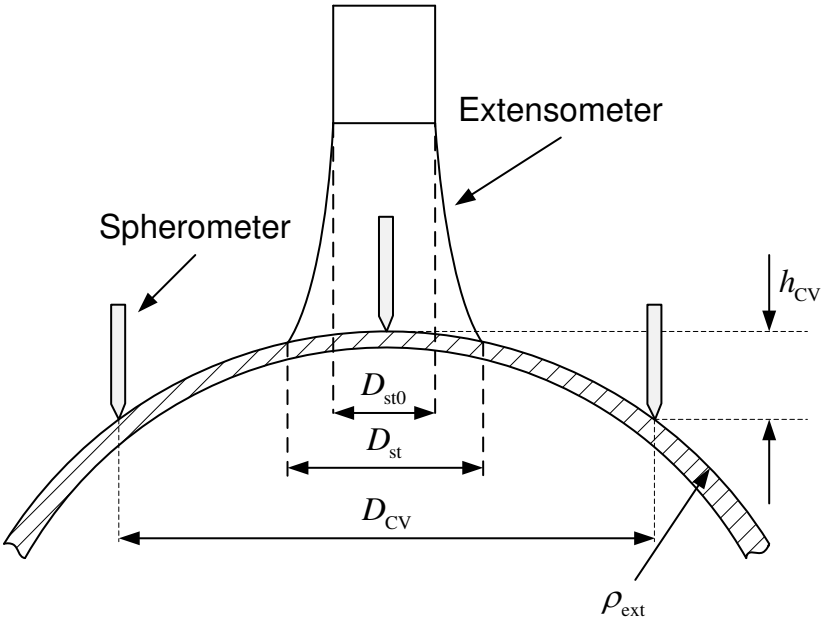

Figure 2.6. Variables used in the analysis of the experimental bulge test (adapted from [20]).

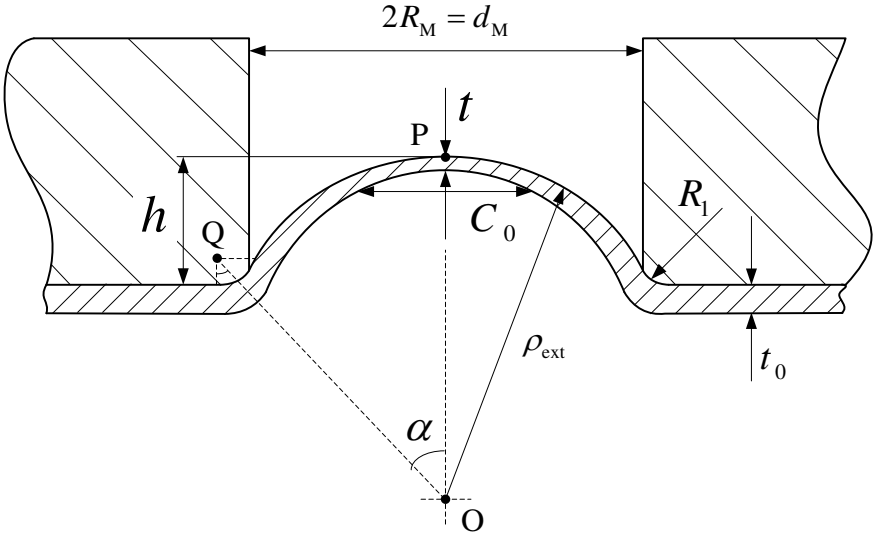

Figure 2.7. Geometrical parameters of the bulge test (adapted from [39]).

Table 2.1. Equations proposed for determining the radius of curvature at the pole of the cap.

References	Radius of Curvature Models
Hill [40] [see: [37]]	$\rho_{ext} = \frac{R_M{}^2 + h^2}{2h}$
Panknin [41] [see: [37]]	$\rho_{ext} = \frac{\left(R_M + R_1\right)^2 + h^2 - 2R_1 h}{2h}$

$$\rho_{ext} = \left(\frac{V\pi}{12}\right)\left\{\left[72V^2 R_M{}^6\pi^2 + 648V^4 + R_M{}^{12}\pi^4 + 12\left(\begin{array}{l}\left(45V^2 R_M{}^{12}\pi^4 + 648V^4 R_M{}^6\pi^2\right)^{\frac{1}{2}} \\ + R_M{}^{18}\pi^6 + 2916V^6\end{array}\right)V\right]\pi^2\right\}^{\frac{1}{3}}$$

$$+\left\{\left(\frac{R_M{}^8\pi^3}{12V}\right)\left\{\left[72V^2 R_M{}^6\pi^2 + 648V^4 + R_M{}^{12}\pi^4 + 12\left(\begin{array}{l}\left(45V^2 R_M{}^{12}\pi^4 + 648V^4 R_M{}^6\pi^2\right)^{\frac{1}{2}} \\ + R_M{}^{18}\pi^6 + 2916V^6\end{array}\right)V\right]\pi^2\right\}^{\frac{1}{3}}\right\}^{-1}$$

$$+\frac{R_M{}^4\pi}{12V}$$

Model of Smith *et al*. [42]

In the last model (Smith *et al*. [42]), the radius of curvature of the outer surface, ρ_{ext}, depends on of the die radius, R_M, and on the total volume of fluid accumulated inside the cap, V.

The experimental results presented in the literature [29,43] show that the Panknin model describes the evolution of the radius of curvature of the cap during the test, better than the others.

2.3.3. Sheet thickness

The determination of the stress *vs*. strain curve with the aid of the membrane theory needs the knowledge of the evolution of the sheet thickness at the pole of the cap, during the bulge test. The procedure for determining the sheet thickness at the pole of the cap [33,34] is based on the knowledge of the initial thickness of the sheet, t_0, and the thickness strain, ε_3, through the following equation:

$$t = t_0 \exp\left(-\varepsilon_3\right). \tag{2.7}$$

The thickness strain, ε_3, can be obtained from the measure of the principal strains in the sheet plane, ε_1 and ε_2, based on the condition of volume constancy during plastic deformation:

$$\varepsilon_1 + \varepsilon_2 + \varepsilon_3 = 0. \tag{2.8}$$

In the general case with anisotropic materials, $\varepsilon_1 \neq \varepsilon_2$, which allows to write:

$$\varepsilon_3 = -\left(\varepsilon_1 + \varepsilon_2\right). \tag{2.9}$$

Assuming isotropy, ($\varepsilon_1 = \varepsilon_2 = \varepsilon$), as commonly used, the thickness strain can be determined as follows:

$$\varepsilon_3 = -\left(\varepsilon_1 + \varepsilon_2\right) = -2\varepsilon. \tag{2.10}$$

Some authors [2,13,29,37,39,44] reported that the small size of the region near the pole of the cap with uniform strain makes it difficult to experimentally determine the adequate value of the sheet thickness. Consequently, these and other authors have proposed models to obtain the sheet thickness at the pole during the test, based on the geometry parameters of the bulge test shown in Figure 2.7.

Table 2.2 summarizes the proposed models for determining the sheet thickness at the pole, based on the parameters defined in Figure 2.7. In this table, $\overline{r}$ is the normal anisotropy coefficient and, K and n (hardening coefficient) are the parameters of the Swift hardening law [45]:

$$\overline{r} = \frac{r_0 + 2r_{45} + r_{90}}{4}. \tag{2.11}$$

$$Y = K\left(\varepsilon_0 + \bar{\varepsilon}\right)^n . \tag{2.12}$$

The purpose of the next paragraph is to briefly analyse and comment some details of the models of Table 2.2.

Table 2.2. Equations to determine the sheet thickness at the pole.

References	Thickness Models
Hill [40] [see: [2]]	$t = t_0\left[\dfrac{1}{1+\left(h/R_{\mathrm{M}}\right)^2}\right]^2$
Chakrabarty and Alexander [46]	$t = t_0\left[\dfrac{1}{1+\left(h/R_{\mathrm{M}}\right)^2}\right]^{2-n}$
Atikson [44]	$t = \dfrac{\rho_{\mathrm{ext}} - \sqrt{{\rho_{\mathrm{ext}}}^2 - \dfrac{t_0\left(C_0\right)^2}{2h_{\mathrm{CV}}}}}{2}$
Enikeev-Kruglov [47]	$t = t_0\left(\dfrac{\sin\alpha}{\alpha}\right)^2 = t_0\left[\dfrac{\left(R_{\mathrm{M}}/\rho\right)}{\sin^{-1}\left(R_{\mathrm{M}}/\rho\right)}\right]^2$
Kruglov modified [47]	$t = t_0\left(\dfrac{\alpha}{\sin\alpha}\right)^{-2(1+c\alpha)}$
Isachenkov [48]	$t = \dfrac{t_0}{\left(1+\varepsilon_1\right)\left(1+K\varepsilon_1\right)}$
Constancy volume law [48]	$t = \dfrac{{R_{\mathrm{M}}}^2 t_0}{{R_{\mathrm{M}}}^2 + h^2}$
Jovane [48]	$t = t_0\left[\dfrac{{R_{\mathrm{M}}}^2}{\sin^{-1}\left(R_{\mathrm{M}}/\rho\right)^2}\right]^2$
Liu *et al*. [49]	$t = t_0\left(\dfrac{\mathrm{dR}}{\mathrm{d}\zeta}\dfrac{1}{\cos\theta}\right)^{-\frac{\beta+1}{(1+\bar{r})-\bar{r}\beta}}$

The model proposed by Hill (see reference [2] of [40]) was improved in order to consider the effect of hardening coefficient of the material. This parameter influences the evolution of the strain values at the pole of the cap during the test and therefore, the sheet thickness, as considered in the model by Chakrabarty and Alexander [46].

Kruglov [47] proposed an analytical model assuming that the strains are homogeneous in the pole region, but the evolution of the sheet thickness depends on the die geometry of the bulge [13].

In the modified Kruglov model, c is a constant coefficient, always positive, that takes in account the non-uniformity of the strain distribution on the surface of the cap. This coefficient can be calculated using the following equation:

$$c = \left(\ln \sqrt{\frac{t_0}{t_{\min}}} - \ln \frac{\alpha_{\max}}{\sin \alpha_{\max}} \right) \Bigg/ \left(\alpha_{\max} \ln \frac{\alpha_{\max}}{\sin \alpha_{\max}} \right), \tag{2.13}$$

where $t_{\min}$ is the minimum value of the thickness, that occurs for the maximum pressure and $\alpha_{\max}$ is the maximum value of α (see Figure 2.7); the value of $\alpha_{\max}$ can be obtained using the following equation:

$$\alpha_{\max} = \arcsin \left[\left(\frac{d_M}{2} + R_1 \right) \Bigg/ \left(\frac{1}{2h_{\max}} \left(\frac{d_M}{2} + R_1 \right)^2 + \frac{h_{\max}}{2} \right) \right], \tag{2.14}$$

where $h_{\max}$ is the pole height for the maximum pressure.

The recently model proposed by Liu *et al*. [49] considers a finite element bounded by section ζ and $(\zeta + \mathrm{d}\zeta)$, as shown in Figure 2.8. This element as an initial thickness t_0. As the pressure in the chamber increases the sheet will bulge to a cap with a height of pole h and a radius of curvature ρ. Thus, the point M which indicates the original location of the element moves to point M', whose position is defined by angle θ (see Figure 2.8), on the deformed element with thickness t. The distance from M' to the symmetry axes is the denoted as R while the original distance is ζ. The mechanical analysis of this element allows to define the differential equation that defines the evolution of R, such as:

$$\frac{\mathrm{dR}}{\mathrm{d}\zeta} = \left(\frac{R}{\zeta} \right)^{-\frac{(\bar{r}+1)-\bar{r}\beta}{(\bar{r}+1)-\bar{r}\beta-(\beta+1)}} \sqrt{1 - \left(\frac{R}{\rho} \right)^2}, \tag{2.15}$$

where the stress path, β, is determined based on the equation:

$$\beta = 1 - (0.5n + 0.3143)\left(\frac{\zeta}{R_M + R_1}\right)^{0.5/n+1.94}, \quad (2.16)$$

where n is hardening coefficient (Swift law) of the material. The authors show that the differential equation (2.15) can be numerically solved, using for instance the third-order Runge-Kutta method, enabling the prediction of the thickness distribution for a certain pole height as a function of the distance from the centre, using the equation presented in Table 2.2. It is also shown that at the pole of the cap the solution presents a numerical instability. Nevertheless, the calculated thickness evaluated at a distance of about 2 mm from the centre corresponds to an accurate estimate of the experimental results.

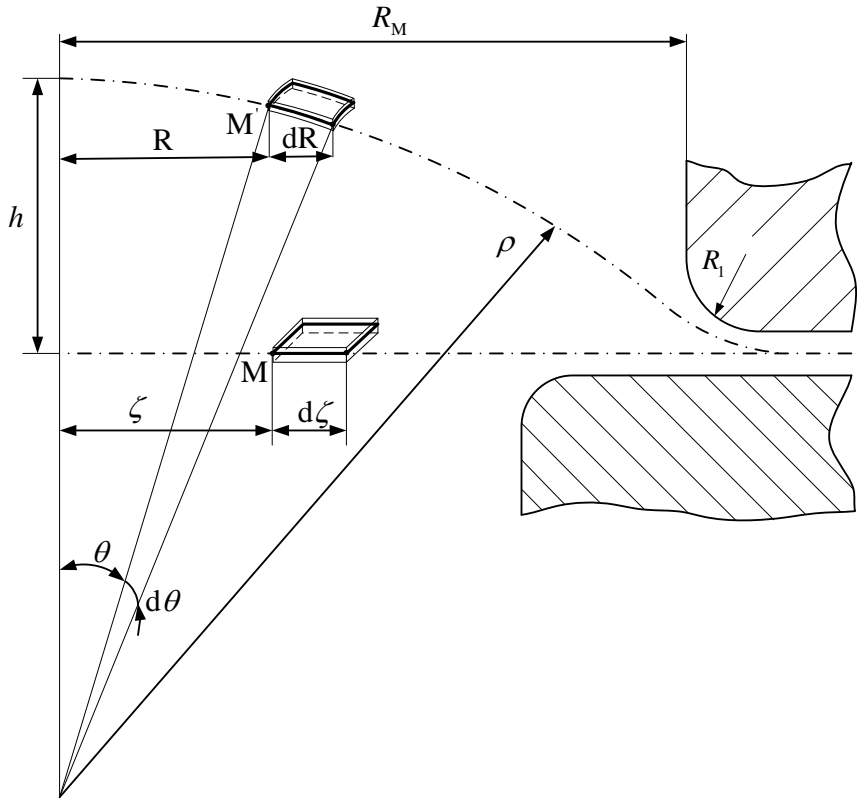

Figure 2.8. Schematic variables with small elements of the bulge test (adapted from [49]).

According to the experimental results available in the literature [29,43], the most recommended model for describing the evolution of sheet thickness at the pole of the cap during the test is the modified Kruglov model (this assessment does not include the recent model by Liu *et al*. [49]).

2.3.4. Strains and stresses

The principal strains in the sheet plane can be directly acquired during the test, using suitable Digital Image Correlation (DIC) equipment [25] or a mechanical extensometer [20]. In this last case, only one principal strain is measured (see Figure 2.6), and the determination of its value, ε, is performed by measuring the expansion of the initial distance between the extensometer, D_{st0}, which turns into D_{st}, during the bulge test, using the following equation:

$$\varepsilon = -\ln\left(\frac{D_{st0}}{D_{st}}\right). \tag{2.17}$$

Smith *et al*. [42] established an equation for determining the strain at the pole of the cap, without using traditional mechanical devices according to the pole height, h, at each moment of the test, and the diameter of the die, d_M, as follows:

$$\varepsilon = \ln\left[1+\left(\frac{h}{d_M}\right)^2\right]. \tag{2.18}$$

Since the measured strain values comprise two components, elastic and plastic, the elastic strain components, ε_1^e, ε_2^e and ε_3^e, must be removed from the measured strains values, ε_1 and ε_2 (before determining the equivalent strain, $\bar{\varepsilon}$) according to the equations of the generalized Hooke law, for isotropic elastic behaviour [28] (assuming null value for principal thickness stress, σ_3):

$$\begin{cases} \varepsilon_1^e = \dfrac{1}{E}\left[\sigma_1 - \nu\sigma_2\right] \\ \varepsilon_2^e = \dfrac{1}{E}\left[\sigma_2 - \nu\sigma_1\right] \\ \varepsilon_3^e = \dfrac{1}{E}\left[-\nu\left(\sigma_1 - \sigma_2\right)\right] \end{cases}. \tag{2.19}$$

The conventional analysis of this test considers that the bending effect is negligible for a low ratio between the sheet thickness and the diameter of the die, but it was pointed out [50,51] that must be taken into consideration. In case of assuming the Kirchhoff bending theory [50], with small strain gradients in the sheet plane, and for insignificant differences

between the principal radius of curvature, the bending strain influence, ε_b, is given by (and also assuming equation (2.4)):

$$\varepsilon_b = \ln\left(\frac{\rho_{ext}}{\rho}\right) = -\ln\left(1 - \frac{0.5t}{\rho_{ext}}\right). \tag{2.20}$$

Figure 2.9 shows the geometry near the pole of the cap with the definitions of the principal strains in the sheet plane, ε_1 and ε_2, and the bending strain, ε_b.

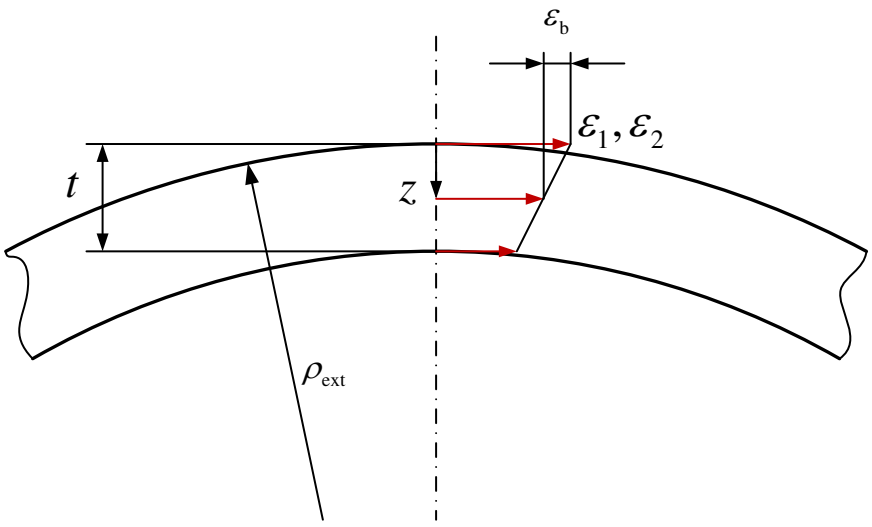

Figure 2.9. Strains definition at the pole of the cap, highlighting ε_b (adapted from [50]).

Using the volume constancy condition and correcting the principal strains with the bending strain, a relationship for the thickness strain at the middle plane, ε_{3mid}, can be used:

$$\varepsilon_{3mid} = -\varepsilon_{1mid} - \varepsilon_{2mid} = -\varepsilon_1 - \varepsilon_2 + 2\varepsilon_b \tag{2.21}$$

where ε_{1mid} and ε_{2mid} are the principal strains at the middle plane. Leppin *et al.* [50] concluded that removing only the bending strain components to the principal strains leads to a better and more straightforward approach than removing the elastic strain and including the bending components.

In general, the determination of the stresses at the pole of the cap is performed considering that the materials have isotropic behaviour [8,13–15,20,29,33,34,37,39,42,44], which generally does not occurs. Accordingly, assuming that the principal stress axes O123

coincide with the coordinate system axes O*xyz*, when the principal stresses are equal ($\sigma_1 = \sigma_2 = \sigma$), as well as the radii of curvature ($\rho_1 = \rho_2 = \rho$), the equation (2.3) can be simplified:

$$\sigma = \frac{p\rho}{2t}. \tag{2.22}$$

Also, in the case of planar anisotropy, Lemoine *et al*. [30] regards that the principal stresses in the sheet plane can be assumed equal ($\sigma_1 = \sigma_2 = \sigma$), although the radii of curvature should be considered different, ($\rho_1 \neq \rho_2$), allowing to simplify the equation (2.3), as follows:

$$\sigma = \frac{p}{t\left(1/\rho_1 + 1/\rho_2\right)}. \tag{2.23}$$

Using equations (2.22) and (2.23), the evaluation of the stress *vs*. strain curve of the materials may not be appropriate for materials with anisotropic behaviour, although Mulder *et al*. [25] describe that for materials with in plane anisotropic behaviour ($r_0 = 0.5$, $r_{45} = r_{90} = 1$) the error in stress is relatively small (less than 3%). Furthermore, the circular bulge test has equal radii of curvature [14].

Knowing the values of stresses and strains at the pole of the cap, the equivalent stress *vs*. strain curve can be determined using the von Mises equations [52]:

$$\bar{\sigma} = \sqrt{\left(\sigma_1\right)^2 + \left(\sigma_2\right)^2 - \sigma_1\sigma_2}\,, \tag{2.24}$$

$$\bar{\varepsilon} = \left(\frac{2}{\sqrt{3}}\right)\sqrt{\varepsilon_1^2 + \varepsilon_2^2 + \varepsilon_1\varepsilon_2}\,. \tag{2.25}$$

The equivalent stress and strain under equibiaxial stress and strain paths, according to von Mises, are given by:

$$\bar{\sigma} = \sigma \text{ and } \bar{\varepsilon} = 2\varepsilon. \tag{2.26}$$

Due to the rolling condition, sheet metal properties varies from each direction with respect to rolling to transverse direction, equivalent stress and strain components should be corrected for anisotropy. This is not considered, in equations (2.22) and (2.23), where no anisotropy correction has been carried out. Assuming Hill'48 criterion, Smith *et al*. [53] proposed equations (2.27) and (2.28) for determination of equivalent stress, $\bar{\sigma}_{\text{aniso}}$, and strain, $\bar{\varepsilon}_{\text{aniso}}$, under anisotropy conditions, taking into account the normal anisotropy coefficient ($\bar{r}$):

$$\bar{\sigma}_{\text{aniso}} = \bar{\sigma}\left[2 - \frac{2\bar{r}}{\bar{r}+1}\right]^{1/2}, \tag{2.27}$$

$$\bar{\varepsilon}_{\text{aniso}} = \frac{\bar{\varepsilon}}{\left[2 - \frac{2\bar{r}}{\bar{r}+1}\right]^{1/2}}. \tag{2.28}$$

where $\bar{\sigma}$ and $\bar{\varepsilon}$ is equivalent stress and strain, determined in isotropic conditions. This correction is only valid for materials whose mechanical behaviour obeys the Hill'48 yield criterion, but the behaviour of real materials can be better described by another yield criterion. In fact, the analysis of the test for anisotropic materials needs to consider that the stresses and strains in two perpendicular directions are different; this actually has not been analysed up to now. In order to more accurately determine the stress *vs*. strain curve, it is essential to take this into account, since the results available in the literature, determined from equations (2.22) and (2.23), show non-negligible errors.

Summarizing, for determining the stress *vs*. strain curve from the bulge test, the membrane theory needs to be used (subchapter 2.2). The evolution of the principal strains, ε_1 and ε_2, in the sheet plane can be obtained with the aid of DIC equipment or mechanical extensometer (that only allows determining one of the principal strains). The radius of curvature, ρ_{ext}, can also be evaluated using DIC equipment or by spherometer, the pressure, p, is acquired during the test and the sheet thickness, t, is obtained based on the thickness strain, ε_3, or using models.

2.4. Inverse analysis methodologies

In addition to traditional strategies making use of measured variables and analysis of the bulge test as stated above, other strategies have also been experienced, generally referred to as inverse methodologies, for determining the hardening curve. However, few literature is available on inverse procedures only using the bulge test. Still, it is possible to notice two works [54,55] that describe inverse approaches for identifying the hardening law parameters. This subchapter presents and analyses these two cases of inverse analysis, which are based on numerical simulations.

The first case [55] uses the circular die to estimate the parameters of the Ludwick hardening law [56] for the case of a stainless steel (AISI 304) and complementarily it uses an elliptical die to re-identify the anisotropy coefficients in the sheet plane. The second case studied [54] uses computer generated results of the circular bulge test to improve the estimate of the parameters of the Voce hardening law, considering an isotropic material [57].

2.4.1. Chamekh *et al.* [55]

Chamekh *et al*. [55] describe an inverse approach, based on Artificial Neural Networks (ANN), to identify the material parameters of a stainless steel (AISI 304). They use the results of the evolutions of pressure with the pole height, which are transferred to a neural network. The ANN is trained using curves generated by finite element simulations of the circular bulge test, using systematically various sets of material parameters, in a total of 27 simulated curves of pressure *vs*. displacement of the central point of the cap. During the training process, the network computes the weight connections, minimizing the total mean squared error between the actual output and the desired output; the obtained square error is less than 0.001, for the case of circular die, and 0.005, for the elliptical die. The neural network generates an approximated function for the material parameters depending on the profile of the evolution of pressure with the pole height curve. Then, it was exploited for the identification of material parameters from experimental results. The Ludwick hardening law was selected:

$$Y = \sigma_0 + K\bar{\varepsilon}^n \tag{2.29}$$

where σ_0 is the initial yield stress and K and n are material parameters, and the Hill'48 yield criterion to describe the orthotropic behaviour. Thus, the set of parameters to be identified also comprise the Lankford coefficients, r_0, r_{45} and r_{90}. These material parameters are identified according to the two following steps: (i) the first step, using the circular bulge test, is to find the parameters of the Ludwick law (assumes the knowledge of Lankford's coefficients determined from the tensile tests) (ii) the second step, using the elliptical bulge test for an off axis angle of 0º, is to identify (recalculate) the Lankford's coefficients. An elliptical die for an off axis angle of 45º is used for the validation of the parameters identification. The flowchart of methodology is shown in Figure 2.10.

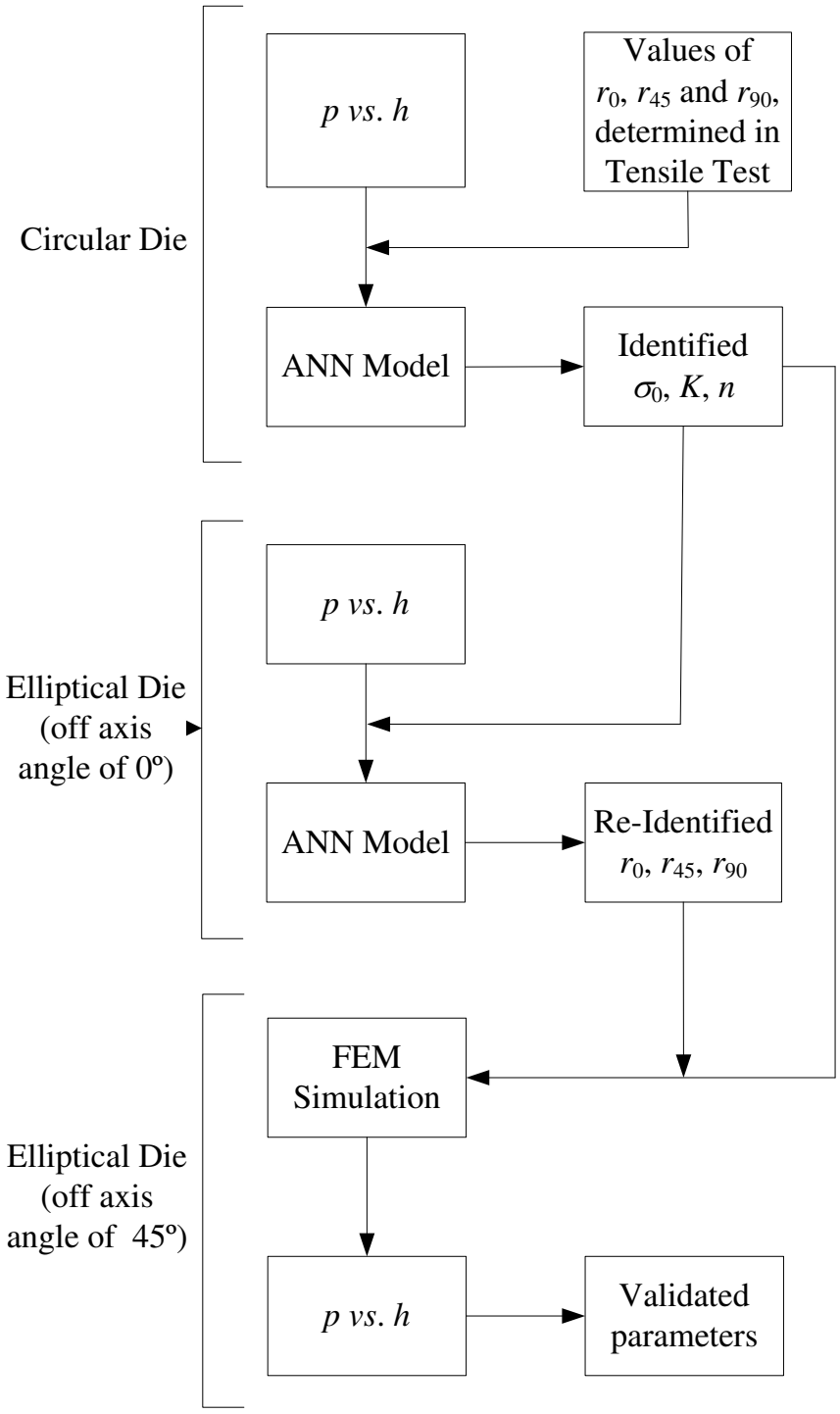

Figure 2.10. Idealized flowchart based on the ANN methodology, as proposed by Chamekh *et al*. [55], including the validation step.

Table 2.3 compares the set of hardening law parameters identified based on experimental tensile test results with those identified from the methodology based on ANN.

The authors conclude: (i) the ANN methodology can predict acceptable combination of material parameters; (ii) once the ANN was trained, output results for a given set of input data are available almost instantaneously. Despite these conclusions, it should be noted that the value of the experimental and identified hardening coefficients, n, are far away (the experimental and identified values of n are 0.67 and 0.4, respectively), which at least in part explains the difference values in stress. The parameters K of the Ludwick law and the Lankford's coefficients also show high difference level (Table 2.3).

Table 2.3. Experimental and identified parameters for the stainless steel (AISI 304) and the respective difference [55].

Variable	Identified Value	Experimental Values of Tensile Test	Difference [%]
σ_0 [MPa]	241.6	238.2	1.4
K [MPa]	1422	1172	21.3
n	0.40	0.67	40.3
r_0	1.19	0.93	28.0
r_{45}	0.80	1.07	25.2
r_{90}	0.70	0.87	19.5

2.4.2. Bambach [54]

Bambach [54] explored the usability of the circular bulge test to identify the material parameters of a fictitious material. This is considered isotropic with hardening behaviour described by Voce hardening law:

$$Y = \sigma_0 + R_{\text{sat}}\left[1 - \exp\left(-c_{\text{y}}\bar{\varepsilon}\right)\right] \tag{2.30}$$

where σ_0 is the initial yield stress and R_{sat} and c_y are material parameters. Initially, the membrane theory is applied to the results as in experimental cases, in order to obtain a set of parameters of the Voce, by fitting the stress *vs*. strain results. The inverse analysis strategy proposed resorts to a gradient-based optimization algorithm, which is known for being sensitive to the initial solution. Thus, by using as initial solution the one previously obtained with the membrane theory, it is expected to avoid convergence problems.

The paper gives special focus to the choice of objective function to be minimized. The re-identification of the constitutive parameters is based on finite element analysis performed with a set of parameters, defined by vector $\underline{a}$, that yields a set of measurements $p_{\underline{a}}(h)$, $\varepsilon_{\underline{a}}(h)$ or $t_{\underline{a}}(h)$, which are used to define the following objective functions, for the pressure, strain and thickness with pole height:

$$\begin{cases} \chi_p^2(\underline{a}) = \int_0^{h_{max}} \left[p_{ref}(h) - p_{\underline{a}}(h) \right]^2 dh \\ \chi_\varepsilon^2(\underline{a}) = \int_0^{h_{max}} \left[\varepsilon_{ref}(h) - \varepsilon_{\underline{a}}(h) \right]^2 dh \\ \chi_t^2(\underline{a}) = \int_0^{h_{max}} \left[t_{ref}(h) - t_{\underline{a}}(h) \right]^2 dh \end{cases} \tag{2.31}$$

A sensitivity analysis of these objective functions was performed and the results obtained at the true value of c_y (input value of the fictitious material) are shown on Figure 2.11. The red mark present in each surface corresponds to the optimum set of parameters. The author concludes from this analysis that the combination of first two types of results of equation (2.31) will significantly improve the re-identification, since it will contribute to reduce the search area were the minimum value of the objective function is located. Table 2.4 present the results of re-identification by inverse analysis for the Voce model.

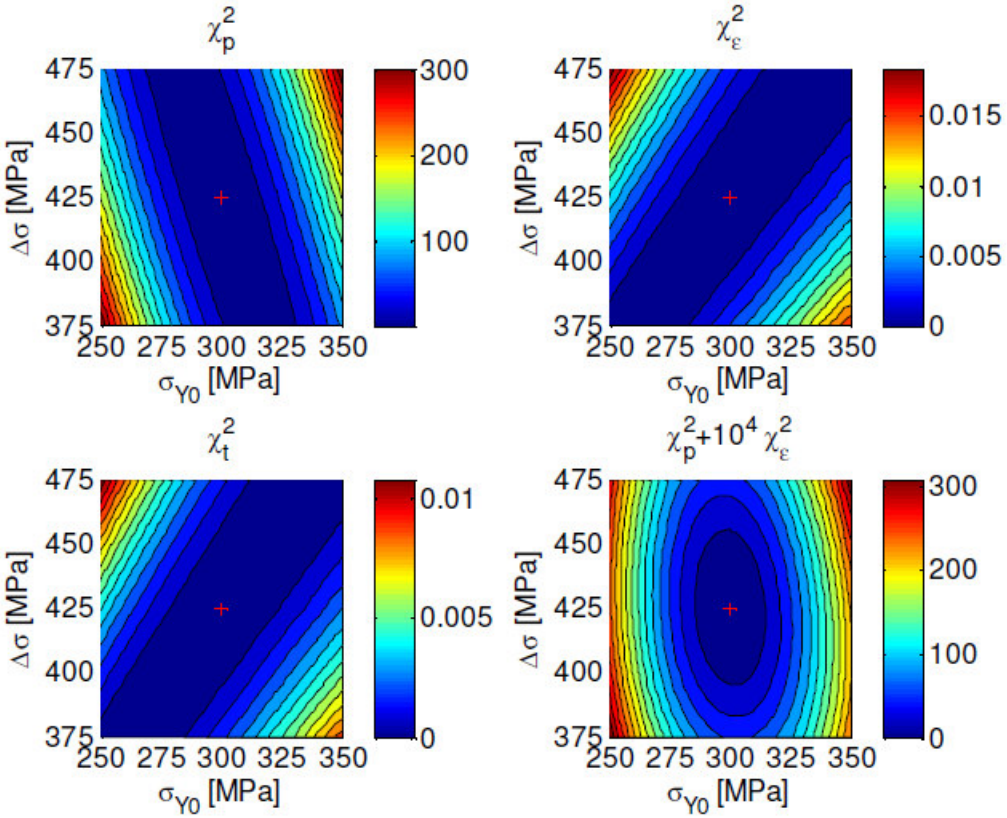

Figure 2.11. Objective function for the Voce model at the true value of c_y [54].

Table 2.4. Results of re-identification by inverse analysis for the Voce model [54].

Objective function	Function calls	σ_{Y0}	R_{sat}	c_y	χ^2	max(|$\sigma_{y,true}$-$\sigma_y(\sigma_0,R_{sat},c_y)$|)
χ_p^2	235	297.50	432.68	2.500	0.082	3.85
χ_ε^2	243	301.42	426.42	2.500	7.14E-06	2.59
χ_t^2	126	293.79	431.66	2.500	1.82E-05	6.21
$\chi_p^2+10^4\,\chi_\varepsilon^2$	215	299.92	425.02	2.500	0.022	0.078
Starting guess:		293.79	431.66	2.535		
True values:		300.00	425.00	2.500		

In summary, the author concluded that the results of inverse analysis is sensitive to the choice of the objective function. The results of the re-identification analysis is more accurate than the results obtained from the test using the membrane theory, if a suitable objective function is chosen, since the last analysis assumes simplifications that influence the accuracy with which the hardening curve can be determined.

Although re-identification present small differences between hardening laws, computed generated and identified, it should be noted that this proposal for re-identification needs to resort to strain results in the pole of the cap during the test, which does not greatly simplify the experimental procedure, relatively to that when using the membrane theory. Moreover, the values of the re-identified parameters are very close to those of the starting parameters (Table 2.4), which were obtain by traditional methodology for analysing the bulge test, i.e. this inverse analysis works like a re-identification procedure (so called by the author), in order to improve the results of the direct identification.

2.5. ISO standardisation

The German DDRG (Deep Drawing Research Group), in the area of deep-drawing of metal sheets, proposes an ISO standard for determining the stress *vs*. strain curve from the bulge test under hydraulic pressure, using optical measuring systems. This standardisation was published as ISO 16808:2014 and contains ten essential topics.

The first topic describes the scope and field of application, which is limited to sheet thickness less than 3mm (due to the unavoidability of using the membrane theory approach for analysing the results), in pure stretch forming without significant friction influence. The second topic displays the symbology, designation and the units of the parameters and variables of the test. The third one deals with the principle of the test and refers, in general terms, the quantities required for the calculation of the stress *vs*. strain curve of the materials: the pressure and, near the centre of the blank, the local curvature and the strains at the surface, which must be evaluated with an optical measurement system. The sheet thickness is determined assuming incompressible deformation of the material. The fourth topic regards the requirements to be fulfilled by the optical measuring equipment, which should determine the spatial coordinates of a grid of points on the surface of the sheet, in order to calculate the

shape and the principal strains in the central area of interest, contactless with the sheet. The recommended measurement precision for the pressure imposed is indicated. The die and blank holder must be rigid enough to prevent deformation during testing. The equipment should contain a drawbead to avoid slipping of the sheet and its clamping should be sufficient for do not lose fluid. The optical measuring system can use a glass for protecting the optical measuring system, which should be as thin as possible. The smallest ratio between the die diameter, d_M, and the sheet thickness, t, must satisfy the condition:

$$\frac{d_M}{t} \geq 33, \tag{2.32}$$

and it is recommended that the die profile radius, R_1, should be 5 to 10 times greater than the sheet thickness, up to the maximum value of 15mm, to avoid cracks in the blank during the test.

The fifth topic is about the optical measurement system for determining the radius of curvature and principal strains in the sheet plane, recommending an optical field measurement system. This topic refers to the local resolution of the system (distance between grid points of measurement), accuracy required for determining the coordinate normal to the sheet (related with the evaluation of the curvature) and the size of measurement area. In the sixth topic concerns the samples, i.e. the blank to be used for testing. It is namely mentioned that the blank must be oriented with the rolling direction parallel to one of the axes of the coordinate measuring system, and recommendations are made about the grid application. The seventh topic is about the testing procedure. This is carried out at room temperature, after previous measurement of the initial sheet thickness. The growth rate of applied pressure, as well as the number of outputs results and images to be collect during the test, are also reported.

The eighth topic describes the procedure for the determination of the radius of curvature and the strains at the pole, assuming the spherical shape of the sheet surface near the pole of the cap. The size of central regions for obtaining the radius of curvature and strains is recommended; the size of the regions is different for the radius of curvature and for the strains.

The ninth topic displays the equations for the biaxial stress *vs*. strain curve determination and the assumed simplifications:

- The equibiaxial stress state is assumed:

$$\sigma_1 = \sigma_2 = \sigma_B \tag{2.33}$$

- The curvature is represented by means of the radius of curvature:

$$\rho = \left[\frac{1}{2} \left(\frac{1}{\rho_1} + \frac{1}{\rho_2} \right) \right]^{-1} \tag{2.34}$$

- Then the biaxial true stress can be calculated by:

$$\sigma_B = \frac{p\rho}{2t} \tag{2.35}$$

- Using the fluid pressure, p, the radius of curvature, ρ, and the actual thickness, t, with:

$$t = t_0 \exp(\varepsilon_3) \tag{2.36}$$

- Assuming plastic incompressible deformation of the material, the total thickness strain for the calculation of the actual thickness (equation (2.36)) can be approximated by the total major and minor true strains:

$$\varepsilon_3 \approx -\varepsilon_1 - \varepsilon_2 \tag{2.37}$$

- Assuming an isotropic linear elastic material behaviour and plastic incompressibility, the plastic thickness strain is then given by:

$$\varepsilon_3^{pl} = -\varepsilon_1 - \varepsilon_2 + 2\frac{1-\nu}{E}\sigma_B \tag{2.38}$$

- Finally, the biaxial stress *vs*. strain curve is obtained plotting the stress, σ_B (equation (2.35)) as function of the plastic thickness strain (equation (2.38)). Under these conditions, the standard states that "*the biaxial stress-strain curve is obtained without any assumption on the type of yield criterion*".

Lastly, the tenth and last topic, states all information that shall be indicated on the test report concerning the test conditions and analyse, besides the biaxial stress *vs*. strain curves as a table of values and as a plot.

The International Standard ISO 16808:2014 still contains four annexes of which is to highlighting the final (Annex D), concerning the determination of the equibiaxial stress point of the yield criterion and the hardening curve. This annex describes a methodology for transforming the biaxial stress *vs*. strain curve into the stress *vs*. strain curve determined from

uniaxial tensile test data in rolling direction, in order to provide hardening data at strains higher than the uniform strain of tensile test.

In conclusion, it should be noted that this International Standard emphasizes the use of optical measuring systems for the determination of the biaxial stress *vs*. strain curve by mean of bulge test. Moreover, assumes the stress state as equibiaxial and isotropy of the materials.

[Page intentionally left blank]

References

[1] Shang HM, Shim VPW. Effects of die shoulder on the prolateness and deformation in the bulge test. J Eng Ind 1982;104:279–84. doi:10.1115/1.3185831.

[2] Slota J, Spišák E. Determination of flow stress by the hydraulic bulge test. Metalurgija 2008;47:13–7.

[3] Zang SL, Thuillier S, Le Port A, Manach PY. Prediction of anisotropy and hardening for metallic sheets in tension, simple shear and biaxial tension. Int J Mech Sci 2011;53:338–47. doi:10.1016/j.ijmecsci.2011.02.003.

[4] Montay G, François M, Tourneix M, Guelorget B, Vial-Edwards C, Lira I. Strain and strain rate measurement during the bulge test by electronic speckle pattern interferometry. J Mater Process Technol 2007;184:428–35. doi:10.1016/j.jmatprotec.2006.12.013.

[5] Nasser A, Yadav A, Pathak P, Altan T. Determination of the flow stress of five AHSS sheet materials (DP 600, DP 780, DP 780-CR, DP 780-HY and TRIP 780) using the uniaxial tensile and the biaxial viscous pressure bulge (VPB) tests. J Mater Process Technol 2010;210:429–36. doi:10.1016/j.jmatprotec.2009.10.003.

[6] Sigvant M, Mattiasson K, Vegter H, Thilderkvist P. A viscous pressure bulge test for the determination of a plastic hardening curve and equibiaxial material data. Int J Mater Form 2009;2:235–42. doi:10.1007/s12289-009-0407-y.

[7] Banabic D, Vulcan M, Siegert K. Bulge Testing under Constant and Variable Strain Rates of Superplastic Aluminium Alloys. CIRP Ann - Manuf Technol 2005;54:205–8. doi:10.1016/S0007-8506(07)60084-5.

[8] Hsu TC, Shang HM. Mechanics of sheet metal formed by hydraulic pressure into axisymmetrical shells. Exp Mech 1976;16:337–42. doi:10.1007/BF02330250.

[9] Shang HM, Hsu TC. Deformation and curvatures in sheet-metal in the bulge test. J Eng Ind 1979;101:341–7.

[10] Aoura Y, Ollivier D, Ambari A, Santo PD. Determination of material parameters for 7475 Al alloy from bulge forming tests at constant stress. J Mater Process Technol 2004;145:352–9. doi:10.1016/j.jmatprotec.2003.09.002.

[11] Cai G, Lang L, Liu K, Alexandrov S, Zhang D, Yang X, et al. Research on the effect

of flow stress calculation on aluminum alloy sheet deformation behavior based on warm bulging test. Met Mater Int 2015;21:365–73. doi:10.1007/s12540-015-2018-0.

[12] Dowling NE. Mechanical behavior of materials : engineering methods for deformation, fracture, and fatigue. 2nd ed. Upper Saddle River, NJ : Prentice Hall; 1999.

[13] Lăzărescu L, Comşa D-S, Banabic D. Determination of stress-strain curves of sheet metals by hydraulic bulge test. AIP Conf Proc 2011;1353:1429–34. doi:10.1063/1.3589717.

[14] Gagov V, Feschiev N, Comşa D-S, Minev E. Strain hardening evalution by bulge testing of sheet metals. In: Travis FW, Hashmi SMSJ, editors. 12th Int. Sci. Conf. Achiev. Mech. Mater. Eng., Gliwice, Poland: 2003, p. 331–4.

[15] Lemoine X, Iancu A, Ferron G. Flow curve determination at large plastic strain levels: limitations of the membrane theory in the analysis of the hydraulic bulge test. 14th Int. ESAFORM Conf. Mater. Form., 2011, p. 1411–6. doi:10.1063/1.3589714.

[16] Yoshida K. Evaluation of stress and strain measurement accuracy in hydraulic bulge test with the aid of finite-element analysis. ISIJ Int 2013;53:86–95. doi:10.2355/isijinternational.53.86.

[17] Hasan RZ, Kinsey BL, Tsukrov I. Effect of element types on failure prediction using a stress-based forming limit curve. J Manuf Sci Eng 2011;133:61002.

[18] Young RF, Bird JE, Duncan JL. An automated hydraulic bulge tester. J Appl Metalwork 1981;2:11–8. doi:10.1007/BF02833994.

[19] Martins B, Teixeira P, Santos AD. Study on the flow stress determination using hydraulic bulge test. In: Andrade-Campos A, Lopes N, Valente RAF, Varum H, editors. First ECCOMAS Young Investig. Conf. Comput. Methods Appl. Sci., Aveiro, Portugal: 2012.

[20] Santos AD, Teixeira P, Barata da Rocha A, Barlat F, Moon YH, Lee M-G. On the determination of flow stress using bulge test and mechanical measurement. In: Barlat F, Moon YH, Lee MG, editors. 10th Int. Conf. NUMIFORM, Pohang, Republic of Korea: American Institute of Physics; 2010, p. 845–52. doi:10.1063/1.3457644.

[21] Mulder J, Vegter H, Aretz H, van den Boogaard AH. Accurate evaluation method for the hydraulic bulge test. Key Eng Mater 2013;554-557:33–40. doi:10.4028/www.scientific.net/KEM.554-557.33.

[22] Bleck W, Blumbach M. Laser-aided flow curve determination in hydraulic bulging. Steel Res Int 2005;76:125–30.

[23] Mutrux A, Hochholdinger B, Hora P. A procedure for the evaluation and validation of the hydraulic biaxial experiment. Numisheet 2008, Interlaken, Switzerland: 2008, p. 6.

[24] Keller S, Hotz W, Friebe F. Yield curve determination using bulge test combined with optical measurements. In: Levy BS, Matlock DK, Van Tyne CJ, editors. Int. Deep Draw. Res. Gr. Conf. IDDRG, Golden, Colorado: IDDRG; 2009, p. 319–30.

[25] Mulder J, Vegter H, Aretz H, Keller S, van den Boogaard AH. Accurate determination of flow curves using the bulge test with optical measuring systems. J

Mater Process Technol 2015;226:169–87. doi:10.1016/j.jmatprotec.2015.06.034.

[26] Güner A, Brosius A, Tekkaya AE. Experimental and numerical investigation of the hydraulic bulge test for accurate flow curve determination. In: B. Levy, D. Matlock CVT, editor. Int. Deep Draw. Res. Gr. Conf. IDDRG, Golden, Colorado: IDDRG; 2009, p. 331–41.

[27] Hallfeldt T, Hotz W, Leppin C, Keller S, Friebe H, Till ET, et al. Comprehensive materials processing. Elsevier; 2014. doi:10.1016/B978-0-08-096532-1.00105-9.

[28] DIN EN ISO 16808:2014-11 (E). Metallic materials - sheet and strip - determination of biaxial stress-strain curve by means of bulge test with optical measuring systems. BSI; 2014.

[29] Koç M, Billur E, Cora ÖN. An experimental study on the comparative assessment of hydraulic bulge test analysis methods. Mater Des 2011;32:272–81. doi:10.1016/j.matdes.2010.05.057.

[30] Lemoine X, Sriram S, Kergen R. Flow curve determination at large plastic strain levels to accurately constitutive equations of AHSS in forming simulation. AIP Conf Proc 2011;1353:1411–6. doi:10.1063/1.3589715.

[31] Ilahi MF, Parmar A, Mellor PB. Hydrostatic bulging of a circular aluminium diaphragm. Int J Mech Sci 1981;23:221–7. doi:10.1016/0020-7403(81)90047-3.

[32] Rodrigues CA, Reis LC, Sakharova NA, Oliveira MC, Fernandes J V. On the characterization of the plastic behaviour of sheet metals with bulge tests: numerical simulation study. In: Eberhardsteiner J. et al., editor. 6th Eur. Congr. Comput. Methods Appl. Sci. Eng. ECCOMAS, Vienna, Austria: ECCOMAS 2012; 2012, p. 4575–89.

[33] Vučetić M, Bouguecha A, Peshekhodov I, Götze T, Huinink T, Friebe H, et al. Numerical validation of analytical biaxial true stress—true strain curves from the bulge test. 8th Int. Conf. Work. Numer. Simul. 3D Sheet Met. Form. Process., Seoul, Korea: NUMISHEET 2011; 2011, p. 107–14. doi:10.1063/1.3623599.

[34] Ranta-Eskola AJ. Use of the hydraulic bulge test in biaxial tensile testing. Int J Mech Sci 1979;21:457–65. doi:10.1016/0020-7403(79)90008-0.

[35] Santos AD, Teixeira P, Barlat F. Flow stress determination using hydraulic bulge test and a mechanical measurement system. Int. Deep Draw. Res. Gr. Conf. IDDRG, Bilbao, Spain: IDDRG; 2011, p. 91–100.

[36] Martins B, Santos AD, Teixeira P, Ito K, Mori N. Determination of flow curve using bulge test and calibration of damage for ito-goya models. Key Eng Mater 2013;554-557:182–9. doi:10.4028/www.scientific.net/KEM.554-557.182.

[37] Gutscher G, Wu H-C, Ngaile G, Altan T. Determination of flow stress for sheet metal forming using the viscous pressure bulge (VPB) test. J Mater Process Technol 2004;146:1–7. doi:10.1016/S0924-0136(03)00838-0.

[38] Lăzărescu L, Comşa D-S, Nicodim I, Ciobanu I, Banabic D. Characterization of plastic behaviour of sheet metals by hydraulic bulge test. Trans Nonferrous Met Soc China 2012;22:s275–9. doi:10.1016/S1003-6326(12)61719-1.

[39] Lăzărescu L, Comşa D-S, Banabic D. Analytical and experimental evaluation of the stress-strain curves of sheet metals by hydraulic bulge tests. Key Eng Mater

2011;473:352–9. doi:10.4028/www.scientific.net/KEM.473.352.

[40] Hill R. C. A theory of the plastic bulging of a metal diaphragm by lateral pressure. London, Edinburgh, Dublin Philos Mag J Sci 1950;41:1133–42. doi:10.1080/14786445008561154.

[41] Panknin W. The hydraulic bulge test and the determination of the flow stress curves. University of Stuttgart, 1970.

[42] Smith LM, Hadad Y, Thotakura R, Gunala S, Manthipragada S. Flow stress curves using new volume measurement method for hydraulic bulge test. AIP Conf. Proc., vol. 908, Porto, Portugal: AIP; 2007, p. 637–42. doi:10.1063/1.2740882.

[43] Janbakhsh M, Djavanroodi F, Riahi M. Utilization of bulge and uniaxial tensile tests for determination of flow stress curves of selected anisotropic alloys. J Mater Des Appl 2012;227:38–51. doi:10.1177/1464420712451963.

[44] Atkinson M. Accurate determination of biaxial stress—strain relationships from hydraulic bulging tests of sheet metals. Int J Mech Sci 1997;39:761–9. doi:10.1016/S0020-7403(96)00093-8.

[45] Swift HW. Plastic instability under plane stress. J Mech Phys Solids 1952;1:1–18. doi:10.1016/0022-5096(52)90002-1.

[46] Chakrabarty J, Alexander JM. Hydrostatic bulging of circular diaphragms. J Strain Anal Eng Des 1970;5:155–61. doi:10.1243/03093247V053155.

[47] Kruglov AA, Enikeev FU, Lutfullin RY. Superplastic forming of a spherical shell out a welded envelope. Mater Sci Eng A 2002;323:416–26. doi:10.1016/S0921-5093(01)01376-4.

[48] Slota J, Spišák E. Comparison of the forming limit diagram (FLD) models for drawing quality (DQ) steel sheets. Metalurgija 2005;44:249–53.

[49] Liu K, Lang L, Cai G, Yang X, Guo C, Liu B. A novel approach to determine plastic hardening curves of AA7075 sheet utilizing hydraulic bulging test at elevated temperature. Int J Mech Sci 2015;100:328–38. doi:10.1016/j.ijmecsci.2015.07.002.

[50] Leppin C, Lange C, Till ET, Daniel D. Evaluation of the hydraulic bulge test for improved material hardening modeling. 5th Form. Technol. Forum, Zurich, Switzerland: 2012, p. 69–74.

[51] Chung WJ, Kim YJ, Yang DY. Rigid-plastic finite element analysis of hydrostatic bulging of elliptic diaphragms using hill's new yield criterion. Int J Mech Sci 1989;31:193–206. doi:10.1016/0020-7403(89)90110-0.

[52] von Mises R. Mechanik der festen Körper im plastisch - deformablen Zustand. Nachrichten von Der Gesellschaft Der Wissenschaften Zu Göttingen, Math Klasse 1913;1:582–92.

[53] Smith LM, Wanintrudal C, Yang W, Jiang S. A new experimental approach for obtaining diffuse-strain flow stress curves. J Mater Process Technol 2009;209:3830–9. doi:10.1016/j.jmatprotec.2008.09.010.

[54] Bambach M. Comparison of the identifiability of flow curves from the hydraulic bulge test by membrane theory and inverse analysis. Key Eng Mater 2011;473:360–7. doi:10.4028/www.scientific.net/KEM.473.360.

[55] Chamekh A, BelHadjSalah H, Hambli R, Gahbiche A. Inverse identification using the bulge test and artificial neural networks. J Mater Process Technol 2006;177:307–10. doi:10.1016/j.jmatprotec.2006.03.214.

[56] Ludwik P. Elemente der technologischen mechanik. Springer-Verlag Berlin Heidelberg; 1909. doi:10.1007/978-3-662-40293-1.

[57] Voce E. The relationship between stress and strain for homogeneous deformations. J Inst Met 1948;74:537–62.

[Page intentionally left blank]

Chapter 3.

Innovative Development

This chapter presents the innovative work of this research on the circular bulge test, in the form of three articles. Firstly, the research is summarised. The remaining subchapters consist of the papers entitled: "*Anisotropy and plastic flow in circular bulge test*"; "*On the determination of the work hardening curve using the bulge test*"; and "*Inverse Identification of Swift law parameters using the bulge test*".

[Page intentionally left blank]

3.1. Overview of the research papers

In this subchapter it is carried out a brief overview of the innovative research conducted within the framework of this thesis, which consist of following three research papers.

The first paper analyses the geometry of the sheet, the principal strains and stresses, and the respective paths near the pole of circular bulge test, at different moments of the test for materials with anisotropic plastic behaviour. This analysis highlights that, in case of in-plane anisotropic materials, the stress and strain paths can be considerably different from equibiaxial, despite the spherical geometry of the cap near the pole (radius of curvature equal in for both orthotropic directions in the sheet plane). The error in equivalent stress involved in conventional analysis, i.e. assuming equibiaxial stress state and isotropy is compared with that obtained under real conditions. Finally, a methodology is suggested for improving the determination of the biaxial stress *vs*. strain curve.

The second paper analyses the evolution of the radius of curvature and sheet thickness with the pole height, during the circular bulge test with the various die geometries. It was observed that the radius of curvature and sheet thickness depend on the die geometry and hardening coefficient of the material. The sheet thickness also depends on these geometrical and material parameters, but depends as well on the normal anisotropy coefficient. Analytical models are developed for describing the evolutions of the radius of curvature and sheet thickness, which are target of numerical and experimental validation and compared with results and models in literature. This approach enables properly assessing of the hardening curve and allows simplifying the experimental procedure.

Lastly, the third paper develops an inverse analysis methodology for determining the parameters of Swift hardening law, which consists on the search for the best coincidence between evolutions of pressure with pole height of experimental and numerical reference curves, the latter being obtained by numerical simulation assuming isotropic material behaviour with various values of the Swift hardening coefficient in the range of the material under study. The overlapping of the curves is performed using appropriate factors for the pressure and the pole height, which is based on two key points: (i) for materials with the same value of the hardening coefficient, the overlapping of the pressure with pole height

curves depends factors which values are correlated with the thickness and yield stress ratios, between the experimental and the reference numerical curve of isotropic material (ii) the influence of the anisotropy on the overlapping of the pressure with pole height curves can be adequately taken into account, acting on the multiplying factors, what allows using isotropic reference curves in inverse analyses, avoiding the knowledge of the parameters of the yield criterion to be used as input in numerical reference curves. This identification enables proper evaluation of the Swift hardening law, simplifies the experimental procedure and is not exposed to various experimental errors.

3.2. Anisotropy and plastic flow in circular bulge test

This subchapter consists of the paper "*Anisotropy and plastic flow in circular bulge test*", submitted for publication. It analyses the geometry of the spherical cap, the strains and stresses distributions and respective paths near the pole of the cap, in order to understand the role of the anisotropy on the determination of the biaxial stress *vs*. strain curve. This study clarifies constraints of the currently used procedure and outlines recommendations for the proper experimental evaluation of that curve.

[Page intentionally left blank]

ANISOTROPY AND PLASTIC FLOW IN THE CIRCULAR BULGE TEST

L.C. Reis[a1], M.C. Oliveira[a], A.D. Santos[b] and J.V. Fernandes[a]

[a] CEMUC, Department of Mechanical Engineering, University of Coimbra, Polo II, Rua Luís Reis Santos, Pinhal de Marrocos, 3030-788 Coimbra, Portugal

[b] Faculty of Engineering, University of Porto, Rua Dr. Roberto Frias, 4200-465 Porto, Portugal

Abstract

The procedures for obtaining the stress *vs*. strain curve from the bulge test are analysed in detail resorting to numerical simulations. Particular attention is given to in-plane anisotropic materials for which remains a lack of knowledge about issues such as the distributions, near the pole of the bulge specimen, of variables such as the radius of curvature, sheet thickness, principal stresses and strains as well as stress and strain paths. This study seeks to understand and evaluate the errors inherent to the commonly used experimental procedures for determining the hardening curve from the bulge test. The usual procedure assumes that the material is isotropic and the stress path at the pole is equibiaxial. An empirical equation relating the stress path with the strain path at the pole of the cap is suggested to improve the determination of the hardening curve, which holds particular prominence in cases of strongly anisotropic sheets.

Keywords: Hydraulic bulge test, Hardening law; Anisotropic metal sheets, Membrane theory, Numerical simulation.

[1] Corresponding author at: CEMUC, Department of Mechanical Engineering, University of Coimbra, Pólo II, Rua Luís Reis Santos, Pinhal de Marrocos, 3030-788 Coimbra, Portugal. Tel.:+351239790700, Fax:+351239790701.
Email addresses: luis.reis@dem.uc.pt (L.C. Reis), marta.oliveira@dem.uc.pt (M.C. Oliveira), abel@fe.up.pt (A.D. Santos) and valdemar.fernandes@dem.uc.pt (J.V. Fernandes).

1. INTRODUCTION

Sheet metal forming processes are demanded to manufacture components for the automotive, aeronautics and other industries. The finite element method (FEM) is commonly used nowadays for simulating and optimizing sheet metal forming processes. However, the numerical simulation results are dependent on the convenient characterization and modelling of the mechanical behaviour of metal sheets. Whatever the constitutive model used in the simulations (i.e. hardening law and anisotropic yield criterion), the strategies for identifying its parameters as well as the experimental tests and procedures used in the analysis play an important role in the characterization of the metal sheets mechanical behaviour [1–5]. The parameters of the models are generally determined with recourse to tensile and other tests, such as shear, cruciform and bulge [6].

The biaxial bulge test under hydraulic pressure allows achieving relatively high strain values before necking and enables the definition of the hardening law for a wide range of plastic deformation [7]. In circular bulge test, the periphery of the metal sheet is immobilized through a drawbead, which prevents the peripheral region of the sheet from moving into the radial direction [8–10]. Then, a hydraulic pressure is applied on one side of the sheet, promoting an approximately spherical shape in the region near the pole of the cap and inside a circle of constant latitude [11,12]. Under these conditions, a biaxial stress path occurs at the pole of the cap.

The bulge test is used for determining the hardening curve [13] and the forming limit diagram [14], not only with circular but also with elliptic dies, which enables a wide range of biaxial stress paths [13,15]. For evaluating the stress *vs*. strain curve, the evolutions of pressure, radius of curvature and strain at the pole of the cap should be recorded during the test. The measurement of the radius of curvature and strain can be performed by a spherometer and an extensometer, respectively [16,17]. An optical system can replace these mechanical systems with advantages, since it enables the description of the geometry and strain distributions on the sheet surface during the bulge test [18,19]. In both cases, the membrane theory that relates the stresses at the pole with the pressure, radius of curvature and sheet thickness must be used [20].

The analysis of the bulge test results, including the application of the membrane theory, still presents uncertainties, despite of the recent recommended procedure by ISO 16808 (2014) [21]. In fact, the accurate evaluation of the stress *vs.* strain curves depends on assumptions and simplifications, whose assessment are still under study. For example, in a

recent study Mulder et al. [22] examine the validity and the conditions for using the membrane theory, which includes issues related to: the evaluations of the radii of curvature and stresses at the middle plane of the sheet, the coordinate system for strain measuring to be used, the equibiaxial stress state assumption in case of in-plane anisotropic materials and the existence of stresses across the sheet thickness. An issue that has received little attention concerns the effect of the anisotropy of the material in the bulge test results, including its influence on the accuracy of the hardening curve determination [23]. Yoshida [24] estimated the stress and strain paths during the bulge test, in case of in-plane anisotropic materials by using finite element analysis. He concludes that the stress path at the pole of the cap deviates from equibiaxial between 1-5%, depending on the degree of anisotropy of the materials. However, this result only concern materials with relatively low anisotropy in the sheet plane.

The current work presents a numerical study on the circular bulge test of metal sheets, performed with the *DD3IMP* in-house code [25,26]. It examines the geometry and the stress and strain distributions near the pole of the cap. This analysis also concerns the relationship between stress and strain paths. Materials with anisotropy in the sheet plane are particularly considered. The methodology for the experimental determination of the hardening law of metal sheets and associated errors is also analysed. The Hill'48 criterion [27] and the Swift law [28] are used due to their simplicity, but other constitutive model is also tested.

2. THEORETICAL BACKGROUND

The analysis of the stress state near the pole of the metal sheet during the bulge test, using either circular or elliptical dies, can be performed with the aid of the membrane theory [29], as long as a small ratio between the sheet thickness and the die diameters is fulfilled. The typical values suggested for this ratio are lower than 1/50, for the circular test [6,30]. Standard ISO 16808:2014 [21] recommends this ratio equal to or lower than 1/33. Under these conditions the bending stress can be neglected, and assuming that the thickness stress σ_3 (= σ_Z) is equal to zero, a relationship between the principal stresses at the pole, the pressure and the geometry of the cap is given by:

$$\frac{\sigma_1}{\rho_1} + \frac{\sigma_2}{\rho_2} = \frac{p}{t}, \tag{1}$$

where σ_1 and σ_2 are the principal stresses in the sheet surface (assuming that the principal stress axes (O123) and anisotropy axes (O*xyz*) coincide), ρ_1 and ρ_2 are the radii of curvature, at half thickness, in the O*xz* and O*yz* planes, respectively, *p* is the hydraulic pressure and *t* is the sheet thickness.

In order to experimentally determine the strain hardening curve, the evolution of the following variables needs to be obtained during the test: pressure, *p*, the radii of curvature, ρ_1 and ρ_2, and the sheet thickness at the pole, *t*. The thickness can be determined based on the knowledge of the initial thickness of the sheet, t_0, and the thickness strain, ε_3, through the following equation:

$$t = t_0 \exp\left(-\varepsilon_3\right). \tag{2}$$

where the principal strain, ε_3, is obtained from the measurement of the principal strains in the sheet plane, ε_1 and ε_2, based on the condition of volume constancy during the plastic deformation:

$$\varepsilon_3 = -\left(\varepsilon_1 + \varepsilon_2\right). \tag{3}$$

Since the radius of curvature is experimentally evaluated on the external surface of the cap, its correction can be done based on the following equation [31]:

$$\rho = \rho_{ext} - \frac{t}{2}, \tag{4}$$

where ρ is the radius of curvature at the half thickness of the cap, and ρ_{ext} is the radius of curvature of the external surface of the cap.

In the general case, i.e. anisotropic metal sheet, the membrane theory equation (equation (1)) contains two unknown variables, σ_1 and σ_2, which requires an additional equation for its determination. This additional equation can be obtained from the plastic stress-strain relationships arising from the associated flow rule. For metal sheets following the Hill'48 criterion [27], assuming coincidence of the coordinate systems of principal stress (O123) and anisotropy (O*xyz*), it is possible to write:

$$\begin{cases} \mathrm{d}\varepsilon_1 = \mathrm{d}\lambda\left[\mathrm{H}\left(\sigma_1 - \sigma_2\right) + \mathrm{G}\left(\sigma_1 - \sigma_3\right)\right] \\ \mathrm{d}\varepsilon_2 = \mathrm{d}\lambda\left[\mathrm{F}\left(\sigma_2 - \sigma_3\right) + \mathrm{H}\left(\sigma_2 - \sigma_1\right)\right] \end{cases}, \tag{5}$$

where F, G and H are the anisotropy parameters, $\mathrm{d}\varepsilon_1$ and $\mathrm{d}\varepsilon_2$ are the increments of plastic deformation in the sheet plane, parallel to the O*x* and O*y* axes, respectively, and $\mathrm{d}\lambda$ is an incremental scalar factor of proportionality. In the bulge test, it can be assumed that $\sigma_3 = 0$

and, based on the equations (5), the incremental strain path can be related with the stress path as follows (Hill'48 criterion):

$$\frac{d\varepsilon_2}{d\varepsilon_1}=\frac{-\mathrm{H}+\frac{\sigma_2}{\sigma_1}\left(\mathrm{F}+\mathrm{H}\right)}{\left(\mathrm{G}+\mathrm{H}\right)-\frac{\sigma_2}{\sigma_1}\mathrm{H}}\ . \tag{6}$$

This equation can also be written as a function of the anisotropy coefficients, r_0 and r_{90}, respectively in the rolling (Ox || O1) and transverse (Oy || O2) directions of the sheet, as follows:

$$\frac{d\varepsilon_2}{d\varepsilon_1}=\frac{-1+\frac{\sigma_2}{\sigma_1}\left(\frac{1}{r_{90}}+1\right)}{\left(\frac{1}{r_0}+1\right)-\frac{\sigma_2}{\sigma_1}}\ . \tag{7}$$

Consequently, the equations (1) and (6) or (7) allow determining the principal stresses, σ_1 and σ_2, in case of circular and elliptical dies, assuming that the Hill'48 criterion describes the anisotropic behaviour of the material.

To calculate the equivalent stress, $\bar{\sigma}$, and the equivalent strain, $\bar{\varepsilon}$, values that characterize the hardening behaviour, the following equations can be used [15,27]:

$$\bar{\sigma}=\sqrt{\left(\mathrm{G}+\mathrm{H}\right)\sigma_1^2+\left(\mathrm{F}+\mathrm{H}\right)\sigma_2^2-2\mathrm{H}\sigma_1\sigma_2}\ , \tag{8}$$

$$\bar{\varepsilon}=\sqrt{\mathrm{F}\left[\frac{\mathrm{G}\varepsilon_2-\mathrm{H}\varepsilon_3}{\mathrm{FG}+\mathrm{GH}+\mathrm{HF}}\right]^2+\mathrm{G}\left[\frac{\mathrm{F}\varepsilon_1-\mathrm{H}\varepsilon_3}{\mathrm{FG}+\mathrm{GH}+\mathrm{HF}}\right]^2+\mathrm{H}\left[\frac{\mathrm{F}\varepsilon_1-\mathrm{G}\varepsilon_2}{\mathrm{FG}+\mathrm{GH}+\mathrm{HF}}\right]^2}\ . \tag{9}$$

In case of isotropic materials, obeying the von Mises yield criterion, the principal stresses, σ_1 and σ_2, in bulge tests performed either with circular or elliptical dies, can be calculated using the equation (1) and the following equation, deduced by simplifying equation (6) (or (7)):

$$\frac{d\varepsilon_2}{d\varepsilon_1}=\frac{-0.5+\frac{\sigma_2}{\sigma_1}}{1-0.5\frac{\sigma_2}{\sigma_1}}\ . \tag{10}$$

Similarly, the equivalent stress and strain can be calculated using the following simplified equations (von Mises):

$$\bar{\sigma} = \sqrt{(\sigma_1)^2 + (\sigma_2)^2 - \sigma_1\sigma_2}\,, \tag{11}$$

$$\bar{\varepsilon} = \left(\frac{2}{\sqrt{3}}\right)\sqrt{\varepsilon_1^2 + \varepsilon_2^2 + \varepsilon_1\varepsilon_2}\,. \tag{12}$$

Finally, in cases of circular die and isotropic or anisotropic materials such that, the anisotropy coefficients at 0º and 90º degrees are equal ($r_0 = r_{90}$), the principal stresses are also equal ($\sigma_1 = \sigma_2 = \sigma$), as well as the principal strains ($\varepsilon_1 = \varepsilon_2 = \varepsilon$) and radii of curvature ($\rho_1 = \rho_2 = \rho$), which simplifies equation (1) as follow:

$$\sigma = \frac{p\rho}{2t}\,. \tag{13}$$

In these cases, equation (13) is sufficient to determine the principal stresses in the sheet plane ($\sigma_1 = \sigma_2 = \sigma$), without requiring any additional equation.

Also, for materials with fully isotropic behaviour, equations (11) and (12) can be simplified for equibiaxial stress and strain paths (von Mises criterion):

$$\bar{\sigma} = \sigma \text{ and } \bar{\varepsilon} = 2\varepsilon\,. \tag{14}$$

Since the total strain presents two additive components, elastic and plastic, the elastic strain components, ε_1^e and ε_2^e, can be removed from the measured strains, ε_1 and ε_2. Assuming isotropic elastic behaviour, the generalized Hooke's law, gives the elastic strain components as:

$$\begin{cases} \varepsilon_1^e = \dfrac{1}{E}\left[\sigma_1 - \nu\left(\sigma_2 + \sigma_3\right)\right] \\ \varepsilon_2^e = \dfrac{1}{E}\left[\sigma_2 - \nu\left(\sigma_1 + \sigma_3\right)\right] \end{cases}. \tag{15}$$

Since in the bulge test it can be assumed that $\sigma_3 = 0$, this equation can be written:

$$\begin{cases} \varepsilon_1^e = \dfrac{1}{E}(\sigma_1 - \nu\sigma_2) \\ \varepsilon_2^e = \dfrac{1}{E}(\sigma_2 - \nu\sigma_1) \end{cases}. \tag{16}$$

3. NUMERICAL MODELLING AND ANALYSIS

In order to perform the study concerning the methodology for the evaluation of the work hardening law using the circular bulge test, a numerical model of the test was built, which is defined in this section. The geometry of the tools considered in the test is schematically shown in Figure 1, where R_M = 75 mm is the die radius, R_1 = 13 mm is the die profile radius, R_D =95 mm is the radius of the central part of the drawbead and R_S = 100 mm is the radius of the circular sheet. This geometry was built based on the experimental bulge test used by Santos *et al*. [32].

The tools were described using Bézier surfaces, considering only one quarter of the geometry due to the material and geometrical symmetry conditions. However, in order to simplify the analysis, the drawbead geometry was neglected and its effect was replaced by a boundary condition imposing radial displacement restrictions on the nodes placed at a distance equal to R_D from the centre of the circular sheet, which has an initial blank radius of R_S [10]. The contact with friction was described by the Coulomb law with a friction coefficient of 0.02 [33]. The numerical simulations were carried out with the *DD3IMP* in-house code [25,26] assuming an incremental increase of the pressure applied to the sheet inner surface. The blank sheet was discretized with solid 8 node elements, using two layers of elements through the thickness, as previously described [34].

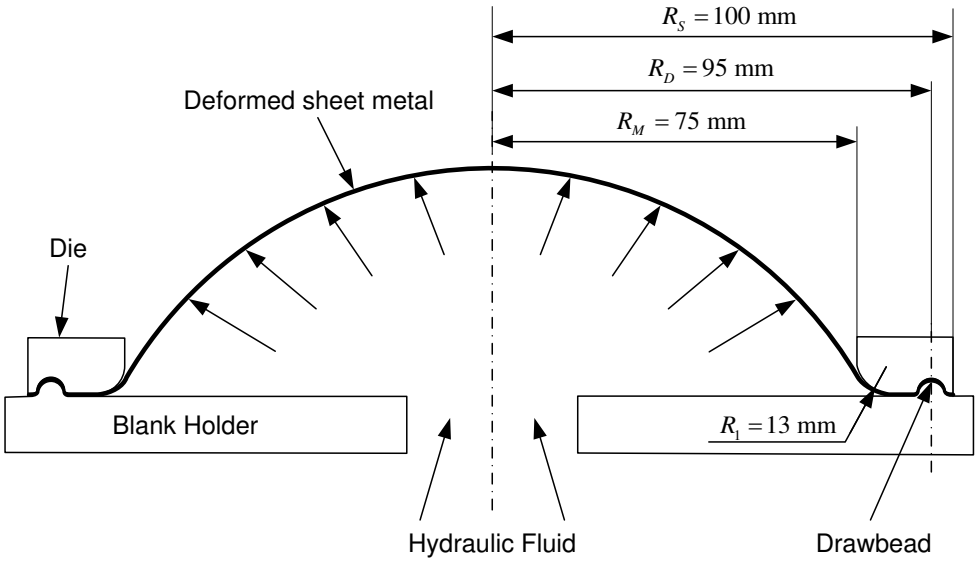

Figure 1. Bulge test, with the identification of the principal dimensions of the tool according to Santos *et al*. [32].

The constitutive model adopted for the finite element analysis assumes that: (1) the isotropic elastic behaviour is defined by the generalized Hooke's law; (2) the plastic behaviour is described by the orthotropic Hill'48 yield criterion and the hardening model by the Swift isotropic law.

The Hill'48 yield surface is described by the equation [27]:

$$\mathrm{F}(\sigma_{yy}-\sigma_{zz})^2+\mathrm{G}(\sigma_{zz}-\sigma_{xx})^2+\mathrm{H}(\sigma_{xx}-\sigma_{yy})^2+2\mathrm{L}\tau_{yz}^2+2\mathrm{M}\tau_{xz}^2+2\mathrm{N}\tau_{xy}^2=Y^2, \qquad (17)$$

where σ_{xx}, σ_{yy}, σ_{zz}, τ_{xy}, τ_{xz} and τ_{yz} are the components of the Cauchy stress tensor, in the principal axes of orthotropy, and F, G, H, L, M and N are the anisotropy parameters of the material. Y represents the yield stress and its evolution during deformation $Y = f(\bar{\varepsilon})$, which is described by the Swift isotropic hardening law [28]:

$$Y = K(\varepsilon_0+\bar{\varepsilon})^n, \qquad (18)$$

where $\bar{\varepsilon}$ is the equivalent plastic strain and K, ε_0 and n are the material parameters to be identified. The initial yield stress, σ_0, can be written as a function of K, ε_0 and n, as follows: $\sigma_0 = K\varepsilon_0^n$. The elastic behaviour is considered isotropic and described by the generalised Hooke's law, with a Young's modulus, E = 210 GPa, and a Poisson's ratio, ν = 0.30. The initial thickness of the sheet is 1 mm.

In few cases, duly identified in the text, the Drucker+L criterion and the Voce law [35] are also used. The Drucker+L yield criterion [36] is an extension of the Drucker isotropic criterion [37] and is described by the equation:

$$\left[\frac{1}{2}\mathrm{tr}(\mathbf{s}^2)\right]^3-c\left[\frac{1}{3}\mathrm{tr}(\mathbf{s}^3)\right]^2=27\left(\frac{Y}{3}\right)^6, \qquad (19)$$

where tr(**s**) is the trace of the stress tensor **s**, resulting from the linear transformation of the Cauchy stress tensor, **σ**, and c is a weighting isotropy parameter, ranging between −27/8 and 9/4, to ensure the convexity of the yield surface. When c equals zero, this criterion coincides with the Hill'48 yield criterion. The **s** stress tensor is given by:

$$\mathbf{s}=\mathbf{L}:\boldsymbol{\sigma}, \qquad (20)$$

where **L** is the linear transformation operator proposed by Barlat *et al*. [38]:

$$\mathbf{L} = \begin{bmatrix} (C_2 + C_3)/3 & -C_3/3 & -C_2/3 & 0 & 0 & 0 \\ -C_3/3 & (C_3 + C_1)/3 & -C_1/3 & 0 & 0 & 0 \\ -C_2/3 & -C_1/3 & (C_1 + C_2)/3 & 0 & 0 & 0 \\ 0 & 0 & 0 & C_4 & 0 & 0 \\ 0 & 0 & 0 & 0 & C_5 & 0 \\ 0 & 0 & 0 & 0 & 0 & C_6 \end{bmatrix}, \quad (21)$$

in which C_i, with $i = 1, \ldots, 6$, are the anisotropy parameters; $C_1 = C_2 = C_3 = C_4 = C_5 = C_6$ for the full isotropy condition. This yield criterion includes one more parameter, the parameter c, when compared to Hill'48 yield criterion, thus being more flexible. So, when the parameter c is not zero, Hill'48 criterion cannot fully describe the behaviour of a material that follows Drucker + L criterion.

The Voce law can be written as:

$$Y = \sigma_{sat} - R_{sat} \exp\left(-c_y \bar{\varepsilon}\right) \quad (22)$$

where σ_{sat}, R_{sat} and c_{y} are materials parameters; the yield stress is $\sigma_0 = \sigma_{sat} - R_{sat}$.

In order to determine the hardening curves, the analysis of the numerical simulation results was performed in the same way that is usually done experimentally, i.e. using step-wise measurements. The evaluation of the surface radius of curvature, ρ_{ext}, at the pole of the cap at various stages during the test, is performed by *NXT Defect Evaluator* code [39]. This software allows the evaluation of surface curvature, based on the coordinates of points located on the same meridian plane. The surface radius of curvature, ρ_{ext}, was analysed for both axes. The radius of curvature at half thickness, ρ, is determined using equation (4). At each stage, the principal strains in the sheet plane were determined by the direct measurement at the pole of the cap, as experimentally performed using digital image correlation technique (DIC).

4. CASES UNDER ANALYSIS

Numerical bulge tests were performed in metal sheets with in-plane isotropy and anisotropy. This section describes and characterizes the materials under study, and also illustrates their mechanical behaviour during the bulge test, by relating the pressure with pole height.

4.1. Sheet materials and analysis procedure

Table 1 shows the parameters of the Hill'48 criterion of the materials under study and the respective designation. It is assumed that the hardening curve corresponds to the stress *vs.* plastic strain curve under uniaxial tensile test along the O*x* axis, i.e. the condition G + H = 1 was used, for the parameters of the Hill'48 criterion [40]. The designation A_B_C corresponds to a material with the anisotropy coefficient, r_α, in the sheet plane such that: r_0 = A, r_{45} = B and r_{90} = C. The selected materials for this study display three different types of anisotropy in the sheet plane: (i) isotropy: $r_0 = r_{45} = r_{90}$; (ii) anisotropy with: $r_0 = r_{90} \neq r_{45}$; (iii) full anisotropy: $r_0 \neq r_{90}$. Figure 2 shows the evolution of the anisotropy coefficient, r_α, in the sheet plane for the materials with in-plane anisotropy.

Table 1. Designation of the materials and the respective parameters of Hill'48 criterion.

Designation	Parameters of the Hill'48 Criterion					
	F	**G**	**H**	**L**	**M**	**N**
Materials with $r_0 = r_{45} = r_{90}$						
0.7_0.7_0.7	0.588	0.588	0.412	1.500	1.500	1.412
1_1_1	0.500	0.500	0.500	1.500	1.500	1.500
2_2_2	0.333	0.333	0.667	1.500	1.500	1.667
3_3_3	0.250	0.250	0.750	1.500	1.500	1.750
Materials with $r_0 = r_{90} \neq r_{45}$						
0.6_3_0.6	0.625	0.625	0.375	1.500	1.500	4.375
3_0.6_3	0.250	0.250	0.750	1.500	1.500	0.550
1.5_3_1.5	0.400	0.400	0.600	1.500	1.500	2.800
3_1.5_3	0.250	0.250	0.750	1.500	1.500	1.000

Materials with $r_0 \neq r_{90}$						
0.6_0.7_0.8	0.469	0.625	0.375	1.500	1.500	1.313
0.6_1.8_3	0.125	0.625	0.375	1.500	1.500	1.725
1.5_2.25_3	0.200	0.400	0.600	1.500	1.500	1.650
1.5_2.75_4	0.150	0.400	0.600	1.500	1.500	1.788
0.5_2.25_4	0.083	0.667	0.333	1.500	1.500	2.063
1.5_3_3	0.200	0.400	0.600	1.500	1.500	2.100
1_2.25_3.5	0.143	0.500	0.500	1.500	1.500	1.768

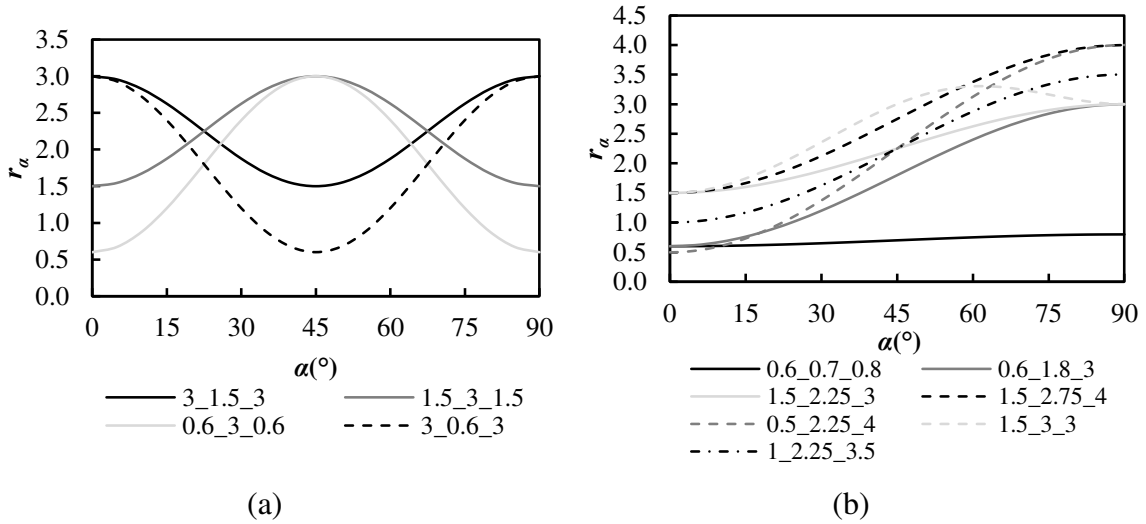

(a) (b)

Figure 2. Distribution of r_α in the sheet plane, for materials with anisotropy in this plane: (a) $r_0 = r_{90} \neq r_{45}$; (b) $r_0 \neq r_{90}$.

In order to better describe the anisotropic state of the materials, Figure 3 shows the evolution of the ratio $\sigma^0{}_\alpha / \sigma^0{}_0$ between the yield stress in tension, $\sigma^0{}_\alpha$, for an angle, α, in the sheet plane, and the yield stress in tension along Ox, $\sigma^0{}_0$, as a function of α angle, for the materials with $r_0 = r_{90} \neq r_{45}$ and for materials with $r_0 \neq r_{90}$.

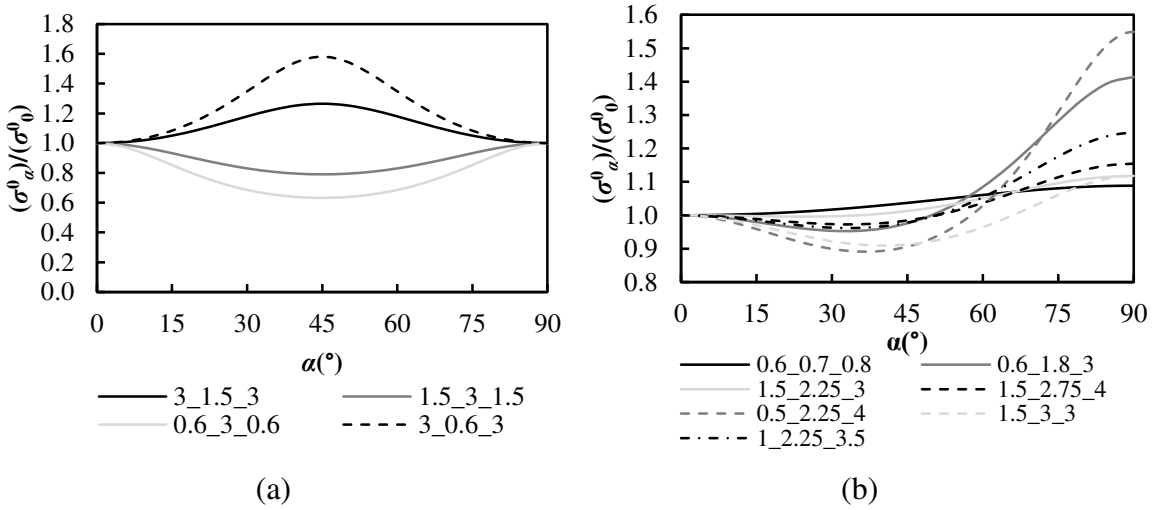

(a) (b)

Figure 3. Distribution of $\sigma^0{}_\alpha/\sigma^0{}_0$ in the sheet plane, for materials with anisotropy in this plane: (a) $r_0 = r_{90} \neq r_{45}$; (b) $r_0 \neq r_{90}$.

Figure 4 and 5 shows the normalized initial yield surfaces in the $\left(\sigma_{xx}/\sigma^0{}_0;\sigma_{yy}/\sigma^0{}_0\right)$ space of the materials with $r_0 = r_{90}$ (Figure 4) and with $r_0 \neq r_{90}$ (Figure 5). The dashed-dotted grey straight lines correspond to the condition $\sigma_2 = \sigma_1$. The solid, dashed and dotted grey and black straight lines in Figure 5 indicate the axes of the ellipses. The yield surface of the materials 3_3_3, 3_1.5_3 and 3_0.6_3 are coincident (see Figure 4), as well as those of the materials 1.5_2.25_3 and 1.5_3_3, by one side, and the materials 1_2.25_3 and 1_3_3, by other side (Figure 5). The axes of the materials 0.6_0.7_0.8 and 1.5_2.75_4 are collinear. The yield surfaces of the materials 0.6_1.8_3 and 0.5_2.25_4, for which $r_0 < 1$ and $r_{90} > 1$, have their axes with higher slope than those of the other materials. The size of the yield surface is clearly smaller in case of the material 0.6_0.7_0.8 than others.

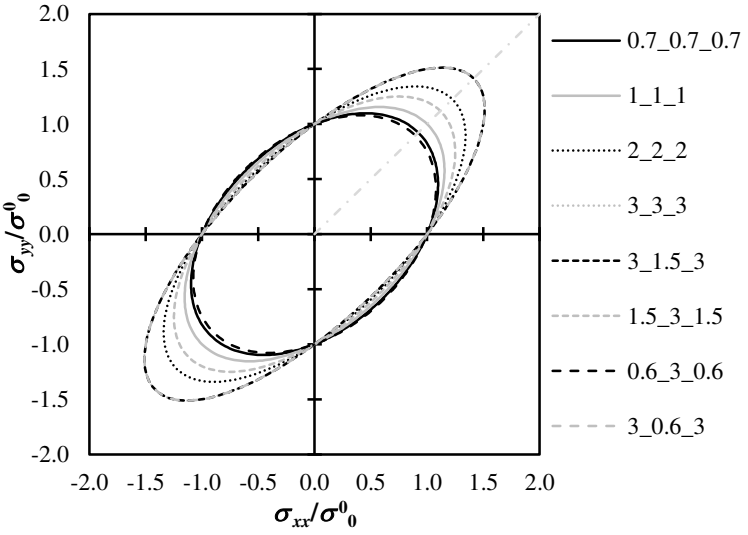

Figure 4. Normalized initial yield surfaces in the plane $\left(\sigma_{xx}/\sigma^0{}_0;\sigma_{yy}/\sigma^0{}_0\right)$ of the materials with $r_0 = r_{90}$. $\sigma^0{}_0$ is the initial tensile yield stress along the Ox axis.

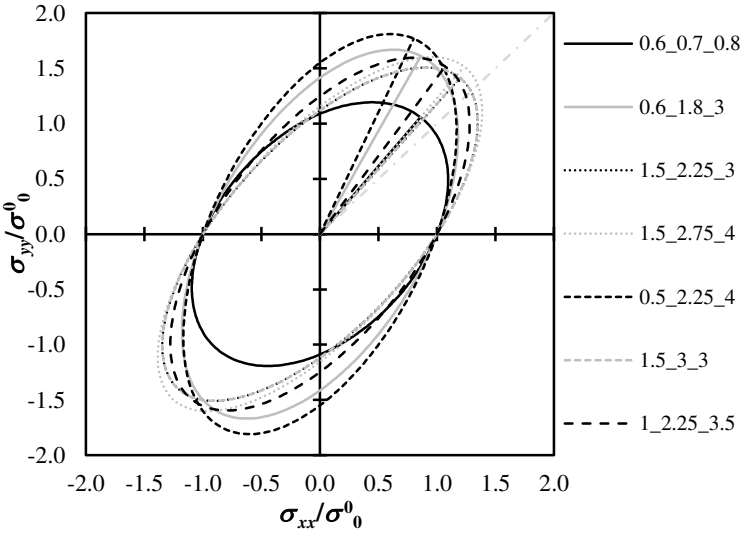

Figure 5. Normalized initial yield surfaces in the plane $\left(\sigma_{xx}/\sigma^0{}_0;\sigma_{yy}/\sigma^0{}_0\right)$ of the materials with $r_0 \neq r_{90}$. $\sigma^0{}_0$ is the initial tensile yield stress along the Ox axis.

The parameters of the Swift hardening law, for the materials studied in the next sections, are shown in Table 2. Simulations were performed for all the materials in Table 1 with the work hardening coefficient, n, equal to 0.20 (see Table 2). The hardening laws with work hardening coefficients, n, equal to 0.10 and 0.35 were only used for simulations of the materials 0.6_0.7_0.8, 1.5_2.75_4 and 0.5_2.25_4 (see Table 1).

Table 2. Parameters of the Swift hardening law.

Materials	Parameters of the Swift law			
	σ_0 [MPa]	K [MPa]	ε_0	n
200_0.10	200	339.73	0.005	0.10
200_0.20	200	577.08	0.005	0.20
200_0.35	200	1277.59	0.005	0.35

4.2. Curves *p vs. h*

This section shows examples of numerical results of pressure *vs.* pole height curves, relating to the materials of Table 1 with hardening coefficient, n, equal to 0.20. Figure 6 (a) concerns the cases of the materials with $r_0 = r_{90}$, indicating that the behaviour depends on the value of these anisotropy coefficients, which define the size of the major axis of the ellipse (for a given hardening curve). The higher the anisotropy coefficients, r_0 and r_{90} (i.e. the longer is the major axis of the ellipse), the higher is the pressure level of the curves. The materials 3_3_3, 3_1.5_3 and 3_0.6_3, which show coincidence of the yield surfaces in the $\left(\sigma_{xx}/\sigma^0{}_0;\sigma_{yy}/\sigma^0{}_0\right)$ space, have the pressure *vs*. pole height curves almost coincident. Also the materials 0.7_0.7_0.7 and 0.6_3_0.6 have very close pressure *vs*. pole height curves.

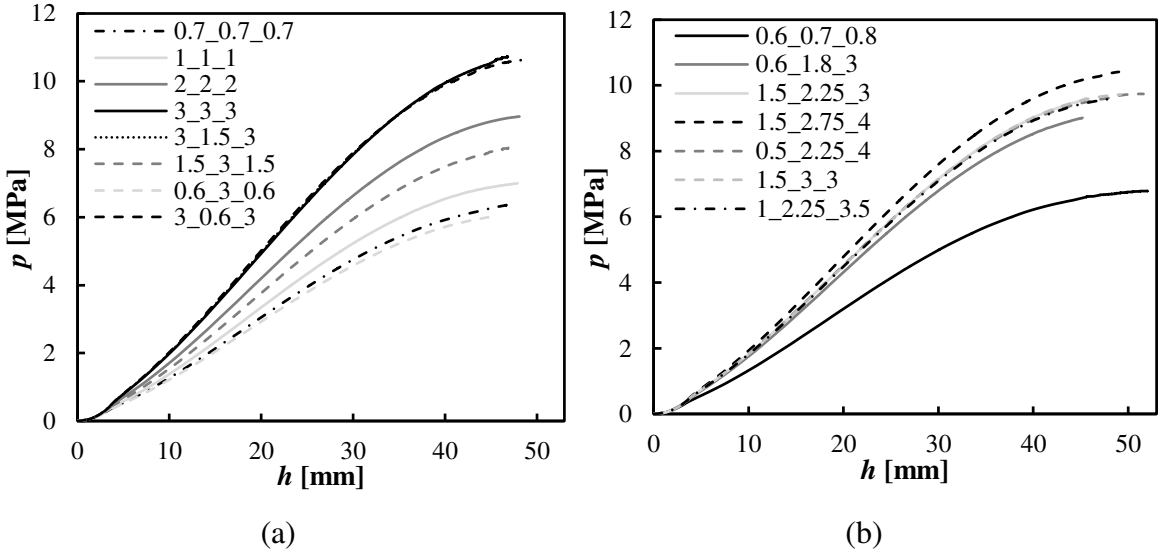

(a) (b)

Figure 6. Evolution of the pressure, p, with the pole height, h, for Hill'48 materials: (a) $r_0 = r_{90}$; (b) $r_0 \neq r_{90}$. The hardening coefficient of the material is $n = 0.20$.

Figure 6 (b) shows the evolution of the pressure with the pole height, for the cases of the materials with in-plane anisotropic behaviour ($r_0 \neq r_{90}$). The values of the anisotropic coefficient influences the level of the curves, in a similar way to the cases of materials with $r_0 = r_{90}$, (the average values of r_0 and r_{90} are related with the magnitude of the major axis of the ellipse). However, for these materials, the level of the pressure *vs.* pole height curves depends on the stress path that does not coincide with the axis of the ellipse, as will be seen later. The material 1.5_2.75_4, with the longest major axis of the ellipse but close to the material 0.5_2.25_4 (Figure 5), presents the curve with the highest level and the material 0.6_0.7_0.8, with the shortest major axis of the ellipse (Figure 5), shows the curve with the lowest level. The other curves have relatively close levels. Moreover, the materials with the same value of r_0 and r_{90}, even with different r_{45} (1.5_2.25_3 and 1.5_3_3 materials), show evolutions of the pressure with the pole height quite coincident. Finally, the materials 1_2.25_3.5 and 0.5_2.25_4 (Figure 4 (b)) show curves very close to the materials 3_1.5_3 and 3_0.6_3 (Figure 4 (a)), with a small difference at the end of the test, which seems to indicate that also the value of the normal anisotropic coefficient influences this evolution.

5. GEOMETRY OF THE CAP AND STRESS AND STRAIN DISTRIBUTIONS

This section analyses the distributions, near the pole of the cap of the bulge test, of variables such as the radius of curvature, the sheet thickness, the principal and equivalent stresses and strains as well as the stress and strain paths. The analysis mainly focuses on the in-plane anisotropic materials with $r_0 \neq r_{90}$, for which there remains a lack of knowledge about these aspects. In fact, in case of in-plane isotropic materials, most of these issues have already been analysed (see for example [22]), in view of their relative simplicity related to the geometrical and material symmetry. Also the materials of the current study with $r_0 = r_{90} \neq r_{45}$ show identical behaviour along the axes Ox and Oy, due to the symmetry of the yield surface in the (σ_{xx}; σ_{yy}) space and the geometrical symmetry of the circular bulge test. That is why the analysis in this section deals primarily with materials such that $r_0 \neq r_{90}$.

Concerning the analysis of the surface shape of the specimen, the results showed that, also for in-plane anisotropic materials, the geometry of the cap has symmetry such that

the radii of curvature at the pole of the cap are equal along the axes Ox and Oy ($\rho_1 = \rho_2 = \rho$), at each moment of the test, the same occurring for the sheet thickness. On the contrary, the principal stress and strain distributions are different along these axis, i.e. the stress and strain paths at the pole of the cap are always different from 1 ($\sigma_1 \neq \sigma_2$ and $\varepsilon_1 \neq \varepsilon_2$).

The materials with strong anisotropy in the sheet plane, 1.5_2.75_4 and 0.5_2.25_4, and with hardening coefficient, n = 0.20, were chosen to illustrate the general detailed behaviour, that is, not only at the pole cap, but also in distant points. Figure 7 shows the evolution of pressure with the pole height for these materials (see also Figure 6) and the moments of the bulge test under analysis. These correspond to four pressure values during the tests, marked in the figure with points, which corresponds to: (i) material 1.5_2.75_4 with pressure values of 4.5, 8.5, 9.5 and 10 MPa (corresponding to the Hill'48 equivalent strains equal to 0.066, 0.231, 0.329 and 0.421 at the pole of the cap, respectively); and (ii) material 0.5_2.25_4 with pressure values of 4, 8, 9 and 9.4 MPa (corresponding to the Hill'48 equivalent strains equal to 0.059, 0.229, 0.336 and 0.421 at the pole of the cap, respectively).

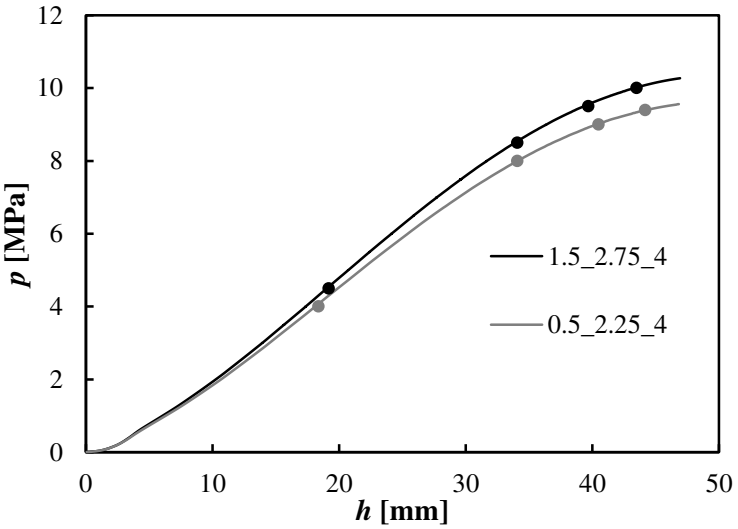

Figure 7. Evolution of the pressure, p, with the pole height, h, for materials 1.5_2.75_4 and 0.5_2.25_4. The dots concern the pressure values on which the analysis is focused: 4.5, 8.5, 9.5 and 10 MPa, for the material 1.5_2.75_4, and 4, 8, 9 and 9.4 MPa, for the material 0.5_2.25_4. The hardening coefficient of both material is n = 0.20.

Figure 8 shows the contours of the cap, i.e. the vertical position of each point, z, as a function of the distance to the centre, d, along the Ox and Oy axes, for the materials 1.5_2.75_4 (Figure 8 (a)) and 0.5_2.25_4 (Figure 8 (b)) and the pressure values above mentioned (see Figure 7). Whatever the pressure value, the Ox and Oy profiles coincide, from the centre to the edge of the cap (Figure 8). This means that the radii of curvature at

the pole of the cap does not depend on the measuring axis, O*x* or O*y*, which was also separately tested.

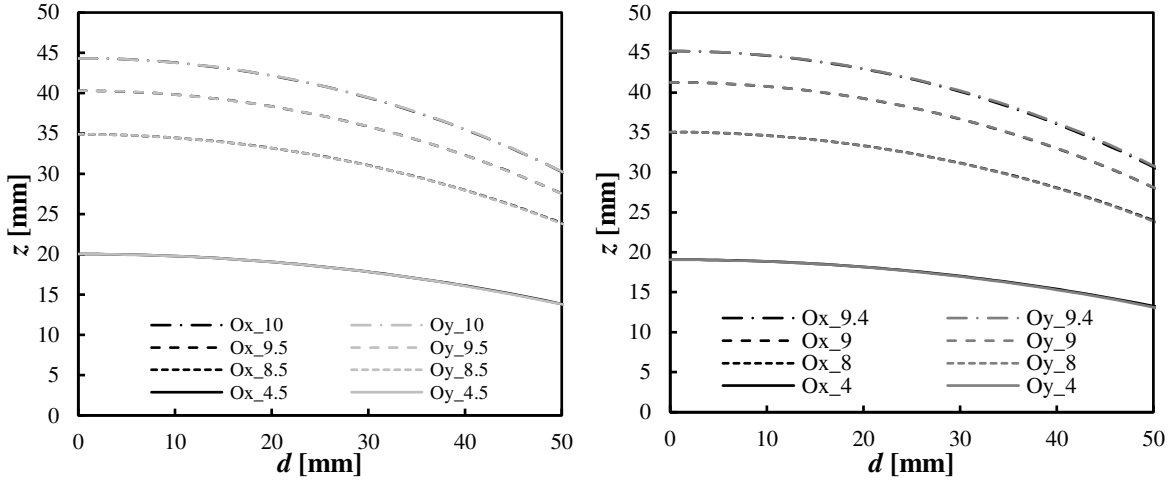

(a) (b)

Figure 8. Contours of the cap at the four pressure values indicated in the Figure 7, i.e. vertical position, *z*, with the distance to the centre, *d*, along the O*x* and O*y* axes, for the materials: (a) 1.5_2.75_4; (b) 0.5_2.25_4. The hardening coefficient of both material is *n* = 0.20.

Figure 9 shows the evolution of the thickness as a function of the distance to the centre, *d*, along the O*x* and O*y* axes, for the materials 1.5_2.75_4 (Figure 9 (a)) and 0.5_2.25_4 (Figure 9 (b)) and the pressure values above mentioned (see Figure 7). As for the profiles, the thickness distributions are almost coincident for the axes O*x* and O*y* at the two first steps analysed, although some differences are noticeable for the two higher pressure values, mainly in case of the material 0.5_2.25_4. These differences in thicknesses occurs in this material for distances from the centre higher than about 20 mm, at a pressure equal to 9 MPa, and higher than at about 15 mm, at a pressure equal to 9.4 MPa.

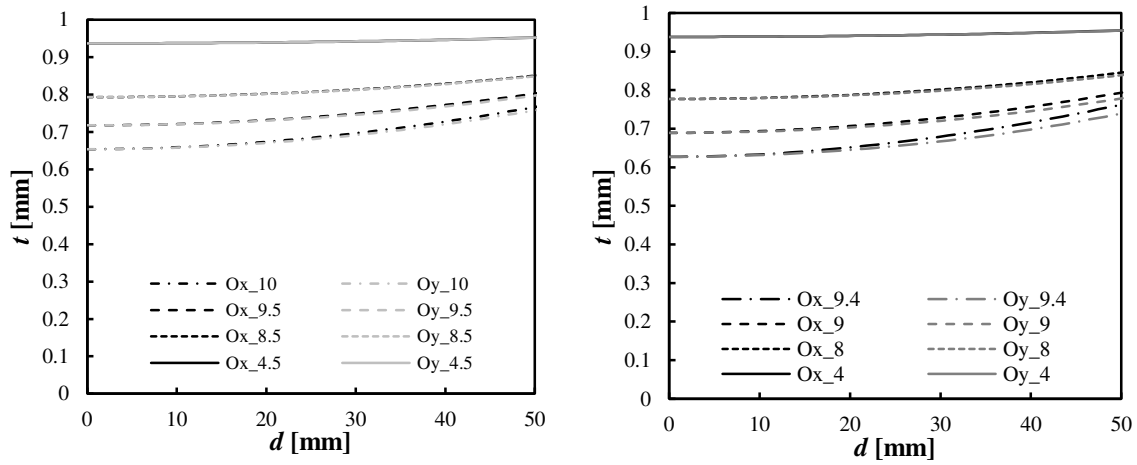

(a) (b)

Figure 9. Evolution of sheet thickness, t, with the distance to the centre, d, along the Ox and Oy axes, at the four pressure values indicated in the Figure 7, for the materials: (a) 1.5_2.75_4; (b) 0.5_2.25_4. The hardening coefficient of both material is n = 0.20.

The analyses of the evolution during the bulge test of the radius of curvature and the sheet thickness at the pole of the cap was performed for all materials of Table 1 with hardening coefficient, n, equal to 0.20. Figure 10 shows the evolution of the radius of curvature, ρ, with the pole height, h. At the beginning of the test, the radius of curvature quickly decreases, but its rate of decrease declines as the pole height increases, so that when the pressure approaches the maximum value, the radius of curvature come close to the radius of the die (R_M = 75 mm in Figure 1). Moreover, the anisotropy does not influences the evolution of the radius of curvature. The coincidence observed, whatever the anisotropy of the material, is in agreement with the results previously reported only for in-plane isotropic materials with different r values in the sheet plane [34]. This work reported that only the hardening coefficient influences the evolution of the radius of curvature during the test, being independent of the value of the yield stress, initial sheet thickness and in-plane isotropy. Identical feature was observed for the three materials analysed with n = 0.10 and 0.35 – see Table 2).

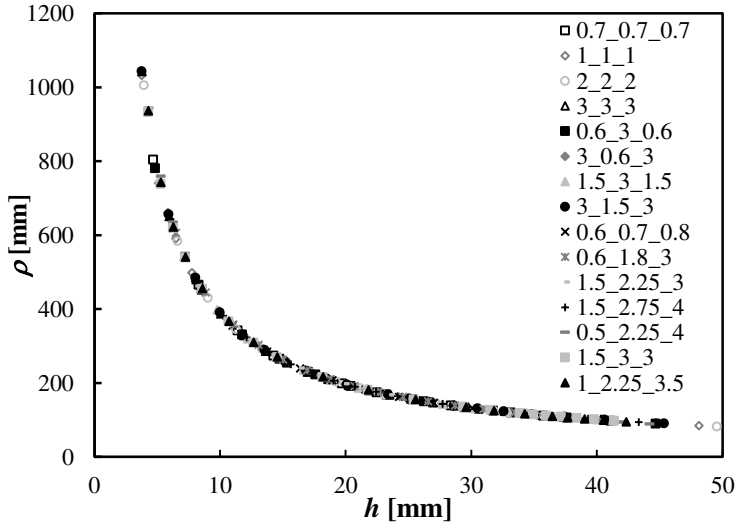

Figure 10. Evolution of the radius of curvature, ρ, with the pole height, h, for all materials with hardening coefficient n = 0.20.

The evolution of the sheet thickness at the pole of the cap during the test is shown in Figure 11, for the materials with hardening coefficient n = 0.20. The values of the thickness at different moments of the test were determined based on the values of the strains measured at the top of the cap and using equations (2) and (3). Figure 11 (a) shows the evolution of the sheet thickness at the pole, t, with the pole height, h, for the materials with $r_0 = r_{90}$ and the results in Figure 11 (b) concern the materials with $r_0 \neq r_{90}$ (the isotropic material, 1_1_1, is also shown for comparative purposes). The evolution of the sheet thickness is sensitive to the anisotropy of the material, as previously observed for in-plane isotropic materials [34]. This work reports that, besides the hardening coefficient, also the anisotropic coefficient influences the evolution of the thickness at the pole during the test, which is independent of the value of the yield stress and the initial sheet thickness. The current results show that the value of the normal anisotropy coefficient in the sheet plane has identical influence on the evolution of the sheet thickness during the test, whether or not the sheet shows in-plane anisotropy (compare Figure 11 (a) with Figure 11 (b)).

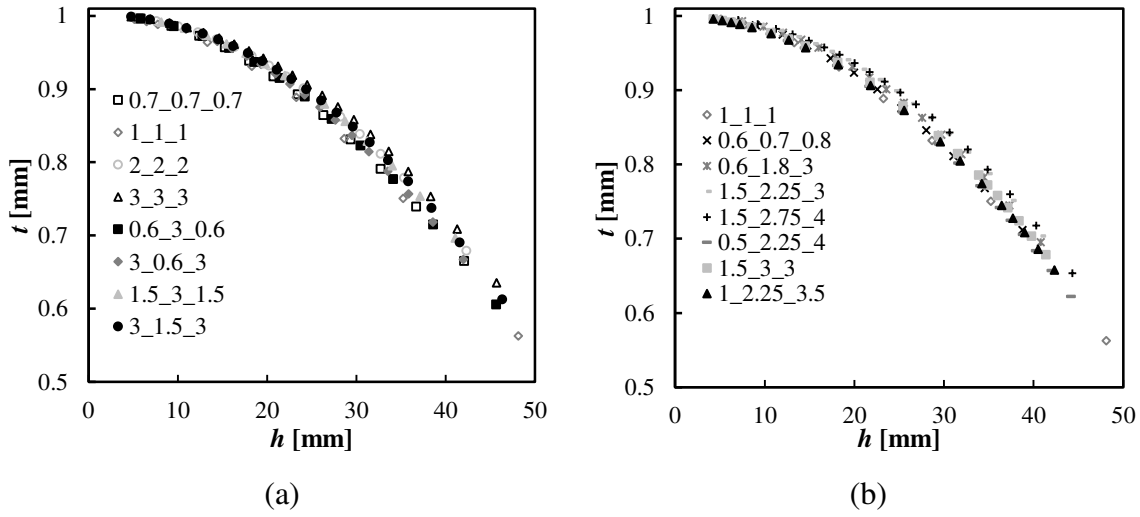

Figure 11. Evolution of the sheet thickness, t, with the pole height, h, for materials with hardening coefficient n = 0.20: (a) materials with $r_0 = r_{90}$; (b) materials with $r_0 \neq r_{90}$. These evolutions concern materials with hardening coefficient equal to 0.20.

Figure 12 and 13 show the distributions of the principal strains and stresses, parallel to the Ox and Oy directions, for the materials and pressure values as in Figure 8 and 9 (see also Figure 7). For a region around the pole of the cap, whose size decreases as the test progresses, the strains and stresses components parallel (normal) to the Ox axis, at a given point on this axis, are equal to the corresponding normal (parallel) components to the Oy axis, for a point on this axis at the same distance from the centre of the cap. At a given pole height, the size of this region is smaller the greater the planar anisotropy of the material, measured by the angle between the major axis of the yield surface and the biaxial stress axis ($\sigma_1 = \sigma_2$), as it can be concluded by comparing the results of materials 1.5_2.75_4 (Figure 12) and 0.5_2.25_4 (Figure 13).

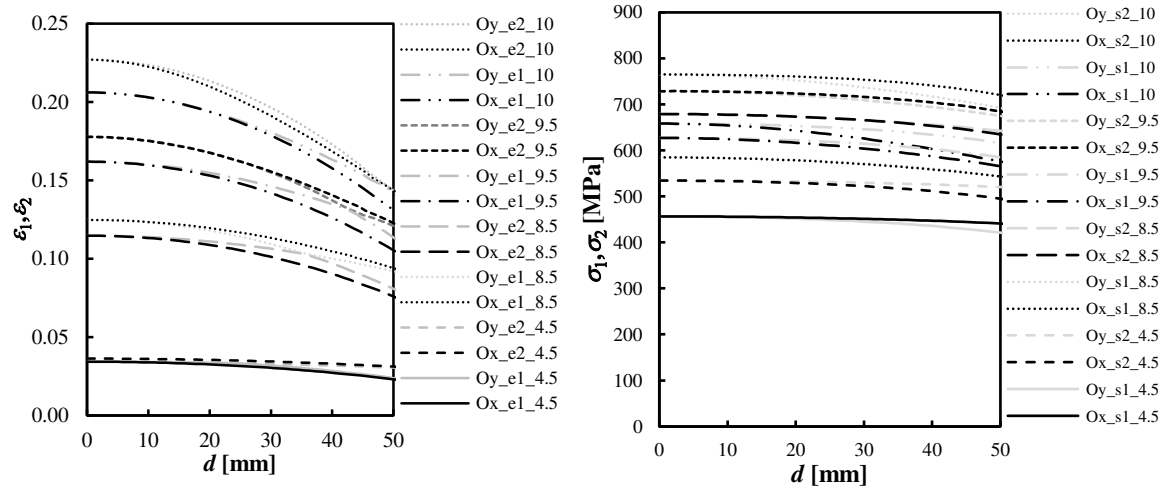

(a) (b)

Figure 12. Evolution of the (a) principal strains and (b) principal stresses, with the distance to the centre along the axes O*x* and O*y* of the sheet, for material 1.5_2.75_4 at the four pressure values indicated in the Figure 7. The hardening coefficient of the material is n = 0.20. The designation in figures can be read as for the example(s): Ox_e1_10 (Oy_s2_4.5), in which O*x* (O*y*) indicates the axis for measuring the distance *d*; e1 (s2) is the strain (stress) value parallel to the O*x* (O*y*) axis; and 10 (4.5) is the pressure value [MPa].

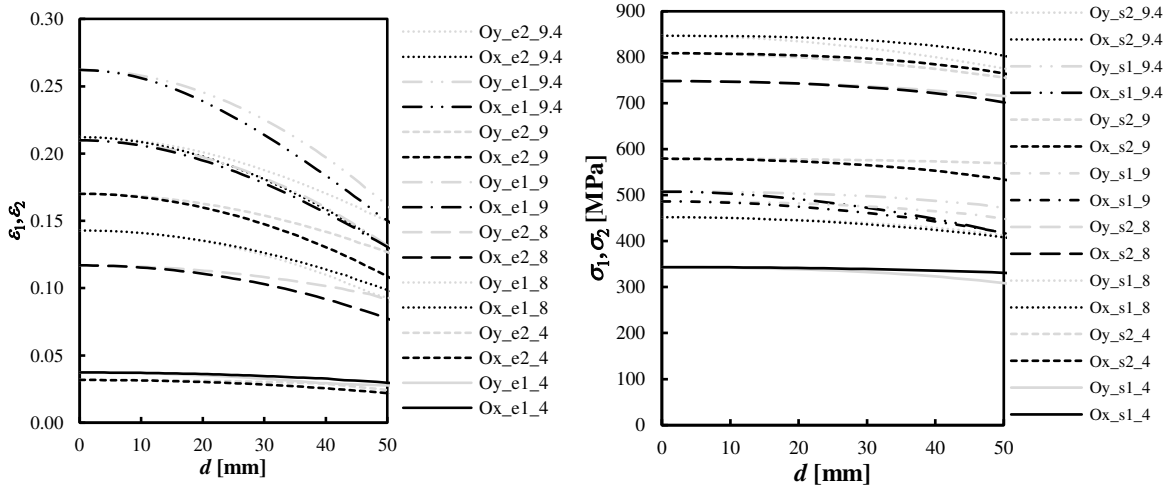

(a) (b)

Figure 13. Evolution of the (a) principal strains and (b) principal stresses, with the distance to the centre of the sheet, for material 0.5_2.25_4 at the four pressure values indicated in the Figure 7. The hardening coefficient of the material is n = 0.20. The designation are as indicated in Figure 12.

Figure 14 and 15 show the distributions of the Hill'48 equivalent strains and stresses, along the O*x* and O*y* directions, for the same materials and pressure values as in Figures 8, 9, 12 and 13 (see also Figure 7). Following the trends in Figures 12 and 13, the equivalent strains and stresses are equal along both orthotropic axes, in a region around the

pole. This region becomes smaller with the increase of the pole height but, even near the end of the test, its size is about 10 mm, for the material 0.5_2.25_4, and higher for the material 1.5_2.75_4, in case of equivalent strain, and covers almost the entire diameter of the die, for both materials in the case of equivalent stress.

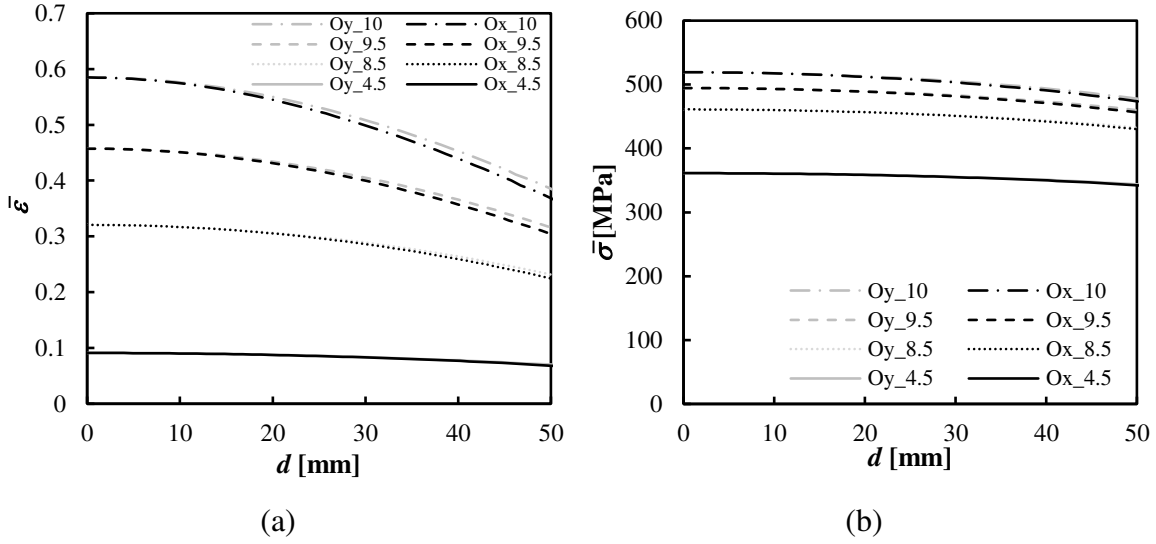

Figure 14. Evolution of the (a) equivalent strain and (b) equivalent stress with the distance to the centre along the O*x* and O*y* axes, for the material 1.5_2.75_4 at the four pressure values indicated in the Figure 7. The hardening coefficient of the material is n = 0.20.

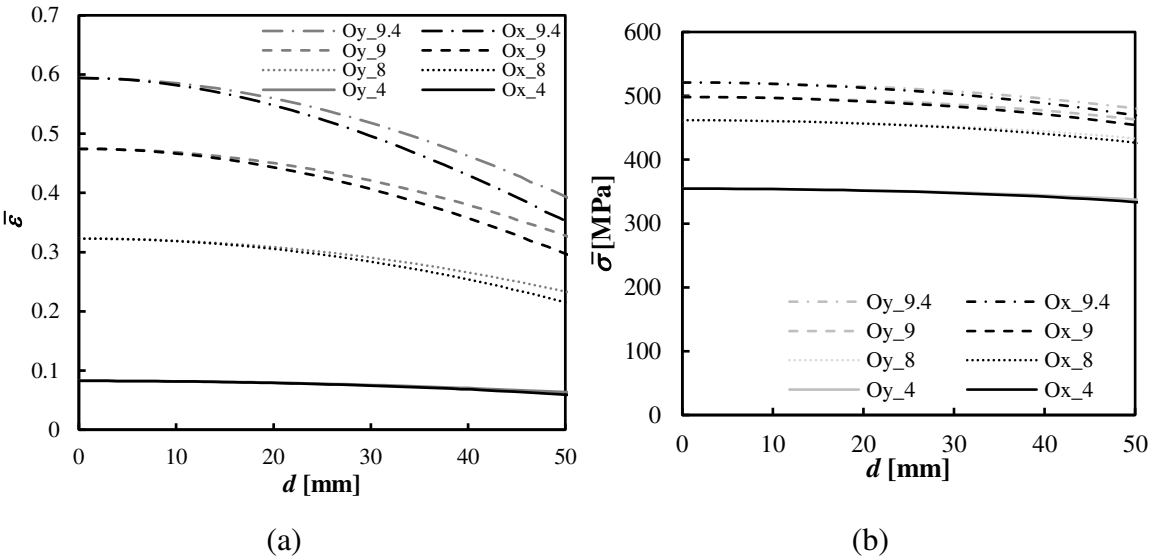

Figure 15. Evolution of (a) equivalent strain and (b) equivalent stress with the distance to the centre along the O*x* and O*y* axes, for the material 0.5_2.25_4 at the four pressure values indicated in the Figure 7. The hardening coefficient of the material is n = 0.20.

Based on results such as in Figures 12 and 13, Figure 16 present respectively the stress (Figure 16 (a)) and strain (Figure 16 (b)) paths observed at the pole of the cap, for in-plane anisotropic materials with hardening coefficient, $n = 0.20$, showing that the stress paths are nearly unchanged during the bulge test, although with minor variations. However, noticeable decreasing of the strain path occurs during the test, in some cases. In fact, small variations in stress paths involve larger variation of amplitude in the strain path that is represented by the normal to the yield surface. The difference between the strain paths during the test is always inferior to 5%, whatever the material (the maximum difference occurs for the material 0.5_2.25_4).

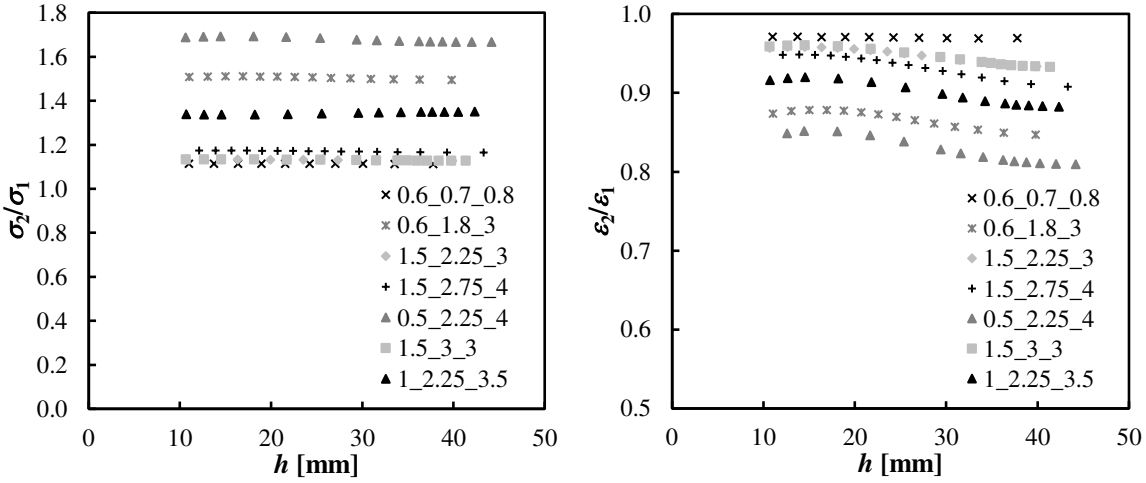

Figure 16. Evolution of the: (a) stress paths and (b) strain paths during the test. These evolutions concern materials with hardening coefficient equal to 0.20.

The stress and strain paths are also influenced by the hardening coefficient of the material, as can be deduced from the results of materials with hardening coefficients, n = 0.10 and 0.35. Figure 17 allow comparing the materials 0.6_0.7_0.8, 1.5_2.75_4 and 0.5_2.25_4, with n = 0.10, 0.20 and 0.35 concerning the stress (Figure 17 (a)) and strain (Figure 17 (b)) paths. The stress paths are almost unchanged during the test, and nearly close to each other for a given value of the hardening coefficient. Nevertheless, the small variations that occurs in the stress path are enough to cause larger variations in the strain path (in agreement with the associated flow rule), which decreases during the test (except for the material 0.5_2.25_4, with n = 0.10), as for results in Figure 16. Finally, it can be observed that in general the strain path is lower for higher values of hardening coefficient.

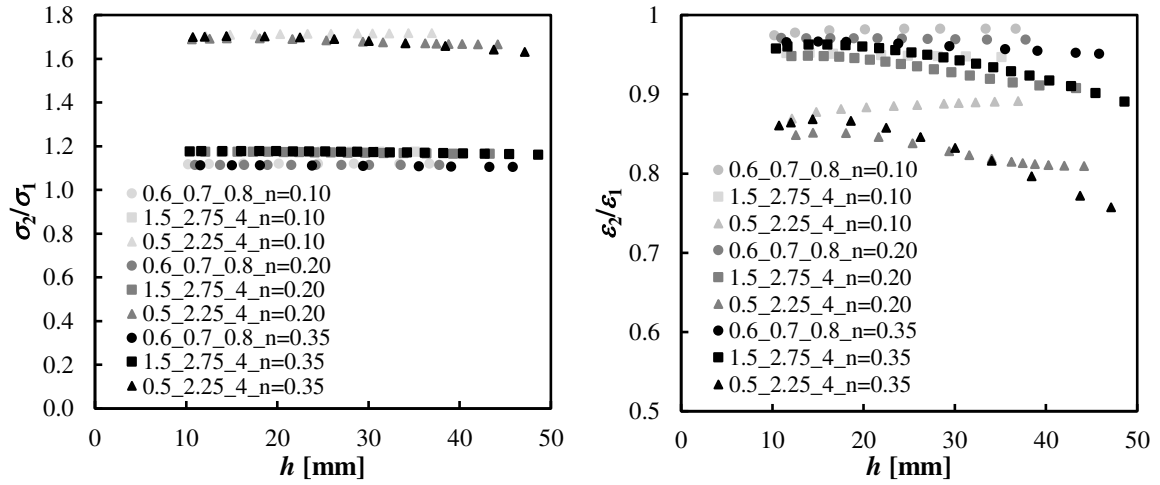

Figure 17. Evolution of the (a) stress paths and (b) strain paths during the test. These evolutions concern the materials 0.6_0.7_0.8, 1.5_2.75_4 and 0.5_2.25_4, with hardening coefficients equal to 0.10, 0.20 and 0.35.

As partial conclusions, it can be stated that for the materials with $r_0 \neq r_{90}$, the geometry of the cap is similar along both orthotropic axes in the sheet plane, with respect to the profile and the thickness of the sheet, which is imposed by the geometrical constrains of the bulge test with circular die. The results show that this type of symmetry can be achieved even though the stress and strain paths in the pole region are away from the biaxial symmetry. The inability to impose equibiaxial stress and strain paths simultaneously, in case of materials with $r_0 \neq r_{90}$, arises from the normality condition (equation (6) or (7), in case of Hill'48 criterion), i.e. the associated flow rule with the yield surface as plastic potential. This is illustrated in Figure 18 showing that, for materials with $r_0 < r_{90}$ as those studied in this work, when the stress path is equal to 1, the strain path is lower than 1, and when the strain path is equal to 1, the stress path is higher than 1 (the opposite occurs when $r_0 > r_{90}$). In fact, the observed stress and strain paths are between these two cases, as schematized in Figure 18.

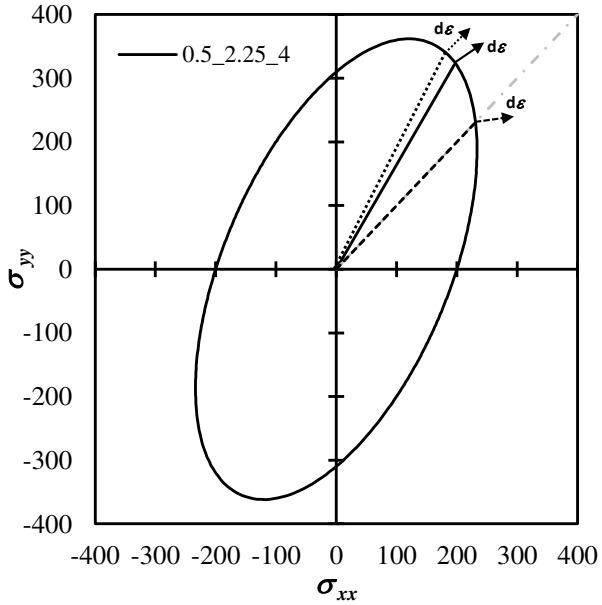

Figure 18. Illustrative example, corresponding to the material 0.5_2.25_4, showing the yield surface and the observed stress and strain paths (solid lines), the stress and strain paths corresponding to equibiaxial stress path (dashed lines) and equibiaxial strain path (dotted lines).

6. Hardening curves

The determination of the biaxial stress *vs*. strain curve from the bulge test is analysed under the experimental procedure generally performed, assuming equibiaxial stress and the von Mises definition of equivalent stress and strain [21]. First of all, the in-plane isotropic materials and anisotropic materials with $r_0 = r_{90}$ are considered. Afterwards, it deals with the in-plane anisotropic materials such that $r_0 \neq r_{90}$.

The assumption of isotropy for determining the equivalent stress consists of considering the equivalence between the real yield surface of the anisotropic material and an isotropic yield surface (von Mises surface), such that these surfaces intercept each other (or are tangent) at the point corresponding to the stress path followed during the bulge test by the real anisotropic material. This implies that the equivalent stress value is the same for both surfaces, namely at the point of coincidence of the curves. Examples are shown in the Figure 19, for materials with in-plane isotropy, 3_3_3 (Figure 19 (a)), and in-plane anisotropy, 0.5_2.25_4 (Figure 19 (b)).

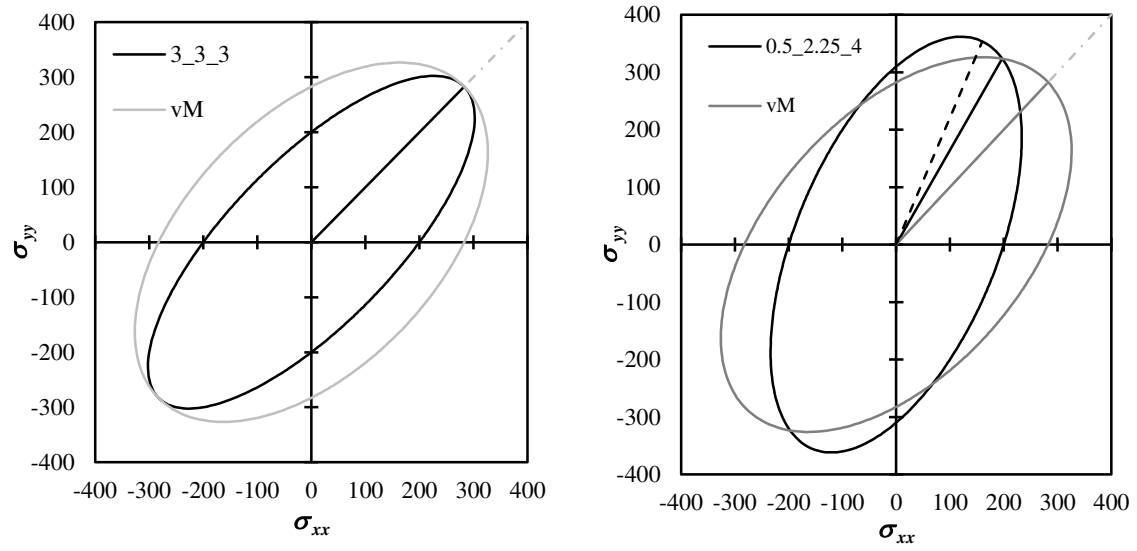

Figure 19. Initial yield surfaces and observed stress paths (black solid line) of the materials: (a) 3_3_3; (b) 0.5_2.25_4. The isotropic materials with equal equivalent stress are also indicated in each figure (grey solid lines). The bulge stress path is equibiaxial in case of (a) and is $\sigma_2/\sigma_1 = 1.678$ (black solid line) in case of (b). The dashed and the grey solid lines in (b) represent the axis of the Hill'48 and von Mises ellipses, respectively. The hardening coefficient of the materials is $n = 0.20$.

At the tangent and intercepting points of the ellipses, respectively in Figures 19 (a) and (b), the equivalent stresses are equal, whether they are calculated using the Hill'48 (equation (8)) or von Mises yield criteria (equation (11)). Consequently, the use of the von Mises criterion for determining the equivalent stress is appropriated, providing that the stress path at the pole of the cap is known. In case of in-plane isotropic materials and materials with $r_0 = r_{90} \neq r_{45}$, this does not involve any difficulty, given that $\sigma_2 = \sigma_1$, at the pole of the cap. In case of materials with $r_0 \neq r_{90}$, the equivalent stress depends on the stress path and the parameters of the anisotropic yield criterion (see equation (8)).

The Hill'48 material parameters in Table 1 follows the condition G + H = 1, which means that the hardening curve is equal to the stress *vs*. strain curve in tension along the O*x* axis. In order to allow the appropriate comparison of results obtained by the membrane theory with the biaxial hardening curves of the studied materials, Tables 3 and 4 show constitutive parameters, equivalent to those in Tables 1 and 2. The constitutive parameters in Tables 3 and 4, were determined such that the Hill'48 equivalent stress is equal to the determined by the von Mises criterion that crosses (or is tangent to) the Hill'48 surface

(see Figure 19), for the observed stress path (average during the test) at the pole of the cap, as shown in Figures 16 (a) and 17 (a). The relationships that allows the equivalence between sets of parameters were previously discussed in [40] and are, for the Hill'48 criterion and the Swift law, respectively:

$$F^* = kF;\ G^* = kG;\ H^* = kH;\ L^* = kL;\ M^* = kM;\ N^* = kN \tag{23}$$

$$n^* = n;\ K^* = K\left(\sqrt{k}\right)^{n+1};\ \varepsilon_0^* = \varepsilon_0/\sqrt{k};\ \sigma_0^* = \sigma_0\sqrt{k} \tag{24}$$

where k is a factor which forces the yield surfaces (Hill'48 and von Mises) to coincide at the point corresponding to the observed stress path during the bulge test. The parameters without asterisk are those in Tables 1 and 2 and with asterisk are shown in Tables 3 and 4 (for convenience of the presentation, the asterisks are not indicated in Table 3). Table 3 shows the hardening law and Hill'48 criterion equivalent parameters of all materials in Table 1 and hardening coefficient n = 0.20 (Table 2), and Table 4 the equivalent parameters of the three materials in Table 1 with $r_0 \neq r_{90}$ and hardening coefficients 0.10 and 0.35 (Table 2).

In Tables 3 and 4, the condition the condition F + G = 1 is observed for the materials with $r_0 = r_{90}$, which means that the hardening curve corresponds to the determined for the equibiaxial stress path. For materials with $r_0 \neq r_{90}$ the sum (F + G) can deviate significantly from one, depending on the stress path observed during the bulge test, and the hardening curve corresponds to the determined for this stress path.

Table 3. Designation of the materials with n = 0.20 and the respective parameters of the Swift law and Hill'48 criterion. The stress path observed during the bulge test is also indicated. The constitutive parameters are equivalent to those in Tables 1 and 2.

Designation	Parameters of the Swift law			Parameters of the Hill'48 criterion					
	σ_0	K	n	F	G	H	L=M	N	σ_2/σ_1
Materials with $r_0 = r_{45} = r_{90}$									
0.7_0.7_0.7	184.43	523.59	0.20	0.500	0.500	0.350	1.201	1.200	1.000
1_1_1	200.00	577.08	0.20	0.500	0.500	0.500	1.500	1.500	1.000
2_2_2	173.23	485.67	0.20	0.500	0.500	1.000	1.125	2.500	1.000
3_3_3	282.84	874.69	0.20	0.500	0.500	1.500	3.000	3.500	1.000

Materials with $r_0 = r_{90} \neq r_{45}$									
3_1.5_3	282.84	874.69	0.20	0.500	0.500	1.500	3.000	2.000	1.000
1.5_3_1.5	223.84	659.75	0.20	0.500	0.500	0.750	1.875	3.500	1.000
0.6_3_0.6	178.89	504.77	0.20	0.500	0.500	0.300	1.200	3.500	1.000
3_0.6_3	282.84	874.69	0.20	0.500	0.500	1.500	3.000	1.100	1.000
Materials with $r_0 \neq r_{90}$									
0.6_0.7_0.8	191.77	548.72	0.20	0.431	0.575	0.345	1.379	1.207	1.114
0.6_1.8_3	260.59	792.79	0.20	0.212	1.061	0.637	2.547	2.929	1.505
1.5_2.25_3	262.53	799.87	0.20	0.344	0.689	1.033	2.585	2.843	1.131
1.5_2.75_4	277.49	854.85	0.20	0.289	0.770	1.155	2.887	3.442	1.171
0.5_2.25_4	282.47	873.30	0.20	0.166	1.330	0.664	2.992	4.115	1.678
1.5_3_3	262.53	799.87	0.20	0.344	0.689	1.033	2.585	3.618	1.130
1_2.25_3.5	264.11	805.65	0.20	0.249	0.872	0.872	2.616	3.083	1.275

Table 4. Designation of the materials with $r_0 \neq r_{90}$ with n = 0.10 and 0.35 and the respective parameters of the Swift law and Hill'48 criterion. The stress path observed during the bulge test is also indicated. The constitutive parameters are equivalent to those in Tables 1 and 2.

Material	**Parameters of the Swift law**			**Parameters of the Hill'48 criterion**					
	σ_0	K	n	F	G	H	$L=M$	N	σ_2/σ_1
0.6_0.7_0.8	192.73	326.17	0.10	0.436	0.580	0.348	1.393	1.219	1.117
	194.65	1215.3	0.35	0.444	0.592	.355	1.421	1.244	1.108
1.5_2.75_4	278.93	489.83	0.10	0.292	0.778	0.666	2.918	4.128	1.173
	279.93	2001.81	0.35	0.292	0.778	1.167	2.918	3.478	1.171
0.5_2.25_4	275.69	483.56	0.10	0.158	1.267	0.633	2.850	3.9197	1.712
	281.42	2026.00	0.35	0.164	1.321	0.659	2.970	4.085	1.680

In summary, when both principal stress, σ_1 and σ_2, are known (i.e. when the stress path is known), the equivalent stresses determined by the Hill'48 criterion (equation (8)), using the parameters in Tables 3 and 4, and by the von Mises criterion (equation (11)) are equal. In case of the bulge tests of the materials with $r_0 = r_{90}$, the stress path is known *a priori* (equal to 1), which allows using equation (13) for determining the equivalent stress ($\bar{\sigma} = \sigma_1 = \sigma_2$). For materials with $r_0 \neq r_{90}$, the stress path is unknown *a priori* and the usual alternative to determine the equivalent stress, assuming equibiaxial stress path [21], leads to inevitable errors. In the next sections, these issues are analysed and the errors due to this assumption are quantified for the materials under study with $r_0 \neq r_{90}$.

6.1. In-plane isotropic materials and materials with $r_0 = r_{90}$

In case of in-plane isotropic materials and materials with $r_0 = r_{90}$, the strain and stress paths are known *a priori* , and equal to 1, and the equivalent yield surfaces are tangent (see example of Figure 19 (a)). Under these context, a full equivalence is obtained between the Hill'48 and von Mises criteria, for determining the hardening curve. In fact, for both cases the principal stresses at the pole of the cap are equal and they can be calculated by using the simplified equation of the membrane theory (equation (13)). Moreover, the equivalent strain values are equal for both criteria, for the equibiaxial strain path. This is illustrated in Figure 20 for the case of the material 3_3_3, which represents in the (ε_1; ε_2) space the lines with equal equivalent strain ($\bar{\varepsilon} = 1$), for the Hill'48 and von Mises criteria, showing that the curves are tangent for the equibiaxial strain path ($\varepsilon_1 = \varepsilon_2$).

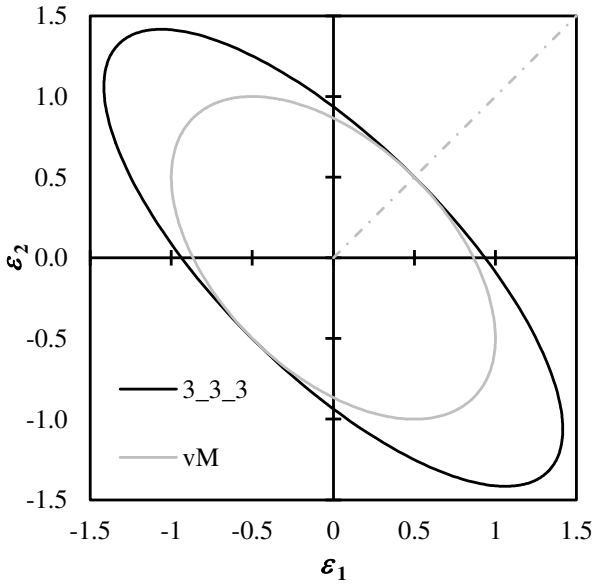

Figure 20. Curves of equivalent strain equal to 1, for the material 3_3_3 and the equivalent isotropic von Mises material (see Figure 19 (a)). The dashed-dotted line represents the equibiaxial strain path.

Under these conditions, the biaxial curves, equivalent stress *vs*. equivalent strain, are equal, whatever the criteria used, Hill'48 or von Mises, since the bulge test imposes $\bar{\varepsilon} = 2\varepsilon_1 = 2\varepsilon_2$ and $\bar{\sigma} = \sigma_1 = \sigma_2$ (equation (14)). From the experimental point of view, mechanical or optical devices can be used for measuring the principal strain values in the sheet plane, which are equal for both axes (O*x* and O*y*).

Figure 21 shows the hardening curves of the materials in Table 3 with $r_0 = r_{90}$ and the points obtained using the membrane theory under isotropy conditions, as experimentally. The respective error in equivalent stress is shown in Figure 22. This error is defined as: Error $= \left(\bar{\sigma}_{HL} - \bar{\sigma}_{MT}\right)/\bar{\sigma}_{HL}$ (where $\bar{\sigma}_{HL}$ and $\bar{\sigma}_{MT}$ are the equivalent stresses estimated by the input hardening law and from the membrane theory, respectively). The results are equal when using the Hill'48 for calculating the equivalent stress and strain values (equations (8) and (9), respectively). That is, the use of the isotropic von Mises criterion for determining the hardening curve is fully justified for materials with $r_0 = r_{90}$. The observed errors arise from the determination of the radius of curvature and the use of the membrane theory approach under bulge test conditions.

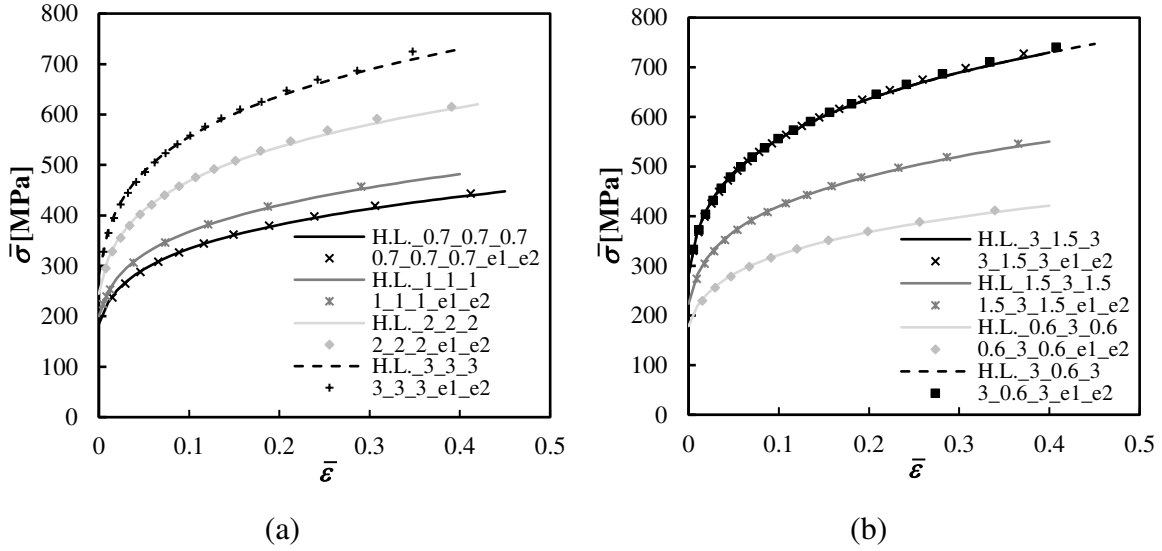

Figure 21. Comparison between the hardening laws in Table 3 (lines) and the results with the membrane theory (symbols), whatever the criterion used for determining the equivalent stress and strain (von Mises or Hill'48) for: (a) in-plane isotropic materials ($r_0 = r_{45} = r_{90}$); (b) materials with $r_0 = r_{90} \neq r_{45}$. The hardening coefficient of the materials is $n = 0.20$.

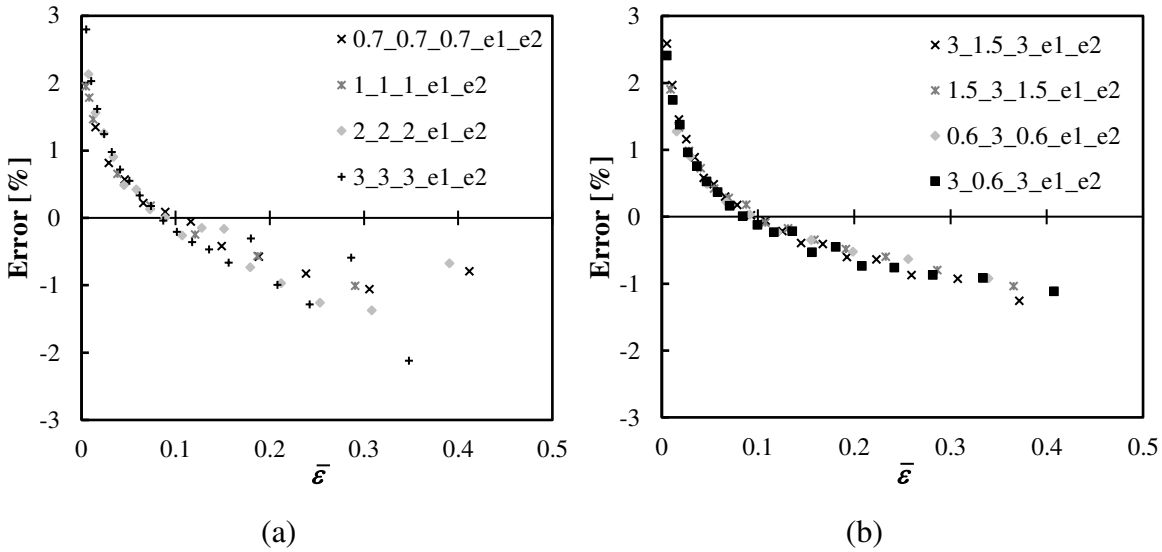

Figure 22. Evolution of the error in stress for the cases in Figure 21 for: (a) in-plane isotropic materials ($r_0 = r_{45} = r_{90}$); (b) materials with $r_0 = r_{90} \neq r_{45}$. The hardening coefficient of the materials is $n = 0.20$.

6.2. In-plane anisotropic materials with $r_0 \neq r_{90}$

The materials with planar anisotropy such that $r_0 \neq r_{90}$ are now analysed. In these cases the stress and strain paths are different from 1 (see Figures 16 and 17) and the simplified equation of membrane theory (equation (13)) does not allow calculating the stresses σ_1 and σ_2. Alternatively, the use of the equation (1) requires the knowledge of the

stress path, in order to obtain the stresses σ_1 and σ_2. Besides, equation (1) assumes a linear relationship between σ_2 and σ_1 with slope equal to -1 ($\rho_1 = \rho_2 = \rho$), and its interception with the equibiaxial stress line corresponds to the stress determined by using the simplified equation of the membrane theory (equation (13)). This is illustrated in Figure 23 for the case of the material 0.5_2.25_4, which shows the initial yield surface of the Hill'48 anisotropic material, the equivalent von Mises surface that crosses Hill'48 surface at the point corresponding to the observed stress path, and the von Mises surface corresponding to an equivalent stress equal to the determined using the simplified equation of the membrane theory (equation (13)), i.e. when considering $\bar{\sigma} = \sigma_1 = \sigma_2$. The equivalent stresses corresponding to both von Mises surfaces can be significantly different, depending on the anisotropy of the material.

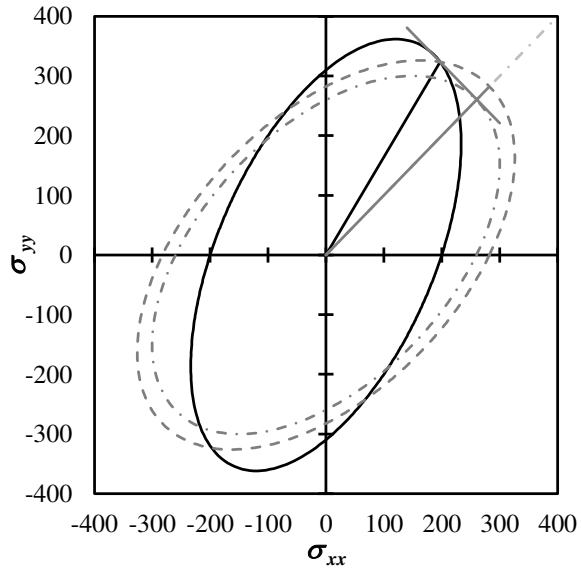

Figure 23. Initial yield surfaces of the material 0.5_2.25_4 (black solid line) and two isotropic materials with: (i) equivalent stress equal to that of the anisotropic Hill'48 material (dashed line) and (ii) equivalent stress equal to the one determined using the simplified equation of the membrane theory (equation (13) – dashed-dotted line). The biaxial stress path observed during the bulge test (black solid line) and the equibiaxial stress path (grey solid line) are also indicated. The line with negative slope corresponds to the equation ($\sigma_2 + \sigma_1$ = constant, i.e. equation (1) at a given moment of the test).

Moreover, the results show that the equivalent strains obtained using Hill'48 or von Mises yield criterion (equations (9) and (12) (or (14)), respectively) are different for materials with $r_0 \neq r_{90}$. This is illustrated in Figure 24 for the case of the material 0.5_2.25_4, which shows, in the (ε_1; ε_2) space, the lines with equal value of equivalent strain ($\bar{\varepsilon} = 1$), for the Hill'48 and equivalent von Mises criteria. The lines with equal equivalent strain intersect each other at a point other than that corresponding to the observed strain path. The difference

in equivalent strains can be higher that 10% for the extreme case of the studied materials (11.6% in case of the material 0.5_2.25_4).

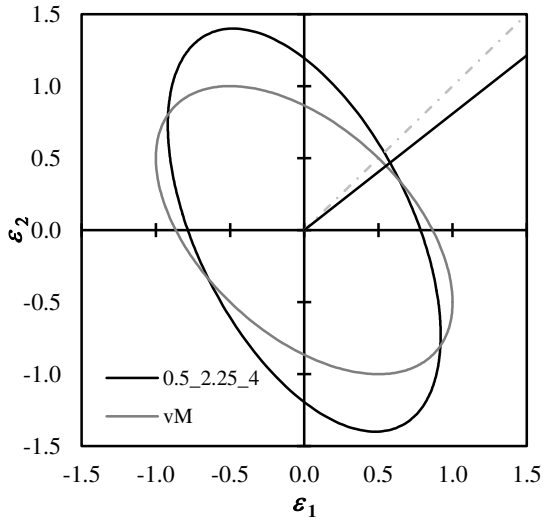

Figure 24. Curves of equivalent strain equal to 1, for the material 0.5_2.25_4 (black solid line) and the equivalent isotropic material (grey solid line). The observed strain path (solid straight line) is also indicated as well as the equibiaxial strain path (dashed-dotted straight line).

Figure 25 shows the ratio between the von Mises and Hill'48 equivalent strains as a function of the strain (Figure 25 (a)) and stress (Figure 25 (b)) paths, observed for all materials with $r_0 \neq r_{90}$ and hardening coefficients studied. This ratio follows a quasi-linear relationship with the stress path, but this does not occur with the strain path. For materials with strain and stress paths close to 1, both equivalent strains are nearly equal. Differences between von Mises and Hill'48 equivalent strains are clearly noticeable only for the stress paths higher than about 1.1 (or strain paths lower than about 0.95). In summary, the von Mises equivalent strain is always higher than the Hill'48 equivalent strain. Thus, the hardening curves determined can be significantly inaccurate, when resorting to the von Mises definition of equivalent strain, as will be seen below.

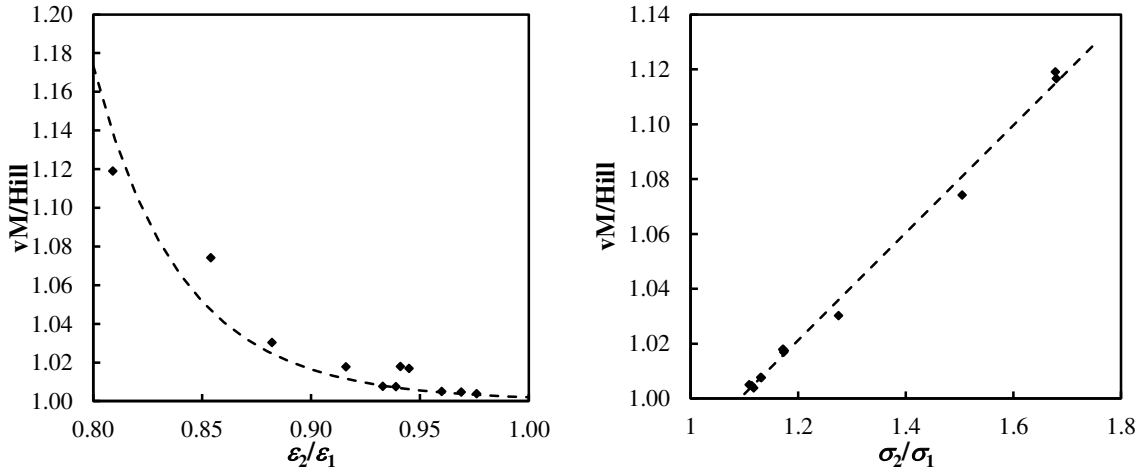

Figure 25. Ratio between the equivalent strains determined by von Mises and Hill'48 for all anisotropic Hill'48 materials studied, as a function of: (a) strain path; (b) stress path. The dashed lines highlight the trend of the evolutions.

In order to test the commonly used methodologies for determining the hardening curve in experimental tests, which use the von Mises criterion and assumes that $\sigma_2 = \sigma_1$, different approaches are analysed, according to the measuring system available:

i) The measurement of the strain and radius of curvature are performed using mechanical devices, i.e. an extensometer and a spherometer. In this case, only one strain value is measured, generally in the rolling direction, ε_1, and the equivalent strain is determined by equation (14) (where $\varepsilon = 2\varepsilon_1$). The equivalent stress is calculated from the membrane theory (equation (13)) considering $\sigma = \sigma_1 = \sigma_2$.

ii) The measurement of the strain and radius of curvature are performed using an optical device, as recommended by ISO 16808:2014 [21]. In this case it is possible to assess both principal strains ε_1 and ε_2, in order to calculate the equivalent strain using equation (12). However, the evaluation of the corresponding principal stresses using the membrane theory (equation (1)) needs the knowledge of the yield criterion and respective parameters (under the observed condition $\rho = \rho_1 = \rho_2$), in order determine the stress ratio from the measured strain ratio (equations (6) or (7) for the Hill'48 criterion). This is not generally the case under experimental conditions, and so the membrane theory is used considering $\sigma = \sigma_1 = \sigma_2$ (equation (13)). This case becomes quite similar to case (i), unless both principal strains in the sheet plane are known, and so equation (12) is used instead of equation (14) for determining the equivalent strain; the equivalent stress has the same value as in case (i).

In this context, the hardening curves of the in-plane anisotropic materials are now determined using the two previously mentioned approaches. The points of the hardening

curve obtained during the test are compared with the hardening curve of the materials (Tables 3 and 4). Figures 26 (a) and 27 (a) compares the hardening curves of the materials in Table 3 (with the hardening coefficient $n = 0.20$), with results obtained from the membrane theory (equations (13)) and von Mises criterion, considering (as above mentioned): (i) $\bar{\varepsilon} = 2\varepsilon_1$ with the principal strain ε_1 measured along Ox (Figure 26 (a)); (ii) $\bar{\varepsilon}$ determined by the equation (12) from the measured values of the principal strains ($\varepsilon_1 \neq \varepsilon_2$) (Figure 27 (b)). Figures 26 (b) and 27 (b) show the evolution of the error in equivalent stress with the equivalent strain, corresponding to Figures 26 (a) and 27 (a). The errors in equivalent stress are relatively high in both approaches for the materials with $r_0 < 1$ and $r_{90} > 1$, simultaneously. For the material 0.5_2.25_4, the errors attain about 12 % in Figure 26 (b) and 10% in Figure 28 (b).

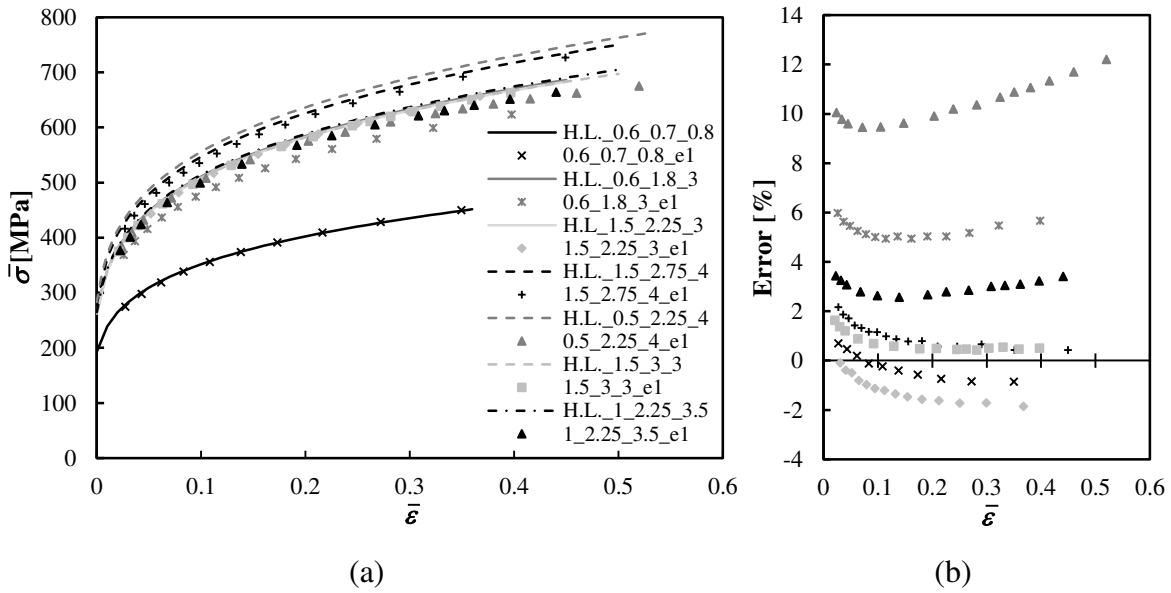

Figure 26. (a) Comparison between the hardening laws in Table 3 (lines) and the results with the membrane theory (symbols) with $\sigma_1 = \sigma_2 = \sigma$ (equation (13)) considering, for the equivalent strain determination, the value of ε in equation (14) equal to the measured value of ε_1; (b) Evolution of the error in equivalent stress with the equivalent strain. The hardening coefficient of the materials is $n = 0.20$.

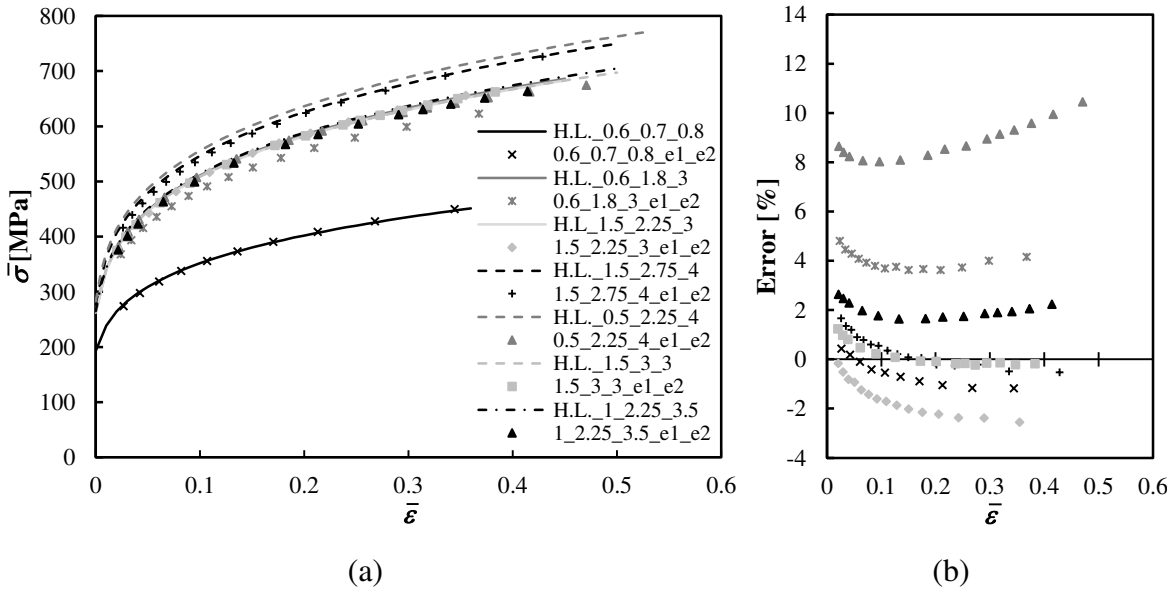

(a) (b)

Figure 27. (a) Comparison between the hardening laws in Table 3 (lines) and the results with the membrane theory (symbols) with $\sigma_1 = \sigma_2 = \sigma$ (equation (13)) considering, for equivalent strain determination, the measured values of ε_1 and ε_2 in equation (12); (b) Evolution of the error in equivalent stress with the equivalent strain. The hardening coefficient of the materials is n = 0.20.

It is important to understand the meaning of the errors shown in Figures 26 (b) and 27 (b), i.e. the manner in which the isotropy assumption commonly used in the experimental analysis, with $\sigma_1 = \sigma_2$ and the von Mises criterion, contributes to these errors in equivalent stress. In this context, Figure 28 (a) compares the hardening laws in Table 3 with the results obtained taking into account the Hill'48 criterion, the observed stress and strain paths at the pole of the bulge test and the general equation of the membrane theory (equation (1)). Figure 28 (b) shows the respective errors in equivalent stress. It should be highlighted again that, in general, this is not the experimental case, i.e. the anisotropic Hill'48 criterion and respective parameters that describe the anisotropy of the material are usually unknown.

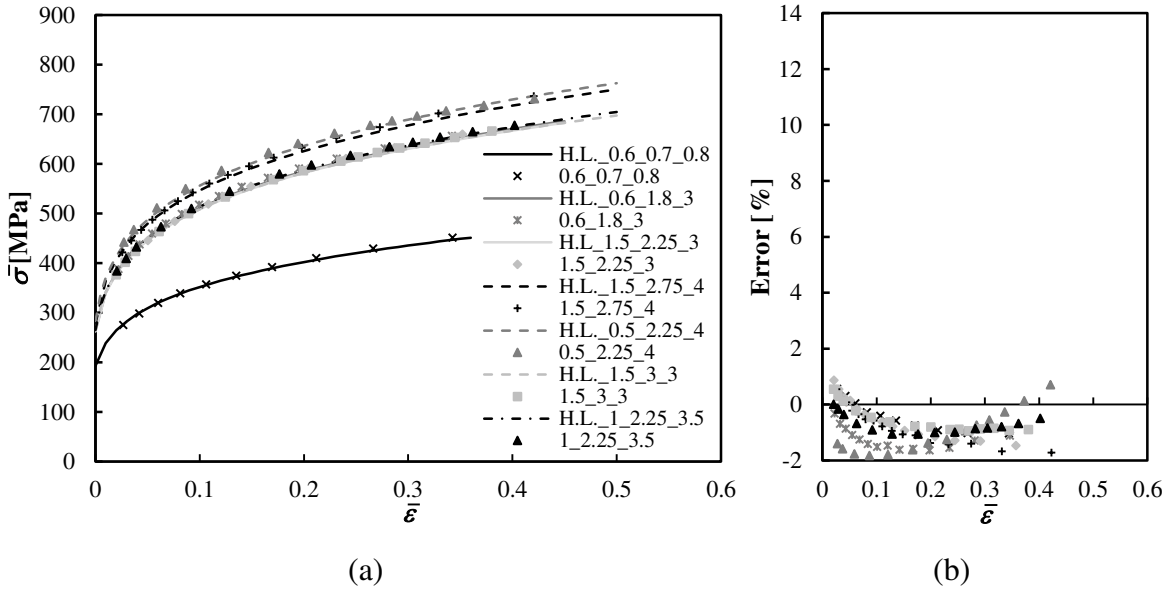

(a) (b)

Figure 28. (a) Comparison between the hardening laws in Table 3 (lines) and the results obtained with the membrane theory (symbols) using the Hill'48 stress and strain definitions; (b) Evolution of the error in equivalent stress with the equivalent strain. The hardening coefficient of the materials is n = 0.20.

As for materials with $r_0 = r_{90}$, the errors in stress in Figure 28 (b) arise from the determination of the radius of curvature and the use of the membrane theory approach under bulge test conditions. Thus, it is appropriate to state that the differences of error in stress between Figure 28 (b) and Figure 27 (b) are due to the approaches used for the equivalent stress and strain determination, using respectively von Mises (combined with equation (13)) and Hill'48 (combined with equation (1)) definitions. In this context, it can be concluded that the errors obtained with the approaches used in Figures 26 and 27 (b) are not negligible, particularly in the case of materials 0.6_1.8_3 and 0.5_2.25_4.

Figures 29 to 34 show the same kind of results, as for materials with hardening coefficient n = 0.20 (Figures 26 to 28), but for the three anisotropic materials studied, with n = 0.10 and 0.35 (see Table 4). The errors in stress follow the same trend although showing slight differences from those of materials with n = 0.20. Also, the comparison of the results obtained with von Mises criterion with those from Hill'48 criterion leads to similar conclusions that for materials with n = 20.

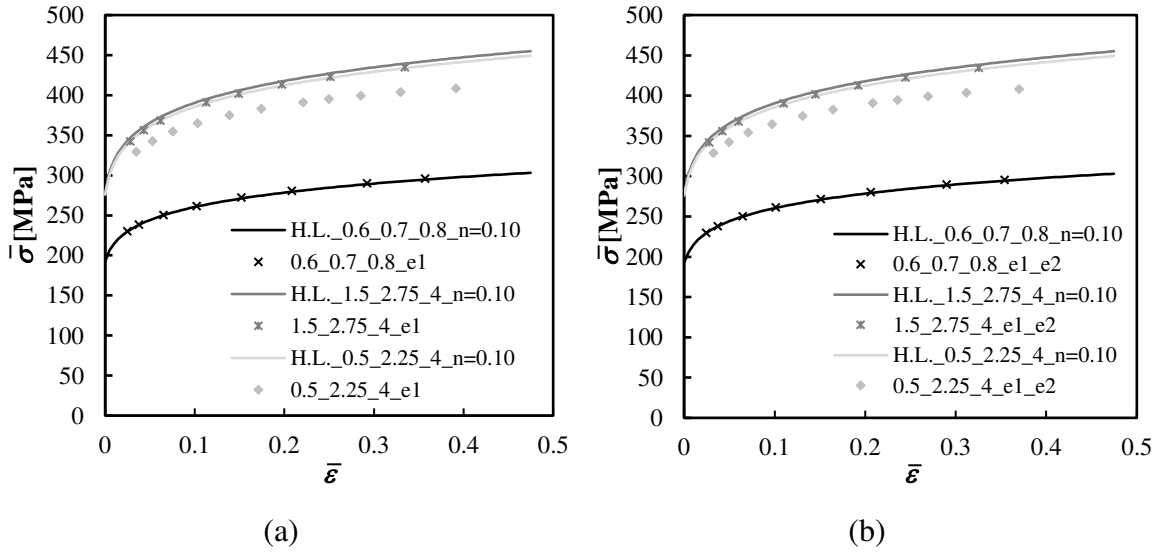

Figure 29. Comparison between the hardening laws in Table 4 (lines) and the results with the membrane theory (symbols) with $\sigma_1 = \sigma_2 = \sigma$ (equation (13)) considering, for the equivalent strain determination: (a) the value of ε in equation (14) equal to the measured value of ε_1; (b) the measured values of ε_1 and ε_2 in equation (12). The hardening coefficient of the materials is n = 0.10.

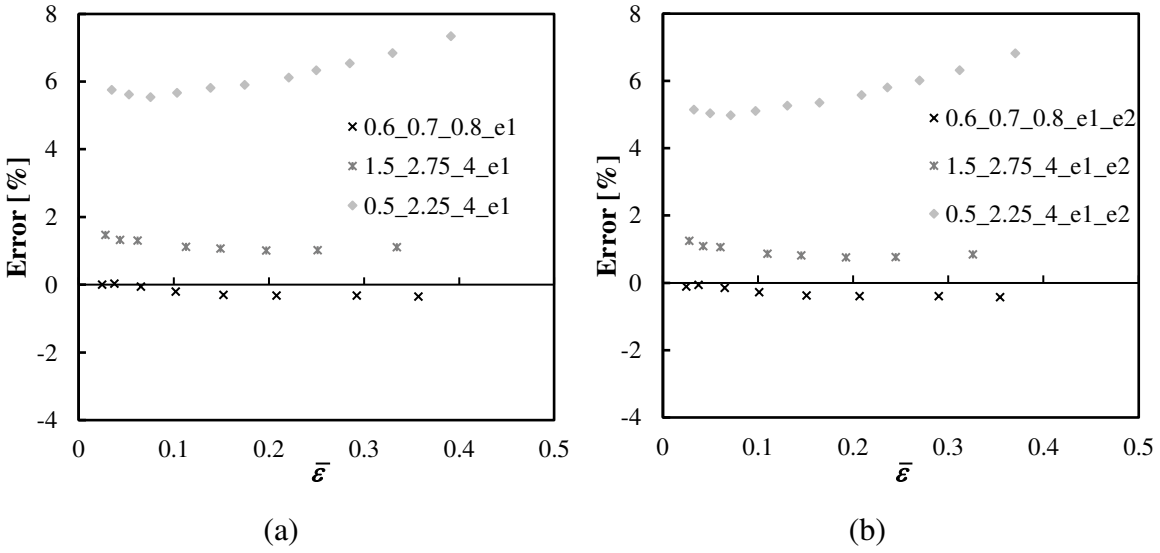

Figure 30. Evolution of the error in equivalent stress corresponding to Figure 29, considering for the equivalent strain determination: (a) the value of ε in equation (14) equal to the measured value of ε_1 – see Figure 29 (a); (b) the measured values of ε_1 and ε_2 in equation (12) – see Figure 29 (b). The hardening coefficient of the materials is n = 0.10.

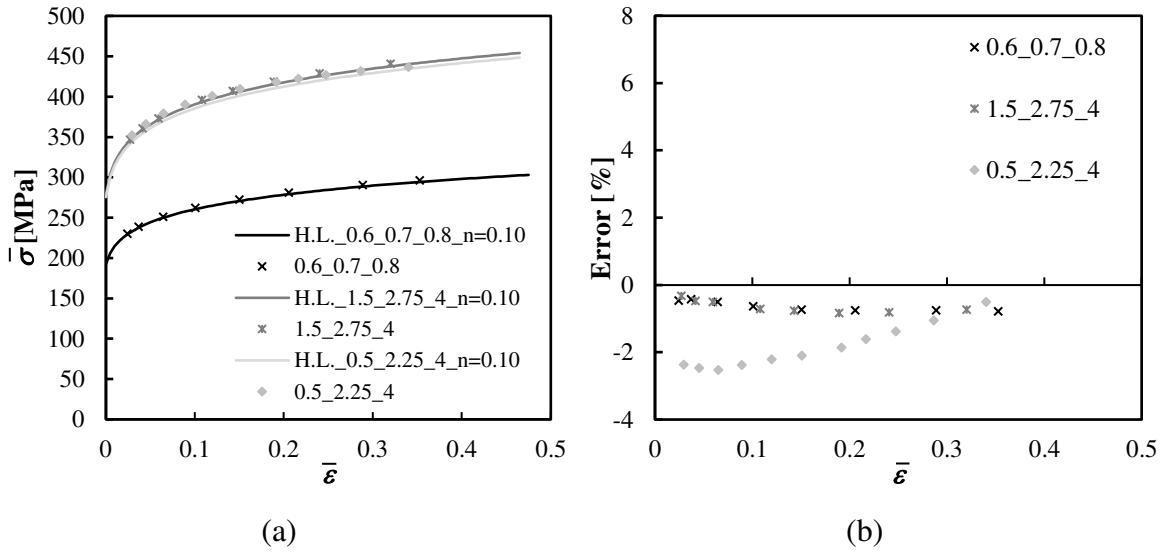

Figure 31. (a) Comparison between the hardening laws in Table 4 (lines) and the results obtained with the membrane theory (symbols) using the Hill'48 stress and strain definitions; (b) Evolution of the errors in equivalent stress with the equivalent strain. The hardening coefficient of the materials is n = 0.10.

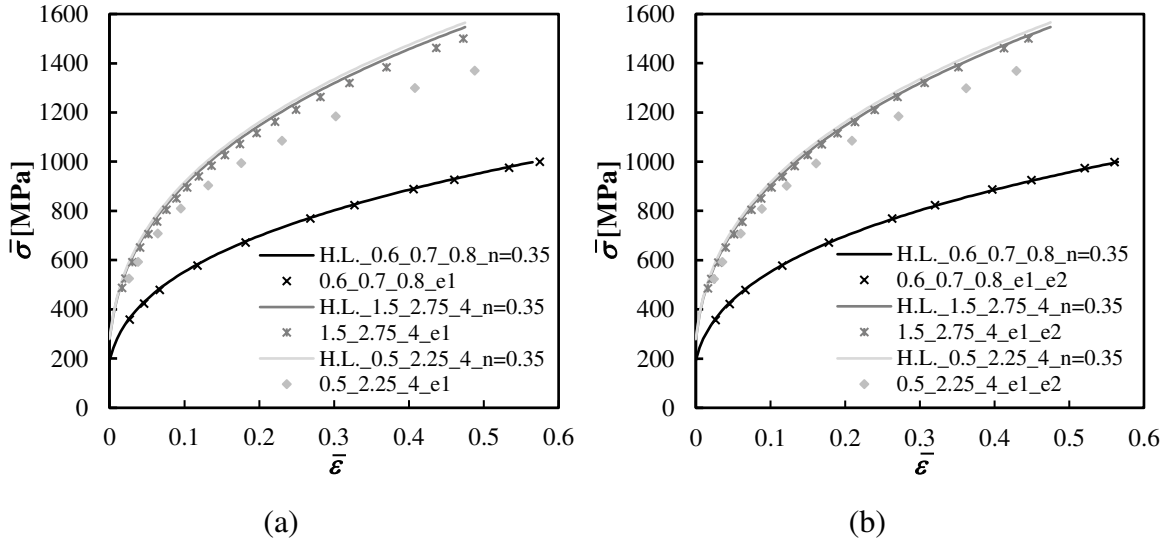

Figure 32. Comparison between the hardening laws in Table 4 (lines) and the results with the membrane theory (symbols) with $\sigma_1 = \sigma_2 = \sigma$ (equation (13)) considering for equivalent strain determination: (a) the value of ε in equation (14) equal to the measured value of ε_1; (b) the measured values of ε_1 and ε_2 in equation (12). The hardening coefficient of the materials is n = 0.35.

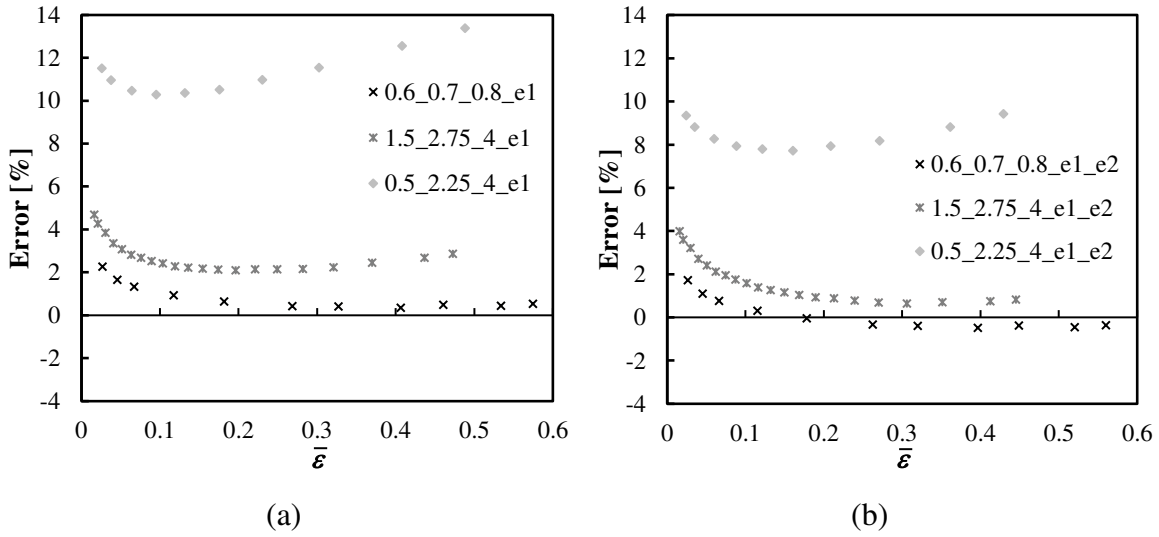

Figure 33. Evolution of the error in equivalent stress corresponding to Figure 32, considering for equivalent strain determination: (a) the value of ε in equation (14) equal to the measured value of ε_1 – see Figure 32 (a); (ii) the measured values of ε_1 and ε_2 in the equation (12) – see Figure 32 (b). The hardening coefficient of the materials is n = 0.35.

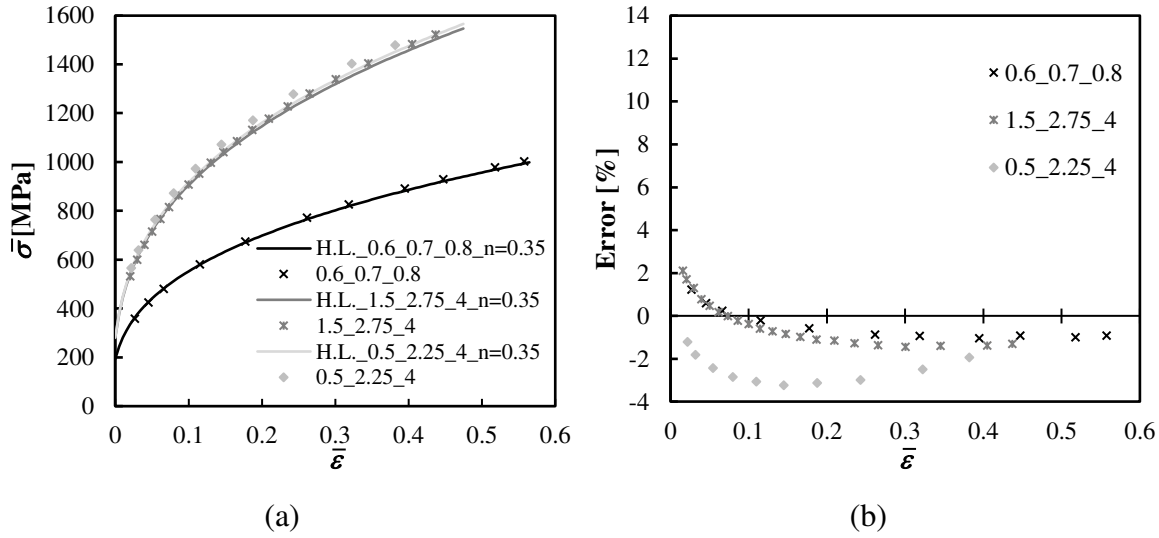

Figure 34. (a) Comparison between the hardening laws in Table 4 (lines) and the results obtained with the membrane theory (symbols) using the Hill'48 stress and strain definitions; (b) Evolution of the errors in equivalent stress with the equivalent strain. The hardening coefficient of the materials is n = 0.35.

In summary the commonly experimentally used approaches to determine the hardening curve from the bulge test, using the von Mises criterion and the assumption of equibiaxial stress (and also often equibiaxial strain), can lead to relatively high errors, in case of in-plane anisotropic materials with $r_0 \neq r_{90}$, especially when the axis of the Hill'48 ellipse in space (σ_{xx}; σ_{yy}) is relatively far away from 45º.

6.3. Is it possible to improve the determination of the hardening curve?

In order to answer to this question, the materials studied in the previous sections, with anisotropy described by Hill'48 materials with hardening coefficient equal to 0.20, 0.10 and 0.35, are firstly analysed. Figure 35 plots the stress path *vs*. strain path of these materials, from the average values of the results previously shown in Figures 16 and 17. Figure 35 shows that it is possible to fit a power law to stablish a correlation between the observed stress and strain paths, which allows a relatively accurate determination of the stress path from the strain path. This can consist of a good enough procedure to determine the stress path from the experimental measured strain path, as an alternative to the associated flow rule that needs the knowledge of the anisotropic yield criterion and the respective parameters of the material. Figure 35 also shows a power law (solid line) with exponent equal to -2:

$$\frac{\sigma_2}{\sigma_1} = \left(\frac{\varepsilon_2}{\varepsilon_1} \right)^{-2} . \tag{25}$$

This equation, with exponent -2, is chosen (instead of the exponent -2.30 which corresponds to the fitted power law) for determining the stress path from the measured strain path. In fact, equation (25) ensures that all points in Figure 35 are very close or above the line defined by this equation, which is not the case of the fitted equation with exponent equal to -2.30. Therefore, equation (25) safeguards excesses in determining the stress path, i.e. seeks that the evaluated hardening curve is between the determined, as in Figures 28, 31 and 34, and as in Figures 27, 29 (b) and 32 (b). Moreover, it safeguards the cases of materials with anisotropic behaviour described by other criteria than Hill'48, for which the fitted power law may also overestimate the stress path. In summary, to ensure that this rarely occur, equation (25) is suggested to be used instead of the fitted power law. Further ahead, in this section, equation (25) will be tested for a non-quadratic yield criterion, the Drucker+L criterion [36].

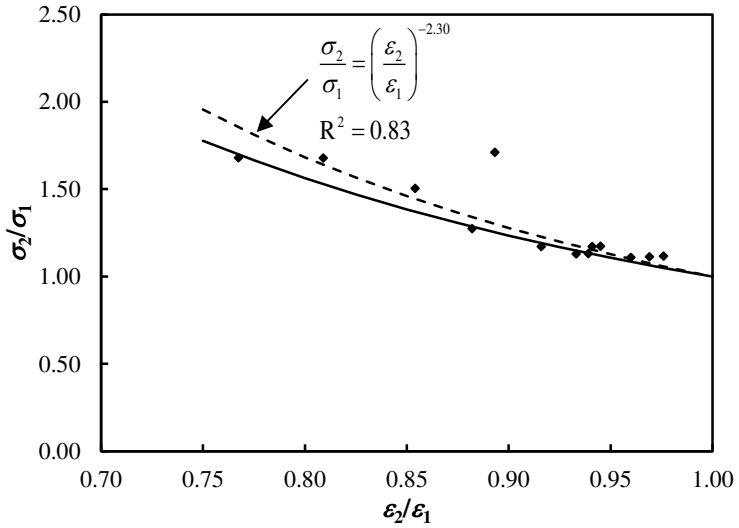

Figure 35. Stress path *vs.* strain path for Hill'48 materials, with n = 0.10, 0.20 and 0.35. The fitted curve (dashed line) and respective parameters is also shown. The lower curve (solid line) corresponds to equation (25).

In the following, the use of equation (25) is tested in case of Hill'48 materials with $r_0 \neq r_{90}$, in order to examine its performance in the prediction of the stress path from the known strain path. For such purpose, equation (25) is combined with equation (6) (or (7)). Figures 36 (a) show the predicted stress paths (lines), as a function of r_0/r_{90}, for the various values of r_0 (r_0 = 0.5, 0.6 1.0, and 1.5) studied in this work. This figure, also shows the observed stress paths for the materials considered in this work (points), which agree with the predicting curves. The stress paths (points) determined by equation (25), directly from the measured strain path, are shown in the Figure 36 (b) and compared with the predicting (lines), as in Figure 37 (a). For most cases, equation (25) allows determining with enough accuracy the stress path at the pole, from the measured strain path. Moreover, the points in Figure 36 (b) are very close or below the corresponding line. It should be mentioned the case of material 0.5_2.25_4 with n = 0.10 (black filled triangle in the Figure 36 (b)), for which the strain path is poorly estimated (this case corresponds to the point in Figure 35, further away from the trend defined by the fitted power law). In all other cases, the stress path is in general well estimated, and never is significantly overestimated.

In summary, it turns out that in experimental cases of the bulge test, the yield criterion and respective parameters of the material under study are not known. But it is possible to assess the principal strains in the sheet plane by using an optical measurement system and, consequently, the stress path at the pole by using equation (25).

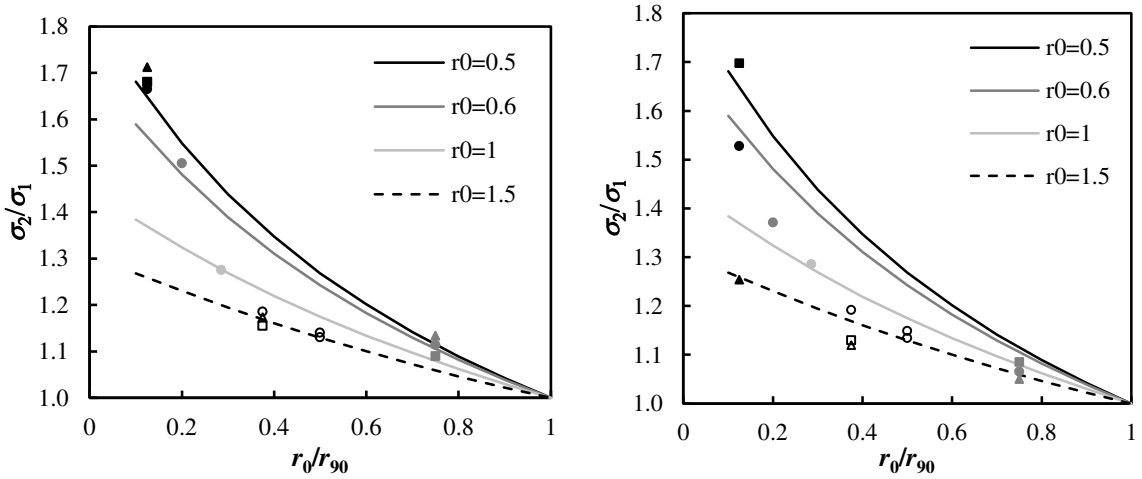

Figure 36. Stress path as a function of the ratio r_0/r_{90}, for different values of r_0 (r_0 = 0.5: black solid lines and black filled symbols; r_0 = 0.6: dark grey solid lines and dark grey filled symbols; r_0 = 1.0: light grey solid lines and light grey filled symbols; r_0 = 1.5: black dashed lines and open symbols). The lines in both figures represent the stress paths predicted from equations (7) and (25), and the symbols represent the stress paths: (a) numerically measured; (b) determined by equation (25), from the measured strain paths. The circles, triangles and squares correspond to materials with n = 0.20, 0.10 and 0.35, respectively.

Now, the use of the equation (25) to improve the determination of the work hardening curve, presuming that the strain path is measured by digital correlation image technique [21], is analysed. Since the stress path is known, the equivalent stress can be determined using equations (1) for determining σ_1 and σ_2 and then equation (11). The remaining question is the determination of the equivalent strain. This is generally done using the von Mises criterion. However, as can be seen by comparing, for example, the strain gap between the corresponding points in Figures 27 (b) and 28 (b), the value of equivalent strain depends on the yield criteria (see also Figures 24 and 25). In this context, there exists a simple way to determine the equivalent strain regardless of the yield criterion. In fact, it can be shown that for linear stress and strain paths, which is approximately the case for the bulge test (see Figures 16 and 17), the definition of plastic work leads to the following relationship:

$$\sigma_1\varepsilon_1 + \sigma_2\varepsilon_2 = \bar{\sigma}\ \bar{\varepsilon}\,. \tag{26}$$

The difference in the equivalent strain obtained by using the equation (26) when compared with equation (9) is negligible (less than 0.3%) for the Hill'48 materials of Tables 3 and 4, which shows that the slight change of the strain path observed during the test does not significantly affects this calculation.

In summary, the measurement of the strain path during the bulge test, which can be performed by means of an optical device, allows to determine the stress path by using

equation (25), that combined with equation (1) gives the principal stresses and, consequently, the von Mises equivalent stress (equal to the equivalent stress of the anisotropic yield criterion; see Figure 19 for von Mises and Hill'48 criteria). Finally, equation (26) allows determining the equivalent strain. This allows for a very accurate determination of the hardening curve whatever the anisotropic yield criterion that describes the anisotropy of the material, as shown below.

Figure 37 (a) shows the hardening curves of materials in Table 3 with $r_0 \neq r_{90}$ and $n = 0.20$, and the obtained points using the suggested strategy, i.e. using equations (25) and (26). The respective errors in stress are show in Figure 37 (b). These errors are less than those in Figures 26 and 27, and quite similar to those in Figure 28, in which they arise almost entirely from the radius of curvature determination and the use of the membrane theory approach under bulge test conditions.

In order to better quantify the error in equivalent stress due to the procedure now proposed, i.e. isolate this error from other sources, the difference in equivalent stress error between those in the Figure 37 (b) and in the Figure 28 (b) are shown in the Figure 38. This difference of error, lower than 1.5%, for the materials 0.6_0.7_0.8, 0.6_1.8_3 and 0.5_2.25_4, and lower than 0.5%, for all the other materials, shows the capability of the proposed methodology for determining the hardening curve.

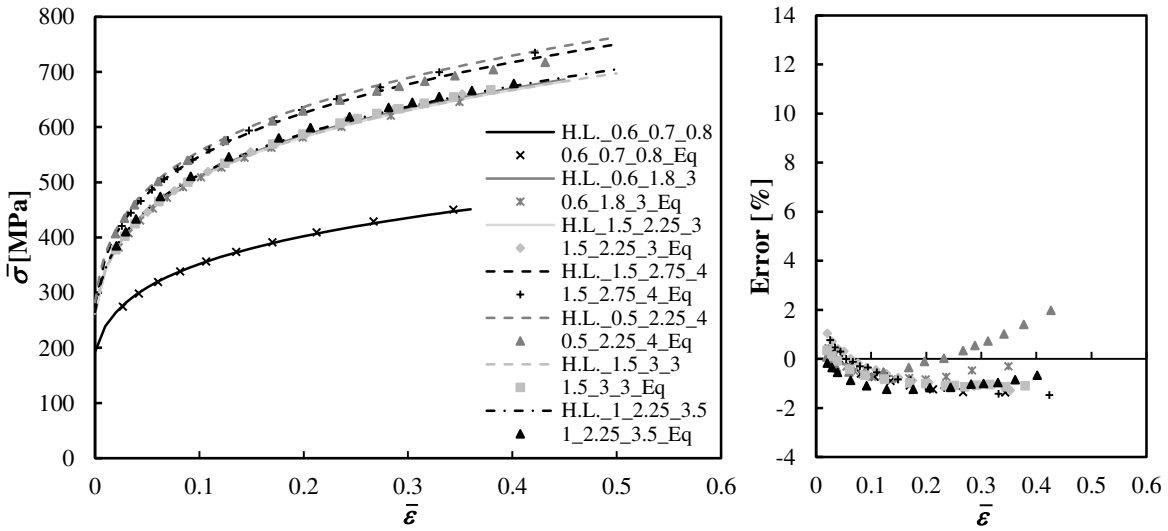

Figure 37. (a) Comparison between the hardening laws in Table 3 (lines) and the results obtained with membrane theory (symbols) using the equations (25) and (26) for the materials with $n = 0.20$; (b) Evolution of the corresponding errors in equivalent stress with the equivalent strain.

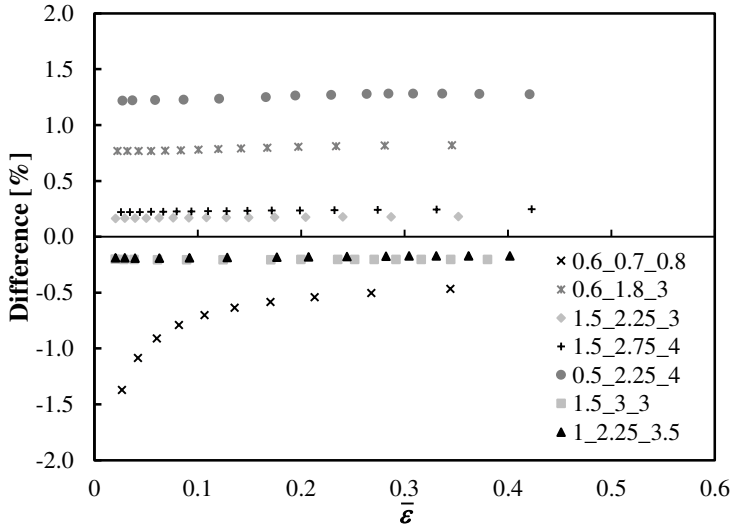

Figure 38. Difference of error between Figure 37 and Figure 28, for the materials with n = 0.20 (Table 3).

Similarly to Figure 37 (a), Figure 39 (a) and 40 (a) show the hardening curves of the materials with n = 0.10 and 0.35 (Table 4), having $r_0 \neq r_{90}$ and the obtained points using the suggested strategy, using equation (25) and (26). The respective errors in equivalent stress are shown in Figures 39 (b) and 40 (b). For the case of the material 0.5_2.25_4, the level of error is still relatively high, but lower than that obtained using the procedure proposed by ISO standard (Figure 33 (b)). The difference in equivalent stress error between those in Figures 39 (b) and 40 (b), and those in Figure 31 (b) and Figure 34 (b), respectively, are shown in Figure 41 (identical to Figure 38 but for n values equal to 0.10, Figure 41 (a), and 0.35, Figure 41 (b)).

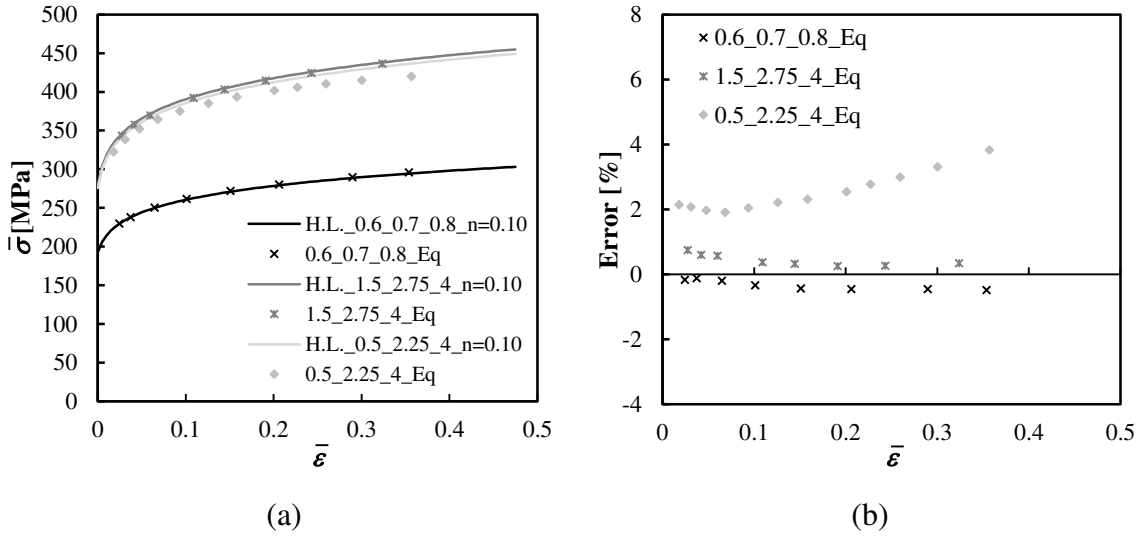

Figure 39. (a) Comparison between the hardening laws in Table 4 (lines) and the results obtained with membrane theory (symbols) using equation (25) and (26) for the materials with n = 0.10; (b) Evolution of the corresponding errors in equivalent stress with the equivalent strain.

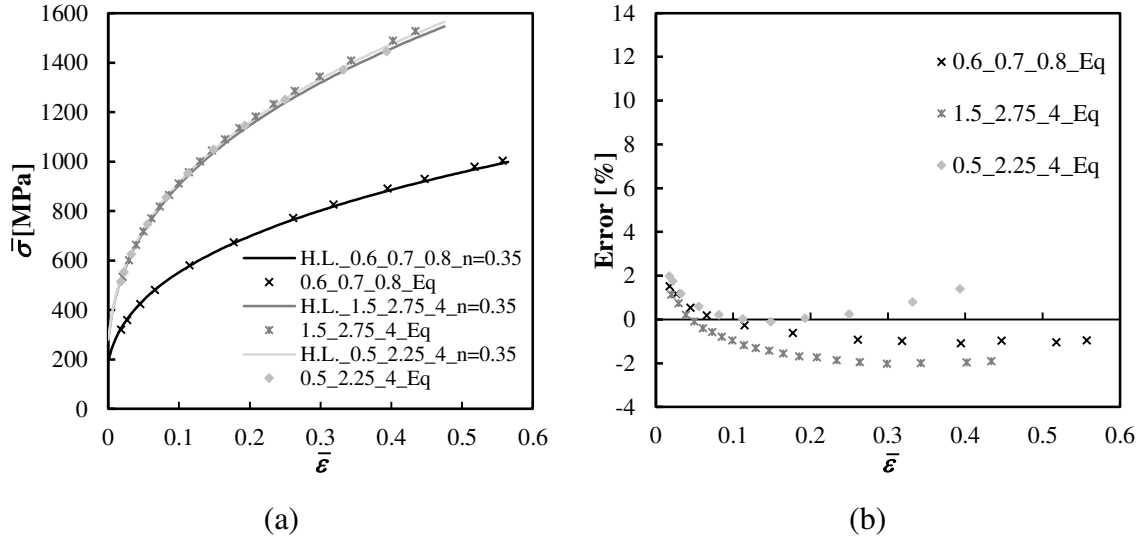

Figure 40. (a) Comparison between the hardening laws in Table 4 (lines) and the results obtained with membrane theory (symbols) using equation (25) and (26) for the materials with n = 0.35; (b) Evolution of the corresponding errors in equivalent stress with the equivalent strain.

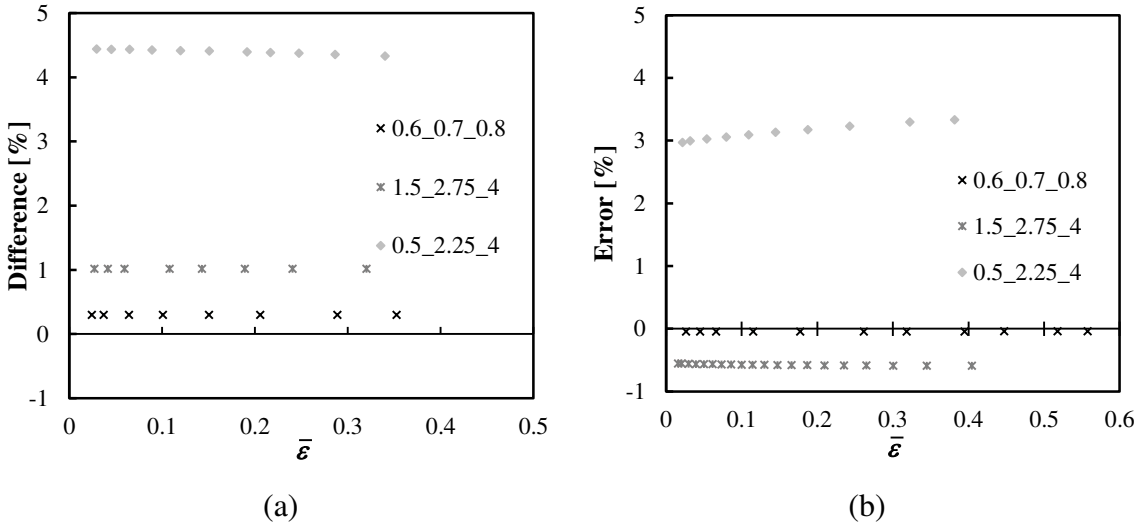

Figure 41. Difference of error between: (a) Figure 39 (b) and Figure 31 (b), for the materials with n = 0.10 (Table 4); (b) Figure 40 (b) and Figure 34 (b), for materials with n = 0.35 (Table 4).

Other materials with the anisotropic behaviour described by a non-quadratic yield criterion, the Drucker+L criterion (equations (19), (20) and (21)), and the hardening behaviour described by the Voce law (equation (22)) are now analysed. Two examples are selected with flattened and sharp yield surfaces in the region around the equibiaxial stress path, and so significantly different from the Hill'48 yield surface. The constitutive parameters of the Drucker+L criterion and the Voce law of these materials are given in Tables 5 and 6, respectively. The hardening curve corresponds to the determined for the observed stress path. Figure 42 shows the evolution of the anisotropic coefficient in the sheet plane and Figure 43 displays the yield surfaces in the space $\left(\sigma_{xx}/\sigma^0{}_0;\sigma_{yy}/\sigma^0{}_0\right)$.

Table 5. Designation of the materials and the respective parameters of Drucker+L criterion.

Designation	**Parameters of the Drucker+L criterion**				
	C_1	**C_2**	**C_3**	**$C_4 = C_5$**	**C_6**
c=2	0.750	1.547	1.149	1.281	1.450
c=-2	0.737	1.518	1.127	1.383	1.423

Table 6. Parameters of Voce law and average values of the observed stress and strain paths for the Drucker+L materials in Table 5.

Designation	Parameters of the Voce law			Stress and strain paths	
	σ_{sat}	R_{sat}	c_y	σ_2/σ_1	$\varepsilon_2/\varepsilon_1$
c=2	657.47	348.59	7.01	1.367	0.908
c=-2	709.73	376.30	7.565	1.665	0.773

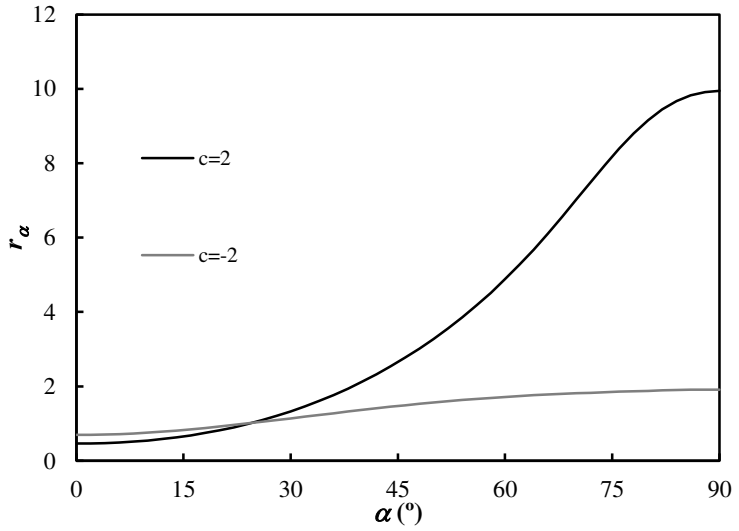

Figure 42. Distribution of r_α in the sheet plane, for the Drucker+L materials in Table 5: c = 2 and c = -2.

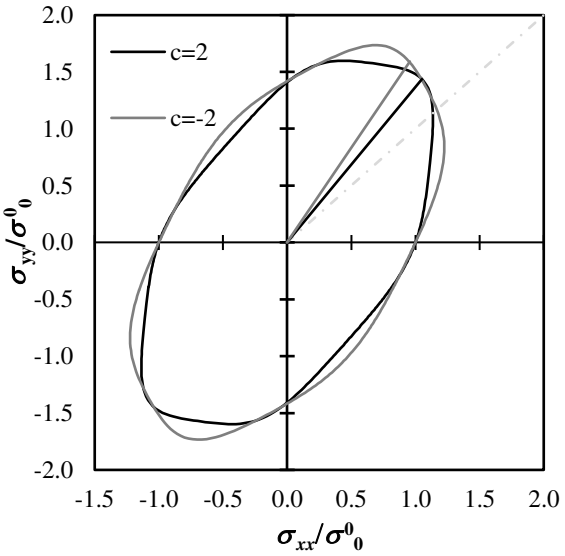

Figure 43. Normalized initial yield surfaces in the plane $\left(\sigma_{xx}/\sigma^0{}_0;\sigma_{yy}/\sigma^0{}_0\right)$ of the Drucker+L materials with c = 2 and c = -2. The observed stress paths are also shown.

Figure 44 (a) shows the hardening curves of the materials with behaviour described by the parameters shown in Tables 5 and 6 and the points obtained by the suggested strategy. The respective errors in equivalent stress are show in Figure 44 (b). Figure 45 show the results obtained from the membrane theory (equations (13)) and von Mises criterion, considering $\bar{\varepsilon}$ determined by equation (12) from the measured values of the principal strains ($\varepsilon_1 \neq \varepsilon_2$), as recommended by ISO 16808:2014. In this case the errors are higher than the obtained with the suggested strategy, for both materials. In particular, the error can attain about 9%, for the material with c = -2. Figure 46 shows the results obtained with the membrane theory (equation (1)), taking into account the observed stress and strain paths; the equivalent stress was determined using the Drucker+L definition and the equivalent strain using the equation (26). The errors of the suggested strategy (Figure 44 (b)) are quite similar to those in Figure 46 (b) and smaller than 2%, for both cases.

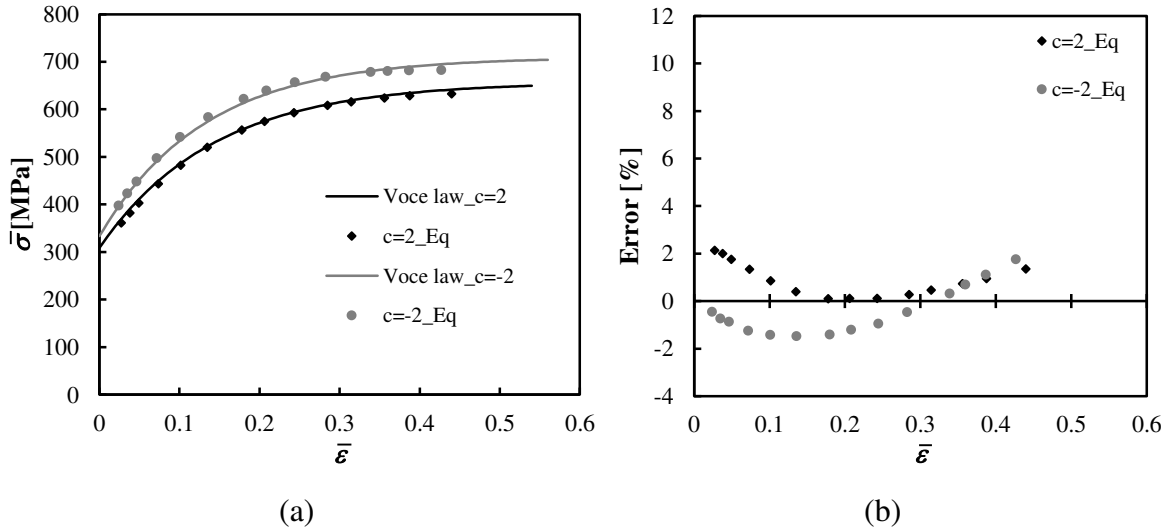

Figure 44. (a) Comparison between the hardening laws of materials in Table 6 (lines) and the results obtained with the membrane theory (symbols) using the equations (25) and (26) for Drucker+L materials; (b) Evolution of the corresponding errors in equivalent stress with the equivalent strain.

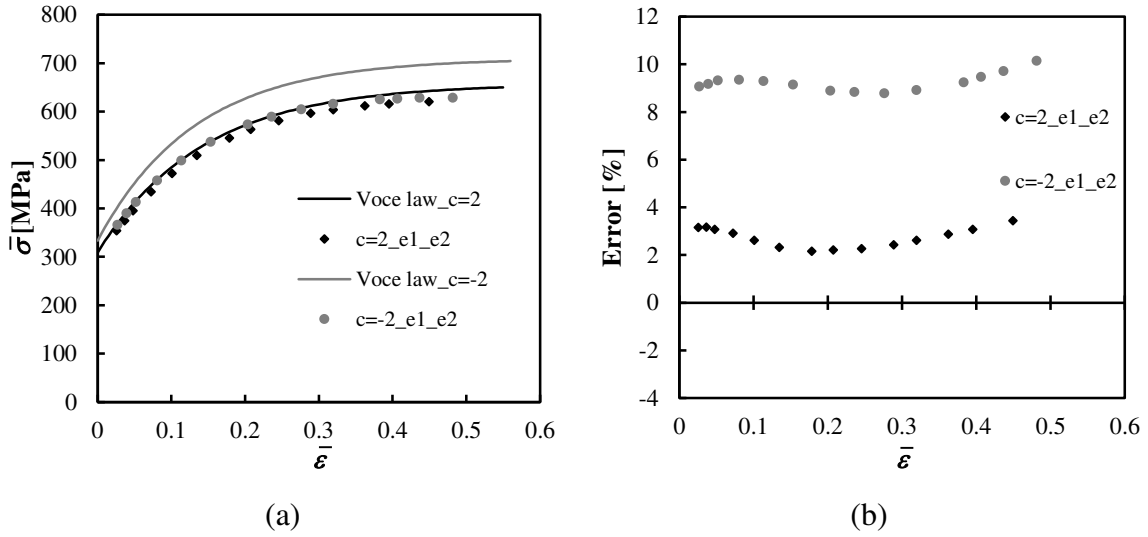

Figure 45. (a) (a) Comparison between the hardening laws of materials in Table 6 (lines) and the results with the membrane theory (symbols) with $\sigma_1 = \sigma_2 = \sigma$ (equation (13)) considering for equivalent strain determination the measured values of ε_1 and ε_2 in equation (12); (b) Evolution of the error in equivalent stress with the equivalent strain.

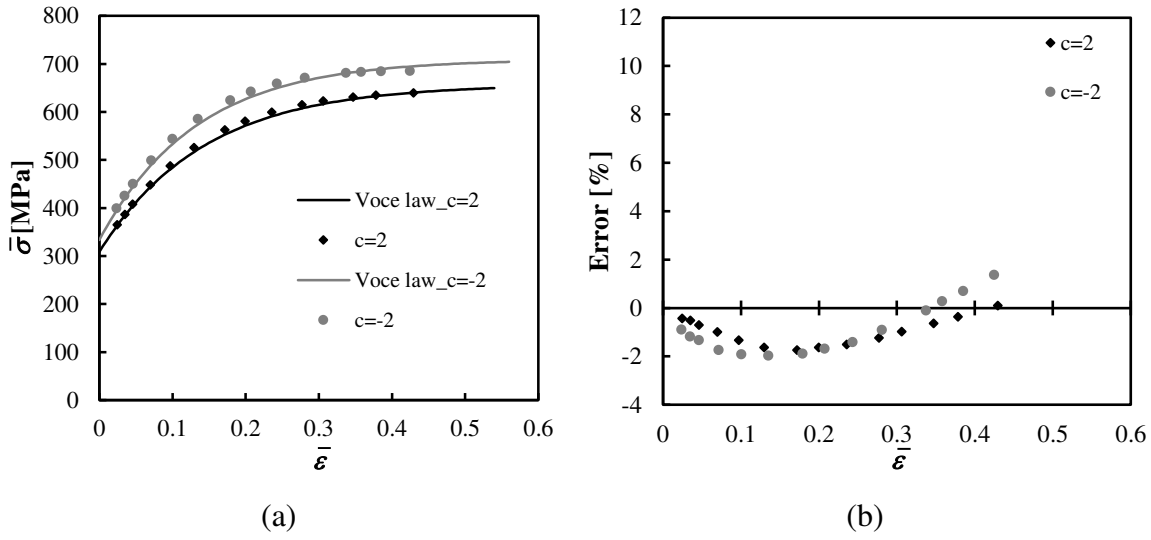

Figure 46. (a) Comparison between the hardening laws of materials in Table 6 (lines) and the results obtained with membrane theory (symbols) using the Drucker+L equivalent stress definition and equation (26); (b) Evolution of the error in equivalent stress with the equivalent strain.

Finally, in order to quantify the error in equivalent stress due to the suggested procedure, i.e. isolate this error from other sources, Figure 47 show the error difference in equivalent stress between those in Figures 44 and 46. This difference of error is always inferior to 2.5%, which shows the capability of the suggested methodology for determining

the hardening curve, as in case of materials described by the Hill'48 criterion and the Swift law.

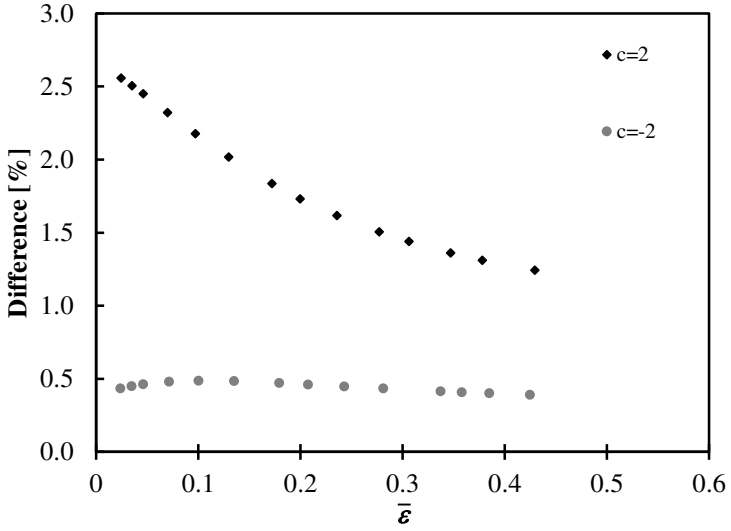

Figure 47. Difference of errors between Figure 44 and Figure 46, for the Drucker+L materials whose behaviour is described in Tables 5 and 6.

7. CONCLUSIONS

An extensive numerical study involving materials with various isotropic and anisotropic behaviours in the sheet plane, described by the Hill'48 criterion, and hardening behaviour described by the Swift law, with three hardening coefficients, n = 0.10, 0.20 and 0.35, was performed in order to determine the hardening curve and respective errors in stress, when using the traditional procedures for analysing the bulge test results. These anisotropic behaviours comprise isotropy in the sheet plane, with $r_0 = r_{45} = r_{90}$, and anisotropy in the sheet plane, with $r_0 = r_{90} \neq r_{45}$ and with $r_0 \neq r_{90}$. Two anisotropic materials, described by the Drucker+L criterion, and the hardening behaviour described by Voce law are also analysed.

The analyses of the geometry of the cap shows that, at each moment of the test, the geometry is identical for both orthotropic directions in the sheet plane, whatever the material anisotropy. This allows simplifying the use of the membrane theory ($\rho_1 = \rho_2$, in equation (1)), since the radius of curvature is equal for both principal axis, O_1 and O_2, parallel to the orthotropic axes, Ox and Oy. Also, the sheet thickness as well as the equivalent stress and strain are equal, along both orthotropic axes, up to a relatively large distance from the centre of the cap.

The principal stresses and strains along both orthotropic axes, and particularly at the pole of the cap, are equal in the case of materials with $r_0 = r_{90}$, as would be expected, but different in case of materials with $r_0 \neq r_{90}$. In this latter case, the inability of occurrence of biaxial stress and strain paths is a natural consequence of the normality condition between the stress and the increment of strain.

The errors associated with the approach traditionally used, which considers equibiaxial stress (and eventually strains) paths at the pole of the cap, isotropy and the simplify equation of the membrane theory, were quantified according to the anisotropy of the sheet. Moreover, an empirical equation for the circular bulge test relating the stress path with the strain path at the pole of the cap ($\sigma_2/\sigma_1 = (\varepsilon_2/\varepsilon_1)^{-2}$) is suggested to be used, regardless of the yield criterion that better describes the anisotropic behaviour of the material. This equation is based on Hill'48 results, but it was tested for a non-quadratic criterion, the Drucker+L criterion. It allows determining the stress path based on the knowledge of the strain path, which can be assessed by digital image correlation. In this context, the use of the simplified equation of the membrane theory (equation (13)) can be overcome by using equations (1) and (25), which greatly improves the accuracy of the estimate hardening curve, mainly in case of materials with strong anisotropy. It is also suggested an alternative to determine the equivalent strain based on the plastic work definition, to be used under the condition that both stress and strain paths are known.

ACKNOWLEDGEMENTS

This research work is sponsored by national funds from the Portuguese Foundation for Science and Technology (FCT) and by FEDER funds "Programa Operacional Factores de Competitividade" via the projects PTDC/EMS-TEC/6400/2014 and UID/EMS/00285/2013.

8. REFERENCES

[1] Chaparro BM, Thuillier S, Menezes LF, Manach PY, Fernandes J V. Material parameters identification: gradient-based, genetic and hybrid optimization algorithms. Comput Mater Sci 2008;44:339–46. doi:10.1016/j.commatsci.2008.03.028.

[2] Flores P, Duchene L, Bouffioux C, Lelotte T, Henrard C, Pernin N, et al. Model identification and FE simulations: effect of different yield loci and hardening laws in sheet forming. Int J Plast 2007;23:420–49. doi:10.1016/j.ijplas.2006.05.006.

[3] Rabahallah M, Balan T, Bouvier S, Bacroix B, Barlat F, Chung K, et al. Parameter identification of advanced plastic strain rate potentials and impact on plastic anisotropy prediction. Int J Plast 2009;25:491–512. doi:10.1016/j.ijplas.2008.03.006.

[4] Pereira AFG, Prates PA, Sakharova NA, Oliveira MC, Fernandes J V. On the identification of kinematic hardening with reverse shear test. Eng Comput 2014;31:681–90. doi:10.1007/s00366-014-0369-7.

[5] Prates PA, Oliveira MC, Fernandes J V. Identification of material parameters for thin sheets from single biaxial tensile test using a sequential inverse identification strategy. Int J Mater Form 2015:1–25. doi:10.1007/s12289-015-1241-z.

[6] Koç M, Billur E, Cora ÖN. An experimental study on the comparative assessment of hydraulic bulge test analysis methods. Mater Des 2011;32:272–81. doi:10.1016/j.matdes.2010.05.057.

[7] Santos AD, Teixeira P, Barlat F. Flow stress determination using hydraulic bulge test and a mechanical measurement system. Int. Deep Draw. Res. Gr. Conf. IDDRG, Bilbao, Spain: IDDRG; 2011, p. 91–100.

[8] Chen K, Scales M, Kyriakides S, Corona E. Effects of anisotropy on material hardening and burst in the bulge test. Int J Solids Struct 2016;82:70–84. doi:10.1016/j.ijsolstr.2015.12.012.

[9] Reis LC, Rodrigues CA, Oliveira MC, Sakharova NA, Fernandes J V. Characterization of the plastic behaviour of sheet metal using the hydraulic bulge test. In: Andrade-Campos A, Lopes N, Valente RAF, Varum H, editors. First ECCOMAS Young Investig. Conf. Comput. Methods Appl. Sci., Aveiro, Portugal: 2012, p. 67.

[10] Alves JL, Bouvier S, Oliveira MC, Menezes LF. Drawbeads: to be or not to be. AIP Conf. Proc., vol. 778, AIP; 2005, p. 655–60. doi:10.1063/1.2011297.

[11] Hsu TC, Shang HM. Mechanics of sheet metal formed by hydraulic pressure into axisymmetrical shells. Exp Mech 1976;16:337–42. doi:10.1007/BF02330250.

[12] Hill R. C. A theory of the plastic bulging of a metal diaphragm by lateral pressure. London, Edinburgh, Dublin Philos Mag J Sci 1950;41:1133–42. doi:10.1080/14786445008561154.

[13] Gagov V, Feschiev N, Comşa D-S, Minev E. Strain hardening evalution by bulge testing of sheet metals. In: Travis FW, Hashmi SMSJ, editors. 12th Int. Sci. Conf. Achiev. Mech. Mater. Eng., Gliwice, Poland: 2003, p. 331–4.

[14] Hasan RZ, Kinsey BL, Tsukrov I. Effect of element types on failure prediction using a stress-based forming limit curve. J Manuf Sci Eng 2011;133:61002.

[15] Rees DWA. Plastic flow in the elliptical bulge test. Int J Mech Sci 1995;37:373–89. doi:10.1016/0020-7403(94)00071-Q.

[16] Young RF, Bird JE, Duncan JL. An automated hydraulic bulge tester. J Appl Metalwork 1981;2:11–8. doi:10.1007/BF02833994.

[17] Martins B, Teixeira P, Santos AD. Study on the flow stress determination using hydraulic bulge test. In: Andrade-Campos A, Lopes N, Valente RAF, Varum H, editors. First ECCOMAS Young Investig. Conf. Comput. Methods Appl. Sci., Aveiro, Portugal: 2012.

[18] Bleck W, Blumbach M. Laser-aided flow curve determination in hydraulic bulging. Steel Res Int 2005;76:125–30.

[19] Mulder J, Vegter H, Aretz H, van den Boogaard AH. Accurate evaluation method for the hydraulic bulge test. Key Eng Mater 2013;554-557:33–40. doi:10.4028/www.scientific.net/KEM.554-557.33.

[20] Lăzărescu L, Comşa D-S, Banabic D. Analytical and experimental evaluation of the stress-strain curves of sheet metals by hydraulic bulge tests. Key Eng Mater 2011;473:352–9. doi:10.4028/www.scientific.net/KEM.473.352.

[21] DIN EN ISO 16808:2014-11 (E). Metallic materials - sheet and strip - determination of biaxial stress-strain curve by means of bulge test with optical measuring systems. BSI; 2014.

[22] Mulder J, Vegter H, Aretz H, Keller S, van den Boogaard AH. Accurate determination of flow curves using the bulge test with optical measuring systems. J Mater Process Technol 2015;226:169–87. doi:10.1016/j.jmatprotec.2015.06.034.

[23] Lemoine X, Sriram S, Kergen R. Flow curve determination at large plastic strain levels to accurately constitutive equations of AHSS in forming simulation. AIP Conf Proc 2011;1353:1411–6. doi:10.1063/1.3589715.

[24] Yoshida K. Evaluation of stress and strain measurement accuracy in hydraulic bulge test with the aid of finite-element analysis. ISIJ Int 2013;53:86–95. doi:10.2355/isijinternational.53.86.

[25] Menezes LF, Teodosiu C. Three-dimensional numerical simulation of the deep-drawing process using solid finite elements. J Mater Process Technol 2000;97:100–6. doi:10.1016/S0924-0136(99)00345-3.

[26] Oliveira MC, Alves JL, Menezes LF. Algorithms and strategies for treatment of large deformation frictional contact in the numerical simulation of deep drawing process. Arch Comput Methods Eng 2008;15:113–62. doi:10.1007/s11831-008-9018-x.

[27] Hill R. A theory of the yielding and plastic flow of anisotropic metals. Proc R Soc A Math Phys Eng Sci 1948;193:281–97. doi:10.1098/rspa.1948.0045.

[28] Swift HW. Plastic instability under plane stress. J Mech Phys Solids 1952;1:1–18. doi:10.1016/0022-5096(52)90002-1.

[29] Dowling NE. Mechanical behavior of materials : engineering methods for deformation, fracture, and fatigue. 2nd ed. Upper Saddle River, NJ : Prentice Hall; 1999.

[30] Lemoine X, Iancu A, Ferron G. Flow curve determination at large plastic strain levels: limitations of the membrane theory in the analysis of the hydraulic bulge test. 14th Int. ESAFORM Conf. Mater. Form., 2011, p. 1411–6. doi:10.1063/1.3589714.

[31] Ranta-Eskola AJ. Use of the hydraulic bulge test in biaxial tensile testing. Int J Mech Sci 1979;21:457–65. doi:10.1016/0020-7403(79)90008-0.

[32] Santos AD, Teixeira P, Barata da Rocha A, Barlat F, Moon YH, Lee M-G. On the determination of flow stress using bulge test and mechanical measurement. In: Barlat F, Moon YH, Lee MG, editors. 10th Int. Conf. NUMIFORM, Pohang, Republic of Korea: American Institute of Physics; 2010, p. 845–52. doi:10.1063/1.3457644.

[33] Alves JL. Simulação numérica do processo de estampagem de chapas metálicas: modelação mecânica e métodos numéricos. PhD Thesis, Universidade do Minho, 2003.

[34] Reis LC, Oliveira MC, Santos AD, Fernandes JV. On the determination of the work hardening curve using the bulge test. Int J Mech Sci 2016;105:158–81. doi:10.1016/j.ijmecsci.2015.11.009.

[35] Voce E. The relationship between stress and strain for homogeneous deformations. J Inst Met 1948;74:537–62.

[36] Cazacu O, Barlat F. Generalization of drucker's yield criterion to orthotropy. Math Mech Solids 2001;6:613–30. doi:10.1177/108128650100600603.

[37] Drucker DC. Relation of experiments to mathematical theories of plasticity. J Appl Mech ASME 1949;16:349–57.

[38] Barlat F, Aretz H, Yoon JW, Karabin ME, Brem JC, Dick RE. Linear transfomation-based anisotropic yield functions. Int J Plast 2005;21:1009–39. doi:10.1016/j.ijplas.2004.06.004.

[39] M & M Research Inc. NXT Defect Evaluator 2007.

[40] Prates PA, Oliveira MC, Fernandes J V. On the equivalence between sets of parameters of the yield criterion and the isotropic and kinematic hardening laws. Int J Mater Form 2015;8:505–15. doi:10.1007/s12289-014-1173-z.

3.3. On the determination of the work hardening curve using the bulge test

This subchapter contains the paper "*On the determination of the work hardening curve using the bulge test*", published in *International Journal of Mechanical Sciences*. In this study, various material behaviours and die geometries were used in order to develop analytical models for relating the radius of curvature and sheet thickness with the pole height during the bulge test. Numerical and experimental validation of the models was performed using the own and literature results. This approach enables the properly assess the hardening curve and allows simplifying the experimental procedure.

[Page intentionally left blank]

International Journal of Mechanical Sciences 105 (2016) 158–181

Contents lists available at ScienceDirect

International Journal of Mechanical Sciences

journal homepage: www.elsevier.com/locate/ijmecsci

On the determination of the work hardening curve using the bulge test

L.C. Reis [a,*], M.C. Oliveira [a], A.D. Santos [b], J.V. Fernandes [a]

[a] CEMUC, Department of Mechanical Engineering, University of Coimbra, Pólo II, Rua Luís Reis Santos, Pinhal de Marrocos, 3030-788 Coimbra, Portugal
[b] Faculty of Engineering, University of Porto, Rua Dr. Roberto Frias, 4200-465 Porto, Portugal

ARTICLE INFO

Article history:
Received 30 July 2015
Received in revised form
2 November 2015
Accepted 5 November 2015
Available online 12 November 2015

Keywords:
Hydraulic bulge test
Membrane theory
Numerical simulation
Hardening law
Anisotropic metal sheets

ABSTRACT

Hydraulic bulge test represents nowadays an important means to obtain higher accuracy on material characterization. One reason is the possibility of using the obtained biaxial stress–strain data to largely extend the hardening information extracted from the tensile test. The other reason is the use of biaxial data as input information when determining parameters for current most advanced yield criteria.

This contribution aims to obtain the material stress–strain hardening curve from the bulge test using a simpler experimental equipment, in which the output data is the hydraulic bulge pressure and the pole bulge height. This information is used to determine the sheet thickness and corresponding radius of curvature at the pole of the cap, which is the needed data to calculate the biaxial stress–strain curve, the stress being determined based on Laplace's equation from the membrane theory, a standard approach for this kind of analysis.

Analytical models are proposed relating the radius of curvature and the sheet thickness with the pole bulge height. These models are based in an extensive analysis of different material behaviors, which in turn are related to characteristic properties of sheet metals, as well as different geometries of bulge test. Geometric variables include bulge die diameter and the fillet radii located at the entrance of the die. The analytical formulas also include the material variables associated with the hardening behavior and the sheet anisotropy, with different interaction and weighting impact.

The extensive study also permits a deeper theoretical understanding of relations among the interconnecting variables and their influence on the accuracy of sheet thickness and radius of curvature determination, which directly influences the obtained biaxial stress–strain curve. This means, for example, the understanding between sheet thinning evolution or bulge curvature evolution during bulging and the corresponding relation with material plastic properties, hardening and anisotropy.

The validation of the methodology and the proposed analytical models is performed with experiments, both from developed experimental system and also from literature with different bulge geometric relations.

1. Introduction

Finite element analysis is currently essential in the design stage of sheet metal forming components. Its implementation, wide use and contribution to better predictability in the design of sheet metal forming processes depends on the accurate characterization of the material properties [1]. Sheet metal mechanical behavior is usually described using mathematical models, i.e. constitutive laws, and for each material, the parameters of such models are generally determined with resource to tensile and other monotonous strain path tests, such as shear test and biaxial tension.

The biaxial bulge test, under hydraulic pressure [2], can achieve relatively high strain values before necking, allowing the definition of the hardening law up to large plastic deformations. In the bulge test, the periphery of the metal sheet is restrained by a drawbead, which prevents its radial displacement. Hydraulic pressure is then applied to the metal blank, forming the sheet into a hemispherical geometry without using a punch, thus, minimizing any influence of contact with friction. The test conditions promote biaxial strain paths at the pole of the cap, which is perfectly spherical in a region close to the pole and inside a circle of constant latitude [3,4]. This test can be used to obtain the strain limits defining the points of Forming Limit Curves (FLC's) and to characterize the material hardening behavior. Normally the region under study is limited to the area around the pole of the cap, which using circular or elliptical dies will allow a wide variety of the principal strain ratios at the pole of the cap [5,6].

* Corresponding author. Tel.: +351239790700; fax: +351239790701.
E-mail addresses: luis.reis@dem.uc.pt (L.C. Reis), marta.oliveira@dem.uc.pt (M.C. Oliveira), abel@fe.up.pt (A.D. Santos), valdemar.fernandes@dem.uc.pt (J.V. Fernandes).

http://dx.doi.org/10.1016/j.ijmecsci.2015.11.009
0020-7403/

The bulge test has been the subject of growing interest with a great relevance on the characterization of strain hardening laws of metal sheets. However, the identification of the parameters of the hardening law presents some difficulties [7]. Various methodologies can be considered and several approaches have been developed and adopted over the years [8]. When determining the strain hardening law of the material, using the membrane theory, it is necessary to record the hydraulic pressure and evaluate the radius of curvature and the sheet thickness at the pole, during the test. As example of using different methodologies, the determination of the sheet thickness can be performed based on strain measurements at the pole or using mathematical models, which take into account the geometry of the test [9,10]. Similarly, the radius of curvature at the pole of the cap can be determined using direct evaluation with different points at the pole or indirect evaluation with mathematical models using total height at the pole [8,10,11].

Regarding the direct evaluation, the use of optical measuring systems allows the description of the geometry and strain distributions on sheet surface during the bulge test. However, the evaluation of the stress *vs.* strain curves depends on assumptions and simplifications, whose assessment are still under study. For example, in a recent study Mulder et al. [12] examine the validity and the conditions for applying the membrane theory, which includes issues such as: radii of curvature evaluation, coordinated system for strain measuring to be used, equibiaxial stress state assumption in case of in-plane anisotropic materials, existence of bending stresses and through thickness stress due to the hydraulic pressure.

This paper presents a numerical study of the hydraulic bulge test with circular die, using the in-house finite element program *DD3IMP* [13,14]. It is assumed that the radii of curvature are evaluated at the mid-plane of the cap, the coordinated system for strain measuring is aligned with the orthogonal axes of symmetry of the sheet and the non-balanced biaxial stress state is determined with the corresponding strain ratio, which needs prior knowledge of the shape of the yield surface [12]. In this context, in-plane isotropic and anisotropic materials were described by Hill'48 criterion. The aim of the work is to propose an approach for analysing the results of the circular bulge test, in order to obtain the stress at the pole of the cap with simple equipment and not requiring further specific devices to determine the radius of curvature and thickness at the pole. The influence of the mechanical properties of the material as well as the geometry of the die on the evolution of the radius of curvature and the sheet thickness with the pole height is considered in this analysis.

2. Theoretical background

The analysis of the stress state near the pole of the metal sheet during the bulge test, using either circular or elliptical dies, can be performed with the aid of the membrane theory [15], as long as it is satisfied a small ratio between the sheet thickness and the bulge die, typically values lower than 1/50 [8,16]. Under these conditions, the bending stress can be neglected and assuming that the thickness stress σ_3 ($=\sigma_Z$) is zero, a relationship between principal stresses at the pole, the pressure and the geometry of the cap is given by:

$$\frac{\sigma_1}{\rho_1}+\frac{\sigma_2}{\rho_2}=\frac{p}{t}. \tag{1}$$

where σ_1 and σ_2 are the principal stresses in the sheet surface (assuming that the principal stress axes (O123) and anisotropy axes (O*xyz*) coincide), ρ_1 and ρ_2 are the radii of curvature, at half thickness, in the O*xz* and O*yz* planes, respectively, p is the hydraulic pressure and t is the sheet thickness.

In order to experimentally determine the strain hardening curve, the evolution of the following variables need to be obtained during the test: pressure, p, the radii of curvature, ρ_1 and ρ_2, and the sheet thickness at the pole, t. The thickness can be determined based on the knowledge of the initial thickness of the sheet, t_0, and the thickness strain, ε_3, through the following equation:

$$t=t_0\exp(-\varepsilon_3). \tag{2}$$

The strain, ε_3, can be obtained from the measurement of the principal strains in the sheet plane, ε_1 and ε_2, based on the condition of volume constancy during plastic deformation:

$$\varepsilon_3=-(\varepsilon_1+\varepsilon_2). \tag{3}$$

Since the radii of curvature are experimentally evaluated on the external surface of the cap, their correction should be done based on the following equation [17]:

$$\rho=\rho_{ext}-\frac{t}{2}, \tag{4}$$

where ρ is the radius of curvature at the half thickness of the cap, and ρ_{ext} is the radius of curvature of the external surface of the cap.

In the general case, i.e. anisotropic metal sheet, the membrane theory equation (Eq. (1)), contains two unknown variables, σ_1 and σ_2, which requires an additional equation for its determination. For metal sheets obeying to the Hill'48 criterion [18], this additional equation can be obtained by the plastic stress-strain relationships, assuming coincidence of the coordinate systems of principal stress (O123) and anisotropy (O*xyz*):

$$\begin{cases} d\varepsilon_1=d\lambda[H(\sigma_1-\sigma_2)+G(\sigma_1-\sigma_3)] \\ d\varepsilon_2=d\lambda[F(\sigma_2-\sigma_3)+H(\sigma_2-\sigma_1)] \end{cases}, \tag{5}$$

where F, G and H are the anisotropy parameters, $d\varepsilon_1$ and $d\varepsilon_2$ are increments of plastic deformation in the sheet plane, parallel to the O*x* and O*y* axes, respectively, and $d\lambda$ is a scalar factor of proportionality.

In the bulge test, it can be assumed that $\sigma_3=0$ and, based on Eq. (5), one can be written:

$$\frac{d\varepsilon_1}{d\varepsilon_2}=\frac{\sigma_1(G+H)-\sigma_2 H}{-\sigma_1 H+\sigma_2(F+H)}. \tag{6}$$

Consequently, Eqs. (1) and (6) allow determining the principal stresses, σ_1 and σ_2, in case of circular and elliptical dies, assuming that the parameters, F, G and H of the Hill'48 criterion are known.

To calculate the equivalent stress, $\overline{\sigma}$, and the equivalent strain, $\overline{\varepsilon}$, values that characterize the hardening behavior, the following equations can be used [6,18]:

$$\overline{\sigma}=\sqrt{(G+H)\sigma_1^2+(F+H)\sigma_2^2-2H\sigma_1\sigma_2}, \tag{7}$$

$$\overline{\varepsilon}=\sqrt{F\left[\frac{G\varepsilon_2-H\varepsilon_3}{FG+GH+HF}\right]^2+G\left[\frac{F\varepsilon_1-H\varepsilon_3}{FG+GH+HF}\right]^2+H\left[\frac{F\varepsilon_1-G\varepsilon_2}{FG+GH+HF}\right]^2}. \tag{8}$$

In case of isotropic materials, obeying the von Mises yield criterion, the principal stresses, σ_1 and σ_2, in bulge tests performed either with circular or elliptical dies, can be calculated using Eq. (1) and simplifying the Eq. (6), as follow:

$$\frac{d\varepsilon_1}{d\varepsilon_2}=\frac{\sigma_1-0.5\sigma_2}{-0.5\sigma_1+\sigma_2}. \tag{9}$$

Similarly, the equivalent stress and strain can be calculated using the following simplified equations (von Mises):

$$\overline{\sigma}=\sqrt{(\sigma_1)^2+(\sigma_2)^2-\sigma_1\sigma_2}, \tag{10}$$

$$\overline{\varepsilon} = \left(\frac{2}{\sqrt{3}}\right)\sqrt{\varepsilon_1^2+\varepsilon_2^2+\varepsilon_1\varepsilon_2}. \quad (11)$$

Finally, in cases of circular die and isotropic materials or anisotropic materials such that, the anisotropy coefficients at 0º and 90º degrees are equal ($r_0=r_{90}$), the principal stresses are also equal ($\sigma_1=\sigma_2=\sigma$), as well as the principal strains ($\varepsilon_1=\varepsilon_2=\varepsilon$) and curvature radii ($\rho_1=\rho_2=\rho$), which simplifies Eq. (1) as follow:

$$\sigma = \frac{p\rho}{2t}. \quad (12)$$

In these cases, Eq. (12) is sufficient to determine the principal stresses in the sheet plane ($\sigma_1=\sigma_2=\sigma$), without requiring any additional equation.

Also, for materials with fully isotropic behavior, Eqs. (10) and (11) can be simplified (von Mises criterion):

$$\overline{\sigma}=\sigma \text{ and } \overline{\varepsilon}=2\varepsilon. \quad (13)$$

Since the total strain present two additive components, elastic and plastic, the elastic strain components, ε_1^e and ε_2^e, can be removed from the measured strains, ε_1 and ε_2. Assuming isotropic elastic behavior, the generalized Hooke's law, gives the elastic strain components as:

$$\begin{cases} \varepsilon_1^e = \frac{1}{E}[\sigma_1 - \nu(\sigma_2+\sigma_3)] \\ \varepsilon_2^e = \frac{1}{E}[\sigma_2 - \nu(\sigma_1+\sigma_3)] \end{cases}. \quad (14)$$

Since in the bulge test it can be assumed that $\sigma_3=0$, this equation can be written:

$$\begin{cases} \varepsilon_1^e = \frac{1}{E}(\sigma_1 - \nu\sigma_2) \\ \varepsilon_2^e = \frac{1}{E}(\sigma_2 - \nu\sigma_1) \end{cases}. \quad (15)$$

3. Numerical modelling

In order to perform the study concerning the methodology for the evaluation of the strain hardening law using the circular bulge test, numerical models of the test were built, which are defined in this section. The geometry of the tools considered in the test is schematically shown in Fig. 1, where R_M is the die radius, R_1 the die profile radius, R_D is the radius of the central part of the drawbead and R_S the radius of the circular sheet. In fact, the geometry and the dimension of the die to perform the bulge test is not standardized and different laboratories may use different dimensions. In this context, various die geometries were chosen. For example, one of the geometries was built based on experimental bulge test used by [19] which a die radius of $R_M=75$ mm and die profile radius of $R_1=13$ mm, the radius of the central part of the drawbead is $R_D=95$ mm and uses sheets with radius $R_S=100$ mm.

Table 1 shows the dimensions of the die profile radius, R_1, and the die radius, R_M, for each studied geometry. Besides of the above mentioned geometry, referred to as 75.0_13.00, two homothetic geometries were selected, i.e. with the same relations between R_1 and R_M, but different dimensions, a lower dimension being 50.0_8.6(6), and a higher dimension being 100.0_17.3(3). The additional selected geometries were the die used by Chamekh et al. [20], designated as 45.5_6.00, and two other geometries designated as 75.0_6.25 and 105.7_6.35.

In all numerical models the tools were described using Bézier surfaces, considering only one quarter of the geometry due to material and geometrical symmetry conditions. However, in order to simplify the analysis, the drawbead geometry was neglected and its effect was replaced by a boundary condition imposing radial displacement restrictions on nodes placed at a distance equal to R_D from the center of the circular sheet, which has an initial blank radius of R_S [21]. The contact with friction was described by the Coulomb law with a constant friction coefficient of 0.02 [22]. All numerical simulations were carried out with *DD3IMP* in-house code [13,14] assuming an incremental increase of the pressure applied to the sheet inner surface.

The blank sheet discretization was previously optimized [23] considering the geometry with the die radius of $R_M=75$ mm and the die profile radius of $R_1=13$ mm. The in-plane finite element mesh geometry is shown in Fig. 2. The sheet geometry was divided into four main zones, in order to describe the central region of the

Table 1
Designation of the studied die geometries.

Designation: R_M_R_1	R_M[mm]	R_1[mm]	R_1/R_M	R_S[mm]	R_D[mm]
50.0_8.6(6)	50.0	8.6(6)	0.17	66.7	63.3
75.0_13.00	75.0	13.00	0.17	100.0	95.0
100.0_17.3(3)	100.0	17.3(3)	0.17	133.3	126.7
45.5_6.00	45.5	6.00	0.13	60.7	57.6
75.0_6.25	75.0	6.25	0.08	100.0	95.0
105.7_6.35	105.7	6.35	0.06	140.9	133.9

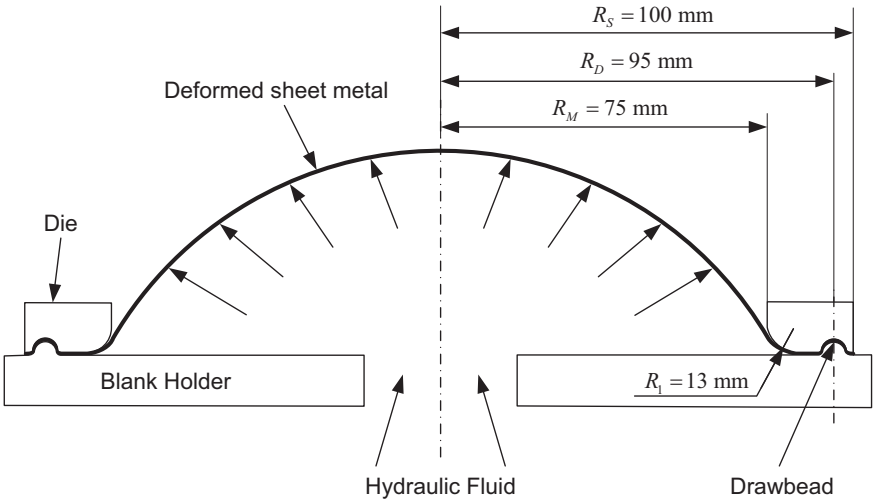

Fig. 1. Bulge test, with the identification of the principal dimensions of the tool according to Santos et al. [7].

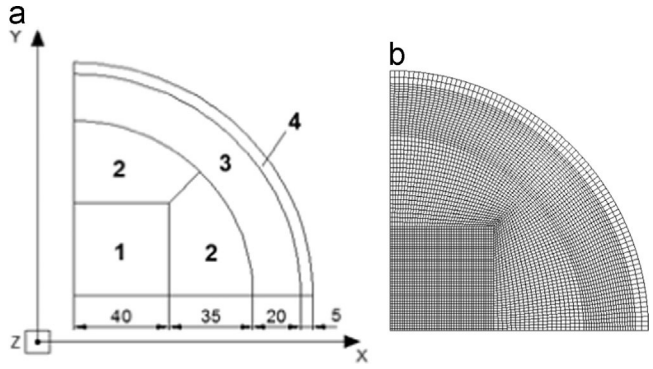

Fig. 2. Geometry of the finite element mesh in the sheet plane showing: (a) the four main zones (the dimensions are in mm) and (b) a general view of the mesh.

specimen with a regular and uniform grid discretization in the sheet plane, using quadrangular elements. For the 75.0_13.00 geometry, this corresponds to a total of 5292 3D solid 8 node elements, using two layers of elements through thickness. The blank discretizations for other die dimensions were obtained using a scaling factor for the in-plane finite element size, based on the R_S values.

4. Results

Numerical simulations of the bulge test were performed for materials with several plastic behaviors, using the die geometries described in the previous chapter. The two next sections concern the circular die designated as 75.0_13.00 geometry, for full isotropic materials (Section 4.1) and materials with transverse anisotropy (Section 4.2). The last section (Section 4.3) is related with the study of every different geometry of Table 1, for isotropic materials.

The materials under study have plastic behavior described by Hill'48 yield criterion and hardening defined by Swift law [24]:

$$\overline{\sigma} = K(\overline{\varepsilon} + \varepsilon_0)^n, \tag{16}$$

where K, ε_0 and n are the parameters of this law, being n the work hardening coefficient. The value of the parameter ε_0 is assumed to be 0.005. The elastic behavior is considered isotropic with a Young's modulus, $E=210$ GPa, and a Poisson's ratio, $\nu=0.30$.

The analysis of the numerical simulation results was performed in the same way that is usually done experimentally, i.e. using step-wise measurements, namely, the radius of curvature at the pole, ρ_{ext}, is evaluated at several stages during the test, with the aid of the *NXT Defect Evaluator* commercial code [25]. This software allows the evaluation of surface curvature, based on the coordinates of points located on the meridian plane. The surface radius of curvature, ρ_{ext}, was analysed only along the Ox axis. In case of transverse anisotropy, the geometrical and material symmetries make equal the evolutions of ρ_{ext} along the Ox and Oy axes. In case of transverse anisotropy, the results show that the curvature radius is also equal along both axes, Ox and Oy, and therefore it is not influenced by material anisotropy, as it was already reported in [26,27]. The radius of curvature at half thickness, ρ, is determined using Eq. (4). During the test, the principal strains in the sheet plane were determined by direct measurement at the pole of the cap, as it can be experimentally performed using digital image correlation technique (DIC), for example. This allows the determination of sheet thicknesses based on the values of the principal strains at the top of the cap, using Eqs. (2) and (3).

Table 2
Materials and corresponding parameters of the Swift hardening law.

Designation	σ_0 [MPa]	n
100_0.05_Z.Z	100	0.05
100_0.20_Z.Z		0.20
100_0.35_Z.Z		0.35
200_0.05_Z.Z	200	0.05
200_0.20_Z.Z		0.20
200_0.35_Z.Z		0.35
300_0.05_Z.Z	300	0.05
300_0.20_Z.Z		0.20
300_0.35_Z.Z		0.35

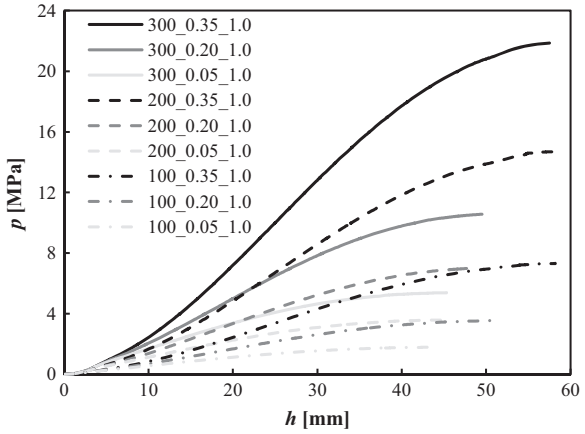

Fig. 3. Evolution of pressure, p, with pole height, h, for sheets of fully isotropic materials with $t_0=1.0$ mm.

4.1. Isotropic materials in 75/13 die ratio geometry

The numerical simulation study of the bulge test is carried out in this section with the circular die designated as 75.0_13.00 geometry. It is concerned with isotropic plastic materials having different hardening law parameters. In this way, materials with different values of yield stress and work hardening coefficient were analysed, in order to study the influence of these parameters on the results of the bulge test, particularly the evolutions of the pressure, radius of curvature and thickness at the pole of the cap, during the test.

Table 2 shows the parameters of the Swift law for the materials under study. Three values of yield stress, σ_0, were chosen, namely 100, 200 and 300 MPa as well as three values of work hardening coefficient, n, namely 0.05, 0.20 and 0.35. In order to simplify the analysis of the results in this section, the following designation is adopted for the material in each test: "XXX_0.YY_Z.Z", where "XXX" is the yield stress value, σ_0, "0.YY" is the work hardening coefficient of the material, n, and "Z.Z" is the initial sheet thickness, t_0. For each material, three different values of thickness were studied: 0.5, 1.0 and 2.0 mm.

In the following, examples of numerical results are presented concerning the materials in Table 2. Fig. 3 shows the evolution of the pressure, p, with the pole height, h, for 1.0 mm thick sheets. Both parameters of the Swift law, σ_0, and, n, influence the pressure evolution during the bulge test. At the beginning of the test, higher pressure evolution is related to higher yield stresses. Subsequently, the level of the curves depends mainly of the work hardening coefficient, for a given n value.

Fig. 4 shows examples of the evolution of the radius of curvature, ρ, with the pole height, h, for 1.0 mm sheet thicknesses. At the beginning of the test, the radius of curvature quickly decreases, but its rate declines as the pole height increases, such that when

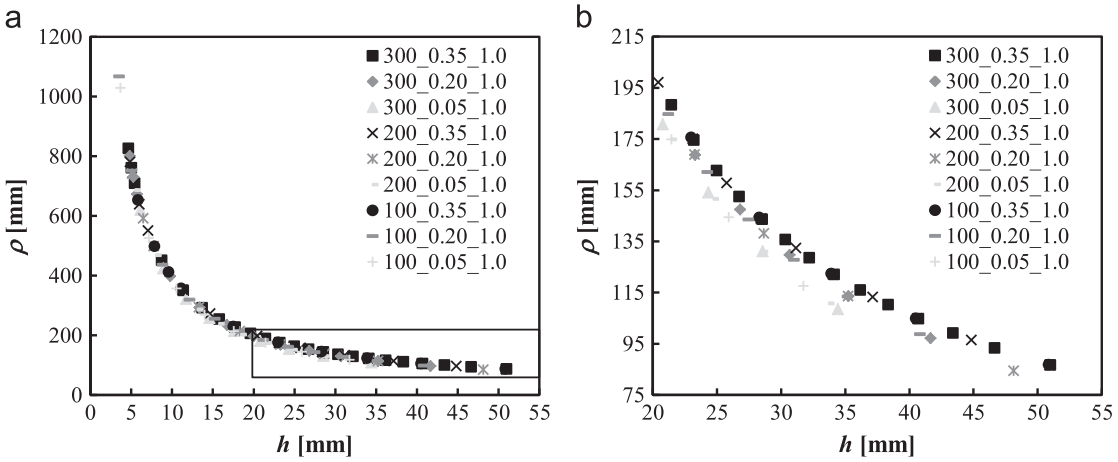

Fig. 4. Evolution of radius of curvature, ρ, with pole height, h, for sheets with fully isotropic materials with $t_0=1.0$ mm: (a) general view and (b) detail for values of pole height greater than 20 mm.

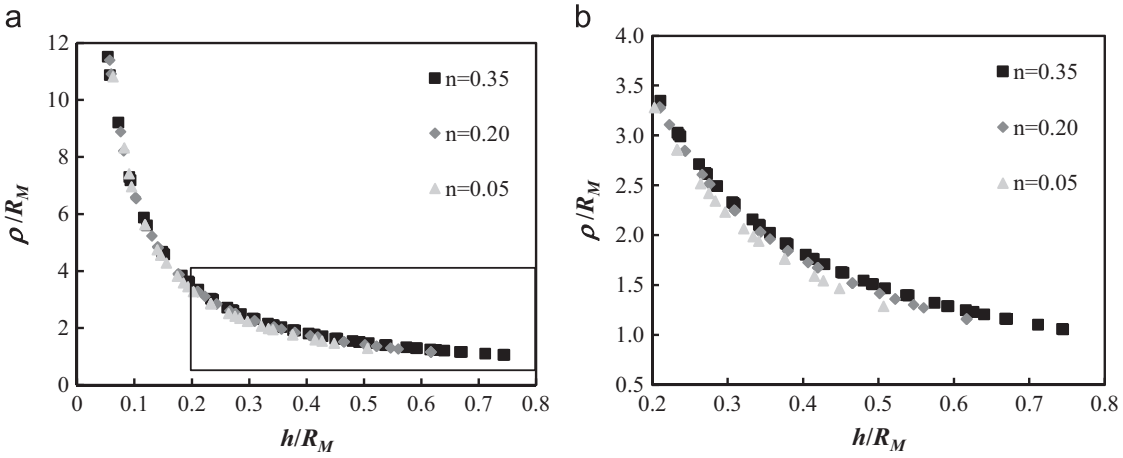

Fig. 5. Evolution of normalized radius of curvature, ρ/R_M, with normalized pole height, h/R_M, for fully isotropic materials in Table 2 and initial thicknesses grouped by the n values: (a) general view and (b) detail for normalized pole heights greater than 0.2.

the pressure approaches the maximum value, the radius of curvature approaches to the radius of the die ($R_M=75$ mm in Fig. 1). Whatever the values of the yield stress and the work hardening coefficient, the curves tend to be superposed at the beginning of the test. But as the pole height increases, the curves tend to separate from each another, depending on the work hardening coefficient: materials with higher work hardening coefficient present a higher radius of curvature for the same value of pole height. These results indicate that it is possible to define a unique curve for each value of work hardening coefficient, whatever the yield stress of the materials. In other words, the successive geometries of the cap, during the test, are identical for materials with the same value of the work hardening coefficient.

The almost coincidence of the curves at the beginning of the test is certainly associated with the fact that, at this stage of the test, the magnitude of the plastic component of the strain is not significant (relatively to the elastic component), i.e. the geometry of the cap is still widely influenced by the elastic properties of the material. For example, prior to the yield stress is attained, only the elastic properties can influence such geometry. Nevertheless, the beginning of the test is not an interesting stage regarding the determination of the work hardening curve, since in experimental bulge tests the value of radius of curvature at the pole of the cap, ρ, is usually not enough accurate.

The results for the sheets with initial thicknesses of 0.5 and 2.0 mm (not represented in Fig. 4 for clarity) are entirely coincident with those of the sheet thickness of 1.0 mm for the same value of the work hardening coefficient, and so it is also possible to define a unique evolution of ρ *vs.* h, for each value of work hardening coefficient, whatever the initial sheet thickness (and the yield stress as already mentioned). This is shown in Fig. 5, where ρ and h are normalized by the die radius R_M.

The evolution of the sheet thickness at the pole of the cap during the test was also analysed. Fig. 6 shows the evolution of the thickness of the sheet at the pole, t, with the pole height, h, for all materials under analysis and initial sheet thickness of 1.0 mm. Also, these evolutions can be grouped by the value of the work hardening coefficient, as for the radius of curvature. The materials with higher work hardening coefficient present lower sheet thickness variation, for the same pole height, whatever the yield stress of the materials.

The same kind of behavior is observed for the other initial sheet thicknesses ($t_0=0.5$ mm and 2.0 mm), providing that the thickness, t, is normalized by the initial thickness of the sheet, t_0. Having previous results in mind, it is possible to define a unique evolution of t/t_0 *vs.* h/R_M, for each value of work hardening coefficient, whatever the value of the initial sheet thickness (and the yield stress, as already mentioned). The results are shown in Fig. 7.

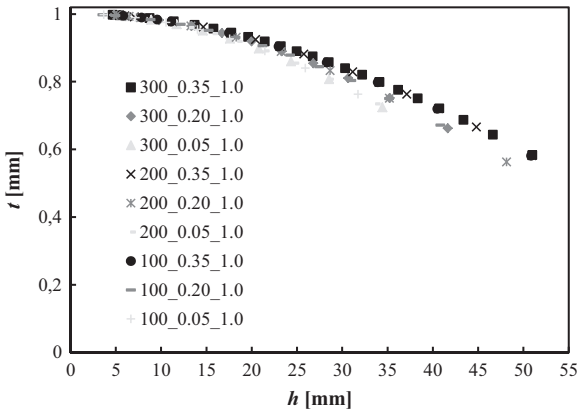

Fig. 6. Evolution of thickness, t, with pole height, h, for fully isotropic materials with $t_0=1.0$ mm.

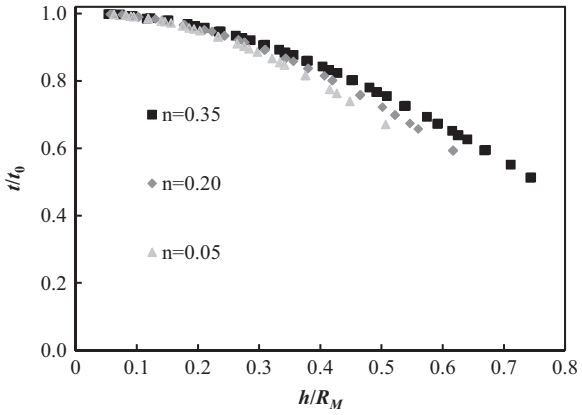

Fig. 7. Evolution of normalized sheet thickness, t/t_0, with normalized pole height, h/R_M, for all materials presented in Table 2 and initial thicknesses ($t_0=0.5$, 1.0 and 2.0 mm), grouped by their n values.

Table 3
Designation of the materials with transverse anisotropy, the corresponding parameters of Hill'48 criterion and the ratio σ_b/σ_0.

Designation	Parameters of the Hill'48 Criterion						
	F	G	H	L	M	N	σ_b/σ_0
0.7_0.7_0.7_*n*	0.588	0.588	0.412	1.500	1.500	1.412	0.922
1_1_1_*n*	0.500	0.500	0.500	1.500	1.500	1.500	1.000
2_2_2_*n*	0.333	0.333	0.667	1.500	1.500	1.667	1.225
3_3_3_*n*	0.250	0.250	0.750	1.500	1.500	1.750	1.414

In summary, for isotropic materials, the evolution of the normalized sheet thickness and the normalized radius of curvature with the normalized pole height are only influenced by the value of the work hardening coefficient and are independent of the yield stress and the initial thickness of the sheet.

4.2. Materials with transverse anisotropy in 75/13 die ratio geometry

The numerical simulation of the bulge test was also carried out on metal sheets with transverse anisotropy. Therefore, the anisotropy coefficient r_α is constant (equal to and different from 1) in the plane of the sheet (α the angle between the tensile direction and the rolling direction). Concerning the die geometry, it is used a circular die designated as 75.0_13.00. The study on the hardening behavior includes materials presented in Table 2 and the initial thickness of the sheet is 1 mm. Table 3 shows the designation adopted for each material, the corresponding parameters of the

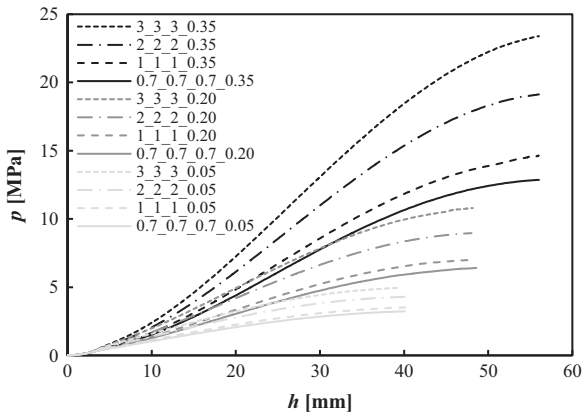

Fig. 8. Evolution of pressure, p, with pole height, h, for materials with transverse anisotropy and $n=0.05$, 0.20 and 0.35 ($\sigma_0=200$ MPa and $t_0=1$ mm).

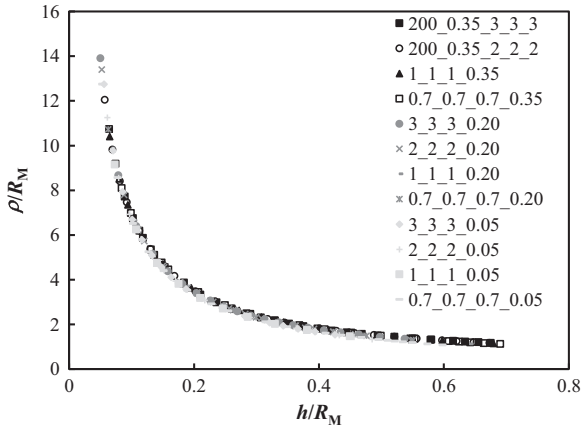

Fig. 9. Evolution of normalized radius of curvature, ρ/R_M, with normalized pole height, h/R_M, for materials with transverse anisotropy and $n=0.05$, 0.20 and 0.35 ($\sigma_0=200$ MPa and $t_0=1$ mm).

Hill'48 criterion and the ratio σ_b/σ_0 (where σ_b and σ_0 are the yield stress in biaxial and uniaxial tension). The designation A_A_A_*n* corresponds to a material with the anisotropy coefficient, r_α, in the sheet plane such that: $r_0=r_{45}=r_{90}$, and so the parameters of the Hill'48 criterion obey to the condition $F=G$. The parameter n is the work hardening coefficient. The condition $F=G$ together with the condition $G+H=1$, which is assumed for the materials in Table 3, means that the tensile curves along any direction in the sheet plane are coincident [28], whatever the value of the anisotropy coefficient, r_α, provided that the parameters of the work hardening law σ_0 and n are the same.

Fig. 8 shows examples of the evolution of the pressure with the pole height, for the cases of transverse anisotropy, with yield stress, $\sigma_0=200$ MPa and work hardening coefficients, $n=0.05$, 0.20 and 0.35. The higher the anisotropy coefficient, the higher is the pressure required to achieve the maximum pole height, for a given value of the work hardening coefficient.

Fig. 9 shows examples of the evolution of the normalized radius of curvature, ρ/R_M, with the normalized pole height, h/R_M, for materials with yield stress, $\sigma_0=200$ MPa, and work hardening coefficients, $n=0.05$, 0.20 and 0.35. These results are similar to those of Fig. 5, for the materials with the same hardening coefficient, n, and so the evolution of ρ does not depend of the anisotropy parameters. This means that the geometry evolution of the cap during the bulge test does not depend on the anisotropy coefficient of the material, and consequently, the evolutions of ρ/R_M *vs.* h/R_M can be superposed regardless of the r_α value.

The evolution of the sheet thickness at the pole of the cap during the test was also analysed. The values of the thickness at different moments of the test were determined based on the values of the principal strains ($\varepsilon_1=\varepsilon_2$) at the top of the cap. Fig. 10 shows the evolution of the normalized thickness of the sheet at the pole, t/t_0, with the normalized pole height, h/R_M, for the transverse anisotropic materials with three values of work hardening coefficient: $n=0.05$, 0.20 and 0.35. The results show that the evolution of the normalized sheet thickness with the normalized pole height depends, not only on the work hardening coefficient (see also Section 4.1), but also on the anisotropy coefficient, r_α.

The current results show that, unlike the work hardening coefficient whose value influences the evolutions of the normalized radius of curvature and the normalized sheet thickness during the test, the anisotropy coefficient only influences the evolution of the normalized sheet thickness with the normalized pole height.

4.3. Isotropic materials with different die ratio geometries

In this section, numerical simulations of the bulge test are performed with several die geometries, corresponding to those presented in Table 1. The material used in these simulations is an isotropic metal sheet with yield stress, $\sigma_0=200$ MPa, work hardening coefficient, $n=0.20$ and the initial thickness is 1 mm.

In the next figures, the designation A_B_C_R_M_R_1 corresponds to a material with the anisotropy coefficient, r_α, in the sheet plane

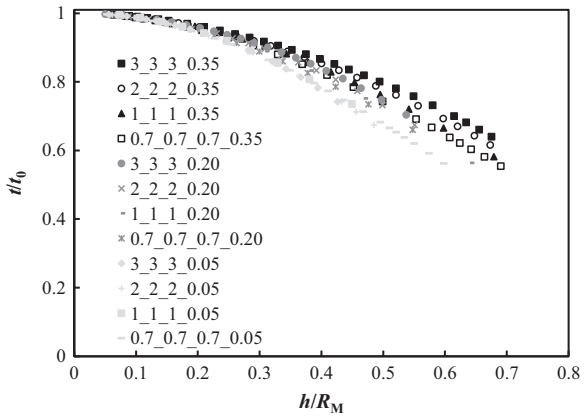

Fig. 10. Evolution of normalized sheet thickness, t/t_0, with normalized pole height, h/R_M, for materials with transverse anisotropy and $n=0.05$, 0.20 and 0.35 ($\sigma_0=200$ MPa and $t_0=1$ mm).

such that: $r_0=A$, $r_{45}=B$, $r_{90}=C$ and $A=B=C=1$; R_M is the measure of the die radius and R_1 is the die profile radius.

Fig. 11 shows the evolution of the pressure with the pole height, for different die geometries. For a given ratio R_1/R_M, the level of the curves decrease and reach higher values of bulge height, when the R_1 (or R_M) value increases (Fig. 11(a)). Moreover, for a given value of R_M, the level of the curves pressure *vs.* pole height decreases and higher values of bulge height are attained, when the value of R_1 increases (compare curves for dies 75.0_13.00 and 75.0_6.25 in Fig. 11(b)), and for a given value of R_1, the level of the curves decreases and higher values of bulge height are attained, when the value of R_M increases (compare curves for dies 45.5_6.00, 75.0_6.25 and 105.7_6.35, with close values of R_1, in Fig. 11 (b)).

Fig. 12 shows the evolutions of the normalized radius of curvature during the test that slightly depends on the ratio R_1/R_M. In fact, in cases of dies in which the ratio is equal, the results show a unique trend, whatever the values of R_M and R_1. For the dies with different ratios of R_1/R_M, the results are very close at the beginning of the test; then, depending on the ratio R_1/R_M, they tend to move away from each other; finally, they tend to overlap each other at the end of the test, for high values of the normalized pole height. The trend shows that the lower the R_1/R_M ratio, the lower is the level of the curves.

Fig. 13 shows the evolution of the normalized thickness during the test. As for the evolution of the normalized radius of curvature, the normalized thickness evolution shows the same trend in case of dies with equal ratio R_1/R_M, whatever the values of R_M and R_1. Otherwise, when the ratio R_1/R_M is the lower the curves have tendency to move down, particularly for high values of h/R_M.

In summary, the evolutions of the normalized sheet thickness and the normalized radius of curvature with the normalized pole height are influenced by the value of the ratio R_1/R_M, and not by the individual values of R_M or R_1.

5. Equations for the evolution of ρ/R_M *vs.* h/R_M and t/t_0 *vs.* h/R_M

The determination of the principal stress, using the membrane theory (Eq. (12)), needs the evaluation of the radius of curvature and the thickness at the top of the cap, which requires the use of appropriate equipment and corresponding data acquisition software, which are not always fully available. As alternative, simplified equipment may be used to obtain only the evolution of the pressure and total bulge height variables, but in this case the radius of curvature and the pole thickness evolutions need to be

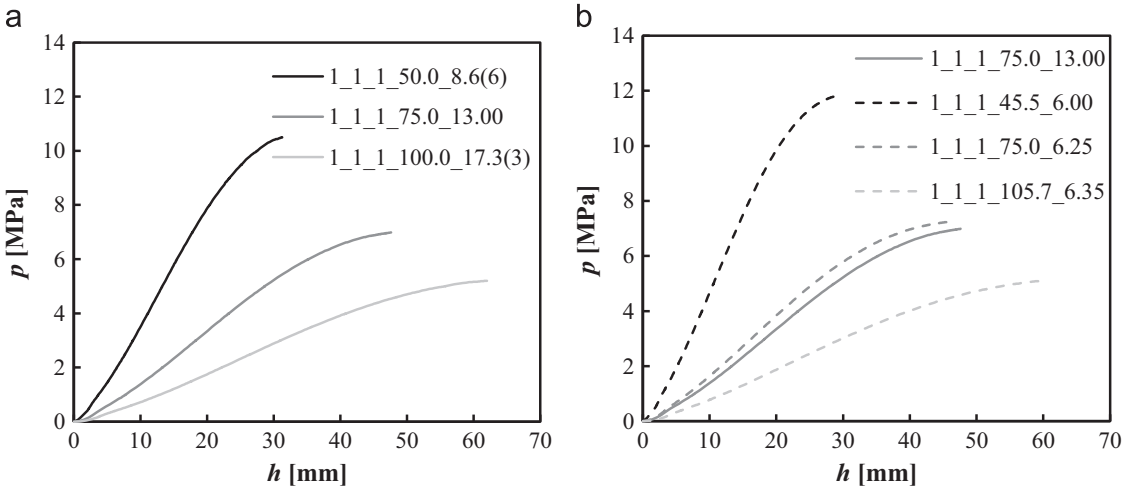

Fig. 11. Evolution of pressure, p, with pole height, h, for different dies geometries: (a) homothetic dies and (b) different ratios R_1/R_M.

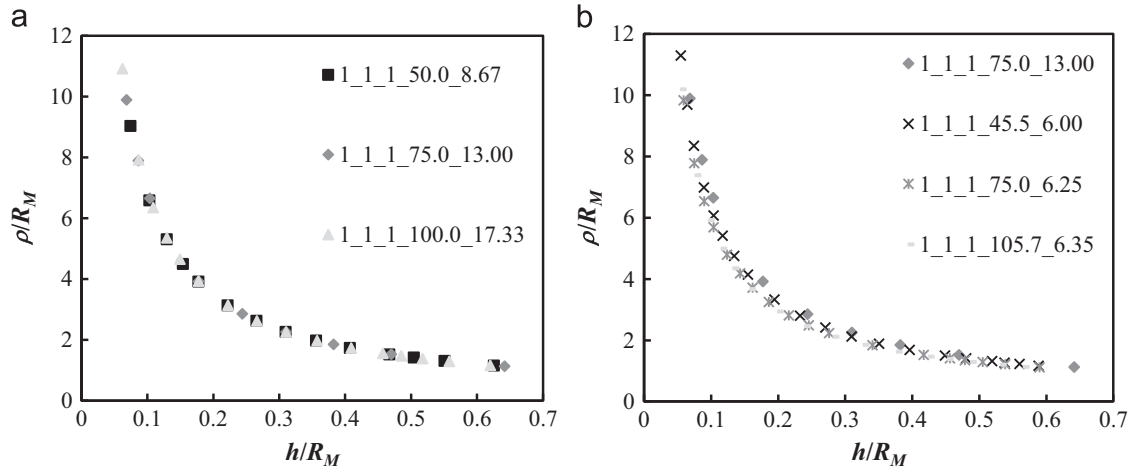

Fig. 12. Evolution of normalized radius of curvature, ρ/R_M, with normalized pole height, h/R_M, for different die geometries (σ_0=200 MPa, n=0.20 and t_0=1 mm): (a) dies with the value of the ratio $R_1/R_M \approx 0.17$; (b) all cases of die ratios under this study.

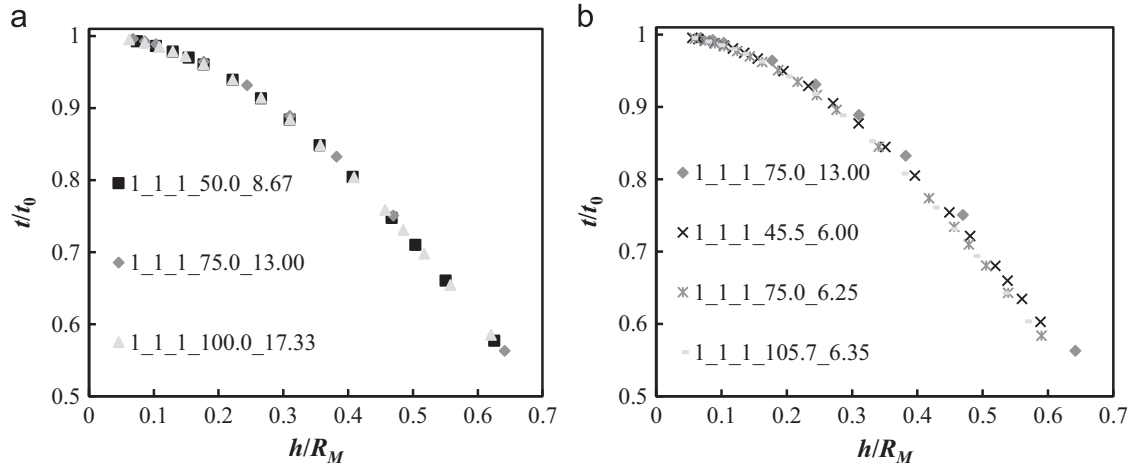

Fig. 13. Evolution of normalized sheet thickness, t/t_0, with normalized pole height, h/R_M, for different die geometries (σ_0=200 MPa, n=0.20 and t_0=1 mm): (a) dies with the value of the ratio $R_1/R_M \approx 0.17$; (b) all cases of die ratios under this study.

Table 4
Parameters obtained for the Eqs. (18), (20) and (21).

Eq. (18)		**Eq.** (20)		**Eq.** (21)	
a_1	0.411050	b_1	1.948236	c_1	1.750625
a_2	0.641438	b_2	2.419649	c_2	2.196396
a_3	0.226993	b_3	1.272563	c_3	2.472235
a_4	−1.017913	b_4	0.230658	c_4	5.829536
		b_5	0.774585	c_5	1.125865
				c_6	0.230658
				c_7	0.774585
R^2	0.9991	R^2	0.9980	R^2	0.9997

evaluated based on these variables. In this section some fundamental analytical equations are developed and proposed, relating curvature and thickness with pressure and bulge height. They will provide not only the possibility of using a simpler equipment for hardening curve determination, but specially a better theoretical understanding of the hydraulic bulge test and the relation among its main variables and material parameters.

As seen in the previous sections, the evolution of the normalized radius of curvature, ρ/R_M, with the normalized pole height, h/R_M, only depends of the work hardening coefficient, n, being independent of the yield stress of the material, σ_0, the anisotropy coefficient, r_α, and the initial sheet thickness, t_0. But, the evolution of the normalized thickness of the sheet at the pole, t/t_0, with the normalized pole height, h/R_M, depends on the work hardening coefficient, n, and on the anisotropic coefficient, r_α. In this context, an approach able to avoid the experimental measurements, and subsequent treatment, in order to determine the radius of curvature at the pole of the cap during the bulge test, must take into account the work hardening coefficient of the material, although it can be independent of the material yield stress, the anisotropy coefficient and the initial sheet thickness. At our knowledge, in the literature, the work hardening coefficient is not considered in equations relating the radius of curvature with the pole height. Therefore, none of the previously proposed equations adequately describe the current results. In this context, various types of equations for radius of curvature determination were fitted to the results of each group of materials in Fig. 5 (i.e. each n value). Among the best fits, the following type of power law was chosen, for its simplicity:

$$\frac{\rho}{R_M} = a_1 \left(\frac{h}{R_M}\right)^{a_2}, \tag{17}$$

where a_1 and a_2 are fitting parameters. The results show that the parameters a_1 and a_2 of these equations exhibit a quasi linear evolution with the work hardening coefficient, n. This knowledge leads to the choice of the equation, developed from Eq. (17), where

the work hardening coefficient is included in the fitting:

$$\frac{\rho}{R_M} = (a_1 n + a_2)\left(\frac{h}{R_M}\right)^{a_3 n + a_4}, \tag{18}$$

where a_1, a_2, a_3 and a_4 are the fitting parameters of the curve, and n is the work hardening coefficient of the material. Fitting this equation simultaneously to the three sets of results of Fig. 5 (n=0.05, 0.20 and 0.35), the following parameters were obtained, as it can see in Table 4.

In case of the sheet thickness at the pole, its evolution with the pole height shows a behavior dependent not only on the work hardening coefficient, as shown in Fig. 7, but also dependent on the anisotropy coefficient of the sheet, as shown in Fig. 10. At our knowledge, only the equation by Chakrabarty and Alexander [29] takes into account the work hardening coefficient when relating the sheet thickness with the pole height, although the influence of the anisotropy coefficient, r_α, is never considered. The equation by Chakrabarty and Alexander is written:

$$\frac{t}{t_0} = \left[\frac{1}{1+\left(\frac{h}{R_M}\right)^2}\right]^{2-n}. \tag{19}$$

Since this equation does not adequately describe the results of the current study, two types of equations, based on the proposed by Chakrabarty and Alexander but with a higher number of parameters, were fitted to results of materials with different values of work hardening coefficient (see Fig. 7) and anisotropy coefficient (see Fig. 10):

$$\frac{t}{t_0} = \left[\frac{1}{1+b_1\left(\frac{h}{R_M}\right)^{b_2}}\right]^{b_3 - x}, \tag{20}$$

and

$$\frac{t}{t_0} = \left[\frac{1}{1+c_1\left(\frac{h}{R_M}\right)^{c_2}+c_3\left(\frac{h}{R_M}\right)^{c_4}}\right]^{c_5 - y}, \tag{21}$$

where x and y are function not only of the work hardening coefficient, n, but also on the anisotropy coefficient, $r_\alpha = \bar{r}$, such that:

$$x = b_4 n\bar{r} + b_5 n \tag{22}$$

and

$$y = c_6 n\bar{r} + c_7 n. \tag{23}$$

In fact, the results in Figs. 7 and 10 show that the influence of the work hardening and anisotropy coefficients on the evolution of the normalized sheet thickness, t/t_0, with the normalized pole height, h/R_M, is similar (i.e. decreasing of n and r_α lowers the level of the curves t/t_0 *vs.* h/R_M), although having different magnitudes. Moreover, the influence of the anisotropy coefficient on this evolution decreases and seems to disappear when the value of the work hardening coefficient approaches to zero (see Fig. 10). The appropriateness of the Eqs. (20) and (21) for describing the evolution of t/t_0, during the bulge test, was analysed with resource to the results of tests with different values of work hardening and anisotropy coefficients, which showed that the fitted exponents (b_3 - x) and (c_5 - y) have a quasi-linear evolution with n and r_α; moreover, as the value of n decreases, the influence of r_α value on the value of the fitted exponents (b_3 - x) and (c_5 - y) decreases, approaching zero. Moreover, the values of the parameters b_1 and b_2, of Eq. (20), and c_1, c_2, c_3 and c_4, of Eq. (21), are stable regardless of the values of n and r_α. Fitting Eqs. (20) and (21) to the results of Figs. 7 and 10, the corresponding parameters are presented in Table 4.

Table 5
Parameters obtained for the Eqs. (24), (25) and (26).

Eq. (24)		**Eq.** (25)		**Eq.** (26)	
a_1	0.411050	b_1	−3.460113	c_1	−3.665349
a_2	0.551581	b_2	2.547989	c_2	2.385952
a_3	0.545831	b_3	2.419649	c_3	2.196396
a_4	0.226993	b_4	1.272563	c_4	2.472235
a_5	−0.356414	b_5	0.230658	c_5	5.829536
a_6	−0.956135	b_6	0.774585	c_6	1.125865
				c_7	0.230658
				c_8	0.774585
R^2	0.9996	R^2	0.9978	R^2	0.9992

Although Eq. (21) has a better correlation coefficient than Eq. (20), the latter is simpler and shows enough accuracy when applied to the determination of the work hardening curve, as it will be discussed below.

Finally, the evolution equations for the normalized radius of curvature and the thickness should take into account the value of the ratio R_1/R_M. Accordingly, the results in Figs. 12 and 13 were used. The appropriateness of the Eqs. (18), (20) and (21) for describing the evolutions of ρ/R_M and t/t_0, during the bulge test, was analysed for all cases of Figs. 12 and 13, which showed that the fitted parameters a_1 and a_3, in Eq. (18) are stable regardless of the values of R_1/R_M; the same occurs for the parameters b_1 in Eq. (20) and c_1 in Eq. (21). Moreover, the parameters a_1 and a_3, shows a quasi-linear evolution with R_1/R_M. This knowledge guide us to modify the Eqs. (18), (20) and (21) in order to include the ratio R_1/R_M. Therefore, Eq. (18) is now written:

$$\frac{\rho}{R_M} = \left(a_1 n + a_2\frac{R_1}{R_M} + a_3\right)\left(\frac{h}{R_M}\right)^{a_4 n + a_5\frac{R_1}{R_M} + a_6}, \tag{24}$$

where a_1, a_2, a_3, a_4, a_5 and a_6 are the fitting parameters. Fitting this equation simultaneously to the results of Fig. 12, the following parameters are obtained, as it can see in Table 5.

Eq. (20) now takes the following form:

$$\frac{t}{t_0} = \left[\frac{1}{1+\left(b_1\frac{R_1}{R_M}+b_2\right)\left(\frac{h}{R_M}\right)^{b_3}}\right]^{b_4 - n\left(b_5\bar{r}+b_6\right)}, \tag{25}$$

where b_1, b_2, b_3, b_4, b_5 and b_6 are the fitting parameters. Fitting this equation simultaneously to the results of Fig. 13, the following parameters are obtained, as it can see in Table 5.

Eq. (21) now takes the following form:

$$\frac{t}{t_0} = \left[\frac{1}{1+\left(c_1\frac{R_1}{R_M}+c_2\right)\left(\frac{h}{R_M}\right)^{c_3}+c_4\left(\frac{h}{R_M}\right)^{c_5}}\right]^{c_6 - n\left(c_7\bar{r}+c_8\right)}, \tag{26}$$

where c_1, c_2, c_3, c_4, c_5, c_6, c_7 and c_8 are the fitting parameters. Fitting this equation simultaneously to the results of Fig. 13, the following parameters are obtained, as it can see in Table 5.

In the next section, the performance of these equations is analysed and validated with resource to numerical results and multiple testing situations.

6. Analysis of the performance of the equations

In this chapter, the membrane theory (Eqs. (1) and (12)) is used to determine the stresses at the pole of the cap, at several moments of the numerical bulge test. In order to test the performance of the two sets of fitting equations for ρ/R_M and t/t_0, equivalent stress (determined using Eqs. (7), (10) or (13)) *versus* equivalent plastic strain (determined using Eqs. (8), (11) or (13))

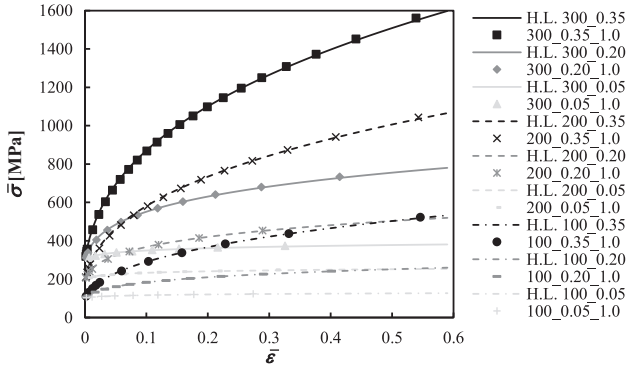

Fig. 14. Comparison between the hardening laws obtained by means of the membrane theory and direct measurements of ρ and t (symbols) and those used as input in the FE code (line), for the case of 1.0 mm thick sheets.

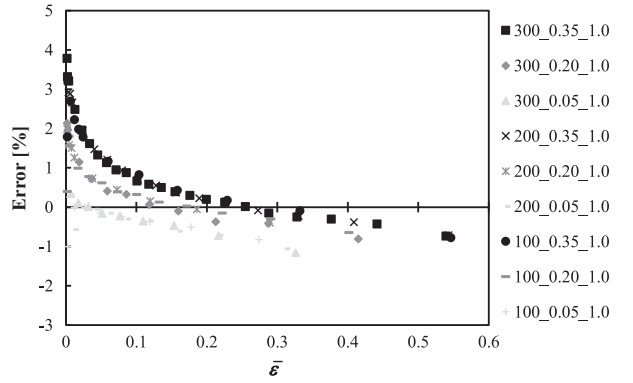

Fig. 15. Evolution of the error in equivalent stress obtained by means of the membrane theory and direct measurements of ρ and t, as a function of the equivalent strain in the pole, $\bar{\varepsilon}$, for the case of 1.0 mm thick sheets.

curves are plotted. As a reference, the usual experimental procedure to obtain these curves, which consists on the direct measurement of ρ and t values during the test, is also analysed. For both cases, the equivalent strain values are obtained from the values of ε_1 and ε_2 directly measured at the top of the cap; the elastic part of the strain tensor was removed, using Eq. (15). The corresponding work hardening curves are compared with the hardening curve used as input (H.L. – Hardening Law) in the numerical simulations. The label "_1a" in the figures corresponds to the use of Eq. (24), for the radius of curvature, together with Eq. (25) of sheet thickness, and "_2a" to Eq. (24), for the radius of curvature, with Eq. (26), for the sheet thickness.

6.1. Isotropic materials

At first, the results of ρ and t obtained by direct measurement and presented in Figs. 4, 6, 9 and 10 (corresponding to materials in Table 2) were used for determining of the stress at the pole of the cap, at different moments of the test. Fig. 14 compares these results with the equivalent stress *versus* equivalent plastic strain curves with those used as input (H.L.) in the numerical simulations, for the case of 1.0 mm thick sheets. A good correspondence is observed, for all materials.

Fig. 15 shows the error in equivalent stress obtained from the results in Fig. 14, defined as $\text{Error} = (\bar{\sigma}_{HL} - \bar{\sigma}_{MT})/\bar{\sigma}_{HL}$ (where $\bar{\sigma}_{HL}$ and $\bar{\sigma}_{MT}$ are the equivalent stresses of the input hardening curve and the one determined by the membrane theory, respectively). For lower equivalent plastic strain values, the error in the estimated equivalent stress can be relatively high (mainly in cases of materials with work hardening coefficient equal to 0.35). In fact,

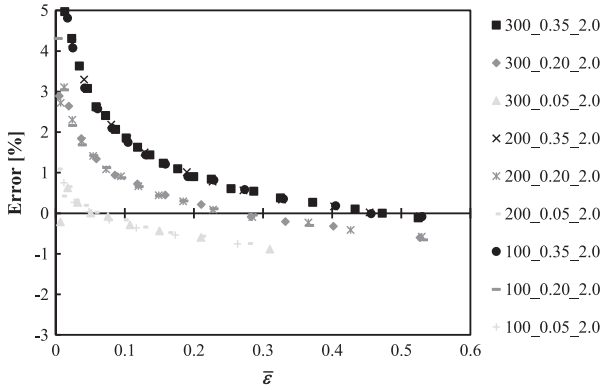

Fig. 16. Evolution of the error in equivalent stress obtained by means of the membrane theory and direct measurements of ρ and t, as a function of the equivalent strain in the pole, $\bar{\varepsilon}$, for the case of 2.0 mm thick sheets.

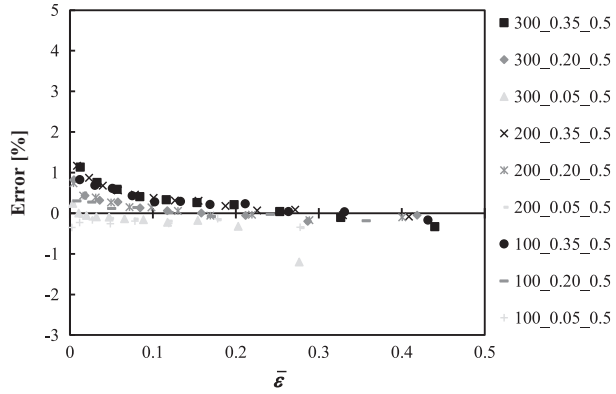

Fig. 17. Evolution of the error in equivalent stress obtained by means of the membrane theory and direct measurements of ρ and t, as a function of the equivalent strain in the pole, $\bar{\varepsilon}$, for the case of 0.5 mm thick sheets.

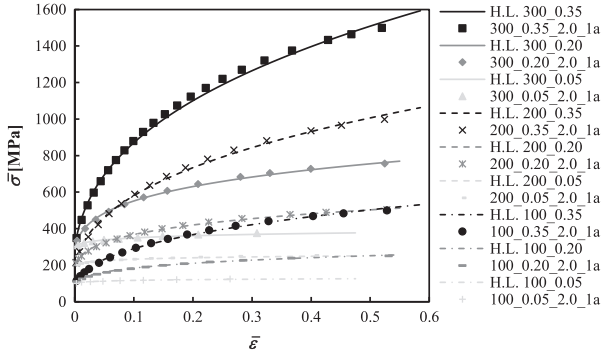

Fig. 18. Comparison between the hardening laws obtained by means of the membrane theory and using Eqs. (24) and (25) (symbols) with those used as input in the FE code (line), for the case of 2.0 mm thick sheets.

for stress values close to the yield stress, the cap has a high value of the radius of curvature at the pole (see Fig. 4), and so the associated errors can induce relatively high errors in stress. Nevertheless, the error in equivalent stress does not exceed 4%, and for strain values higher than 0.015, the error is always lower than about 2.5%.

For all cases of isotropic materials and sheet thickness, the evolution of the error in equivalent stress shows the same trend: positive for lower equivalent strain values and changing to negative values for higher values of strain, as shown in Figs. 16 and 17 for the cases of sheet thickness equal to 2.0 and 0.5 mm, respectively. The maximum error in stress, of about 7.2%, was obtained at

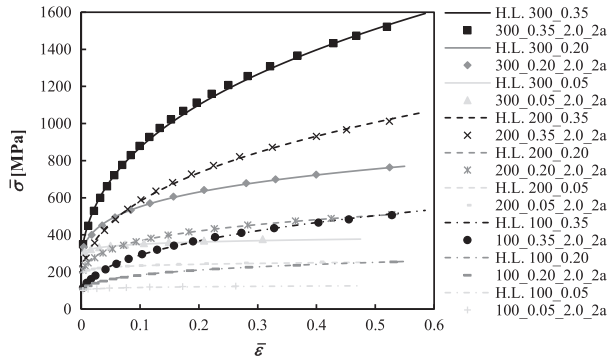

Fig. 19. Comparison between the hardening laws obtained by means of the membrane theory and using Eqs. (24) and (26) (symbols) with those used as input in the FE code (line), for the case of 2.0 mm thick sheets.

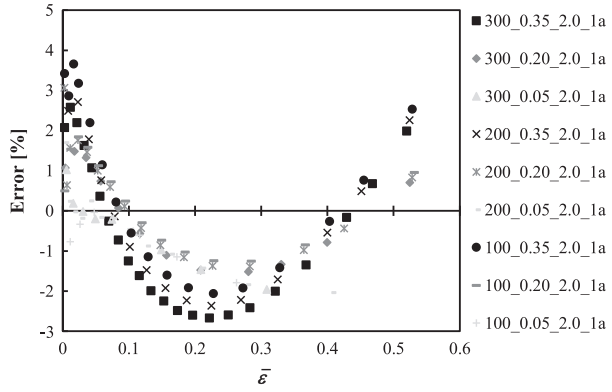

Fig. 20. Evolution of the error in equivalent stress obtained by means of the membrane theory and using Eqs. (24) and (25) as a function of the equivalent strain in the pole, $\bar{\varepsilon}$, for the case of 2.0 mm thick sheets.

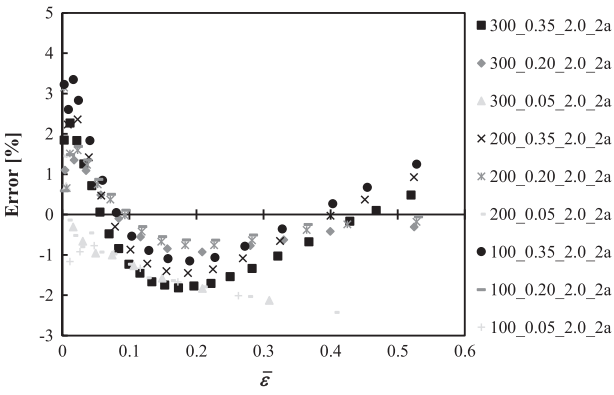

Fig. 21. Evolution of the error in equivalent stress obtained by means of the membrane theory and using Eqs. (24) and (26) as a function of the equivalent strain in the pole, $\bar{\varepsilon}$, for the case of 2.0 mm thick sheets.

the beginning of the test for the case of the initial sheet thickness of 2.0 mm (Fig. 16). At the end of the test, the error in stress never exceeds 1.2%, whatever the material and the sheet thickness (Fig. 16). For the initial sheet thickness of 0.5 mm, the error in stress is always less than 1.5%, and after 0.10 of equivalent strain is even inferior to 0.5%, at the end of the test. The lowest error for the smallest thickness (0.5 mm) is justified by the fact that very thin sheet are closer to membrane behavior and membrane theory.

The equations for ρ/R_M (Eq. (24)) and t/t_0 (Eqs. (25) and (26)), proposed in the last chapter, were also used for determining the equivalent stress at different moments of the test. The following examples only concern the 2 mm thick sheets that exhibited the lowest accuracy of results, as in previous cases (see Figs. 15, 16 and

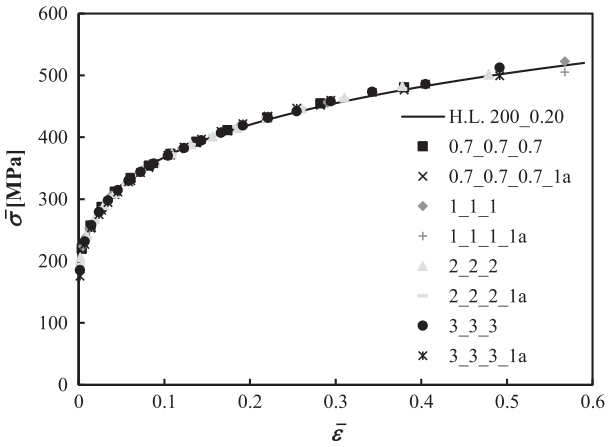

Fig. 22. Work hardening law used as input in the numerical simulation (line) and results obtained by membrane theory using direct measurement of ρ and t (symbols), and using Eqs. (24) and (25) (symbols "_1a"), for transverse anisotropic materials (σ_0=200 MPa, n=0.20 and t_0=1 mm).

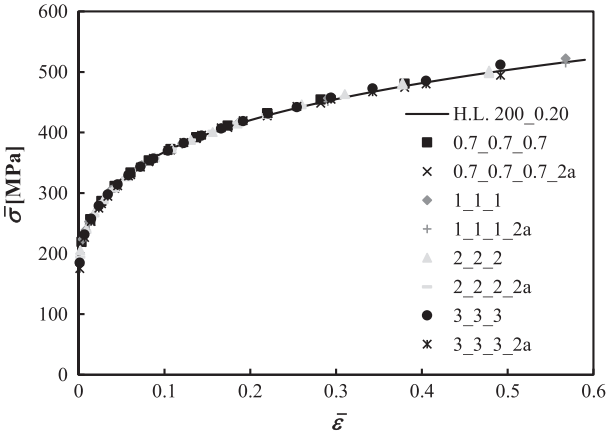

Fig. 23. Work hardening law used as input in the numerical simulation (line) and results obtained by membrane theory using direct measurement of ρ and t (symbols), and using Eqs. (24) and (26) (symbols "_2a"), for transverse anisotropic materials (σ_0=200 MPa, n=0.20 and t_0=1 mm).

17). Figs. 18 and 19 show the comparison between the hardening laws (H.L.), used as input in numerical simulation of the bulge test, and the results obtained using the membrane theory together with the Eqs. (24) and (25) (Fig. 18), and with the Eqs. (24) and (26) (Fig. 19) for calculation of the equivalent stress, $\bar{\sigma}$. Figs. 20 and 21 show the evolution of the error, in equivalent stress with equivalent strain, which corresponds to Figs. 18 and 19, respectively.

The comparison of Figs. 20 and 21 shows that, in this last case, the errors are slightly smaller than the former case. Moreover, the comparison of these figures with Fig. 16 shows that the maximum errors obtained using both sets of the fitted equations are lower than those obtained from direct measurement (Figs. 20 and 21). In cases of thicknesses of 0.5 and 1.0 mm, the errors obtained using both sets of equations, although not shown here, lead to the same conclusion, i.e. the errors are of the same magnitude or slightly lower (at the beginning of the test) when compared to direct measurement.

6.2. Materials with transverse anisotropy

The materials with transverse anisotropy in the sheet plane, i.e. with $r_0=r_{45}=r_{90}$, which parameters of the Hill'48 criterion are shown in Table 3, were also analysed. The hardening behavior of

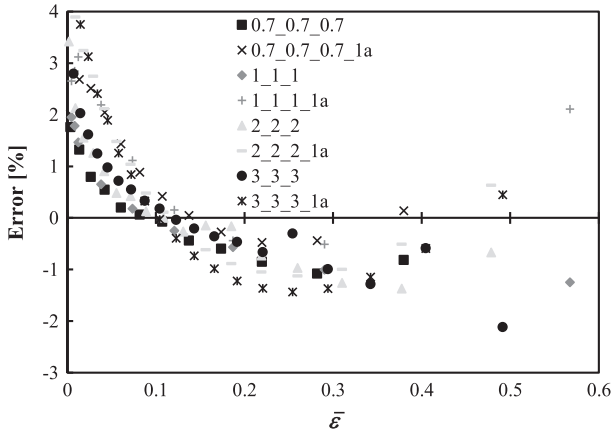

Fig. 24. Comparison of the evolution of the error in equivalent stress obtained by membrane theory using direct measurement of ρ and t (symbols), and using Eqs. (24) and (25) (symbols "_1a"), for transverse anisotropic materials (σ_0=200 MPa, n=0.20 and t_0=1 mm).

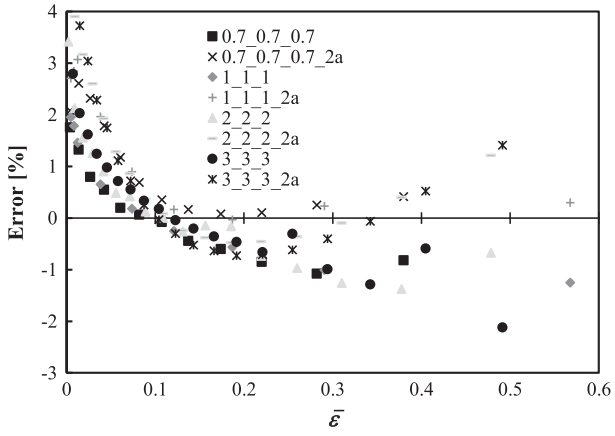

Fig. 25. Comparison of the evolution of the error in equivalent stress obtained by membrane theory using direct measurement of ρ and t (symbols), and using Eqs. (24) and (26) (symbols "_2a"), for transverse anisotropic materials (σ_0=200 MPa, n=0.20 and t_0=1 mm).

the materials is described by the Swift law (Eq. (16)), and includes materials with mechanical properties defined in Table 2 having the initial sheet thickness of 1 mm.

Figs. 22 and 23 show example of the results of the equivalent stress *versus* equivalent strain curves: (i) used as input in the numerical test; (ii) in which the equivalent stress was obtained from Eq. (7), using the membrane theory (Eq. (12) and direct measurement of ρ and t (iii) in which the equivalent stress was obtained from Eq. (7), using the membrane theory together with Eqs. (24) and (25) (Fig. 22) or Eqs. (24) and (26) (Fig. 23). The strain values, to enter into the Eq. (8), were obtained from the numerical simulations, at the pole of the cap. This procedure will be also applied in the following sub-sections. Figs. 24 and 25 show the evolution of the error in equivalent stress with the equivalent strain, corresponding to the Figs. 22 and 23.

The analysis of Figs. 24 and 25 show that the errors in equivalent stress when using both sets of equations are similar to those obtained from the direct measurement of the radius of curvature and the sheet thickness, except for the case of material with the isotropy parameter equal to 3. In this case, the direct measurement of the radius of curvature and the sheet thickness leads to a slightly lower error until values of equivalent strain of about 10%. Both set of equations lead to identical results.

Table 6
Designation of the materials, their respective parameters of Hill'48 criterion and ratio σ_b/σ_0.

Designation	Parameters of the Hill'48 Criterion						
	F	*G*	*H*	*L*	*M*	*N*	σ_b/σ_0
0.6_3_0.6	0.625	0.625	0.375	1.500	1.500	4.375	0.894
3_0.6_3	0.250	0.250	0.750	1.500	1.500	0.550	1.414
1.5_3_1.5	0.400	0.400	0.600	1.500	1.500	2.800	1.118
3_1.5_3	0.250	0.250	0.750	1.500	1.500	1.000	1.414
0.6_0.7_0.8	0.469	0.625	0.375	1.500	1.500	1.313	0.956
0.6_1.8_3	0.125	0.625	0.375	1.500	1.500	1.725	1.155
1.5_2.25_3	0.200	0.400	0.600	1.500	1.500	1.650	1.291
1.5_2.75_4	0.150	0.400	0.600	1.500	1.500	1.788	1.349

6.3. Planar anisotropic materials

The equations that describe the evolutions of radius of curvature and the sheet thickness during the test were also tested in case of sheets with planar anisotropy. The parameters of the Swift hardening law, for the materials studied in this section, are: yield stress, σ_0=200 MPa, work hardening coefficient, n=0.20. The elastic properties of the material are: Young's modulus E =210 GPa and Poisson's ratio ν=0.30. The initial thickness of the sheet is 1 mm.

Table 6 shows the designation adopted for each material, the parameters of the Hill'48 criterion and the ratio σ_b/σ_0 (where σ_b and σ_0 are the yield stress in biaxial and uniaxial tension). The designation A_B_C corresponds to a material with the anisotropy coefficient, r_α, in the sheet plane such that: r_0=A, r_{45}=B and r_{90}=C. The selected materials for this study display two different types of anisotropy such that: (i) $r_0=r_{90} \neq r_{45}$, corresponding to the first four materials in Table 6; (ii): $r_0 \neq r_{45} \neq r_{90}$, corresponding to the last four materials in Table 6. The condition $G+H=1$ is assumed for the parameters of the Hill'48 criterion, which means that the work hardening law is equal to the tensile curve along the rolling direction [28], providing that σ_0, n and ε_0 are the same.

In order to better describe the anisotropic state of the materials in Table 6, Figs. 26 and 27 show the evolution of the anisotropy coefficient, r_α, and of the ratio $\sigma_\alpha^0/\sigma_0^0$ between the yield stress, σ_α^0, for an angle, α, in the sheet plane, and the yield stress along Ox, σ_0^0, as a function of α angle, for materials with $r_0=r_{90} \neq r_{45}$ and for materials with $r_0 \neq r_{45} \neq r_{90}$, respectively.

In case of metal sheets with planar anisotropy, the value of $\bar{r}$ in Eqs. (25) and (26) is assumed as the normal anisotropy coefficient:

$$\bar{r}=\frac{r_0+2r_{45}+r_{90}}{4}. \quad (27)$$

6.3.1. Materials with $r_0=r_{90} \neq r_{45}$

The analysis of the materials with anisotropy behavior having $r_0=r_{90} \neq r_{45}$, is presented in this section. Figs. 28 and 29 show examples of the results of the equivalent stress *versus* equivalent strain curves: (i) used as input in the numerical test; (ii) in which the equivalent stress was obtained using the membrane together with Eqs. (24) and (25) as in Fig. 28; (iii) and in which the equivalent stress were obtained using the membrane together with Eqs. (24) and (26) as in Fig. 29. Figs. 30 and 31 show the evolution of the error in equivalent stress with the equivalent strain, corresponding to the Figs. 28 and 29.

Figs. 30 and 31 show that the errors in equivalent stress when using both sets of equations are similar to those obtained from the direct measuring of the radius of curvature and the sheet thickness determination, except at the beginning of the deformation, where the direct measuring of the radius of curvature and the sheet

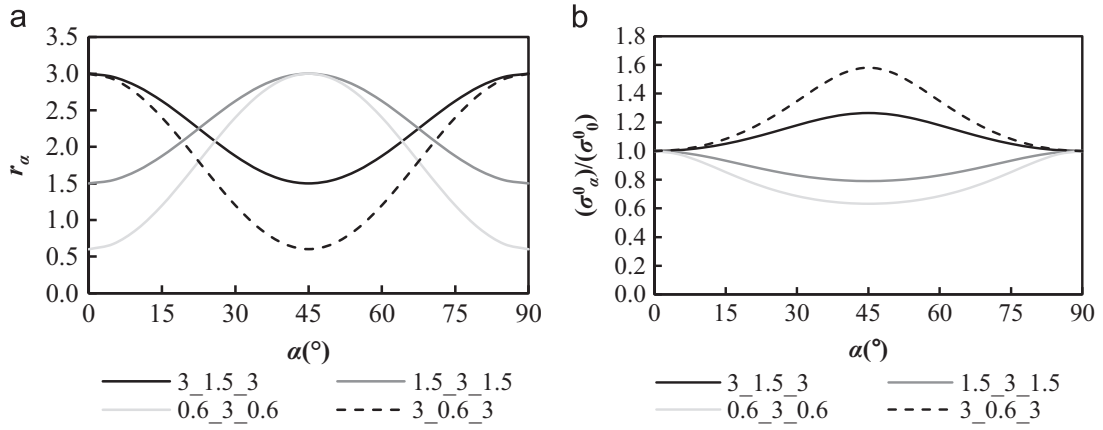

Fig. 26. Distribution of r_α and $\sigma^0_\alpha/\sigma^0_0$ in the sheet plane, for materials with anisotropy such that $r_0=r_{90}\neq r_{45}$.

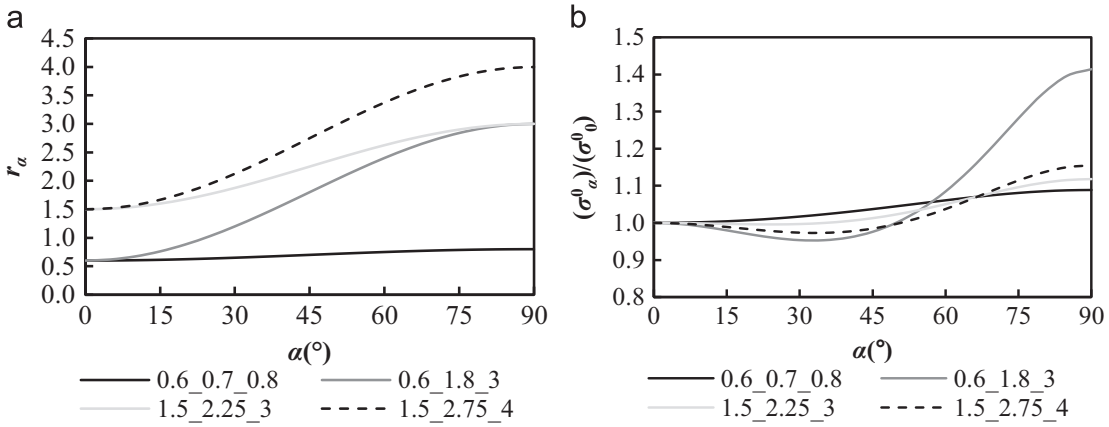

Fig. 27. Distribution of r_α and $\sigma^0_\alpha/\sigma^0_0$ in the sheet plane, for materials with anisotropy such that $r_0\neq r_{45}\neq r_{90}$.

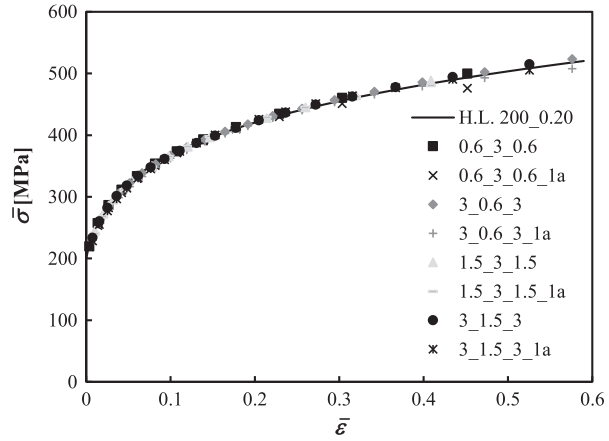

Fig. 28. Work hardening law used as input in the numerical simulation (line) and results obtained by membrane theory using direct measurement of ρ and t (symbols), and using Eqs. (24) and (25) (symbols with "_1a"), for sheet metals with $r_0=r_{90}\neq r_{45}$ ($\sigma_0=200$ MPa, $n=0.20$ and $t_0=1$ mm).

thickness allows obtaining a slightly lower error in stress (up to values of equivalent strain of about 0.10). Also it is seen that both set of equations give identical results.

The errors obtained with the fitting equations and by direct measurement of the radius of curvature and sheet thickness are identical during the test for the materials 1.5_3_1.5 and 3_1.5_3; in the case of the remaining two anisotropic behaviors the error tends to increase after 0.20 of equivalent plastic strain but nevertheless, this error does not exceed 3.5%.

6.3.2. *Materials with $r_0\neq r_{45}\neq r_{90}$*

The results of materials with anisotropy behavior having $r_0\neq r_{45}\neq r_{90}$, is presented in this section. Figs. 32 and 33 show examples of equivalent stress *versus* equivalent strain curves, comparing the results obtained using the direct measurement with the ones: (i) used as input in the numerical test; (ii) obtained by the membrane theory together with Eqs. (24) and (25) as in Fig. 32; and (iii) obtained by the membrane theory together with Eqs. (24) and (26) as in Fig. 33. Figs. 34 and 35 show the evolution of the error in equivalent stress with the equivalent strain, corresponding to results of Figs. 32 and 33.

Figs. 34 and 35 show that the errors in equivalent stress when using both sets of equations are similar to those obtained from the direct measuring of the radius of curvature and the sheet thickness determination, except at the beginning of the deformation, where the direct measuring of the radius of curvature and the sheet thickness gives a slightly lower error (up to values of equivalent strain of about 0.10). Again it is seen that both set of equations lead to identical results.

The errors obtained with the fitting equations and the direct measurement of the radius of curvature and sheet thickness are identical during the test for the materials 0.6_0.7_0.8 and 0.6_1.8_3; in the case of the remaining two anisotropic behaviors the error tends to increase after 0.20 of equivalent plastic strain but nevertheless, this error does not exceed 2.5%.

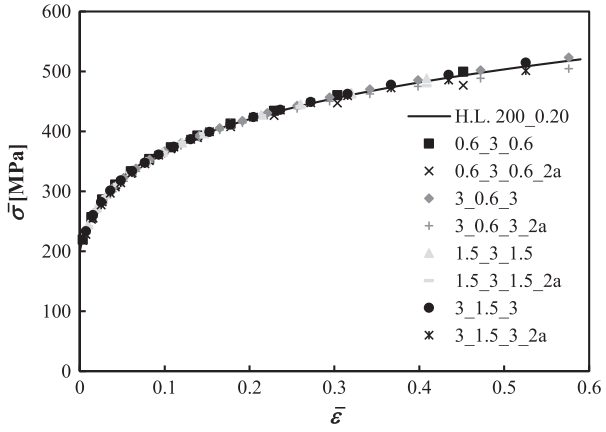

Fig. 29. Work hardening law used as input in the numerical simulation (line) and results obtained by membrane theory using direct measurement of ρ and t (symbols), and using Eqs. (24) and (26) (symbols with "_2a"), for sheet metals with $r_0=r_{90} \neq r_{45}$ ($\sigma_0=200$ MPa, $n=0.20$ and $t_0=1$ mm).

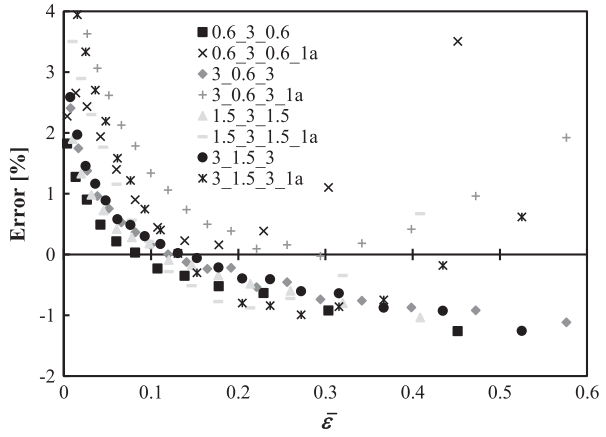

Fig. 30. Comparison of the evolution of the error in equivalent stress obtained by membrane theory using direct measurement of ρ and t (symbols), and using Eqs. (24) and (25) (symbols with "_1a"), for sheet metals with $r_0=r_{90} \neq r_{45}$ ($\sigma_0=200$ MPa, $n=0.20$ and $t_0=1$ mm).

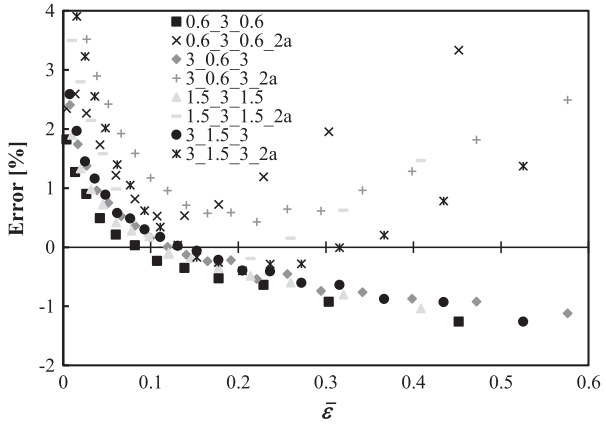

Fig. 31. Comparison of the evolution of the error in equivalent stress obtained by membrane theory using direct measurement of ρ and t (symbols), and using Eqs. (24) and (26) (symbols with "_2a"), for sheet metals with $r_0=r_{90} \neq r_{45}$ ($\sigma_0=200$ MPa, $n=0.20$ and $t_0=1$ mm).

6.4. Different die ratio geometries

The analysis in this section is performed for two materials, an isotropic material with designation "1_1_1_R_M_R_1" and an anisotropic material with designation "1.5_2.75_4 _R_M_R_1", where R_M is the die radius and R_1 is the die profile radius. The following examples use 1 mm thick sheets for the both materials.

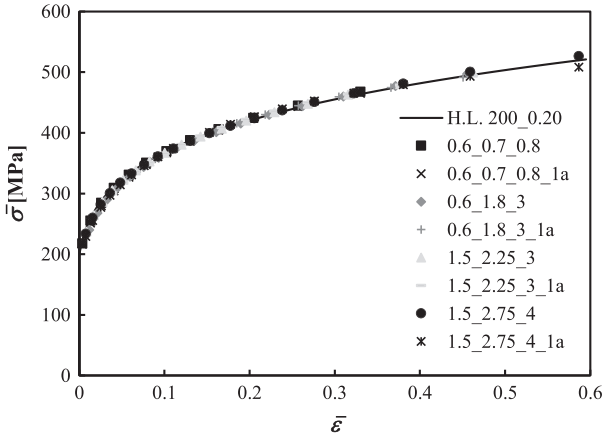

Fig. 32. Work hardening law used as input in the numerical simulation (line) and results obtained by membrane theory using direct measurement of ρ and t (symbols), and using Eqs. (24) and (25) (symbols with "_1a"), for sheet metals with $r_0 \neq r_{45} \neq r_{90}$ ($\sigma_0=200$ MPa, $n=0.20$ and $t_0=1$ mm).

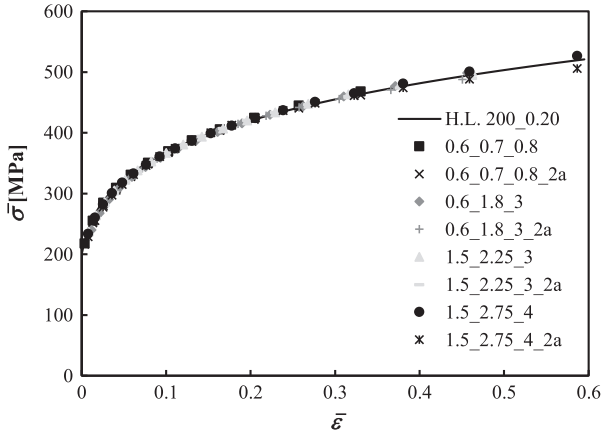

Fig. 33. Work hardening law used as input in the numerical simulation (line) and results obtained by membrane theory using direct measurement of ρ and t (symbols), and using Eqs. (24) and (26) (symbols with "_2a"), for sheet metals with $r_0 \neq r_{45} \neq r_{90}$ ($\sigma_0=200$ MPa, $n=0.20$ and $t_0=1$ mm).

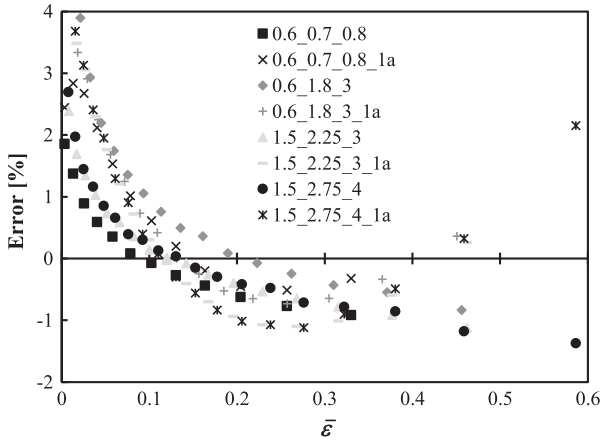

Fig. 34. Comparison of the evolution of the error in equivalent stress obtained by membrane theory using direct measurement of ρ and t (symbols), and using Eqs. (24) and (25) (symbols with "_1a"), for sheet metals with $r_0 \neq r_{45} \neq r_{90}$ ($\sigma_0=200$ MPa, $n=0.20$ and $t_0=1$ mm).

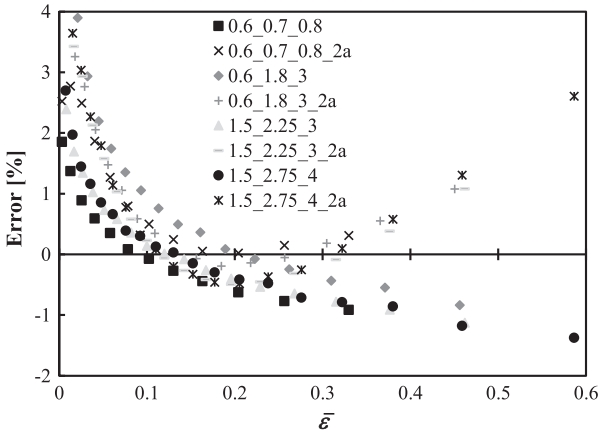

Fig. 35. Comparison of the evolution of the error in equivalent stress obtained by membrane theory using direct measurement of ρ and t (symbols), and using Eqs. (24) and (26) (symbols with "_2a"), for sheet metals with $r_0 \neq r_{45} \neq r_{90}$ (σ_0=200 MPa, n=0.20 and t_0=1 mm).

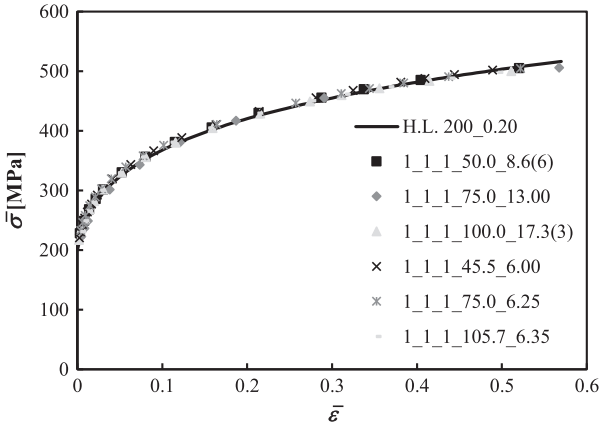

Fig. 36. Work hardening law used as input in the numerical simulation (line) and results obtained by membrane theory using Eqs. (24) and (25) (symbols), for isotropic material with different die geometries (σ_0=200 MPa, n=0.20 and t_0=1 mm).

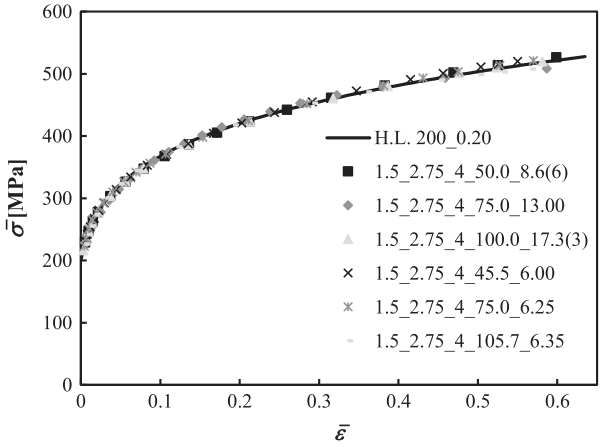

Fig. 37. Work hardening law used as input in the numerical simulation (line) and results obtained by membrane theory using Eqs. (24) and (25) (symbols), for anisotropic material with different die geometries (σ_0=200 MPa, n=0.20 and t_0=1 mm).

In this section, it is only analysed the performance of the Eq. (24), for the radius of curvature, with Eq. (25), for the sheet thickness, since this last equation is simpler than Eq. (26) and the results presented in the previous sections show no significant differences.

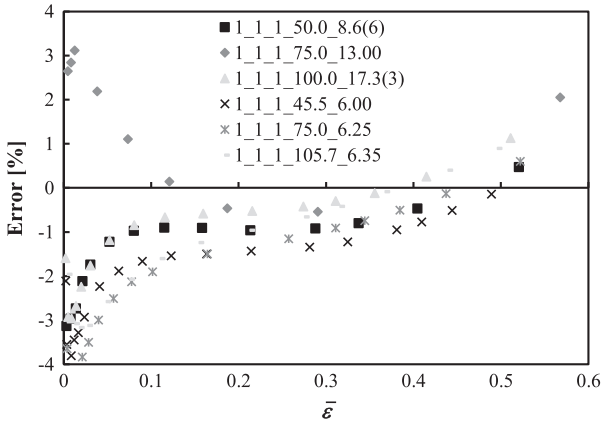

Fig. 38. Evolution of the error in equivalent stress obtained by membrane theory using Eqs. (24) and (25), as a function of the equivalent strain in the pole, $\bar{\varepsilon}$, for isotropic material with different die geometries (σ_0=200 MPa, n=0.20 and t_0=1 mm).

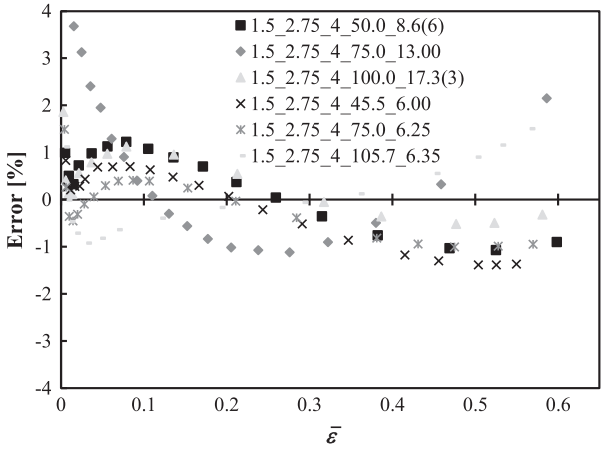

Fig. 39. Evolution of the error in equivalent stress obtained by membrane theory using Eqs. (24) and (25), as a function of the equivalent strain in the pole, $\bar{\varepsilon}$, for anisotropic material with different die geometries (σ_0=200 MPa, n=0.20 and t_0=1 mm).

Figs. 36 and 37 show examples of the equivalent stress *versus* equivalent strain for the isotropic material and for the anisotropic material with comparison between: (i) as used in input for numerical test, the hardening law (H.L.); (ii) with the equivalent stress were obtained using the membrane theory together with Eqs. (24) and (25).

Figs. 38 and 39 show the evolution of the error in equivalent stress with the equivalent strain, corresponding to Figs. 36 and 37, respectively.

Figs. 38 and 39 show that, for each material, the error has almost identical behavior for every different die, whatever the geometry. Only for the geometry (75.0_13.00), the error evolution is different from the other die geometry. In case of Fig. 39, the error for the geometry (75.0_13.00) is slightly higher than the others at the beginning of the test.

The errors obtained with the fitting equations for the case of isotropic material is relatively high at the beginning of the test, of the order of 4.5%, but tends to decrease as the deformation of the test increase. In case of the anisotropic material, the error at the beginning is 4.5%, but decreases quickly to 2.5% for a strain of about 0.05. As the test continues the error tends to increase up to a maximum of 2.2% in stress. The maximum error in stress for these materials is about 4.5%, being obtained at the beginning of the test. At the end of the test, the error in stress never exceeds 3%, whatever the material and die configuration. Based on this analysis it seems possible to conclude that it is viable to determine the

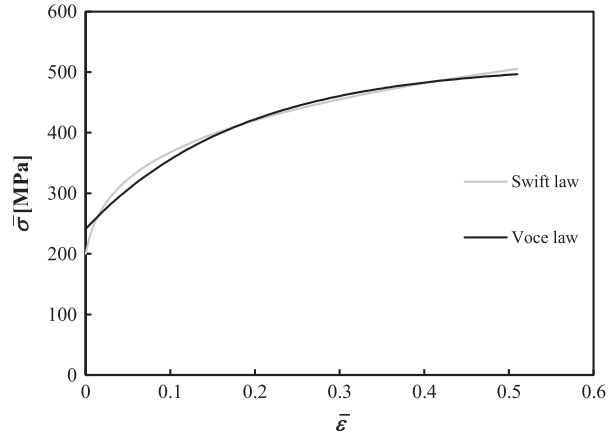

Fig. 40. Swift and Voce laws used in this section that fit to one another.

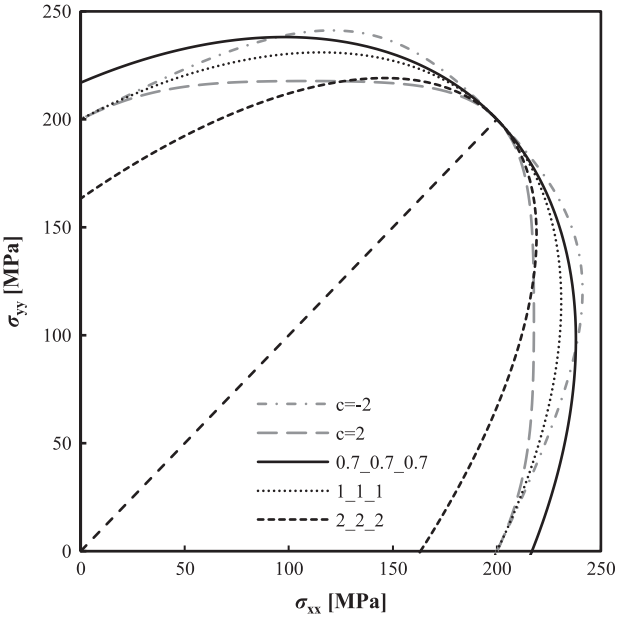

Fig. 41. Yield surfaces in plane (σ_{xx}; σ_{yy}), for the Hill'48 criterion, with $r=0.7$, 1 and 2, and for the Drucker criterion, with $c=2$ and -2.

work hardening curve using the proposed equations for different configuration of dies, whatever the material being considered.

6.5. Other yield criterion and hardening law

In this section, the performance of the equations is tested for materials whose behavior is described by constitutive models, not including the Swift law and/or the Hill'48 criterion, in order to test under which conditions the Eqs. (24), (25) (or (26)) can be applied to these materials. In fact, the behavior of materials such as aluminium alloys can be better described by a saturation hardening law and a non-quadratic yield criterion. The selected constitutive model includes the Voce law [30] and the Drucker's yield criterion [31].

The Voce law does not contain a hardening parameter with the same meaning as the Swift law, as required for using Eqs. (24) and (25) (or (26)). To overcome this difficulty the Swift law can be fitted to the experimental results, even though they are best fitted by the Voce law. In the current example, a Swift law is fitted to the Voce law, in order to obtain an approximated hardening parameter, n, to be used in the equations. The Voce law can be written as:

$$\overline{\sigma} = \sigma_{sat} - R_{sat}\exp(-c_y\varepsilon) \tag{28}$$

where σ_{sat}, R_{sat} and c_y are materials parameters; the yield stress is $\sigma_0=\sigma_{sat}$ - R_{sat}. In the current illustrative example the values of these parameters are: $\sigma_{sat}=513.17$ MPa, $R_{sat}=272.08$ and $c_y=5.47$. The parameters of the fitted Swift law are: $\sigma_0=200.00$ MPa; $K=577.08$ and $n=0.20$. Fig. 40 compare both laws.

The purpose of testing the use of Eqs. (25) (or (26)), in case the material behavior is not well described by the criterion Hill'48, relates to the change of the yield surface shape in the region around biaxial stress (corresponding to the stress paths observed in circular bulge tests), for a given value of the anisotropic coefficient. To clarify this issue, the Drucker's isotropic yield criterion is used with c values equal to 2 and -2, which severely change the shape of the yield surface in the biaxial region, relative to the material 1_1_1, (see Table 3) as shown in Fig. 41 for the yield surface plotted in plane (σ_{xx} ; σ_{yy}). In this figure the 0.7_0.7_0.7 and 2_2_2 materials are also shown. For $c=2$, the shape of the yield surface in this region approximates (from the outside) to the Hill'48 criterion with $r>1$ (2_2_2 material), and for $c=-2$, approximates (from the inside) to Hill'48 with $r<1$ (0.7_0.7_0.7 material). This is in agreement with the pressure *vs.* pole height evolutions shown in Fig. 42 for these materials, whose hardening behavior is described by the Swift law ($\sigma_0=200.00$ MPa; $K=577.08$ MPa and $n=0.20$). Fig. 42(a) shows that the curves are close to each other, whatever the material. However, the detail of the middle region of the curves (Fig. 42 (b)) shows that there are differences between them. In cases of Hill'48 material with $r=2.0$ (2_2_2 material) and Drucker material with $c=2$, the curves are close to each other and their level is lower than 1_1_1 curve. In cases of Drucker material with $c=-2$ and Hill'48 material with $r=0.7$ (0.7_0.7_0.7 material), the level of the curves is higher than 1_1_1 curve; the curve for $c=-2$ has the highest level.

The next figures show the stress *vs.* strain results and the corresponding error in stress, obtained by using Eqs. (24) and (25) for different configurations of the constitutive model (hardening law - yield criteria): (i) Voce – Hill'48, in Fig. 43; (ii) Swift - Drucker (with $c=2$ and -2), in Fig. 44; (iii) Voce – Drucker (with $c=2$ and -2), in Fig. 45. For comparison, the error obtained for the traditional procedure, by direct measurement of the radius of curvature and strain values are also shown in each figure.

In all cases (Voce – Hill'48, Swift - Drucker and Voce – Drucker) the maximum absolute value of the error in stress is less than 4%, which is of the same order as in case of Swift - Hill'48 materials (see previous sections), although the use of the proposed equations leads to errors in stress slightly higher than by direct measurement of the curvature radius and strains. Nevertheless, the results show that small variations in the values of the hardening and anisotropy coefficients, as those arising from the fact that the material behavior is not well described by the Swift law and Hill'48 criteria, does not significantly alter the results of Eqs. (24) and (25). That is, these equations can be used for these materials, within an acceptable accuracy.

7. Experimental validation

Examples of experimental results available in the literature concerning the evolutions of radius of curvature and sheet thickness during the bulge test are compared to the equations previously defined and others from literature (Section 7.1). Moreover, the bulge test was performed using two materials with the die geometry 75.0_13.00. This allows the performance analysis of the proposed equations when determining the hardening curve of materials (Section 7.2).

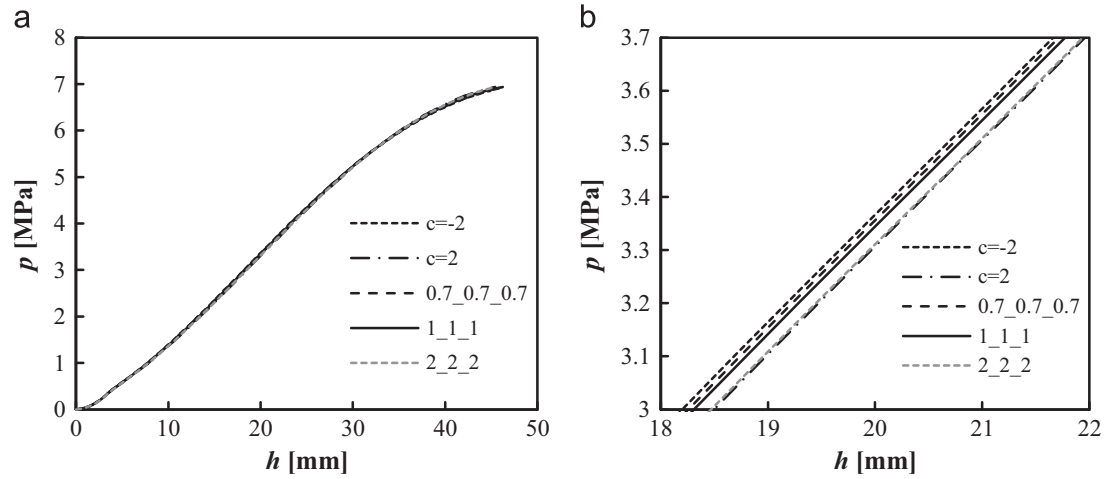

Fig. 42. (a) Evolution of pressure with the pole height for the materials with yield surfaces described in Fig. 41 and hardening behavior described by Swift law (σ_0=200.00 MPa; K=577.08 MPa and n=0.20); (b) detail of middle region.

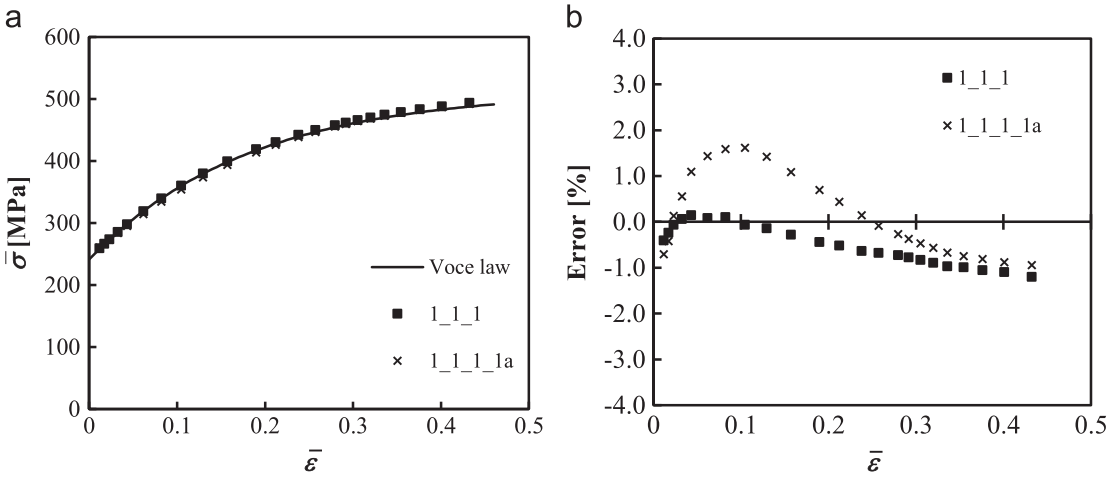

Fig. 43. (a) Stress *vs.* strain curves and (b) error in stress, for the Voce – Hill'48 material, by using Eqs. (24) and (25) (symbols "_1a"). The results obtained by direct measurement of the radius of curvature and strain values are also shown, for comparison (symbols).

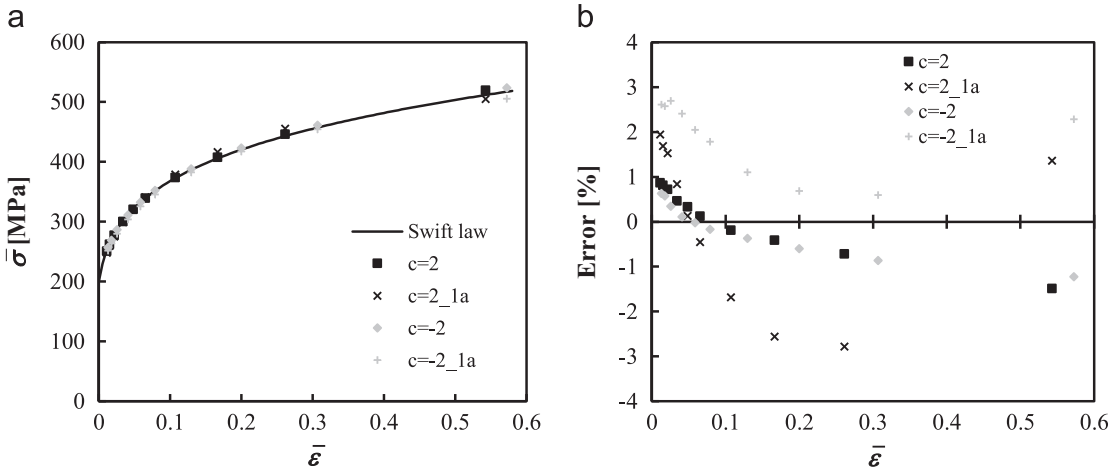

Fig. 44. (a) Stress *vs.* strain curves and (b) error in stress, for the Swift – Drucker materials, by using Eqs. (24) and (25) (symbols "_1a"). The results obtained by direct measurement of the radius of curvature and strain values are also shown, for comparison (symbols).

7.1. Results in literature of ρ and t

The equations for the evolution of the normalized radius of curvature (ρ/R_M) and the normalized sheet thickness (t/t_0) with the normalized pole height (h/R_M), are now compared with some examples of experimental results available in the literature. In this context, some existing results for bulge test involving five die geometries and nine materials are analysed, as shown in Table 7.

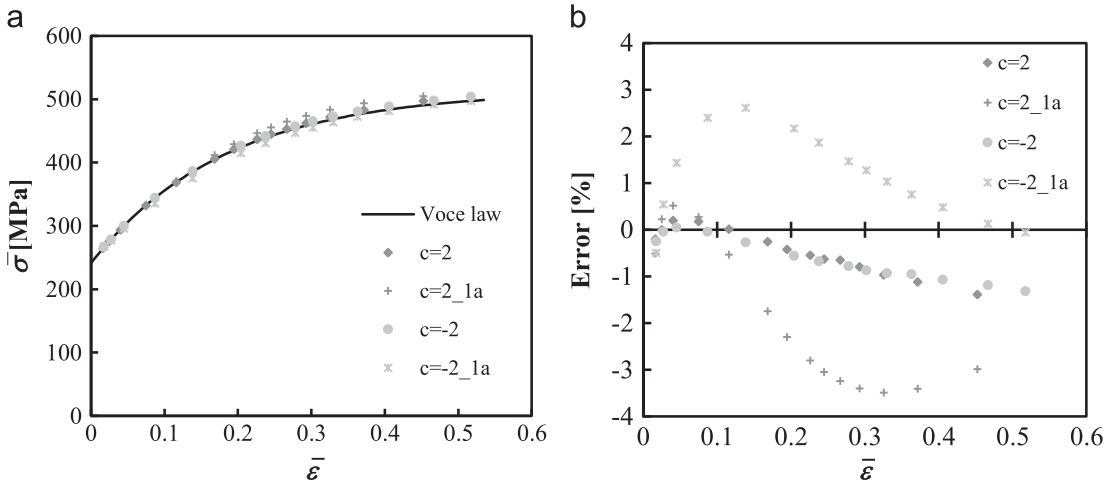

Fig. 45. (a) Stress *vs.* strain curves and (b) error in stress, for the Voce – Drucker materials, by using Eqs. (24) and (25) (symbols "_1a"). The results obtained by direct measurement of the radius of curvature and strain values are also shown, for comparison (symbols).

Table 7
Designation of the dies geometries and materials for experimental validation.

Die designation	R_M[mm]	R_1[mm]	R_1/R_M	Material (Designation)	t_0[mm]	n^a	$\bar{r}$
75.0_1.00 [32]	75.0	1.00	0.01	Mild Steel (MS)	1.00	0.24	1.57
50.0_6.50 [8]	50.0	6.50	0.13	AA5754 Aluminium alloy (AA5754)	1.00	0.35	0.67
50.0_6.50 [8]	50.0	6.50	0.13	AISI 201 Steel (AISI 201)	0.55	0.49	1.10
50.0_6.50 [8]	50.0	6.50	0.13	AA5754 Aluminium alloy at 260 ºC (AA5754_260)	1.00	0.31	0.67
50.0_6.50 [8]	50.0	6.50	0.13	AISI 201 Steel at 150 ºC (AISI 201_150)	0.55	0.39	1.10
35.0_4.50 [33]	35.0	4.50	0.13	AA2024-T3 Aluminium alloy (AA2024-T3)	0.30	0.15	0.88
45.0_6.00 [33]	45.0	6.00	0.13	Ti-6Al-4V Titanium alloy (Ti-6Al-4V)	1.08	0.15	3.63
35.0_4.50 [33]	35.0	4.50	0.13	AA5083-H111 Aluminium alloy (AA5083-H111)	1.00	0.22	0.84
40.0_7.00 [1]	40.0	7.00	0.18	DC04 Steel (DC04)	0.85	0.23	1.68

[a] Determined from the fit of the Hollomon law to experimental tensile test results.

Table 8
Equations from different authors for the evolution of the bulge radius.

Designation	Approach	Bulge radius
Hill_R_M_R_1	Hill (1950) [4]	$\rho_{ext}=\frac{R_M^2+h^2}{2h}$
Panknin_R_M_R_1	Panknin (1959) [34]	$\rho_{ext}=\frac{(R_M+R_1)^2+h^2-2R_1h}{2h}$

Table 9
Equations from different authors for the evolution of the sheet thickness at the top of the cap.

Designation	Approach	Thickness at the top of the cap
Hill_R_M_R_1	Hill (1950) [4]	$t=t_0\left[\frac{1}{1+(h/R_M)^2}\right]^2$
Chakrabarty_R_M_R_1	Chakrabarty and Alexander (1970) [29]	$t=t_0\left[\frac{1}{1+(h/R_M)^2}\right]^{2-n}$
Kruglov - Panknin_R_M_R_1	Kruglov *et* al. (2002) [35]	$t=t_0\left[\frac{(R_M/\rho_{ext})}{\sin^{-1}(R_M/\rho_{ext})}\right]^2$

Seven materials were tested at room temperature and two (AISI 201 Steel and AA5754 Aluminium Alloy) were also tested at higher temperatures.

Equations previously defined by other researchers for evolution of the radius of curvature and the sheet thickness are also used for comparison. These equations are shown in Tables 8 and 9, which are the most commonly used for bulge test. The sheet thickness using Kruglov equation is determined based on the radius of curvature determined by Panknin equation.

In the next figures, the designation "Eq_R_M_R_1 "corresponds to the results of the Eqs. (24) and (25), for the die with die radius, R_M, and die profile radius, R_1; the materials designation to which concern the experimental results are also indicated in Table 7.

Fig. 46–54 show, for different die geometries and materials, the comparison between experimental and calculated evolution of the: (a) radius of curvature and (b) normalized sheet thickness. Regarding the radius of curvature, the Hill's equation deviates from the experimental results, in all cases. When comparing the herein proposed Eq. (24) with the one suggested by Panknin it is not completely evident which one fits better all experimental results. Anyhow, globally the proposed Eq. (24) is well adjusted to majority of situations. However, for the thickness evolution at the pole bulge it is evident the better prediction of proposed Eq. (25), when compared to other currently available equations. Examples of good correlation is seen for experimental results of Figs. 48, 49 and 50. The remaining results, although show higher deviation, express a correct tendency for such experimental evolution.

In summary it is seen that experimental results validate the herein proposed equations for determination of radius of curvature as well as thickness evolution. To be highlighted is that proposed equation for thickness evaluation is shown to represent a significant added value, thus contributing to a better accuracy on material hardening curve determination using bulge test with simpler equipment.

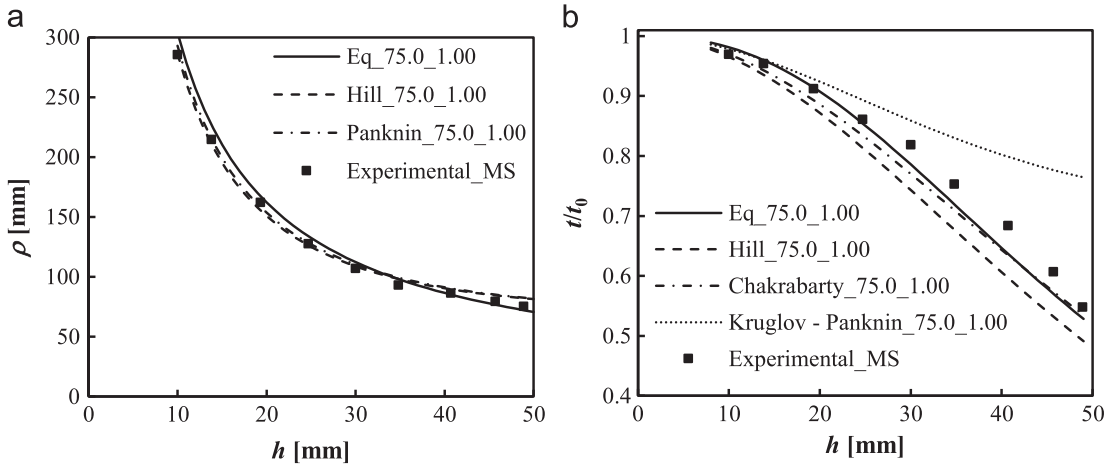

Fig. 46. Comparison between the evolution of the experimental results (symbols) and the equations (lines), for the Mild Steel (MS) material [32]: (a) radius of curvature and (b) sheet thickness.

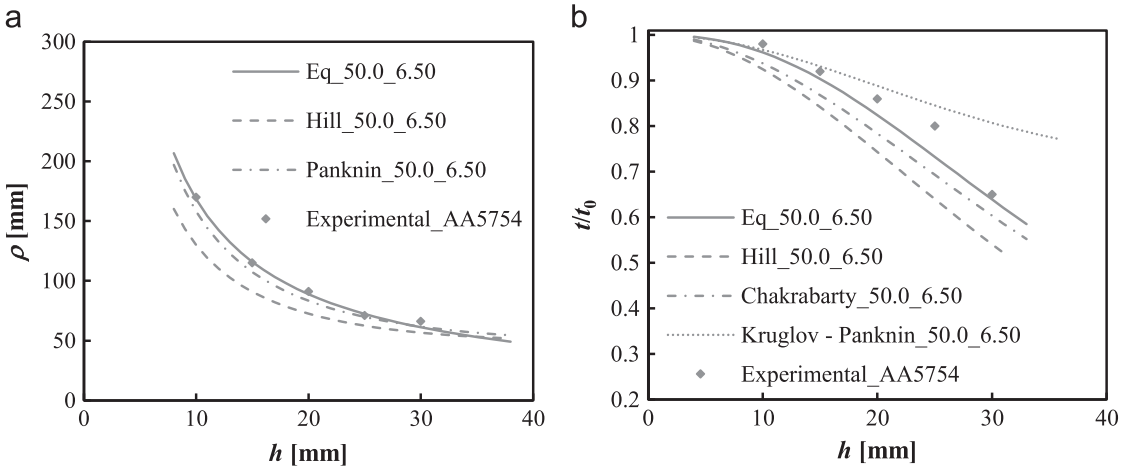

Fig. 47. Comparison between the evolution of the experimental results (symbols) and the equations (lines), for the AA5754 Aluminium Alloy material [8]: (a) radius of curvature and (b) sheet thickness.

7.2. *Results of die 75.0_13.00*

In this section, the experimental results of the bulge test for two metal sheets are analysed, one is DP600 steel and the other is AA6061 aluminium alloy, with initial sheet thickness equal to 0.80 and 1.04 mm, respectively. The die geometry used is 75.0_13.00 (Fig. 1). Table 10 shows the parameters of the Swift law obtained by fitting the tensile curves and the anisotropy coefficients, at 0, 45 and 90º with the rolling direction (RD). The average values of the hardening and anisotropy coefficients are $\overline{n}=0.19$ and $\overline{r}=0.87$, for DP600 steel, and $\overline{n}=0.13$ and $\overline{r}=0.65$, for AA6061 aluminium alloy.

The above proposed equations for the evolution of the normalized radius of curvature and the normalized sheet thickness with the normalized pole height are compared with the experimental results. Also, equations previously proposed by other researchers (see Tables 8 and 9), are used for comparison.

Figs. 55 and 56 show the comparison between experimental and calculated evolution of the radius of curvature (Figs. 55 and 56 (a)) and normalized sheet thickness (Figs. 55 and 56 (b)), during the bulge test.

As seen in the previous section, the Hill's equation is always giving higher difference to experimental results. Concerning the radius of curvature, the Eq. (24) and that suggested by Panknin give results similar to the experimental ones, at the initial stage of the test. At the final stage, Eq. (24) gives a more accurate prediction to experimental results. For the evolution of sheet thickness at the pole, the accurate prediction of Eq. (25) is in contrast with the available equations from literature (Table 9).

Figs. 57 and 58 (a) show the results of the equivalent stress *versus* equivalent strain curves. The equivalent strain values are obtained from the direct measurement at the top of the cap. The equivalent stress is determined by the von Mises criterion (Eq. (10)) assuming balanced biaxial stress state ($\sigma_1=\sigma_2=\sigma$), where σ is evaluated by membrane theory (Eq. (12)) using: (i) experimental measurement of ρ and t, during the bulge test and (ii) the values of ρ and t are obtained by Eqs. (24) and (25).

Figs. 57 and 58(b) show the error in equivalent stress with the equivalent strain, when comparing the results obtained using Eqs. (24) and (25) with those from experimental measurement. The errors in equivalent stress when using the proposed equations is quite small, except at the initial stage of deformation, where the determination of the radius of curvature and the sheet thickness can be less accurate.

8. Conclusions

A comprehensive numerical study concerning the bulge test of metal sheets was performed with materials presenting various plastic behaviors, namely different values of the yield stress, strain

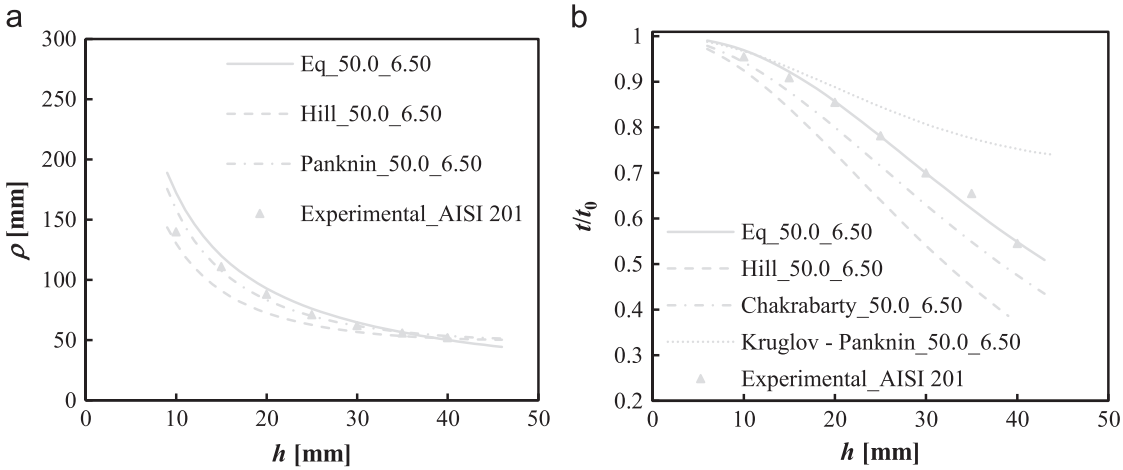

Fig. 48. Comparison between the evolution of the experimental results (symbols) and the equations (lines), for the AISI 201 Steel material [8]: (a) radius of curvature and (b) sheet thickness.

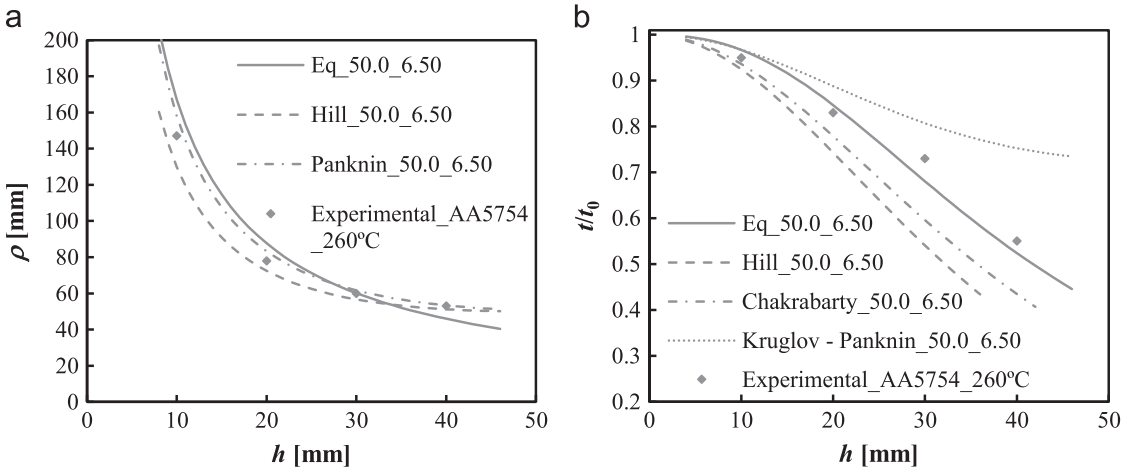

Fig. 49. Comparison between the evolution of the experimental results (symbols) and the equations (lines), for the AA5754 Aluminium Alloy material at high temperature [8]: (a) radius of curvature and (b) sheet thickness.

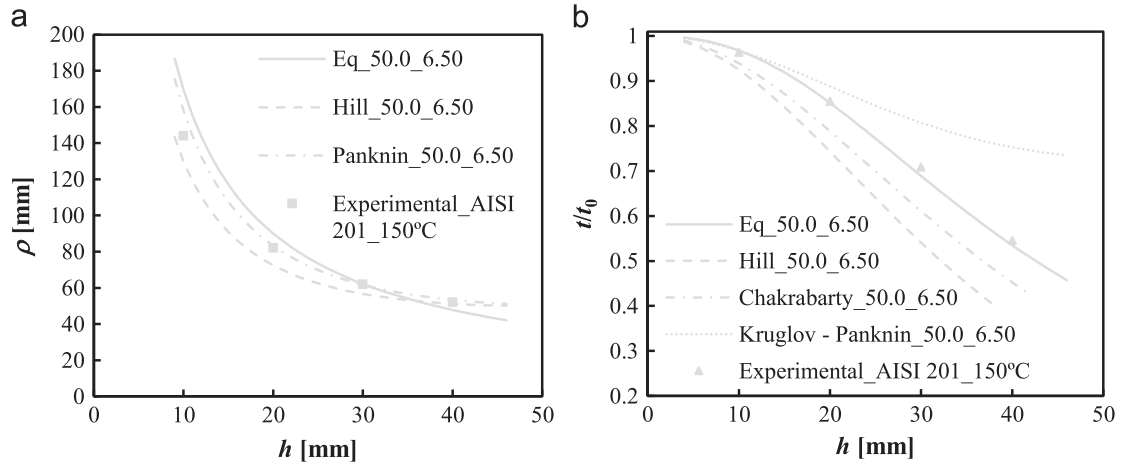

Fig. 50. Comparison between the evolution of the experimental results (symbols) and the equations (lines), for the AISI 201 Steel material at high temperature [8]: (a) radius of curvature and (b) sheet thickness.

hardening, anisotropy coefficients and sheet thickness. Different die geometries were also used.

This systematic study shows that the evolution of the radius of curvature at the pole of the cap during the test only depends on the work hardening coefficient of the material. The evolution of the sheet thickness depends on both, the work hardening coefficient and the anisotropy. Both evolutions are independent of the value of the yield stress and the initial sheet thickness. The geometry of the die influences both evolutions.

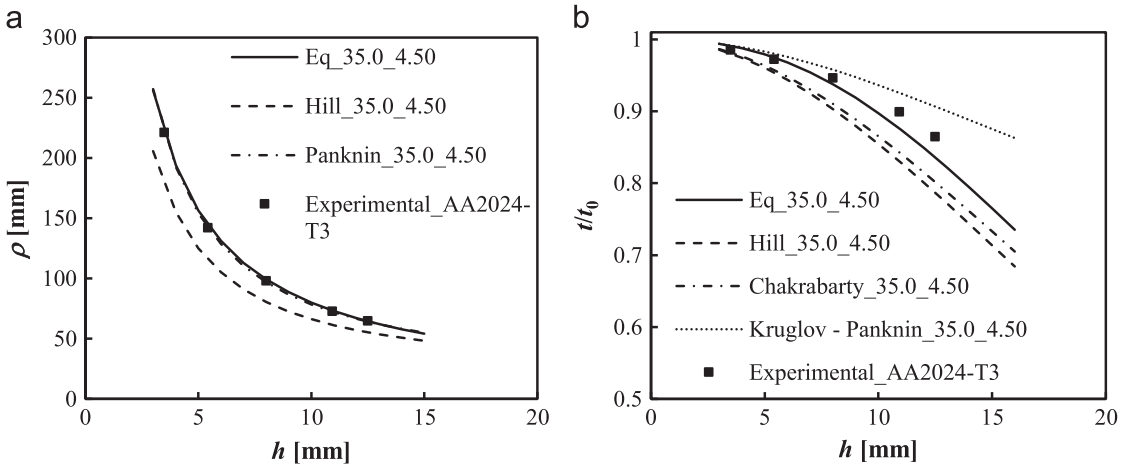

Fig. 51. Comparison between the evolution of the experimental results (symbols) and the equations (lines), for the AA2024-T3 Aluminium Alloy material [33]: (a) radius of curvature and (b) sheet thickness.

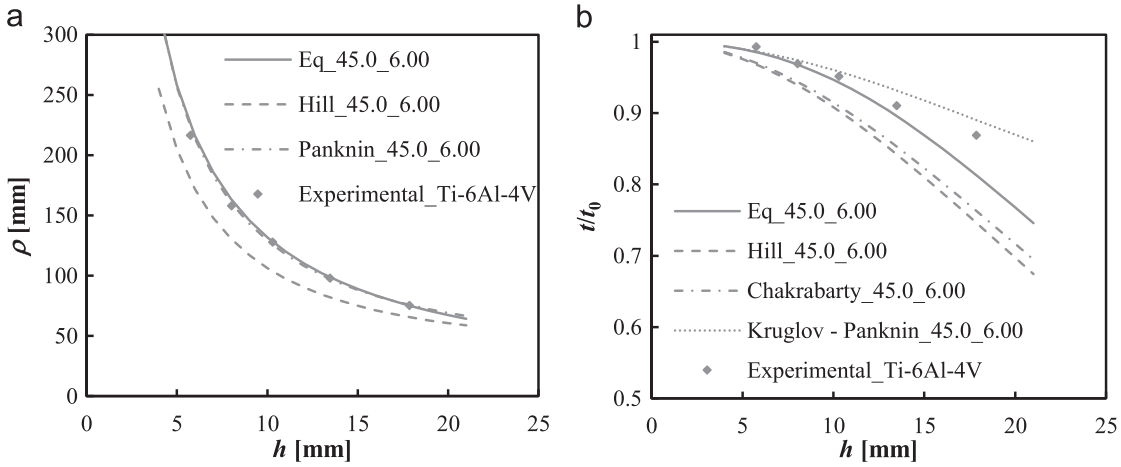

Fig. 52. Comparison between the evolution of the experimental results (symbols) and the equations (lines), for the Ti–6Al–4V Titanium Alloy material [33]: (a) radius of curvature and (b) sheet thickness.

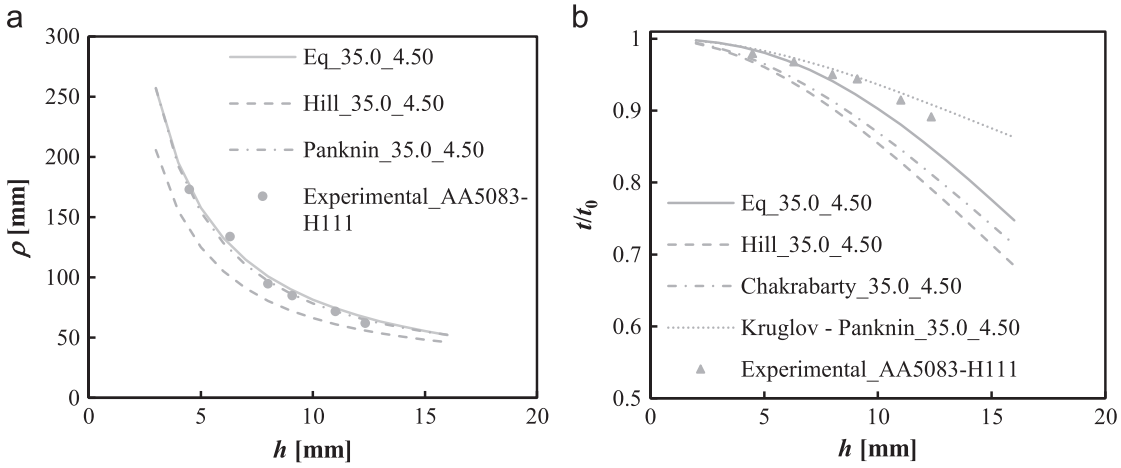

Fig. 53. Comparison between the evolution of the experimental results (symbols) and the equations (lines), for the AA5083-H111 Aluminium Alloy material [33]: (a) radius of curvature and (b) sheet thickness.

These results allowed the development of equations to define the evolution of the curvature radius and the sheet thickness at the pole with the pole height, which take into account the material parameters (hardening coefficient in case of curvature radius, and also the sheet anisotropy in case of sheet thickness) and the die geometry. Numerical stress *versus* strain curves were plotted for comparing stress obtained by direct measurement of the curvature radius and the sheet thickness at the pole, as well as the stress obtained by the proposed equations. In the last case, the errors in stress rarely exceeded 4%, which is comparable to the ones obtained with the direct measurement of the curvature radius and sheet thickness.

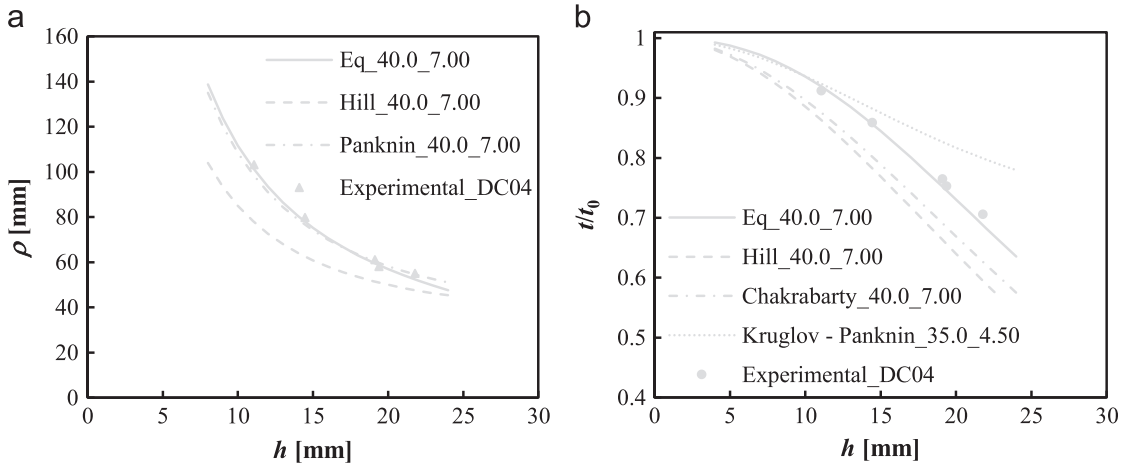

Fig. 54. Comparison between the evolution of the experimental results (symbols) and the equations (lines), for the DC04 Steel material [1]: (a) radius of curvature and (b) sheet thickness.

Table 10
Swift law parameters obtained by fitting the stress–strain curves in tension and the anisotropy coefficient, at 0, 45 and 90º with the rolling direction (RD), of the materials.

Designation	Swift law parameters											
	0º with RD				45º with RD				90º with RD			
	σ_0 [MPa]	K	n	r	σ_0 [MPa]	K	n	r	σ_0 [MPa]	K	n	r
DP600 Steel	392.22	1045.77	0.19	0.62	406.49	1040.11	0.19	1.03	433.02	1066.24	0.18	0.87
AA6061 Aluminium alloy	275.10	489.43	0.13	0.66	270.58	484.95	0.13	0.69	272.22	483.19	0.12	0.65

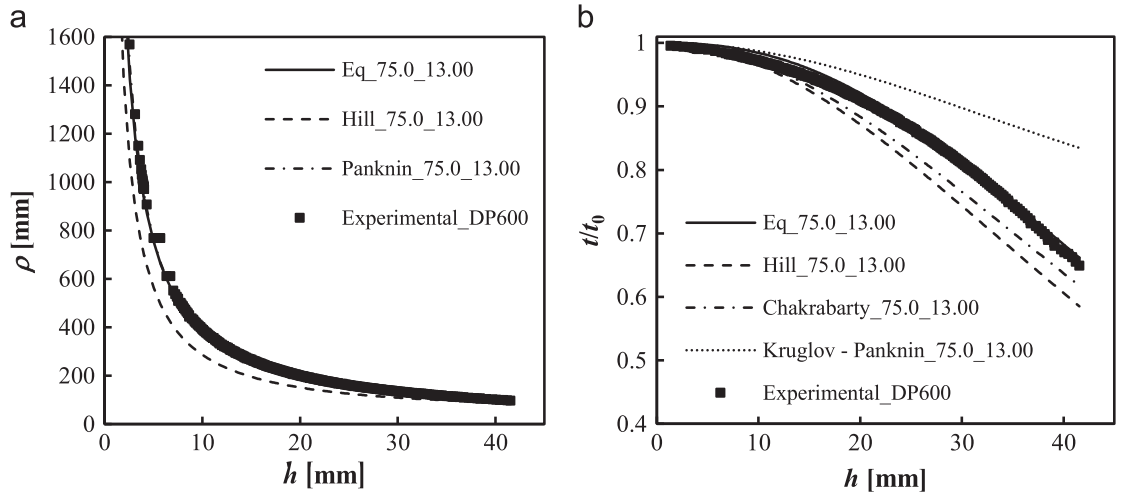

Fig. 55. Comparison between the evolution of the experimental results (symbols) and the equations (lines), for the DP600 Steel material: (a) radius of curvature and (b) sheet thickness.

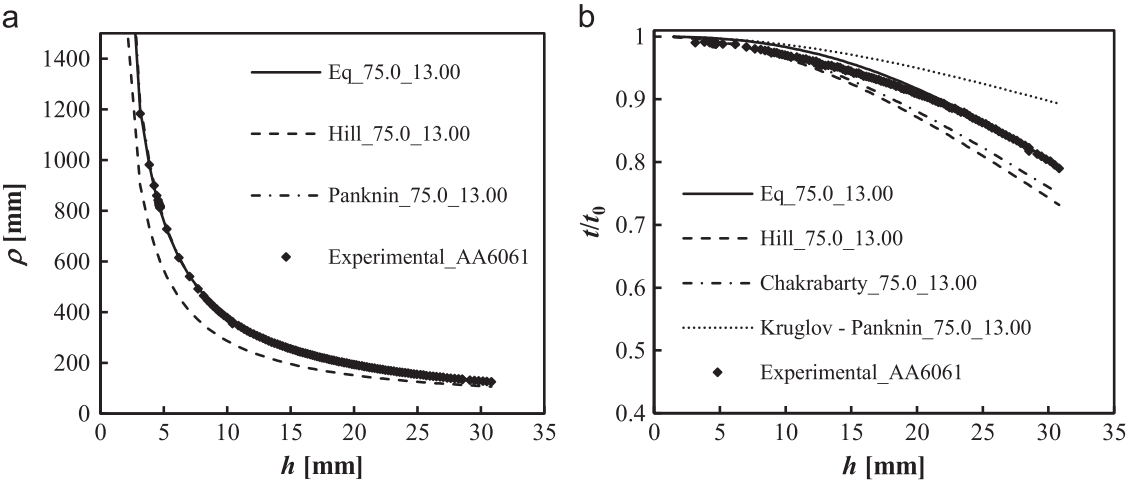

Fig. 56. Comparison between the evolution of the experimental results (symbols) and the equations (lines), for the AA6061 Aluminium alloy material: (a) radius of curvature and (b) sheet thickness.

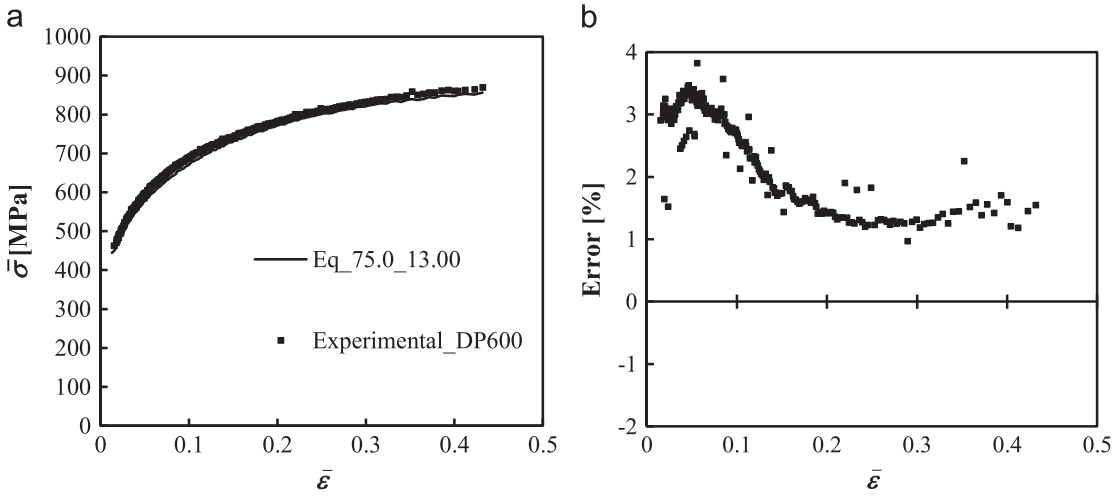

Fig. 57. Results for DP600 steel: (a) work hardening law obtained using Eq. (12), by using experimental results (symbols) and by using Eqs. (24) and (25) (line); (b) Evolution of the error in equivalent stress obtained by membrane theory using Eqs. (24) and (25).

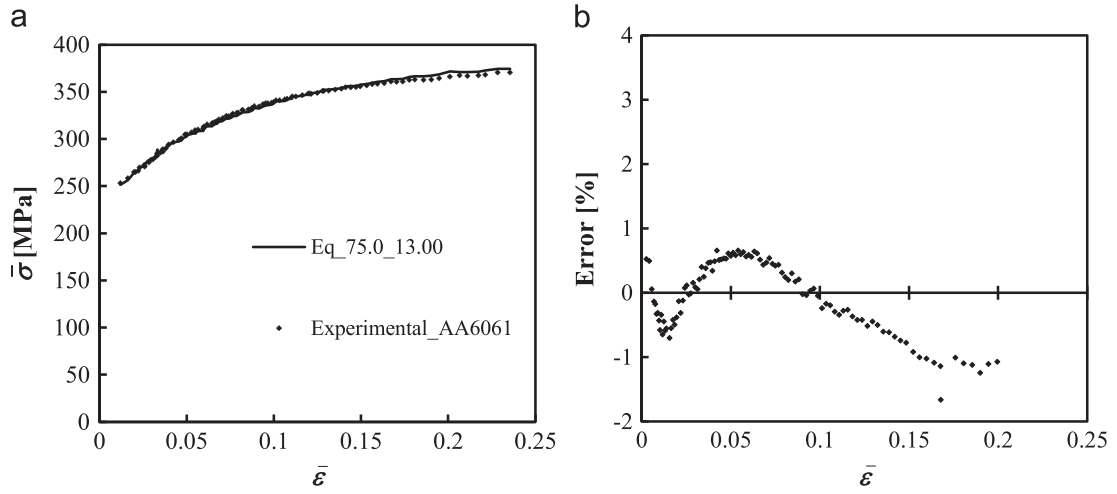

Fig. 58. Results for AA6061 aluminium alloy (a) work hardening law obtained using Eq. (12), by using experimental results (symbols) and by using Eqs. (24) and (25) (line); (b) Evolution of the error in equivalent stress obtained by membrane theory using Eqs. (24) and (25).

Also, the evolutions described by the herein proposed equations for the curvature radius and the sheet thickness at the pole were compared with experimental results obtained in the framework of the current work, for a defined die geometry (75.0_13.00), as well as results from literature, for various die geometries. In the former case, the stress *versus* strain curves are also compared with those, where the stress were obtained by direct experimental measurement of the curvature radius and the sheet thickness at the pole. When the proposed equations are used, the maximum error in stress is close to 3%, excluding a region at the initial stage of the test.

These findings indicate the appropriateness of a simplified experimental methodology for determining the hardening curve from the biaxial tensile test under hydraulic pressure. Namely, it is possible to avoid the complex experimental procedure for determining the stress values at different moments of the test, which requires a specific device for measuring the curvature radius at the pole of the cap and the determination of the sheet thickness.

Acknowledgments

This research work is sponsored by National Funds from the Portuguese Foundation for Science and Technology (FCT) via the projects PTDC/EMS-TEC/1805/2012, PEst-C/EME/UI0285/2013 and CENTRO-07-0224-FEDER-002001 (MT4MOBI), and by FEDER funds through the program COMPETE – "*Programa Operacional Factores de Competitividade*".

References

[1] Lăzărescu L, Comşa D-S, Banabic D. Analytical and experimental evaluation of the stress–strain curves of sheet metals by hydraulic bulge tests. Key Eng Mater 2011;473:352–9. http://dx.doi.org/10.4028/www.scientific.net/KEM.473.352.

[2] Santos AD, Teixeira P, Barlat F. Flow stress determination using hydraulic bulge test and a mechanical measurement system. International Deep Drawing Research Group Conference IDDRG, Bilbao, Spain: IDDRG; 2011. p. 91–100.

[3] Hsu TC, Shang HM. Mechanics of sheet metal formed by hydraulic pressure into axisymmetrical shells. Exp Mech 1976;16:337–42. http://dx.doi.org/10.1007/BF02330250.

[4] Hill RC. A theory of the plastic bulging of a metal diaphragm by lateral pressure. Lond Edinb Dublin Philos Mag J Sci 1950;41:1133–42. http://dx.doi.org/10.1080/14786445008561154.

[5] Gagov V, Feschiev N, Comşa D-S, Minev E. Strain hardening evalution by bulge testing of sheet metals. In: Travis FW, Hashmi SMSJ, editors. Proceedings of the 12th International Scientific Conference Achievements in Mechanical and Materials Engineering. Gliwice, Poland; 2003. p. 331–334.

[6] Rees DWA. Plastic flow in the elliptical bulge test. Int J Mech Sci 1995;37:373–89. http://dx.doi.org/10.1016/0020-7403(94)00071-Q.

[7] Santos AD, Teixeira P, Barata da Rocha A, Barlat F, Moon YH, Lee M-G. On the determination of flow stress using bulge test and mechanical measurement.

In: Barlat F, Moon YH, Lee MG, editors. Proceedings of the 10th International Conference on NUMIFORM. American Institute of Physics Pohang, Republic of Korea; 2010. p. 845–852. http://dx.doi.org/10.1063/1.3457644.
[8] Koç M, Billur E, Cora ÖN. An experimental study on the comparative assessment of hydraulic bulge test analysis methods. Mater Des 2011;32:272–81. http://dx.doi.org/10.1016/j.matdes.2010.05.057.
[9] Slota J, Spišák E. Determination of flow stress by the hydraulic bulge test. Metalurgija 2008;47:13–7.
[10] Lăzărescu L, Comşa D-S, Banabic D. Determination of stress–strain curves of sheet metals by hydraulic bulge test. AIP Conference Proceedings; 2011. Vol. 1353. p. 1429–1434. http://dx.doi.org/10.1063/1.3589717.
[11] Liu K, Lang L, Cai G, Yang X, Guo C, Liu B. A novel approach to determine plastic hardening curves of AA7075 sheet utilizing hydraulic bulging test at elevated temperature. Int J Mech Sci 2015;100:328–38. http://dx.doi.org/10.1016/j.ijmecsci.2015.07.002.
[12] Mulder J, Vegter H, Aretz H, Keller S, van den Boogaard AH. Accurate determination of flow curves using the bulge test with optical measuring systems. J Mater Process Technol 2015;226:169–87. http://dx.doi.org/10.1016/j.jmatprotec.2015.06.034.
[13] Menezes LF, Teodosiu C. Three-dimensional numerical simulation of the deep-drawing process using solid finite elements. J Mater Process Technol 2000;97:100–6. http://dx.doi.org/10.1016/S0924-0136(99)00345-3.
[14] Oliveira MC, Alves JL, Menezes LF. Algorithms and strategies for treatment of large deformation frictional contact in the numerical simulation of deep drawing. Process. Arch Comput Methods Eng 2008;15:113–62. http://dx.doi.org/10.1007/s11831-008-9018-x.
[15] Dowling NE. Mechanical behavior of materials: engineering methods for deformation, fracture, and fatigue. 2nd ed. Upper Saddle River, NJ: Prentice Hall; 1999.
[16] Lemoine X, Iancu A, Ferron G. Flow curve determination at large plastic strain levels: limitations of the membrane theory in the analysis of the hydraulic bulge test. In: Proceedings of the 14th International ESAFORM Conference on Material Forming; 2011. p. 1411–1416. http://dx.doi.org/10.1063/1.3589714.
[17] Ranta-Eskola AJ. Use of the hydraulic bulge test in biaxial tensile testing. Int J Mech Sci 1979;21:457–65. http://dx.doi.org/10.1016/0020-7403(79)90008-0.
[18] Hill R. A theory of the yielding and plastic flow of anisotropic. metals. Proc R Soc A Math Phys Eng Sci 1948;193:281–97. http://dx.doi.org/10.1098/rspa.1948.0045.
[19] Martins B, Teixeira P, Santos AD. Study on the flow stress determination using hydraulic bulge test. In: Andrade-Campos A, Lopes N, Valente RAF, Varum H, editors. First ECCOMAS Young Investigators Conference on Computational Methods in Applied Science. Aveiro, Portugal; 2012.
[20] Chamekh A, BelHadjSalah H, Hambli R, Gahbiche A. Inverse identification using the bulge test and artificial neural networks. J Mater Process Technol 2006;177:307–10. http://dx.doi.org/10.1016/j.jmatprotec.2006.03.214.
[21] Alves JL, Bouvier S, Oliveira MC, Menezes LF. Drawbeads: to be or not to be, AIP Conference Proceedings; 2005. Vol. 778, p. 655–660 http://dx.doi.org/10.1063/1.2011297.AIP.
[22] Alves JL. Simulação numérica do processo de estampagem de chapas metálicas: modelação mecânica e métodos numéricos (PhD Thesis). Guimarães, Portugal: Universidade do Minho; 2003.
[23] Reis LC, Prates PA, Oliveira MC, Sakharova NA, Fernandes JV. Caracterização do comportamento plástico de chapas metálicas com recurso ao ensaio de expansão biaxial simétrica. In: Tadeu A, Figueiredo IN, Menezes LF, Mendes PA, Rodríguez-Ferran A, Arias I, et al., editors. Congresso de Métodos Numéricos em Engenharia. Coimbra, Portugal: APMTAC; 2011. p. 54.
[24] Swift HW. Plastic instability under plane stress. J Mech Phys Solids 1952;1:1–18. http://dx.doi.org/10.1016/0022-5096(52)90002-1.
[25] M & M Research Inc. NXT Defect Evaluator; 2007.
[26] Rodrigues CA, Reis LC, Sakharova NA, Oliveira MC, Fernandes JV. On the characterization of the plastic behaviour of sheet metals with bulge tests: numerical simulation study. In: Eberhardsteiner J et al., editors. Proceedings of the 6th European Congress on Computational Methods in Applied Sciences and Engineering ECCOMAS. Vienna, Austria; 2012. p. 4575–4589.
[27] Reis LC, Rodrigues CA, Oliveira MC, Sakharova NA, Fernandes JV. Characterization of the plastic behaviour of sheet metal using the hydraulic bulge test. In: Andrade-Campos A, Lopes N, Valente RAF, Varum H, editors, First ECCOMAS Young Investigators Conference on Computational Methods in Applied Science. Aveiro, Portugal; 2012. p. 67.
[28] Prates PA, Oliveira MC, Fernandes JV. On the equivalence between sets of parameters of the yield criterion and the isotropic and kinematic hardening laws. Int J Mater Form 2015;8:505–15. http://dx.doi.org/10.1007/s12289-014-1173-z.
[29] Chakrabarty J, Alexander JM. Hydrostatic bulging of circular diaphragms. J Strain Anal Eng Des 1970;5:155–61. http://dx.doi.org/10.1243/03093247V053155.
[30] Voce E. The relationship between stress and strain for homogeneous deformations. J Inst Met 1948;74:537–62.
[31] Drucker DC. Relation of experiments to mathematical theories of plasticity. J Appl Mech ASME 1949;16:349–57.
[32] Fernandes JV. Dislocation microstructures in steel during deep drawing (PhD Thesis). Coimbra, Portugal: University of Coimbra; 1984.
[33] Janbakhsh M, Djavanroodi F, Riahi M. Utilization of bulge and uniaxial tensile tests for determination of flow stress curves of selected anisotropic alloys. J Mater Des Appl 2012;227:38–51. http://dx.doi.org/10.1177/1464420712451963.
[34] Gutscher G, Wu H-C, Ngaile G, Altan T. Determination of flow stress for sheet metal forming using the viscous pressure bulge (VPB) test. J Mater Process Technol 2004;146:1–7. http://dx.doi.org/10.1016/S0924-0136(03)00838-0.
[35] Kruglov AA, Enikeev FU, Lutfullin RY. Superplastic forming of a spherical shell out a welded envelope. Mater Sci Eng A 2002;323:416–26. http://dx.doi.org/10.1016/S0921-5093(01)01376-4.

3.4. Inverse identification of Swift law parameters using the bulge test

This subchapter refers to the paper "*Inverse Identification of Swift law parameters using the bulge test*", published in *International Journal of Material Forming*. It explores the opportunity to develop an inverse analysis methodology for determining the Swift law parameters, based on the capability of overlapping the curves of evolution of pressure with the pole height for materials with the same value of hardening coefficient, regardless of the values of the others parameters of the Swift law and the anisotropy of the material. This is achieved by multiplying the pressure and the pole height by factors to be determined. The inverse identification enables the proper evaluation of the Swift hardening law, simplifies the experimental procedure and is not exposed to various experimental errors, in particular those related to the use of the membrane theory.

[Page intentionally left blank]

Int J Mater Form
DOI 10.1007/s12289-016-1296-5

ORIGINAL RESEARCH

Inverse identification of the Swift law parameters using the bulge test

L. C. Reis[1] · P. A. Prates[1] · M. C. Oliveira[1] · A. D. Santos[2] · J. V. Fernandes[1]

Received: 12 November 2015 / Accepted: 14 April 2016

Abstract An inverse methodology is proposed for determining the work hardening law of metal sheets, from the results of pressure vs. pole height, obtained from the bulge test. This involves the identification of the parameters of the Swift law. The influence of these parameters as well as the sheet anisotropy and the sheet thickness on the results of pressure with pole height is studied following a forward analysis, based on finite element simulation. This allows understanding that the overlapping of the pressure vs. pole height curves of different metal sheets is possible, provided that the hardening coefficient has the same value, whatever the values of the remaining parameters of the Swift law, the sheet anisotropy and the initial sheet thickness. The overlapping of the curves is performed by multiplying the values of the pressure and the pole height using appropriate factors, which depend on the ratios between the yield stresses and the thicknesses of the sheets, and also on their anisotropy. Afterwards, an inverse methodology is established, consisting of the search for the best coincidence between pressure vs. pole height of experimental and reference curves, the latter being obtained by numerical simulation assuming isotropic behaviour with various values of the Swift hardening coefficient in the range of the material under study. This methodology is compared with a classical strategy and proves to be an efficient alternative for determining the parameters of the Swift law. It aims to be simple from an experimental point of view and, for that purpose, only uses results of the load evolution during the test. The methodology is limited to materials with the hardening behaviour adequately described by the Swift law.

Keywords Bulge test · Inverse analysis · Swift hardening law · Numerical simulation

✉ L. C. Reis
luis.reis@dem.uc.pt

[1] CEMUC, Department of Mechanical Engineering, University of Coimbra, Pólo II, Rua Luís Reis Santos, Pinhal de Marrocos, 3030-788 Coimbra, Portugal

[2] Faculty of Engineering, University of Porto, Rua Dr. Roberto Frias, 4200-465 Porto, Portugal

Introduction

The manufacturing of sheet metal forming components, with complex geometries and tight requirements, obliges the accurate characterization of the sheet metals behaviour. Very often, high values of strain are imposed in the components by the forming conditions. Therefore, the adequate characterization of the hardening law up to large plastic deformation is required. This is generally accomplished using the bulge test that achieves strain values not possible in the tensile test, for example. The traditional methodology, for performing the bulge test and analysing the results, requires the use of specific devices, one for assessing the radius of curvature and another for measuring the strain at the pole of the cap during the test, in case of mechanical measuring systems [1]. Simultaneously, it is also necessary to follow the pressure evolution during the test. The use of optical measuring systems makes it easier the description of the geometry and strain distributions on the sheet surface during the bulge test [2, 3]. However, the evaluation of the stress vs. strain curves depends on assumptions and simplifications, whose assessment are still under study. For example, in a recent study Mulder et al. [4] examine the validity and the conditions for using the membrane theory, which includes issues such as the existence of bending stresses and a through thickness stress due to the hydraulic pressure.

Published online: 25 April 2016

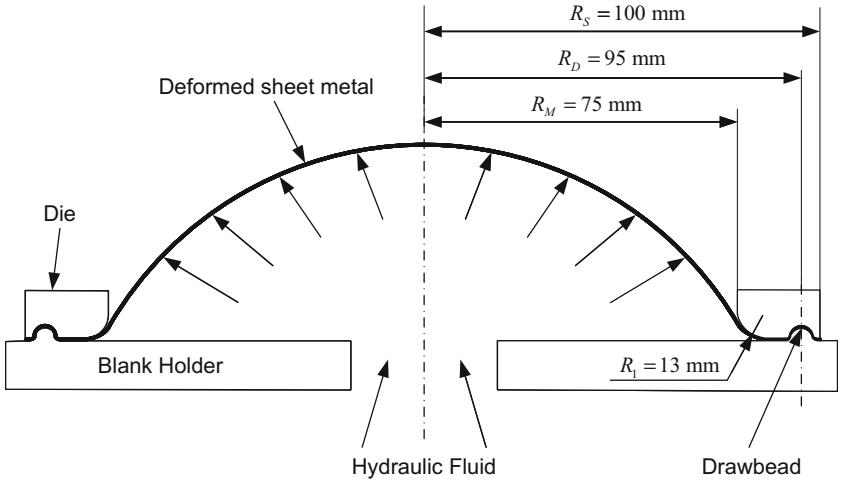

Fig. 1 Bulge test, with the identification of the principal dimensions of the tool [17]

Some equations have been proposed [5–8] in order to avoid the use of the above mentioned devices, just exploiting the data concerning pressure vs. pole height and thereby simplifying the implementation and analysis of the bulge test results. These equations allow determining the equivalent stress and strain under isotropic condition, relating the radius of curvature and sheet thickness with the pole height. However, this procedure presents some disadvantages. First of all, there exists in the literature a multitude of equations to describe the evolutions of the radius of curvature and sheet thickness at the pole of the cap with the pole height [9–11], which makes it difficult to select the most appropriate. The use of some of them, in general the most accurate, requires the knowledge a priori of the hardening coefficient of the Swift law, which is intended to be identified. Although tensile tests can be previously performed to assess the value of the hardening coefficient, its value in tension can be different from that in biaxial stretching. Also, other constitutive parameters such as those of the anisotropic yield criterion, related with the in-plane description of the anisotropy, can influence the evolutions of the radius of curvature and sheet thickness at the pole during the test, as mentioned in recent works [4, 5]. Not always the equations for the evolutions of the radius of curvature and sheet thickness with the pole height properly consider the geometry of the bulge test device, i.e. the die radius and the die profile radius. In fact, only in rare cases the die profile radius is considered, as in Panknin model for the curvature radius evolution, which in turn takes no account for the hardening coefficient [11]. In a recent work, a numerical iterative method was proposed to determine the stress–strain curve of the AA7075 metal sheet using pressure vs. pole height results of circular bulge tests performed at elevated temperatures [5]. This iterative scheme is coupled with the Panknin model for the curvature radius and explicit integral formulas proposed by the authors to evaluate the thickness at the pole of the bulge, taking into account the Lankford's anisotropy coefficient.

Few literature is available on inverse analysis procedures for identifying the hardening law parameters from the bulge test. Still, it is possible to notice that Chamekh et al. [12]

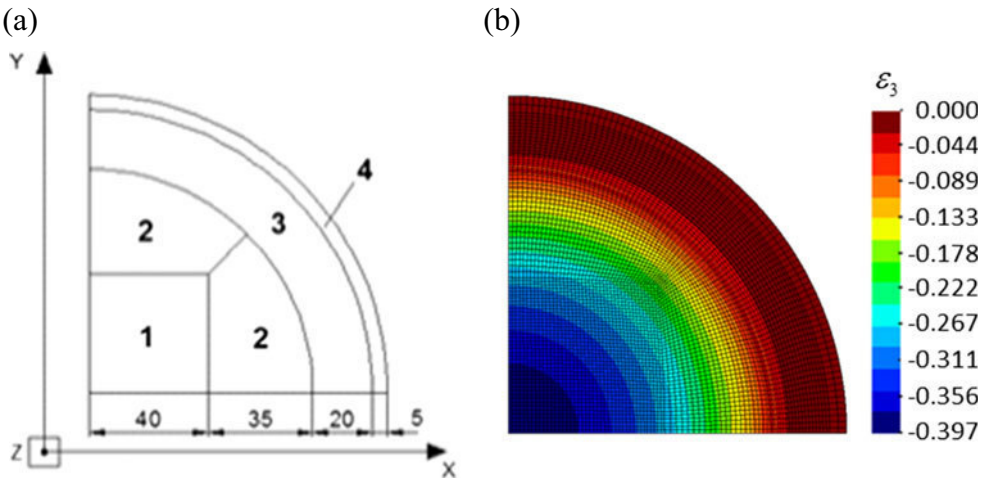

Fig. 2 (**a**) Four main zones adopted to define the finite element mesh in the sheet plane (the dimensions are in mm) and (**b**) general view of the mesh with illustration of the thickness strain distribution predicted for an isotropic material with the yield stress of 100 MPa, the hardening coefficient of the Swift law $n = 0.20$ and the initial sheet thickness of 1.0 mm, for the pressure of 3.29 MPa (pole height: $h = 41.65$ mm)

Table 1 Materials designation and their parameters of Swift hardening law

Designation	Y_0 [MPa]	K [MPa]	n
100_0.05_Z.Z	100	130.3	0.05
100_0.20_Z.Z		288.5	0.20
100_0.35_Z.Z		638.8	0.35
200_0.05_Z.Z	200	260.7	0.05
200_0.20_Z.Z		577.1	0.20
200_0.35_Z.Z		1277.6	0.35
300_0.05_Z.Z	300	391.0	0.05
300_0.20_Z.Z		865.6	0.20
300_0.35_Z.Z		1916.4	0.35

describe an inverse approach for identifying the constitutive parameters of a stainless steel, based on artificial neural networks. They use the results of pressure vs. pole height, which are transferred to a neural network. This is trained using curves generated by finite element simulations of the bulge test. During the training process, the neural network generates an approximate function for the inverse problem relating the material parameters to the shape of the pressure vs. pole height curve of the bulge test. A circular die geometry is used for identifying the Ludwick hardening law [13], assuming the knowledge of the Lankford's parameters values evaluated from tensile tests. Afterwards, an elliptical die for an off axis angle of 0° is used to recalculate the Lankford's coefficients, which are validated using an elliptical die with an off axis angle of 45°. They claim that artificial neural networks can predict a combination of the material parameters with acceptable accuracy for most design considerations, although with a strong exception that is the value of the parameter n of the hardening law (the experimental and identified values of n are 0.67 and 0.4, respectively). Also, Bambach [14] tried to

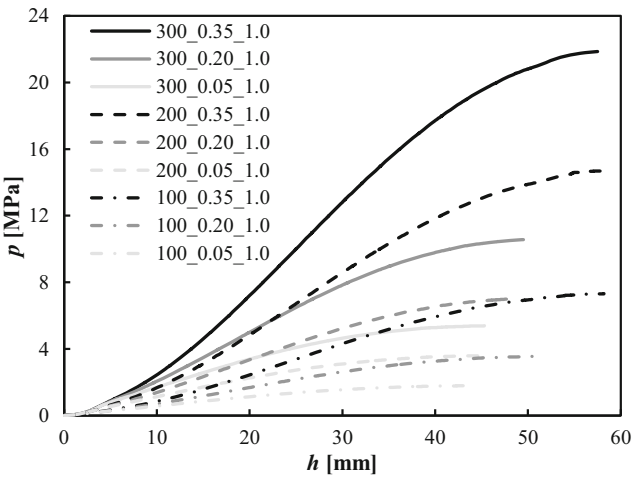

Fig. 3 Evolution of pressure, p, with pole height, h, for sheets of fully isotropic materials with $t_0 = 1.0$ mm

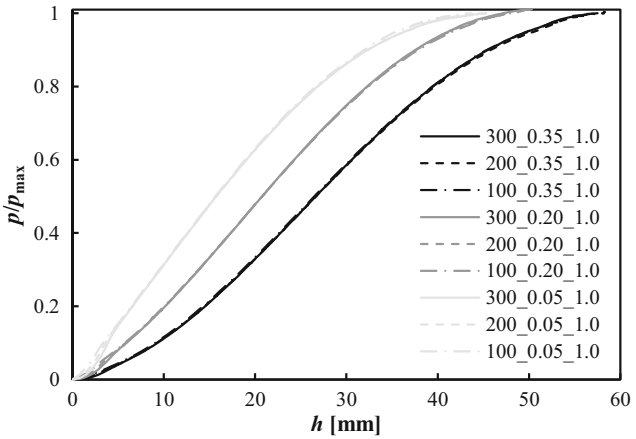

Fig. 4 Evolution of normalized pressure, p/p_{max}, with pole height, h, for sheets of fully isotropic materials with $t_0 = 1.0$ mm (from the results of Fig. 3)

implement an identification procedure for the parameters of the Voce law [15] resorting to objective functions making use, separately or simultaneously, of results of pressure vs. pole height, pole strain vs. pole height and pole thickness vs. pole height. In the studied cases, using virtual computer generated data, the author concluded that the combination of the first two types of results significantly improves the identification.

Furthermore, the influence of the values of the constitutive parameters, i.e. of the hardening law and the anisotropic yield criterion, on the evolution of pressure with the pole height has never been explored under inverse identification strategies, to our knowledge. The current results show that it is possible to overlap the curves concerning the evolution of the pressure with pole height and exploit this insight in order to build an inverse strategy for identifying the parameters of the hardening law. The main aim of this work is to develop and evaluate the performance of an inverse analysis methodology for the identification of the parameters of the Swift law [16], just

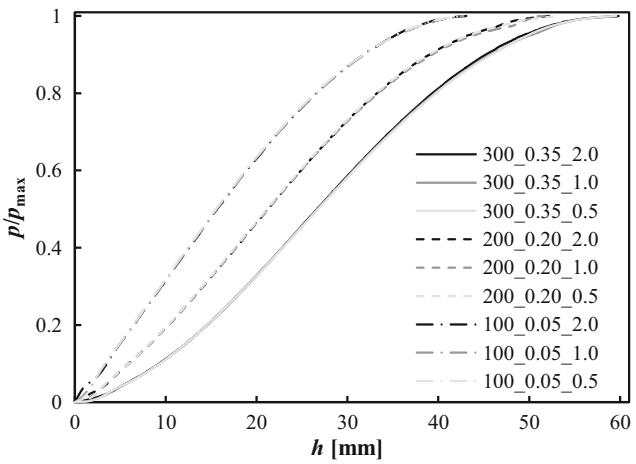

Fig. 5 Examples of the evolution of normalized pressure, p/p_{max}, with pole height, h, for sheets of fully isotropic materials with different initial sheet thicknesses

Table 2 Designation of the materials with transverse anisotropy and their parameters of Hill'48 criterion; a fully isotropic material is also considered

Designation	Parameters of the Hill'48 Criterion ($G+H=1$)					
	F	G	H	L	M	N
0.7_0.7_0.7_n	0.588	0.588	0.412	1.500	1.500	1.412
1_1_1_n	0.500	0.500	0.500	1.500	1.500	1.500
2_2_2_n	0.333	0.333	0.667	1.500	1.500	1.667
3_3_3_n	0.250	0.250	0.750	1.500	1.500	1.750

using the results of the evolution of the pressure with the pole height. This methodology is limited to materials with hardening behaviour adequately described by the Swift law and aims to be simple and accurate. Numerical and experimental results are used for validation.

Numerical modelling

In order to perform the study concerning the methodology for the evaluation of the Swift hardening law using the circular bulge test, numerical models of the test were built. The geometry of the tools considered in the test is schematically shown in Fig. 1, where $R_M = 75$ mm is the die radius, $R_1 = 13$ mm is the die profile radius, $R_D = 95$ mm is the radius of the central part of the drawbead and $R_S = 100$ mm the radius of the circular sheet. This geometry was built based on the experimental bulge test used by Santos et al. [17].

The tools were described using Bézier surfaces, considering only one quarter of the geometry due to material and geometrical symmetry conditions. However, in order to simplify the analysis, the drawbead geometry was neglected and its effect was replaced by a boundary condition imposing

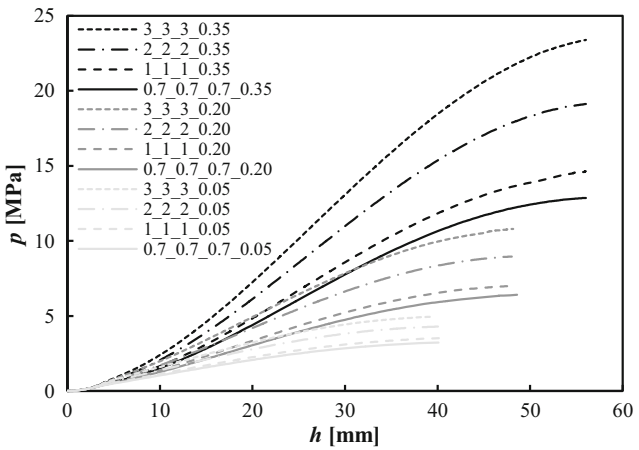

Fig. 6 Evolution of pressure, p, with pole height, h, for materials with planar isotropy and $n = 0.05$, 0.20 and 0.35 ($Y_0 = 200$ MPa and $t_0 = 1.0$ mm)

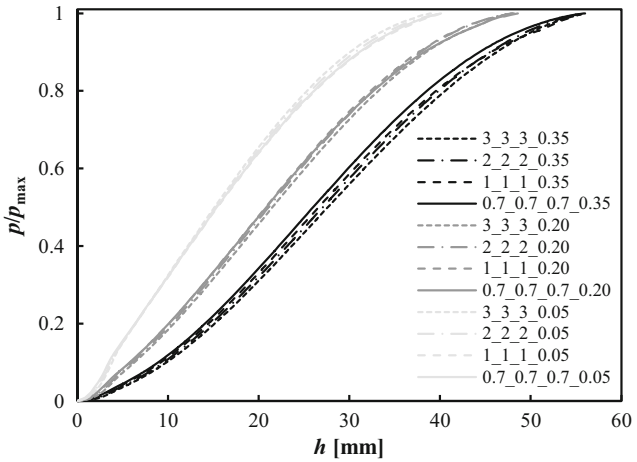

Fig. 7 Evolution of normalized pressure, p/p_{max}, with pole height, h, for materials with planar isotropy and $n = 0.05$, 0.20 and 0.35 ($Y_0 = 200$ MPa and $t_0 = 1.0$ mm)

radial displacement restrictions on nodes placed at a distance equal to R_D from the centre of the circular sheet, which has an initial blank radius of R_S [18]. The contact with friction was described by the Coulomb law with a constant friction coefficient of 0.02 [19]. All numerical simulations were carried out with DD3IMP in-house code [20, 21] assuming an incremental increase of the pressure applied to the sheet inner surface.

The blank sheet discretization was previously optimized [22] such that the sheet geometry was divided into four main zones, as shown in Fig. 2(a). This enables to describe the central region of the specimen with a regular and uniform grid discretization in the sheet plane, using quadrangular elements, as shown in Fig. 2(b). A total of 5292 3D solid 8 node elements with two layers of elements through thickness were used. Figure 2(b) also shows the thickness strain distribution predicted for an isotropic material, at an instant preceding the maximum pressure, highlighting its axisymmetric distribution.

The constitutive model adopted for the finite element analysis assumes [23, 24]: (1) the isotropic elastic behaviour

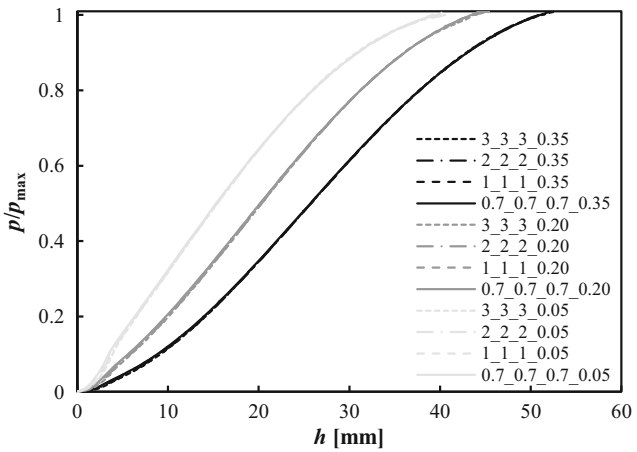

Fig. 8 As Fig. 7, but the values of the pole height, h, are multiplied by an appropriated factor, allowing the overlapping of curves for each value of n

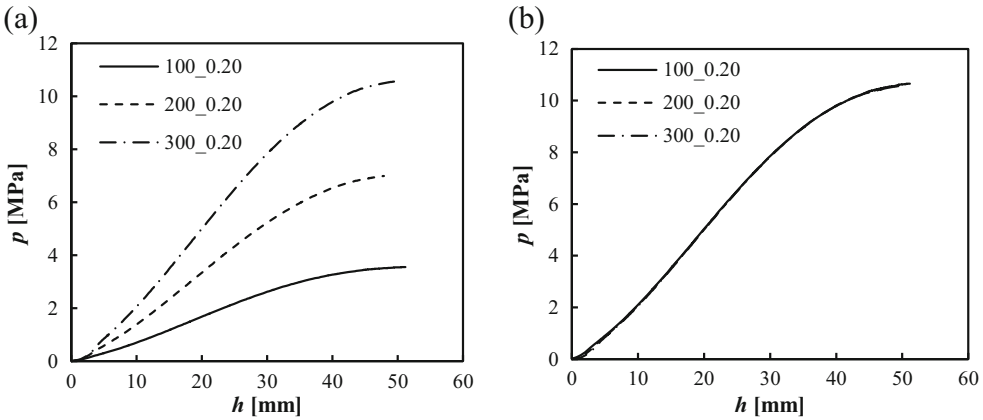

Fig. 9 Evolution of pressure, p, with pole height, h, for three isotropic sheet metals with $Y_0 = 100$, 200 and 300 MPa ($n = 0.20$ and $t_0 = 1.0$ mm): (**a**) Curves as obtained; (**b**) Overlapping curves after multiplying by 3 and 1.5 the pressure values of the curve with $Y_0 = 100$ and 200 MPa, respectively

defined by the generalized Hooke's law; (2) the plastic behaviour described by the orthotropic Hill'48 yield criterion and the hardening model by the Swift isotropic law.

The Hill'48 yield surface is described by the equation [25]:

$$F\left(\sigma_{yy}-\sigma_{zz}\right)^2 + G\left(\sigma_{zz}-\sigma_{xx}\right)^2 + H\left(\sigma_{xx}-\sigma_{yy}\right)^2 + 2L\tau_{yz}^2 + 2M\tau_{xz}^2 + 2N\tau_{xy}^2 = Y^2 \quad (1)$$

where σ_{xx}, σ_{yy}, σ_{zz}, τ_{xy}, τ_{xz} and τ_{yz} are the components of the Cauchy stress tensor, in the principal axes of orthotropy, and F, G, H, L, M and N are the anisotropy parameters of the material. Y represents the yield stress and its evolution during deformation $Y = f\left(\overline{\varepsilon}\right)$, which is described by the Swift isotropic hardening law [16]:

$$Y = K\left(\varepsilon_0 + \overline{\varepsilon}\right)^n \quad (2)$$

where $\overline{\varepsilon}$ is the equivalent plastic strain and K, ε_0 and n are material parameters to be identified. The initial yield stress, Y_0, can be written as a function of K, ε_0 and n, as follows: $Y_0 = K\varepsilon_0{}^n$. The value of the parameter ε_0 is assumed equal to 0.005 unless other is indicated. The elastic behaviour is considered isotropic and is described by the generalised Hooke's law, with a Young's modulus, $E = 210$ GPa, and a Poisson's ratio, $\nu = 0.30$.

Results

Numerical bulge tests were performed for two types of metal sheets: isotropic (section: Isotropic metal sheets) and transverse anisotropic (section: Transverse anisotropic metal sheets). The influence of the hardening parameters of the Swift law, the anisotropy of the material and the sheet thickness on the results of pressure vs. pole height is analysed. The aim is the search for features that describe the sheet metal behaviour during bulge test in a unified way, as much as possible.

Isotropic metal sheets

Bulge tests of metal sheets with various values of initial sheet thickness, yield stress and hardening parameter were analysed, in order to study the influence of these parameters on the evolutions of the pressure with the pole height. The plastic behaviour of the materials studied in this section is fully isotropic.

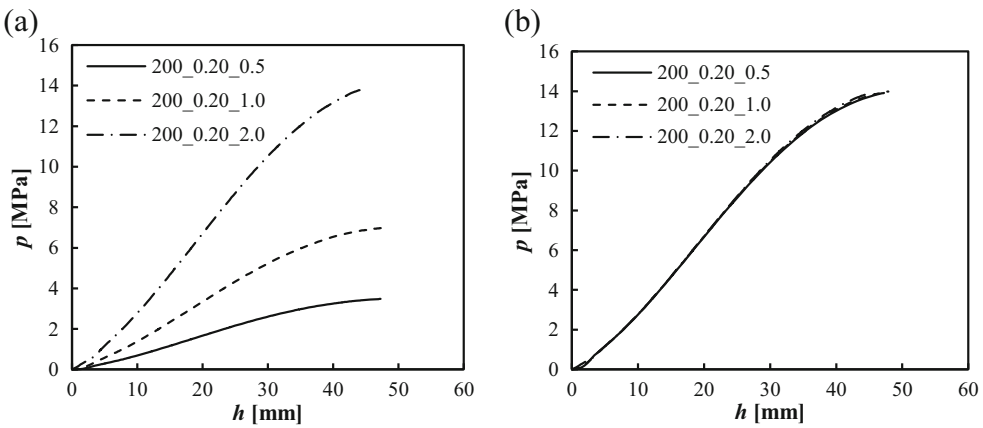

Fig. 10 Evolution of pressure, p, with pole height, h, for three isotropic sheet metals with $t_0 = 0.5$, 1.0 and 2.0 mm ($n = 0.20$ and $Y_0 = 200$ MPa): (**a**) Curves as obtained; (**b**) Overlapping curves after multiplying by 4 and 2 the pressure values of the curve with $t_0 = 0.5$ and 1.0 mm, respectively

Table 3 Designation of the anisotropy of the tested materials and respective parameters for Hill'48 criterion; the fully isotropic material (1_1_1) is also shown

Tested materials anisotropy ($F+G=1$)	Hill'48 criterion parameters			
	F	G	H	N
0.5_0.5_0.5	0.500	0.500	0.250	1.000
0.7_0.7_0.7	0.500	0.500	0.350	1.200
1_1_1	0.500	0.500	0.500	1.500
2_2_2	0.500	0.500	1.000	2.500
3_3_3	0.500	0.500	1.500	3.500
4_4_4	0.500	0.500	2.000	4.500

Table 1 shows the parameters of the Swift law for the materials under study. Three values of initial yield stress, Y_0, were chosen ($Y_0 = 100$, 200 and 300 MPa) and also three values of hardening coefficient, n, were selected ($n = 0.05$, 0.20 and 0.35). In order to simplify the analysis of the results in this section, the following designation is adopted for the material in each test: "XXX_0.YY_Z.Z", where "XXX" is the initial yield stress value, Y_0, "0.YY" is the hardening coefficient, n, and "Z.Z" is the initial sheet thickness, t_0. For each material, three values of initial sheet thickness were studied: 0.5, 1.0 and 2.0 mm.

In the following, examples of numerical results are presented concerning the materials in Table 1. Figure 3 shows the evolution of the pressure, p, with the pole height, h, for 1.0 mm thick sheets. The parameters of the Swift law, Y_0 and n, influence the evolution of pressure during the bulge test. At the beginning of the test, the pressure increases faster for materials with higher yield stresses. Subsequently, the level of the curves depends mainly of the hardening coefficient. The results also show that the materials with higher values of the hardening coefficient have greater pole heights when the pressure approaches the maximum value.

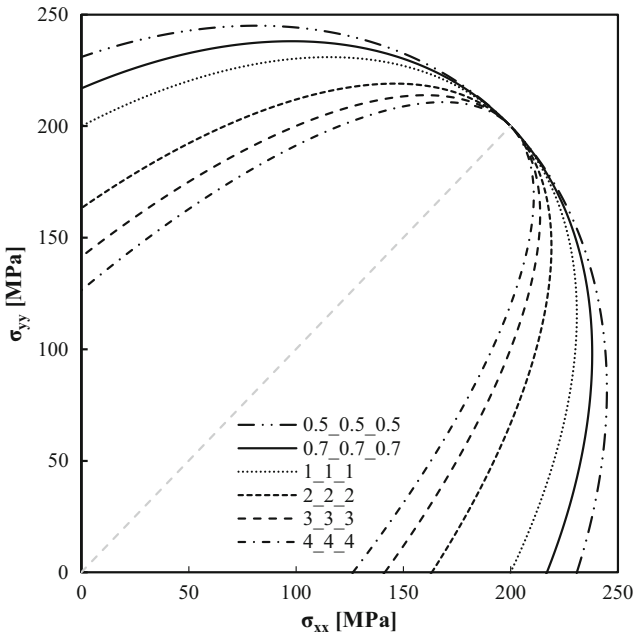

Fig. 11 Initial yield surfaces in plane (σ_{xx}; σ_{yy}) of the materials of Table 3

The analysis of pressure evolution during the test shows that, for a given n value of the material, the curves p vs. h overlap each other when the pressure, p, is normalized by the yield stress of the material, p/Y_0. Consequently, the value of the pressure at a given value of the pole height, and therefore also for the maximum pressure, is proportional to the value of the yield stress of the material, and so it is possible to normalize the curves by the maximum pressure value for each yield stress, i.e. using p/p_{max} instead of p, as shown in Fig. 4 for the cases of Fig. 3.

The same kind of behaviour is observed for the other initial sheet thicknesses ($t_0 = 0.5$ mm, 1.0 mm and 2.0 mm). Moreover, the analysis of pressure evolution during the test shows that, for a given n value of the material, the curves p vs. h overlap each other when the pressure, p, is normalized by the initial thickness value, p/t_0. Consequently, since the maximum pressure is proportional to the initial thickness value, it is possible to normalize the curves by the maximum pressure value for each initial thickness, i.e. using p/p_{max} instead of p, as shown in the examples of Fig. 5.

In summary, for isotropic materials with strain hardening described by the Swift law, the evolutions of the normalized pressure vs. pole height are only influenced by the value of the hardening coefficient, i.e. are independent of the yield stress and the initial thickness of the sheet.

Transverse anisotropic metal sheets

The numerical simulation of the bulge test was also carried out on metal sheets with transverse anisotropy (also known as planar isotropy), i.e. with the anisotropy coefficient $r(\alpha)$ constant in the plane of the sheet (α is the angle between the tensile direction, TD, and the rolling direction, RD): $r(\alpha) = r$ and different from 1. The hardening behaviour study includes materials as in Table 1 (an isotropic material is also considered). The initial sheet thickness is 1.0 mm. Table 2 shows the designation adopted for the material and their parameters of the Hill'48 criterion. The designation A_A_A_n corresponds to a material with the hardening coefficient equal to n and the anisotropy coefficient, $r = r(\alpha)$, in the sheet plane equal to A.

Table 4 Parameters of the Swift hardening law

Y_0 [MPa]	K [MPa]	n
200	260.7	0.05
	577.1	0.20
	1277.6	0.35
	2828.4	0.50

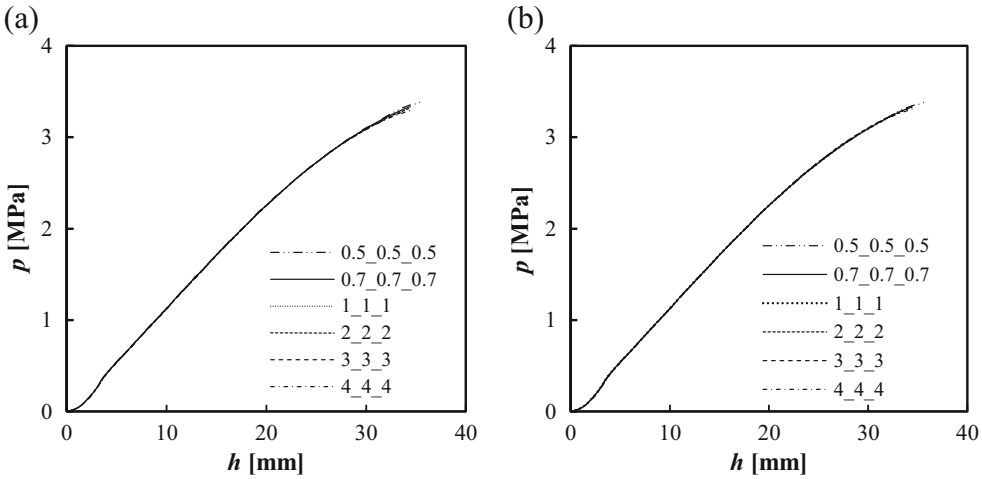

Fig. 12 Evolution of pressure, p, with pole height, h, for sheet metals with different transverse anisotropy and hardening coefficient $n = 0.05$ ($Y_0 = 200$ MPa and $t_0 = 1.0$ mm): (a) Curves as obtained; (b) Overlapping curves after multiplying the pressure and the pole height values by appropriated factors

The parameters of the Hill'48 criterion obey to the conditions $F = G$ and $N = F + 2H$. These conditions together with the condition $G + H = 1$, which is also assumed for the materials in Table 2, means that the tensile curves along any direction in the sheet plane are coincident, whatever the value of the anisotropy coefficient, $r = r(\alpha)$, for a given set of parameters of the Swift hardening law.

Figure 6 shows examples of the evolution of the pressure with the pole height, for the cases of planar isotropic materials (Table 2), with yield stress, $Y_0 = 200$ MPa and hardening coefficients, $n = 0.05$, 0.20 and 0.35 (see Table 1). The higher is the anisotropy coefficient the higher is the pressure required to achieve the maximum pole height, for a given value of the hardening coefficient.

As in the previous section, the curves in Fig. 6 were normalized using p/p_{max}, as shown in Fig. 7. It can be seen that for a given hardening coefficient, there is no full coincidence between curves. The influence of the anisotropy coefficient on the normalized curves increases when the value of n increases.

Moreover, for each value of n, the curves in Fig. 7 can be superimposed using a multiplying factor for the value of h, the results of which are shown in Fig. 8. The issues related with this multiplying factor will be analysed in the next section.

In summary, it is always possible the overlap the curves pressure vs. pole height, by multiplying the pressure and/or the pole height by conveniently chosen factors, for materials with equal values of the hardening coefficient of the Swift law. Conversely, the overlapping is not possible for different values of the hardening coefficient.

Identification strategy

The results described in the previous section suggested the development of an inverse strategy for the identification of the Swift law parameters, using the bulge test. The first step consists on a forward analysis, in order to study in detail how the pressure vs. pole height curves can be overlapped, for a given value of the hardening coefficient. The sensitivity of the

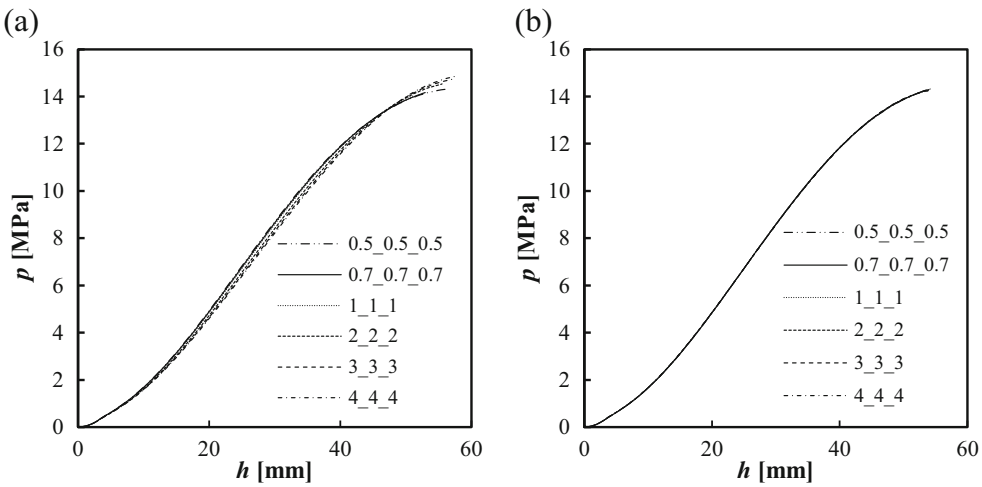

Fig. 13 Evolution of pressure, p, with pole height, h, for sheet metals with different transverse anisotropy and hardening coefficient $n = 0.35$ ($Y_0 = 200$ MPa and $t_0 = 1.0$ mm): (**a**) Curves as obtained; (**b**) Overlapping curves after multiplying the pressure and the pole height values by appropriated factors

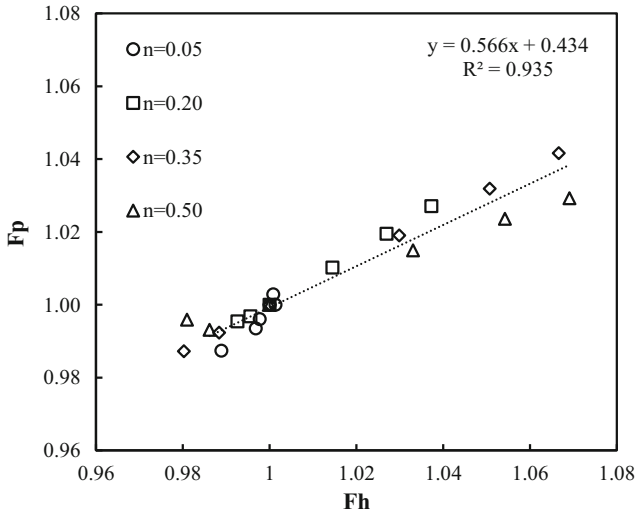

Fig. 14 Fp vs. Fh, for $n = 0.05$, 0.20, 0.35 and 0.50. The overlapping was performed such that the isotropic curve is superimposed on the anisotropic curves, which remain unchanged. For each n value, the following r values were used: $r = 0.5$, 0.7, 1, 2, 3 and 4

results of the pressure evolution during the test to variations of the hardening law parameters is studied. Also, the sensitivity of these results to the variations of the yield stress, anisotropy and sheet thickness, for a given value of the hardening coefficient is analysed. This forward study allowed the development of an inverse analysis methodology, applied to the identification of the Swift hardening law parameters, namely Y_0, K and n of Eq. (2).

Forward analysis

In this forward study, the analysis is focused on the coincidence between pressure vs. pole height curves of:

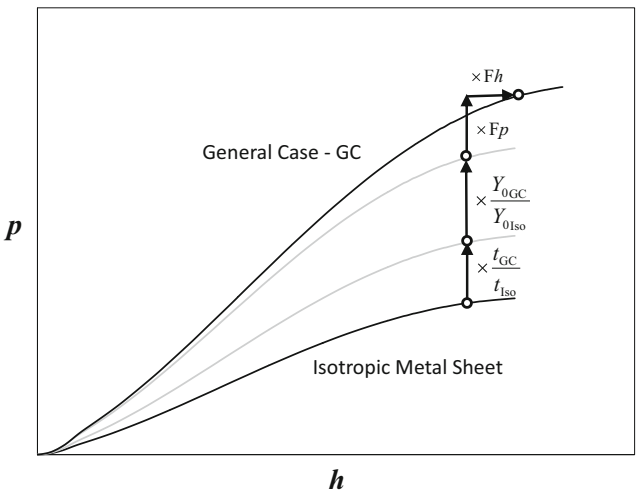

Fig. 15 Schematic representation for generating the pressure vs. pole height curve of any anisotropic metal sheet (General Case - GC) from the knowledge of the curve concerning an Isotropic Metal sheet with different yield stress and thickness, in case of equal hardening coefficients

(i) Isotropic metal sheets with different yield stresses and thicknesses;
(ii) Isotropic and transverse anisotropic metal sheets.

Isotropic metal sheets

The results in Figs. 4 and 5 show that, in case of full isotropic materials, (i.e. the behaviour can be described by von Mises yield criterion) with equal values of the hardening coefficient, the pressure vs. pole height curves can be superposed whatever the yield stress and the sheet thickness. In order to superpose the curves, a multiplicative factor should be applied to the pressure, which depends on and is proportional to the ratios between yield stresses and sheet thicknesses of the materials. Figures 9 and 10 give examples of such behaviour, for the yield stress and the thickness, respectively. In these figures, the cases of metal sheets with $Y_0 = 300$ MPa (Fig. 9(a)) and $t_0 = 2.0$ mm (Fig. 10(a)), are taken as reference, respectively. It should be noted the perfect overlapping of the curves when the multiplicative factor is applied (Figs. 9(b) and 10(b)). This factor is equal to the yield stresses ratio and thicknesses ratio, in Figs. 9 and 10, respectively.

Transverse anisotropic metal sheets

The results in Fig. 7 show that, in case of anisotropic metal sheets, the use of a pressure factor is not enough to superpose the pressure vs. pole height curves. Nevertheless, Fig. 8 shows that the simultaneous use of a multiplying factor for the pole height allows the overlapping. In this section a detailed study concerning this aspect is performed.

Table 5 Designation of isotropic materials used for identification and respective parameters of the Swift hardening law

Isotropic materials	Swift hardening law parameters		
	Y_0 [MPa]	K [MPa]	n
100_0.12_1_1_1	100	188.85	0.12
100_0.13_1_1_1	100	199.13	0.13
100_0.14_1_1_1	100	209.96	0.14
100_0.15_1_1_1	100	221.39	0.15
100_0.16_1_1_1	100	233.43	0.16
100_0.17_1_1_1	100	246.14	0.17
100_0.18_1_1_1	100	259.53	0.18
100_0.19_1_1_1	100	273.65	0.19
100_0.20_1_1_1	100	288.54	0.20
100_0.21_1_1_1	100	304.24	0.21
100_0.22_1_1_1	100	320.79	0.22
100_0.23_1_1_1	100	338.25	0.23

Table 6 Designation of tested materials used as numerical case studies and respective parameters of Hill'48 criterion and Swift hardening law

Tested materials	Hill'48 criterion parameters				Swift hardening law parameters		
	F	G	H	N	Y_0 [MPa]	K [MPa]	n
200_0.20_3_3_3	0.5000	0.5000	1.5000	3.5000	200	577.08	0.20
200_0.20_1.5_3_3	0.3446	0.6892	1.0338	3.6185			

The sheet thickness is equal to 2.0 mm

The study is focused on the comparison between numerical curves of pressure vs. pole height, obtained for the full isotropy and planar isotropy conditions. Table 3 summarizes the parameters of the Hill'48 criterion of illustrative cases. The Hill'48 criterion parameters obey to the condition ($F + G = 1$), as is noticeable from Table 3, which means that the yield surfaces for all materials go through the same point, which corresponds to equibiaxial stretching ($\sigma_{xx} = \sigma_{yy}$), as shown in Fig. 11. Consequently, the biaxial stress vs. strain curve is the same for all materials and coincident with the Swift hardening law used as input [26]. For each case of Table 3, the hardening coefficients are $n = 0.05$, 0.20, 0.35 and 0.50, and the parameters Y_0 and ε_0 of the Swift law are $Y_0 = 200$ MPa and $\varepsilon_0 = 0.005$. The full set of parameters of the Swift law are shown in Table 4. The initial sheet thickness is 1.0 mm.

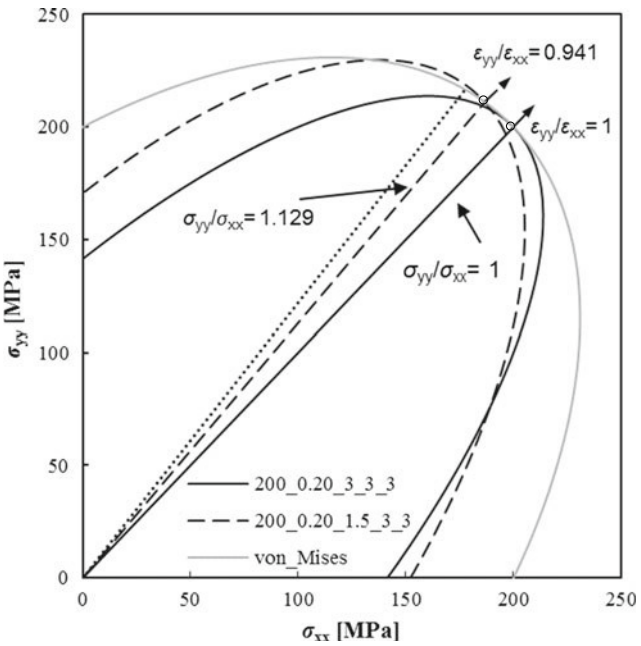

Fig. 16 Initial yield surfaces in the plane (σ_{xx}; σ_{yy}) of the materials of Table 6 and equivalent von Mises material. The stress and strain paths are also shown as well as the axis (dotted line) of the yield surface of the material 1.5_3_3. The two open circles denote the coincidence between the isotropic and the two anisotropic materials

Figures 12 and 13 show examples of the pressure vs. pole height curves, for metal sheets with transverse anisotropy (see Table 3), in cases of hardening coefficient $n = 0.05$ and 0.35 (see Table 4), respectively. Figures 12(a) and 13(a) show the curves just as were obtained. In case of $n = 0.05$, these curves are almost indistinguishable. In case of $n = 0.35$, although still close to each other, the curves are distinguishable. However, the curves entirely overlap to each other when the values of pressure and pole height are multiplied by appropriate factors, respectively Fp and Fh, as shown in Figs. 12(b) and 13(b), where the curve for the full isotropic material (1_1_1, i.e. with $r = 1$) was kept unchanged. Both factors are close to 1, particularly in case of $n = 0.05$. Their importance within the framework of the forward and reverse analyses will be discussed below.

A typical procedure for finding the Fh and Fp factors that applied to the isotropic numerical pressure vs. pole height curve minimises the difference between this curve and those of transverse anisotropic materials, which remain unchanged, consists on using the following least squares cost function:

$$F(\mathbf{A}) = (1/q)\left[\sum_{i=1}^{q}\left(p_i^{\text{anis}} - p_i^{\text{iso}}(\mathbf{A})\right)^2\right]^{\frac{1}{2}} \quad (3)$$

where p_i^{anis} and $p_i^{\text{iso}}(\mathbf{A})$ are the values of pressure for anisotropic and isotropic sheet metals, respectively; $\mathbf{A}$ is the set of factors Fh and Fp to be optimised, i is the measuring point of

Table 7 Fh and Fp* values that minimize $F(\mathbf{A})$ and corresponding estimated Swift law parameters for the material 200_0.20_3_3_3 (see Table 6)

Numerical simulation	Fh	Fp*	F(A)	Swift law - estimated		
				Y_0 [MPa]	K [MPa]	n
100_0.19_1_1_1	1.073	4.382	2.62×10^{-4}	210.52	576.08	0.19
100_0.20_1_1_1	1.047	4.144	1.42×10^{-4}	202.00	582.85	0.20
100_0.21_1_1_1	**1.021**	**3.917**	$\mathbf{4.19 \times 10^{-5}}$	**193.56**	**588.88**	**0.21**
100_0.22_1_1_1	0.994	3.694	1.73×10^{-4}	185.50	595.07	0.22
100_0.23_1_1_1	0.966	3.476	3.45×10^{-4}	177.39	600.00	0.23

Table 8 Fh and Fp* values that minimize $F(\mathbf{A})$ and corresponding estimated Swift law parameters for the material 200_0.20_1.5_3_3 (see Table 6)

Numerical simulation	Fh	Fp*	F(A)	Swift law - estimated		
				Y_0 [MPa]	K [MPa]	n
100_0.19_1_1_1	1.064	4.321	2.17×10^{-4}	208.68	571.06	0.19
100_0.20_1_1_1	1.037	4.084	1.25×10^{-4}	200.20	577.65	0.20
100_0.21_1_1_1	**1.011**	**3.860**	$\mathbf{4.29 \times 10^{-5}}$	**191.96**	**584.02**	**0.21**
100_0.22_1_1_1	0.984	3.639	1.84×10^{-4}	183.77	589.51	0.22
100_0.23_1_1_1	0.955	3.422	3.54×10^{-4}	175.63	594.08	0.23

pressure (which corresponds to a certain value of the pole height, h) and q is the total number of pressure measuring points. The evaluation of the pressure for equal values of pole height can be carried out expeditiously using a polynomial approximation for each curve. In this study all evolutions of pressure with pole height were fitted using a sixth degree polynomial to achieve a proper fit of the results (with a minimum correlation factor $R^2 = 0.9999$) within a range of pole height values that excludes the initial part of the curve, more prone to higher experimental errors, and the final part, which may be sensitive to numerical parameters such as the mesh refinement.

Figure 14 plots the results of Fp as a function of Fh, for the values of the hardening coefficients ($n = 0.05$, 0.20, 0.35 and 0.50) and anisotropy coefficients ($r = 0.5$, 0.7, 1.0, 2.0, 3.0 and 4.0) under study. The results in this figure are grouped by the hardening coefficient and show that this parameter slightly influences their evolution. In case of $n = 0.05$, the values of Fp and Fh are slightly higher than 1 and increasing with decreasing of the r value, for $r < 1$, and are slightly lower than 1 and decreasing with increasing of the r value, when $r > 1$. On the contrary, in cases of $n = 0.20$, 0.35 and 0.50, the values of Fp and Fh are slightly lower than 1 and decreasing with decreasing of the r value, when $r < 1$, and are slightly higher than 1 and increasing with the increasing of r value, when $r > 1$. In other words, the results in Fig. 14 shows that the values of Fh and Fp are related with the shape of the yield surface near the equibiaxial region (see Fig. 11): for sharp yield surfaces, as for example the material 4_4_4, relatively high values of Fh and Fp are observed, and for flattened yield surfaces, as for example the material 0.5_0.5_0.5, relatively low values of Fh and Fp occur (close to 1), in cases of the values of the hardening coefficient are $n = 0.20$, 0.35 and 0.50; the opposite is observed for $n = 0.05$, with the values of Fh and Fp close to 1 whatever the yield surface shape near the equibiaxial region.

The results in Fig. 14 are enough well described by a linear fit:

$$\mathrm{Fp} = 0.566\ \mathrm{Fh} + 0.434 \tag{4}$$

In fact, this equation allows determining with acceptable accuracy the value of the parameter Fp knowing the value of Fh. In Fig. 14, the relative distance between the Fp values at each point (i.e. at a given Fh value) and the corresponding value on the trend line is always less than 1 %, whatever the value of the hardening coefficient and the anisotropy.

Final remarks

In summary, it can be concluded that the evolution of the pressure with the pole height during the bulge test, depends

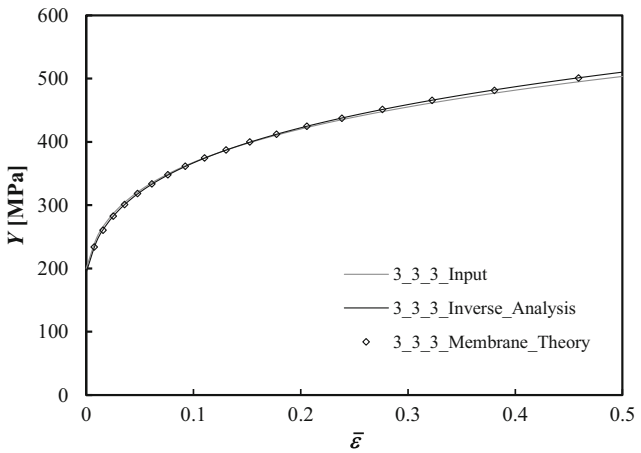

Fig. 17 Hardening curves obtained by the inverse analysis and the membrane theory and the input numerical curve for the material 200_0.20_3_3_3

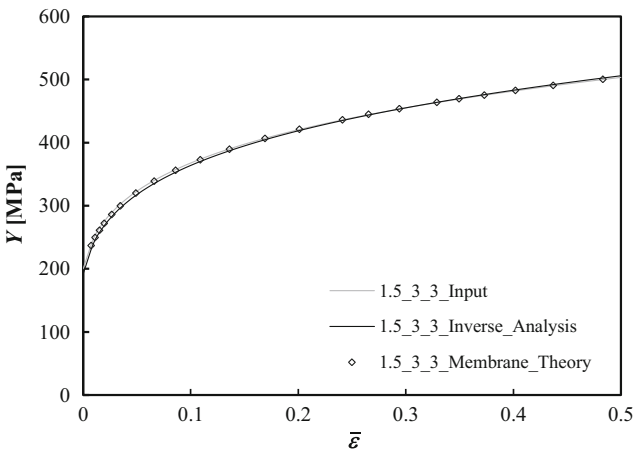

Fig. 18 Hardening curves obtained by the inverse analysis and the membrane theory and the input numerical curve for the material 200_0.20_1.5_3_3

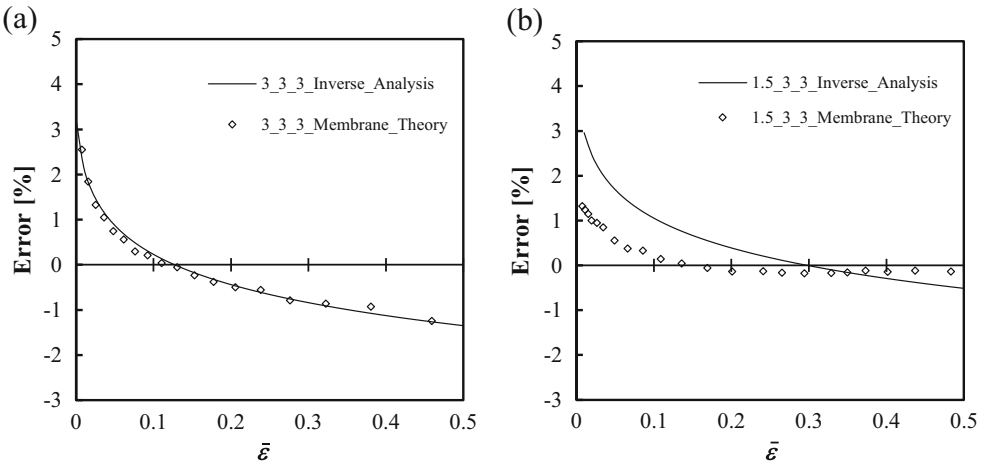

Fig. 19 Evolution of the error in stress obtained by the inverse analysis and the membrane theory for the cases: (**a**) 200_0.20_3_3_3; (**b**) 200_0.20_1.5_3_3

on the parameters of the Swift law, the anisotropy of the material, and the sheet thickness. It is always possible to overlap the curve of the pressure vs. pole height for materials with the same value of the hardening coefficient of the Swift law, by multiplying the values of the pressure and the pole height by factors, Fp and Fh, respectively, appropriately chosen; the overlapping does not occur for materials with different values of the hardening coefficient.

In case of isotropic materials (von Mises) with equal values of the hardening coefficient, the coincidence between pressure vs. pole height curves can be obtained by using a multiplying factor for the pressure, Fp, which is equal to the yield stresses ratio of the material (at equal thicknesses) and to the sheet thicknesses ratio (at equal yield stresses); in both cases, the multiplying factor for the pole height, Fh, is equal to 1.

The curves of pressure vs. pole height of anisotropic materials can also be overlapped to those of isotropic materials, providing that the hardening coefficient is equal. In this case, the Fp and Fh are in general different from 1. For equal values of the biaxial yield stress and the sheet thickness, the relationship between Fp and Fh is almost independent of the hardening coefficient and suitably described by a linear equation (see Fig. 14).

The key finding of the forward analysis is summarized schematically in Fig. 15. This figure describes how to generate the pressure vs. pole height curve of any sheet metal with a given yield stress, anisotropy and thickness (General Case - GC), from the results of an isotropic sheet metal (Isotropic Metal Sheet) with different thickness and yield stress, for a given hardening coefficient. The curve of the general case is obtained by multiplying the pressure values of the curve of the isotropic sheet metal by the following factors: (t_{GC}/t_{Iso}) and (Y_{0GC}/Y_{0Iso}) ratios and Fp (where t_{GC} and Y_{0GC} are the thickness and the yield stress of the general case and t_{Iso} and Y_{0Iso} are the thickness and the yield stress of the isotropic sheet metal, respectively); and the pole height values of the same curve must be multiplied by Fh. Under these conditions, the overall factor, Fp*, to be applied to the pressure is:

$$\mathrm{Fp}^* = (t_{GC}/t_{Iso}) \times (Y_{0GC}/Y_{0Iso}) \times \mathrm{Fp} \tag{5}$$

Inverse analysis

Following the previous forward analysis, an approach for solving the problem of identification of the parameters of the Swift law consists in using numerical pressure vs. pole height curves obtained for isotropic materials with various values of hardening coefficient, in the range of the material under study. Then, using multiplying factors for the pressure and the pole height, the best overlapping between the experimental curve and those numerically obtained, allows assessing the hardening and the yield stress parameters of the material.

Table 9 Fh and Fp* values that minimize F(**A**) and corresponding estimated Swift law parameters for the material 344.6_0.20_1_1_1

Numerical simulation	Fh	Fp*	F(A)	Swift law - estimated			
				Y_0 [MPa]	K [MPa]	n	ε_0
100_0.16_1_1_1	1.096	1.872	1.75×10^{-3}	355.43	829.70	0.16	0.005
100_0.17_1_1_1	1.062	1.762	9.24×10^{-4}	340.74	838.68	0.17	0.005
100_0.18_1_1_1	**1.031**	**1.661**	$\mathbf{3.43 \times 10^{-4}}$	326.67	847.79	**0.18**	0.005
100_0.19_1_1_1	1.002	1.567	9.74×10^{-4}	313.16	856.96	0.19	0.005
100_0.20_1_1_1	0.973	1.474	2.01×10^{-3}	299.61	864.48	0.20	0.005

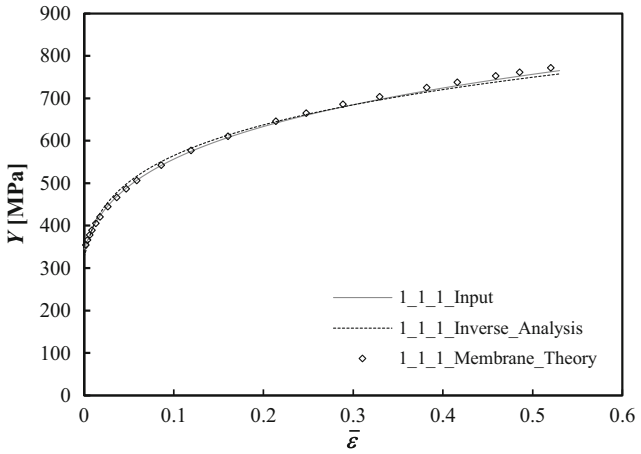

Fig. 20 Hardening curves obtained by the inverse analysis and the membrane theory and the input numerical curve for the material 344.6_0.20_1_1_1

The proposed inverse methodology can be detached in four steps:

(i) Plot the experimental pressure vs. pole height curve for the material under test.

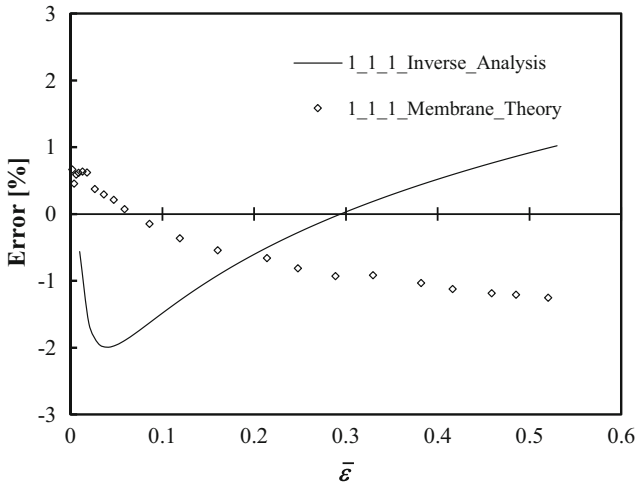

Fig. 21 Evolution of the error in stress obtained by the inverse analysis and the membrane theory for the case 344.6_0.20_1_1_1

(ii) Plot the same type of numerical curves of isotropic materials with selected values of the yield stress and the sheet thickness, for various values of hardening coefficient in the range expected for the material under test; the ε_0 value of the Swift law must be kept constant (ε_0 equal to 0.005 is recommended); the elastic properties of the material tested, Young's modulus and Poisson ratio, are assumed to be known (the typical values for each class of materials - e.g. steel, aluminium alloys - can be used); a unique set of numerical curves can be used for a given class of materials, within a relatively wide range of hardening coefficients, i.e. covering the values usually found within each class, without having to remake the simulations every time an identification is performed; the values of the hardening coefficient should be away from each other 0.01, but if the cost function (see Eq. (6) of the next step) presents two similar minima values, it is recommended to test an intermediate value of the hardening coefficient; the range of pole height of the numerical curves of isotropic materials used for the inverse analysis should go up to a strain value higher than twice the value of the hardening coefficient of the Swift law.

(iii) Estimation of the hardening coefficient of the experimental material under study. This consists on finding the factors Fh and Fp* that applied to the numerical curves, with the various hardening coefficient, minimise the difference between these curves and the experimental curve of pressure vs. pole height; the following least squares cost function, similar to Eq. (3), was used:

$$F(\mathbf{A}) = (1/\mathrm{q})\left[\sum_{i=1}^{\mathrm{q}} \left(p_i^{\exp} - p_i^{\mathrm{num}}(\mathbf{A})\right)^2\right]^{\frac{1}{2}} \tag{6}$$

where $p_i^{\exp}$ and $p_i^{\mathrm{num}}(\mathbf{A})$ are the experimental and numerical values of pressure, respectively; **A** is the set of factors Fh and Fp^* to be optimised, i is the measuring point of pressure (which corresponds to a certain value of the pole height, h) and q is the total number of pressure measuring points.

Table 10 Designation of tested materials used as numerical case studies and respective parameters of Drucker + L criterion and Swift hardening law

Tested materials	Drucker + L criterion parameters					Swift hardening law parameters		
	C_1	C_2	C_3	C_6	c	Y_0 [MPa]	K [MPa]	n
Isot_c = −2	0.9577	0.9577	0.9577	0.9577	−2	200	577.08	0.20
Isot_c = 2	1.0603	1.0603	1.0603	1.0603	2			
Anisot_c = −2	0.8294	1.1139	1.3985	1.4896	−2			
Anisot_c = 2	0.9145	1.2283	1.5421	1.6425	2			

The sheet thickness is equal to 2.0 mm

The values of the Lankford' coefficients of the in-plane anisotropic materials are: (i) Anisot_c = 2 → $r_0 = 1.33$, $r_{45} = 2.17$ and $r_{90} = 2.07$; (ii) Anisot_c = 2 → $r_0 = 1.88$, $r_{45} = 5.92$ and $r_{90} = 6.99$.

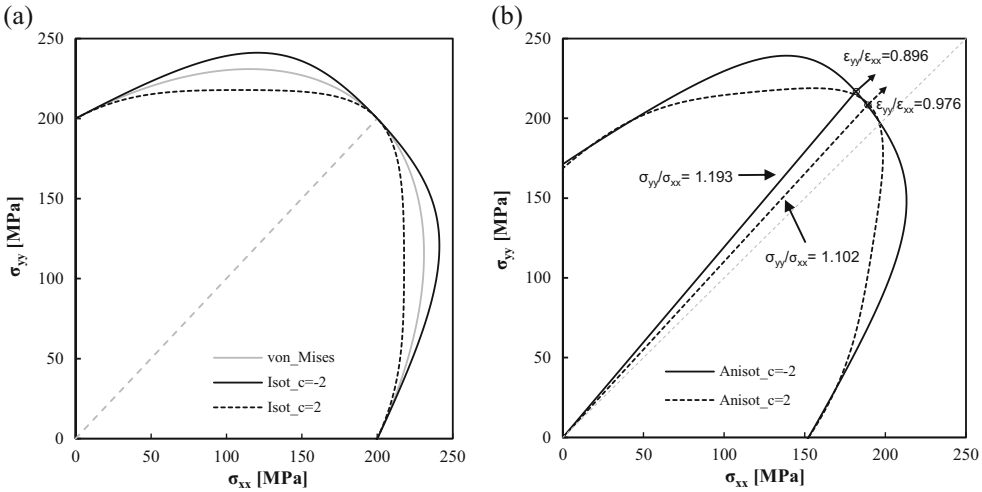

Fig. 22 Initial yield surfaces in the plane (σ_{xx}; σ_{yy}) of the Drucker + L materials of Table 10: (a) isotropic materials (the "equivalent" von Mises material is also shown); (b) anisotropic materials (the stress and strain paths are also shown)

The lowest value of the cost function $F(\mathbf{A})$, among all numerical curves used, defines the numerical curve that can be used as reference, i.e. allows to generate the experimental curve, following the procedure shown in Fig. 15. The hardening coefficient of this reference curve is the identified parameter of the experimental material.

(iv) Estimation of the yield stress of the experimental material under study. The Fh value allows determining the value of Fp (Eq. (4) and Fig. 14), which correspond to the anisotropy effect on the pressure vs. pole height curves. Under these assumptions, the yield stress of the experimental material can be identified as follows:

$$Y_0^{\exp} = Y_0^{\text{num}} \times \left(t^{\text{num}}/t^{\exp}\right) \times \left(\text{Fp}^*/\text{Fp}\right) \tag{7}$$

where $Y_0^{\exp}$ and Y_0^{num} are the yield stresses and $t^{\exp}$ and t^{num} are the thicknesses, of the experimental and the numerical reference sheet, respectively. The Fp* value used in Eq. (7) must be obtained such that the numerical curve is superimposed on the experimental curve, which remains unchanged. Finally, as the value of the Swift law parameter, ε_0, is considered fixed (equal to 0.005 in the current work), the estimated value of $K^{\exp}$ in this law (Eq. (2)) can also be obtained by multiplying K^{num} by the same value as for Y_0^{num} (Eq. (7)):

Table 11 Fh and Fp* values that minimize $F(\mathbf{A})$ and corresponding estimated Swift law parameters for the material Isot_c = −2 (see Table 10)

Numerical simulation	Fh	Fp*	F(A)	Swift law - estimated		
				Y_0 [MPa]	K [MPa]	n
100_0.19_1_1_1	1.018	4.199	1.88×10^{-4}	207.97	569.12	0.19
100_0.20_1_1_1	0.990	3.960	8.53×10^{-5}	199.31	575.09	0.20
100_0.205_1_1_1	**0.974**	**3.839**	$\mathbf{5.14 \times 10^{-5}}$	**194.92**	**577.53**	**0.205**
100_0.21_1_1_1	0.962	3.734	9.89×10^{-5}	190.90	580.78	0.21
100_0.22_1_1_1	0.934	3.512	2.41×10^{-4}	182.55	585.62	0.22

Note: the parameters of the Swift hardening law used as input in numerical simulation **100_0.205_1_1_1** (not included in Table 5) are: $\boldsymbol{Y_0} = 100$ MPa, $\boldsymbol{K} = 296.29$ MPa, and $\boldsymbol{n} = 0.205$.

Table 12 Fh and Fp* values that minimize $F(\mathbf{A})$ and corresponding estimated Swift law parameters for the material Isot_c = 2 (see Table 10)

Numerical simulation	Fh	Fp*	F(A)	Swift law - estimated		
				Y_0 [MPa]	K [MPa]	n
100_0.19_1_1_1	1.065	4.362	2.62×10^{-4}	210.46	575.93	0.19
100_0.20_1_1_1	1.035	4.112	1.28×10^{-4}	201.73	582.08	0.20
100_0.21_1_1_1	**1.007**	**3.877**	$\mathbf{5.08 \times 10^{-5}}$	**193.27**	**588.00**	**0.21**
100_0.22_1_1_1	0.978	3.651	2.05×10^{-4}	184.97	593.37	0.22
100_0.23_1_1_1	0.947	3.421	3.90×10^{-4}	176.50	597.02	0.23

Table 13 Fh and Fp* values that minimize $F(\mathbf{A})$ and corresponding estimated Swift law parameters for the material Anisot_c = −2 (see Table 10)

Numerical simulation	Fh	Fp*	F(A)	Swift law - estimated		
				Y_0 [MPa]	K [MPa]	n
100_0.19_1_1_1	1.035	4.232	4.85×10^{-4}	207.50	567.82	0.19
100_0.20_1_1_1	1.012	4.011	1.83×10^{-4}	199.21	574.81	0.20
100_0.205_1_1_1	**1.001**	**3.904**	$\mathbf{6.67 \times 10^{-5}}$	**195.17**	**578.25**	**0.205**
100_0.21_1_1_1	0.990	3.802	1.56×10^{-4}	191.21	581.73	0.21
100_0.22_1_1_1	0.969	3.606	4.58×10^{-4}	183.51	588.67	0.22

Note: the parameters of the Swift hardening law used as input in numerical simulation **100_0.205_1_1_1** (not included in Table 5) are: $\boldsymbol{Y0} = 100$ MPa, $\boldsymbol{K} = 296.29$ MPa, and $\boldsymbol{n} = 0.205$

$$K^{\exp} = K^{\text{num}} \times \left(t^{\text{num}}/t^{\exp}\right) \times \left(\text{Fp}^*/\text{Fp}\right) \tag{8}$$

In order to exemplify this inverse methodology, computer-generated results are firstly used. The use of computer-generated results is a simple and efficient way to test inverse analysis methodologies, since the behaviour of the tested material is properly defined, without the errors commonly associated with experimental measurements. Subsequently, the same methodology is applied to experimental cases.

Numerical cases

Table 5 shows the selected Swift law parameters for generating numerical pressure vs. pole height curves (under isotropy condition - see step (ii) of the proposed inverse methodology) used to identify the parameters of the computer-generated results. The selected yield stress value of all materials in this table is equal to 100 MPa and the hardening coefficient is within $n = 0.12$ and $n = 0.23$. The numerical simulations were performed with an initial sheet thickness equal to 1.0 mm.

Hill'48 criterion Table 6 shows the parameters of the Hill's criterion and the Swift law for the two tested materials, one with transverse anisotropy (200_0.20_3_3_3) and the other with planar anisotropy (200_0.20_1.5_3_3). The parameters of the Hill criterion of these materials follow a condition ensuring that the equivalent stress–strain curve for the stress path obtained in the bulge test is equal to that for an equivalent von Mises material, i.e. with the same values of the Swift law parameters. Figure 16 shows the initial yield surface of both materials in the (σ_{xx}; σ_{yy}) plane as well as the equivalent von Mises material. In case of the material 200_0.20_3_3_3, the stress and strain paths observed during the bulge test are $\sigma_{yy}/\sigma_{xx} = d\varepsilon_{yy}/d\varepsilon_{xx} = 1$; in case of material 200_0.20_1.5_3_3, these paths are respectively: $\sigma_{yy}/\sigma_{xx} = 1.129$ and $d\varepsilon_{yy}/d\varepsilon_{xx} = 0.941$. Table 5 shows the parameters of the Swift law of the selected isotropic materials (with $n = 0.19$, 0.20, 0.21, 0.22 and 0.23) used for numerical simulation and identification of the Hill'48 materials in Table 6.

Tables 7 and 8 show the values of the factors Fh and Fp* that were applied to the numerical pressure vs. pole height curves of the materials in Table 5, in order to minimise the difference between these curves and that of each material in Table 6. The corresponding values of the objective function $F(\mathbf{A})$ and the estimated parameters of the Swift hardening law are also shown in the Tables 7 and 8. The parameters of the Swift law that minimise $F(\mathbf{A})$ correspond to the material with $n = 0.21$, for both case studies. Also, the minimum values of $F(\mathbf{A})$ are similar for both identifications.

In order to visualise the results of the identifications, Figs. 17 and 18 show the hardening curves as obtained by the inverse analysis and by the membrane theory [27]. The analysis by the membrane theory follows the procedure recommended by ISO 16808:2014 [1]. Therefore, the equivalent stress is calculated assuming an equibiaxial stress state at the pole of the cap and using the average value of the curvature radii in the Oxz and Oyz planes as input in the membrane theory equation. The equivalent strain is considered equal to the absolute value of the plastic thickness strain, which is

Table 14 Fh and Fp* values that minimize $F(\mathbf{A})$ and corresponding estimated Swift law parameters for the material Anisot_c = 2 (see Table 10)

Numerical simulation	Fh	Fp*	F(A)	Swift law - estimated		
				Y_0 [MPa]	K [MPa]	n
100_0.19_1_1_1	1.100	4.445	7.21×10^{-4}	210.31	575.50	0.19
100_0.20_1_1_1	1.073	4.203	4.52×10^{-4}	201.79	582.25	0.20
100_0.21_1_1_1	**1.048**	**3.976**	$\mathbf{2.81 \times 10^{-4}}$	**193.58**	**588.94**	**0.21**
100_0.22_1_1_1	1.024	3.763	3.86×10^{-4}	185.67	595.63	0.22
100_0.23_1_1_1	1.001	3.563	6.32×10^{-4}	178.05	602.25	0.23

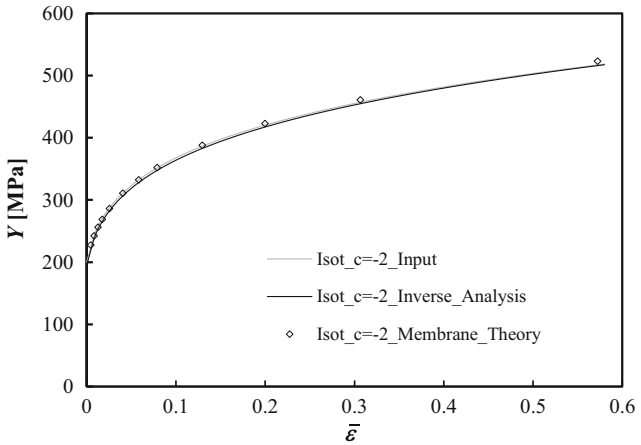

Fig. 23 Hardening curves obtained by the inverse analysis and the membrane theory and the input numerical curve for the material Isot_c = −2

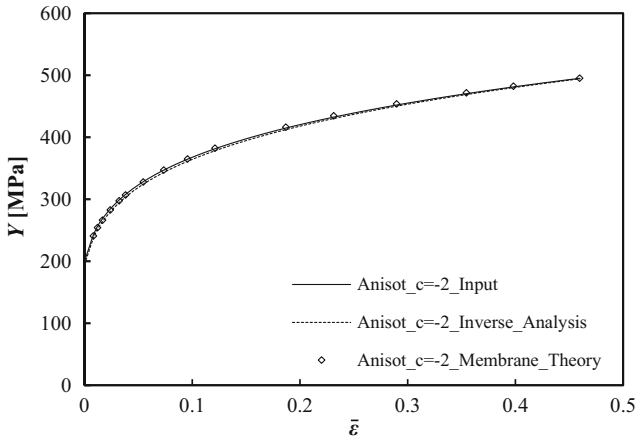

Fig. 25 Hardening curves obtained by the inverse analysis and the membrane theory and the input numerical curve for the material Anisot_c = −2

determined from the numerical measured values of surface strains at the pole of the cap, ε_1 and ε_2, and corrected for the elastic components, assuming an isotropic linear elastic material behaviour. In summary, this corresponds to the use of the von Mises definitions of equivalent stress and strain under the assumption of equibiaxial stress state. The corresponding input curves, used in the numerical simulations, of the studied materials (see Table 6) are also shown in these figures. Figure 19 compares the errors in stress obtained by the inverse analysis and using the membrane theory, referred to the input curves. The errors are similar for both materials when using the inverse analysis, which is consistent with the fact that the objective function is equal for the best fitting (see Tables 7 and 8, for $n = 0.21$). The n value obtained by the inverse analysis ($n = 0.21$ for both materials) are not entirely in accordance, but are very close to the input value ($n = 0.20$). Moreover, this does not lead to significant error in the estimate of the hardening curve. For both materials, 200_0.20_3_3_3 (Fig. 19(a)) and 200_0.20_1.5_3_3 (Fig. 19(b)), the inverse analysis gives comparable accuracy than the methodology using the membrane theory.

So far, the value of the parameter ε_0 has been considered fixed and equal to 0.005. In fact, this value is close to the values found for most cases of identification of sheet metals able to achieve large deformations, such as those used in deep drawing. Moreover, the experimental values of the parameter ε_0 are lower than 0.01, with extremely rare exceptions [28]. In order to understand the extent to which the value of this parameter can affect the inverse analysis results, identification cases with the value of the parameter ε_0 lower than 0.01 (and different from 0.005) were performed. The following illustrative example consists of an isotropic material with 0.5 mm thick sheet and the following Swift law parameters: $Y_0 = 344.61$ MPa, $K = 865.62$ MPa, $n = 0.20$ and $\varepsilon_0 = 0.01$ (hereafter referred to as: 344.6_0.20_1_1_1). As this is an isotropic material, the anisotropy will not affect the identification (anisotropic cases were addressed in the previous examples). Table 5 shows the parameters of the Swift law of the

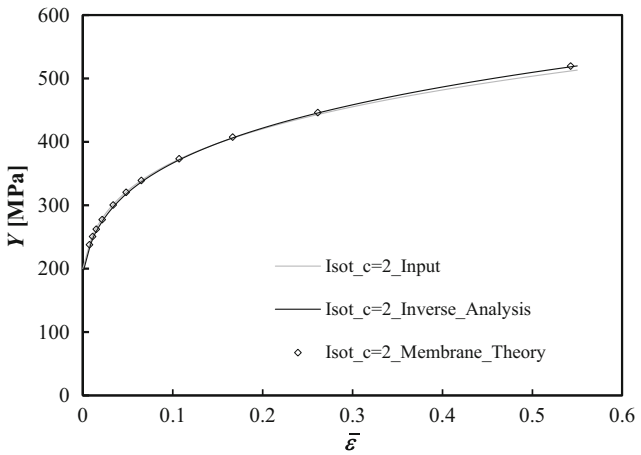

Fig. 24 Hardening curves obtained by the inverse analysis and the membrane theory and the input numerical curve for the material Isot_c = 2

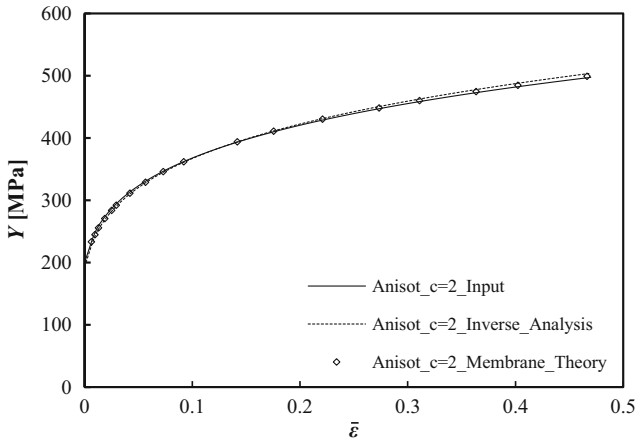

Fig. 26 Hardening curves obtained by the inverse analysis and the membrane theory and the input numerical curve for the material Anisot_c = 2

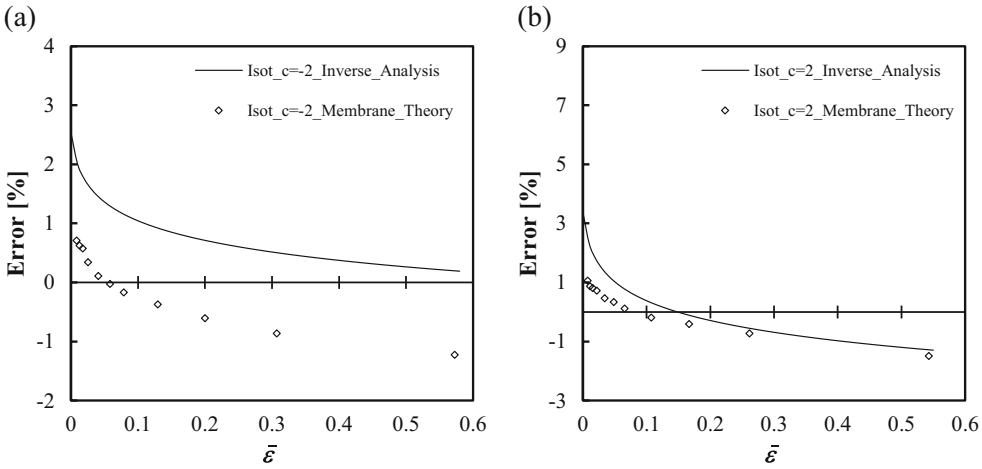

Fig. 27 Evolution of the error in stress obtained by the inverse analysis and the membrane theory for the cases: (**a**) Isot_c = −2; (**b**) Isot_c = 2

selected isotropic materials (with $n = 0.16$, 0.17, 0.18, 0.19 and 0.20) used for numerical simulation and identification of this material.

Table 9 shows the values of the objective function $F(\mathbf{A})$ and the estimated parameters of the Swift hardening law. The parameters of the Swift law that minimise $F(\mathbf{A})$ correspond to the material with $n = 0.18$. The smallest value of $F(\mathbf{A})$ occurs for the case 100_0.18_1_1_1, and is equal to 3.43×10^{-4}. This value is higher than the obtained for the previous cases of identification (slightly higher than 4×10^{-5} – see Tables 7 and 8), in which the material to be identified has the ε_0 value equal to that of the materials used in identification ($\varepsilon_0 = 0.005$). However, the input hardening curve is well described by the inverse analysis results, as can be concluded from Figs. 20 and 21. Figure 20 shows the input hardening curve and those obtained by the inverse analysis and the membrane theory and Fig. 21 compares the errors in stress obtained by the inverse analysis and the membrane theory, referred to the input curve. Table 9 also shows the values of the factors Fh and Fp* that were applied to the numerical curves pressure vs. pole height of the materials in Table 5, in order to minimise the difference between these curves and that of the material under study. This leads to an identification value for the Fh factor equal to 1.031, which is not so close to 1, as expected for the von Mises identified material. This is due in part (besides the error inherent to identification strategy) to the difference in the values of the parameter ε_0 of the material to be identified and the materials whose numerical curves are used for identification. It turns out that, in general case of identification, the ε_0 value of the material to be identified is unknown. Despite this, the input hardening curve is well described for values of ε_0 lower than that of the experimental material, 0.01, i.e. using $\varepsilon_0 = 0.005$ to generate the numerical curves for identification, as in this illustrative case. Finally, it should be mentioned that the identification can be improved by using, in a second stage of the identification, values of ε_0 greater and lower than 0.005 (separated from 0.0025, for example) for the materials used in the identification. That is, the above procedure can be repeated for different values of ε_0, and the values of $F(\mathbf{A})$ must be used as guidance for the final choice of parameters.

Other yield criterion The proposed inverse methodology makes use of reference numerical tests of isotropic

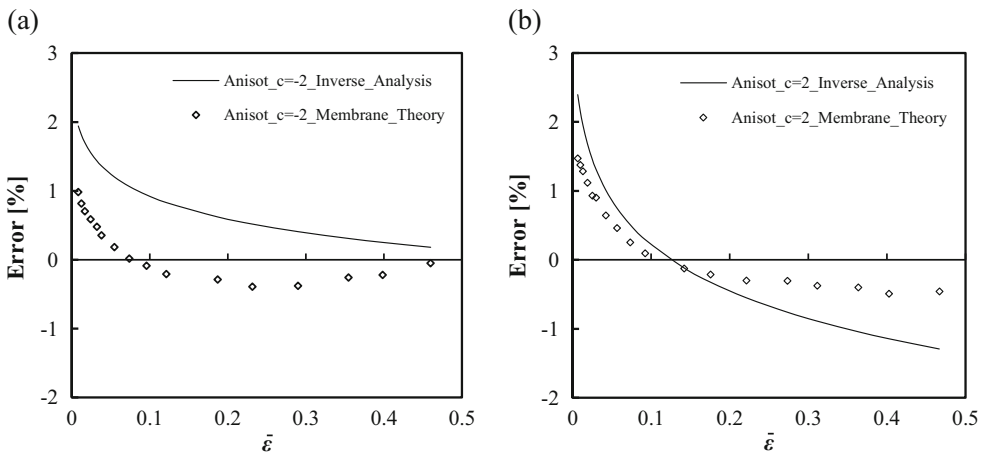

Fig. 28 Evolution of the error in stress obtained by the inverse analysis and the membrane theory for the cases: (**a**) Anisot_c = −2; (**b**) Anisot_c = 2

Table 15 Materials studied and anisotropy characterization ($\bar{r} = (r_0 + 2r_{45} + r_{90})/4$ where r are the anisotropy coefficients; the numbers in subscript indicate the angle between the tensile axis and the rolling direction)

Material	t_0 [mm]	r_0	r_{45}	r_{90}	$\bar{r}$
DP600 steel	0.80	0.62	1.03	0.80	0.87
AA6061 aluminium alloy	1.04	0.66	0.69	0.56	0.65

materials and the influence of the anisotropy of the material on the procedure is taken into account by means of the Fh and Fp factors. In this context, the inverse parameters identification of materials with behaviour described by other criterion than Hill'48 was also numerically performed. The non-quadratic yield criterion Drucker + L [29] was chosen to test the inverse analysis procedure and concomitantly to reinforce the conclusion that the value of the Fh and Fp factors are related with the shape of the yield surface near the equibiaxial region (see section: Transverse anisotropic metal sheets) and so their relationship does not depend on the yield criteria. In fact, the Drucker + L yield criterion allows flexibility of the yield surface, particularly in biaxial region, when compared with the Hill'48 criterion, as shown in the following.

In this subsection, illustrative cases of identification of the Swift law parameters of materials with isotropic and anisotropic behaviour described by Drucker + L criterion [29] are shown. The Drucker + L is an extension of the Drucker isotropic criterion [30] to anisotropy:

$$\left[\frac{1}{2}\mathrm{tr}\left(\mathbf{s}^2\right)\right]^3 - c\left[\frac{1}{3}\mathrm{tr}\left(\mathbf{s}^3\right)\right]^2 = 27\left(\frac{Y}{3}\right)^6 \tag{9}$$

where tr(**s**) is the trace of the stress tensor **s**, resulting from the linear transformation of the Cauchy stress tensor, **σ**, and c is a weighting isotropy parameter, ranging between −27/8 and 9/4, to ensure the convexity of the yield surface. When c equals zero, this criterion coincides with the Hill'48 yield criterion. The **s** stress tensor is given by:

$$\mathbf{s} = \mathbf{L}{:}\boldsymbol{\sigma} \tag{10}$$

where L is the linear transformation operator proposed by Barlat et al. [31]:

$$\mathbf{L} = \begin{bmatrix} (C_2+C_3)/3 & -C_3/3 & -C_2/3 & 0 & 0 & 0 \\ -C_3/3 & (C_3+C_1)/3 & -C_1/3 & 0 & 0 & 0 \\ -C_2/3 & -C_1/3 & (C_1+C_2)/3 & 0 & 0 & 0 \\ 0 & 0 & 0 & C_4 & 0 & 0 \\ 0 & 0 & 0 & 0 & C_5 & 0 \\ 0 & 0 & 0 & 0 & 0 & C_6 \end{bmatrix} \tag{11}$$

in which C_i, with $i = 1, \ldots, 6$, are the anisotropy parameters; $C_1 = C_2 = C_3 = C_4 = C_5 = C_6$ for the full isotropy condition. This yield criterion includes one more parameter, the parameter c, than Hill'48 yield criterion, thus being more flexible. In fact, the Hill'48 criterion cannot fully describe the behaviour of a material that follows the Drucker + L criterion with the parameter c different from zero.

Table 10 shows the parameters of the Drucker + L criterion and the Swift law of the tested materials: (i) two with full isotropy, one of which with $c = -2$ (Isot_c = −2) and the other with $c = 2$ (Isot_c = 2) and also (ii) two anisotropic materials, one of which with $c = -2$ (Anisot_c = −2) and the other with $c = 2$ (Anisot_c = 2). Figure 22 shows the initial yield surface of these materials in the (σ_{xx}; σ_{yy}) plane. For the isotropic materials represented in Fig. 22(a), the stress and strain paths observed during the bulge test are $\sigma_{yy}/\sigma_{xx} = d\varepsilon_{yy}/d\varepsilon_{xx} = 1$; for the anisotropic materials, the stress and strain paths are represented in Fig. 22(b). Table 5 shows the parameters of the Swift law of the selected isotropic materials (with $n = 0.19$, 0.20, 0.21, 0.22 and 0.23) used for numerical simulation and identification of the Drucker + L materials.

Tables 11, 12, 13 and 14 show the values of the factors Fh and Fp* that were applied to the numerical pressure vs. pole height curves of the materials in Table 10, in order to minimise the difference between these curves and that of each material in Table 5. The corresponding values of the objective function $F(\mathbf{A})$ and the estimated parameters of the Swift hardening law are also shown in Tables 11, 12, 13 and 14. The parameters of

Table 16 Swift law parameters obtained by fitting the stress–strain curves in tension, at 0, 45 and 90° with the rolling direction (RD), of the materials under study

Material	Swift law parameters								
	0° with RD			45° with RD			90° with RD		
	Y_0 [MPa]	K [MPa]	n	Y_0 [MPa]	K [MPa]	n	Y_0 [MPa]	K [MPa]	n
DP600 steel	392.22	1045.77	0.19	406.49	1040.11	0.19	433.02	1066.24	0.18
AA6061 aluminium alloy	275.10	489.43	0.13	270.58	484.95	0.13	272.22	483.19	0.12

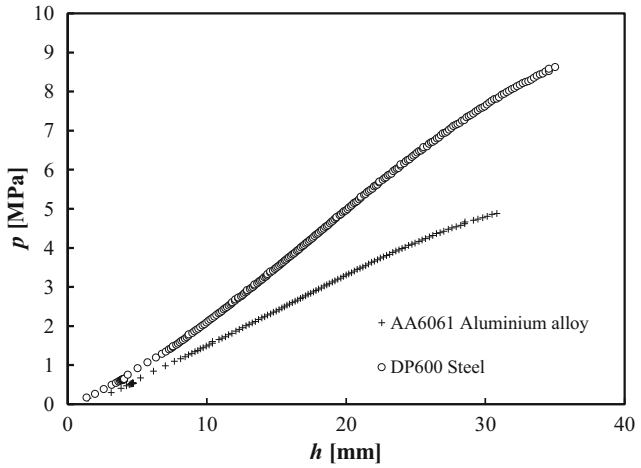

Fig. 29 Experimental evolution of the pressure, p, with pole the height, h, for the two metal sheets under study

the Swift law that minimise $F(\mathbf{A})$ correspond to the materials with $n = 0.205$ (for Isot_c = −2 and Anisot_c = −2) and with $n = 0.21$ (for Isot_c = 2 and Anisot_c = 2).

It should be noted that, for example, in the case of the isotropic Drucker + L material with $c = -2$, with flattened yield surface, the best fit occurs for a value of the factor Fh less than 1 (Fh = 0.974) and in case of the anisotropic Drucker + L material with $c = 2$, with sharp yield surface, the best fit corresponds to a factor Fh higher than 1 (Fh = 1.048). This is in line with the above mentioned at the end of section: Transverse anisotropic metal sheets, about the influence of the shape the yield surface near the equibiaxial region on the value of Fh.

Figures 23, 24, 25 and 26 show the hardening curves as obtained by inverse analysis and by membrane theory, for isotropic (Figs. 23 and 24) and anisotropic (Figs. 25 and 26) Drucker + L materials. The corresponding input curve, used in the numerical simulations, of the studied materials (see Table 10) is also shown in these figures. Figures 27 and 28 compare, respectively for the isotropic and anisotropic materials, the errors in stress obtained by the inverse analysis and using the membrane theory, referred to the input curves. The errors when using the inverse analysis are in general similar to the obtained using the membrane theory.

In conclusion, the results of the inverse identification performed on materials with isotropic and anisotropic behaviours, described by the Drucker + L criterion, more flexible than the Hill'48 criterion, lead to the conclusion that it can be applied to other yield criteria without loss of accuracy.

Experimental cases

This methodology is now tested for experimental cases. Two metals sheets were tested, a DP600 steel and an AA6061 aluminium alloy, with the initial thicknesses t_0 of 0.80 mm and 1.04 mm, respectively. The anisotropy and the work hard-

Table 17 Fh and Fp* values that minimize $F(\mathbf{A})$ and corresponding estimated Swift law parameters for the material DP600 (see Table 16)

Numerical simulation	Fh	Fp*	$F(\mathbf{A})$	Swift law - estimated		
				Y_0 [MPa]	K [MPa]	n
100_0.18_1_1_1	1.003	3.130	1.62×10^{-3}	390.51	1013.48	0.18
100_0.19_1_1_1	0.973	2.944	7.22×10^{-4}	373.76	1022.80	0.19
100_0.195_1_1_1	**0.958**	**2.855**	$\mathbf{4.41 \times 10^{-4}}$	**365.54**	**1027.17**	**0.195**
100_0.20_1_1_1	0.944	2.768	6.21×10^{-4}	357.47	1031.43	0.20
100_0.21_1_1_1	0.905	2.570	1.16×10^{-3}	339.40	1032.59	0.21

Note: the parameters of the Swift hardening law used as input in numerical simulation **100_0.195_1_1_1** (not included in Table 5) are: $\boldsymbol{Y_0} = 100$ MPa, $\boldsymbol{K} = 281.00$ MPa and $\boldsymbol{n} = 0.195$.

Table 18 Fh and Fp* values that minimize $F(\mathbf{A})$ and corresponding estimated Swift law parameters for the material AA6061 (see Table 16)

Numerical simulation	Fh	Fp*	$F(\mathbf{A})$	Swift law - estimated		
				Y_0 [MPa]	K [MPa]	n
100_0.12_1_1_1	1.001	2.432	9.61×10^{-4}	235.24	444.26	0.12
100_0.13_1_1_1	0.965	2.282	5.50×10^{-4}	225.34	448.71	0.13
100_0.135_1_1_1	**0.944**	**2.220**	$\mathbf{4.85 \times 10^{-4}}$	**220.40**	**450.66**	**0.135**
100_0.14_1_1_1	0.926	2.131	5.63×10^{-4}	215.25	451.94	0.14
100_0.15_1_1_1	0.893	1.997	8.88×10^{-4}	205.79	455.60	0.15

Note: the parameters of the Swift hardening law used as input in numerical simulation **100_0.135_1_1_1** (not included in Table 5) are: $\boldsymbol{Y_0} = 100$ MPa, $\boldsymbol{K} = 204.47$ MPa and $\boldsymbol{n} = 0.135$

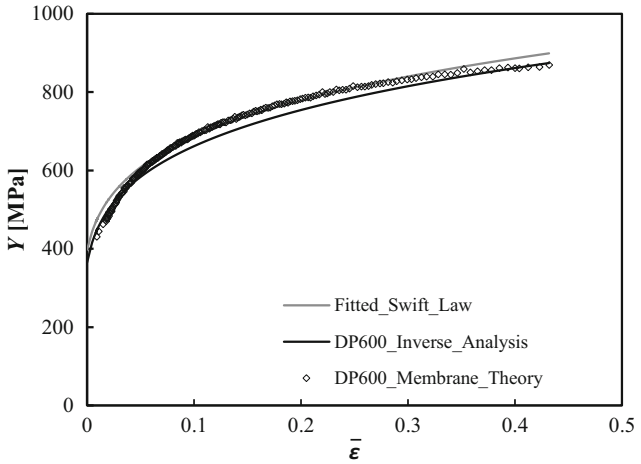

Fig. 30 Hardening curves obtained by the inverse analysis, the membrane theory and by fitting the Swift law to the membrane theory results, for the DP600 steel

ening behaviours of the materials were characterised in tension, and the respective parameters are shown in Tables 15 and 16, respectively. Figure 29 shows the evolution of the pressure with pole height, for both materials.

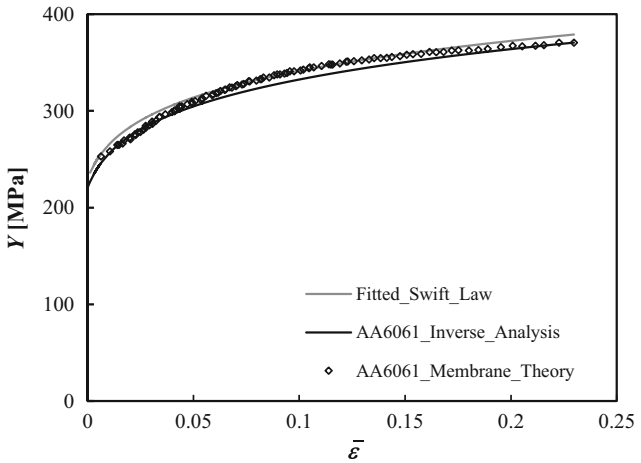

Fig. 31 Hardening curves obtained by the inverse analysis, the membrane theory and by fitting the Swift law to the membrane theory results, for the AA6061 aluminium alloy

The parameters of the Swift law of the isotropic materials used in the numerical simulations for identification are indicated in Table 5, as for numerical cases in the previous section. The numerical simulations were performed with an initial sheet thickness equal to 1.0 mm. The elastic parameters values are: Young's modulus $E = 200$ GPa and Poisson ratio $\nu = 0.3$, in case of DP600 steel; and $E = 70$ GPa and Poisson ratio $\nu = 0.3$, in case of AA6061 aluminium alloy.

Tables 17 and 18 show the values of the factors Fh and Fp* that were applied to the numerical pressure vs. pole height curves of the materials in Table 5, in order to minimise the difference between these curves and those for each material (Fig. 29). The corresponding values of the objective function $F(\mathbf{A})$ and the estimated parameters of the Swift hardening law are also shown in the Tables 17 and 18. The parameters of the Swift law that minimise $F(\mathbf{A})$ correspond to the materials with $n = 0.195$, for the DP600 steel, and 0.135, for the AA6061 aluminium.

Figures 30 and 31 compare the identified stress–strain curves by inverse analysis (solid black lines) with those determined using the membrane theory (symbols), for the DP600 steel and the AA6061 aluminium alloy, respectively. In these cases, a measurement tactile system was used to estimate the curvature radius and the strain at the pole [17], which is considered valid by ISO 16808:2014 [1] for bulge test investigation. A three point spherometer evaluates the height difference between the pole and three positions at a fixed radius, in order estimate the radius of curvature during the test. An extensometer allows following the strain value in the rolling direction, in a region near the pole of the cap, during the test. The equivalent strain is considered twice the value of the strain along the rolling direction. In summary, this corresponds to the use of the von Mises definitions of equivalent stress and strain, under the assumption of equibiaxial stress and strain states. Figures 30 and 31 also show the stress–strain curves obtained

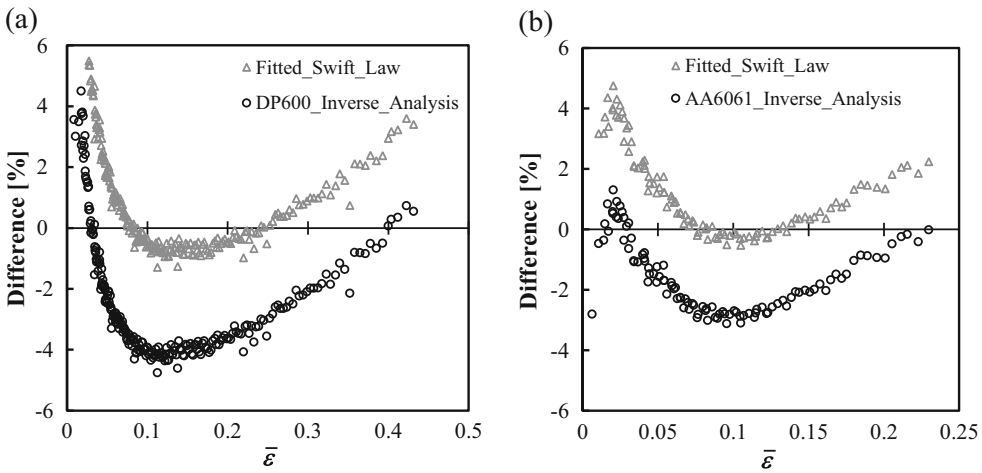

Fig. 32 Evolution of the difference in stress between the inverse analysis and the membrane theory results and the same difference for the fitted Swift law, in cases: (**a**) DP600 steel; (**b**) AA6061 aluminium alloy

by fitting the Swift law to the membrane theory results (solid grey lines), leading to the following parameters: $Y_0 = 397.79$ MPa, $K = 1051.48$ MPa and $n = 0.19$ ($\varepsilon_0 = 0.006$), for the steel DP600; and $Y_0 = 229.76$ MPa, $K = 457.51$ MPa and $n = 0.13$ ($\varepsilon_0 = 0.005$), for the aluminium AA6061. Figure 32 compares the difference in stress between the hardening laws assessed by the inverse analysis and by fitting the Swift law to the membrane theory results, taking the experimental membrane theory results as reference, for the DP600 steel (Fig. 32(a)) and the AA6061 aluminium alloy (Fig. 32(b)). It must be mentioned that although the experimental stress vs. strain results obtained by the membrane theory only fairly obey to the Swift equation (see fitted Swift law in Figs. 30 and 31), it can be concluded that the proposed inverse analysis is sufficiently accurate for determining the stress–strain curve from the bulge test. Finally, as mentioned with regard to the last example of the numerical cases in section : Hill'48 criterion, the identified parameters can certainly be improved, by repeating the identification procedure using values of ε_0, different but close to 0.005, for the numerical materials used in identification.

Conclusions

This work allows achieving a unified description of the evolution of the pressure with pole height, during the bulge test, for a given value of the hardening coefficient of the Swift law. This allowed the development of an inverse analysis strategy for determining the parameters of the Swift law, just using the results of pressure vs. pole height. Moreover, it is easily implemented, requiring a few numerical simulations of isotropic reference materials with various values of the hardening coefficient, in the expected range of the material under test. The inverse procedure was tested for the cases of computer-generated and experimental materials. In both cases, the strategy is compared with the classical strategy of analysis of the bulge test results using the membrane theory, based on determining the radius of curvature, and the direct measurement of the strains at the pole. The proposed inverse strategy is easy to implement and more efficient than classical, since it is not exposed to experimental errors related to the experimental evaluation of radius of curvature and strain at the pole of the bulge and the assumptions and simplifications associated to the use of membrane theory approach under bulge test conditions, which is usually the major source of errors.

Finally, it should be mentioned that this inverse analysis methodology to evaluate the parameters of the Swift law, although accurate and easy to apply, does not fully answer to the issue of determining the hardening law from the bulge test, if the behaviour is better described by other laws than Swift. In fact, the behaviour of a number of materials, as for example certain aluminium alloys, is best described by the Voce's law and also other laws with increasing complexity are currently being used.

Compliance with ethical standards

Funding This research work is sponsored by national funds from the Portuguese Foundation for Science and Technology (FCT) and by FEDER funds "Programa Operacional Factores de Competitividade" via the projects PTDC/EMS-TEC/1805/2012 and UID/EMS/00285/2013 as well as by FEDER funds "Programa Operacional da Região Centro" via the project CENTRO-07-0224-FEDER-002001 (MT4MOBI). One of the authors, P.A. Prates, was supported by a grant for scientific research from the Portuguese Foundation for Science and Technology (SFRH/BPD/101465/2014). All supports are gratefully acknowledged.

Conflict of interest The authors declare that they have no conflict of interest.

References

1. DIN EN ISO 16808:2014–11 (E) (2014) Metallic materials - sheet and strip - Determination of biaxial stress–strain curve by means of bulge test with optical measuring systems. BSI
2. Mulder J, Vegter H, Aretz H, van den Boogaard AH (2013) Accurate evaluation method for the hydraulic bulge test. Key Eng Mater 554–557:33–40. doi:10.4028/www.scientific.net/KEM.554-557.33
3. Keller S, Hotz W, Friebe F (2009) Yield curve determination using bulge test combined with optical measurements. In: Levy BS, Matlock DK, Van Tyne CJ (eds) Int. Deep Draw. Res. Gr. Conf. IDDRG. IDDRG, Golden, Colorado, pp 319–330
4. Mulder J, Vegter H, Aretz H et al (2015) Accurate determination of flow curves using the bulge test with optical measuring systems. J Mater Process Technol 226:169–187. doi:10.1016/j.jmatprotec.2015.06.034
5. Liu K, Lang L, Cai G et al (2015) A novel approach to determine plastic hardening curves of AA7075 sheet utilizing hydraulic bulging test at elevated temperature. Int J Mech Sci 100:328–338. doi:10.1016/j.ijmecsci.2015.07.002
6. Atkinson M (1997) Accurate determination of biaxial stress—strain relationships from hydraulic bulging tests of sheet metals. Int J Mech Sci 39:761–769. doi:10.1016/S0020-7403(96)00093-8
7. Hill R (1950) C. A theory of the plastic bulging of a metal diaphragm by lateral pressure. London Edinburgh Dublin Philos Mag J Sci 41:1133–1142. doi:10.1080/14786445008561154
8. Smith LM, Hadad Y, Thotakura R, et al. (2007) Flow stress curves using new volume measurement method for hydraulic bulge test. In: AIP Conf. Proc. AIP, Porto, Portugal, pp 637–642
9. Chakrabarty J, Alexander JM (1970) Hydrostatic bulging of circular diaphragms. J Strain Anal Eng Des 5:155–161. doi:10.1243/03093247V053155
10. Slota J, Spišák E (2008) Determination of flow stress by the hydraulic bulge test. Metalurgija 47:13–17
11. Panknin W (1970) The hydraulic bulge test and the determination of the flow stress curves. University of Stuttgart
12. Chamekh A, BelHadjSalah H, Hambli R, Gahbiche A (2006) Inverse identification using the bulge test and artificial neural networks. J Mater Process Technol 177:307–310. doi:10.1016/j.jmatprotec.2006.03.214

13. Ludwik P (1909) Elemente der Technologischen Mechanik. doi:10.1007/978-3-662-40293-1
14. Bambach M (2011) Comparison of the identifiability of flow curves from the hydraulic bulge test by membrane theory and inverse analysis. Key Eng Mater 473:360–367. doi:10.4028/www.scientific.net/KEM.473.360
15. Voce E (1948) The relationship between stress and strain for homogeneous deformations. J Inst Met 74:537–562
16. Swift HW (1952) Plastic instability under plane stress. J Mech Phys Solids 1:1–18. doi:10.1016/0022-5096(52)90002-1
17. Santos AD, Teixeira P, Barata da Rocha A, et al (2010) On the determination of flow stress using bulge test and mechanical measurement. In: Barlat F, Moon YH, Lee MG (eds) 10th Int. Conf. NUMIFORM. American Institute of Physics, Pohang, Republic of Korea, pp 845–852
18. Alves JL (2005) Drawbeads: to Be or Not to Be. In: AIP Conf. Proc. AIP, pp 655–660
19. Alves JL (2003) Simulação numérica do processo de estampagem de chapas metálicas: Modelação mecânica e métodos numéricos. Universidade do Minho
20. Menezes LF, Teodosiu C (2000) Three-dimensional numerical simulation of the deep-drawing process using solid finite elements. J Mater Process Technol 97:100–106. doi:10.1016/S0924-0136(99)00345-3
21. Oliveira MC, Alves JL, Menezes LF (2008) Algorithms and strategies for treatment of large deformation frictional contact in the numerical simulation of deep drawing process. Arch Comput Methods Eng 15:113–162. doi:10.1007/s11831-008-9018-x
22. Reis LC, Prates PA, Oliveira MC, et al. (2011) Caracterização do comportamento plástico de chapas metálicas com recurso ao ensaio de expansão biaxial simétrica. In: Tadeu A, Figueiredo IN, Menezes LF, et al. (eds) Congr. Métodos Numéricos em Eng. APMTAC, Coimbra, Portugal, p 54
23. Reis LC, Rodrigues CA, Oliveira MC, et al (2012) Characterization of the plastic behaviour of sheet metal using the hydraulic bulge test. In: Andrade-Campos A, Lopes N, Valente RAF, Varum H (eds) First ECCOMAS Young Investig. Conf. Comput. Methods Appl. Sci. Aveiro, Portugal, p 67
24. Rodrigues CA, Reis LC, Sakharova NA, et al (2012) On the characterization of the plastic behaviour of sheet metals with bulge tests: numerical simulation study. In: Eberhardsteiner J. et al. (ed) 6th Eur. Congr. Comput. Methods Appl. Sci. Eng. ECCOMAS. ECCOMAS 2012, Vienna, Austria, pp 4575–4589
25. Hill R (1948) A theory of the yielding and plastic flow of anisotropic metals. Proc R Soc A Math Phys Eng Sci 193:281–297. doi:10.1098/rspa.1948.0045
26. Prates PA, Oliveira MC, Fernandes JV (2015) On the equivalence between sets of parameters of the yield criterion and the isotropic and kinematic hardening laws. Int J Mater Form 8:505–515. doi:10.1007/s12289-014-1173-z
27. Santos AD, Teixeira P, Barlat F (2011) Flow stress determination using hydraulic bulge test and a mechanical measurement system. In: Int. Deep Draw. Res. Gr. Conf. IDDRG. IDDRG, Bilbao, Spain, pp 91–100
28. Chaparro BM (2006) Comportamento plástico de materiais metálicos: identificação e optimização de parâmetros. Universidade de Coimbra
29. Cazacu O, Barlat F (2001) Generalization of Drucker's yield criterion to orthotropy. Math Mech Solids 6:613–630. doi:10.1177/108128650100600603
30. Drucker DC (1949) Relation of experiments to mathematical theories of plasticity. J Appl Mech ASME 16:349–357
31. Barlat F, Aretz H, Yoon JW et al (2005) Linear transfomation-based anisotropic yield functions. Int J Plast 21:1009–1039. doi:10.1016/j.ijplas.2004.06.004

Chapter 4.

Conclusions and Perspectives

This chapter highlights the main conclusions of the present research work on the hydraulic bulge test and outlines perspectives of further studies.

[Page intentionally left blank]

4.1. Conclusions

Although available in the literature for over 50 years, the hydraulic bulge test, used for characterising the mechanical behaviour of metal sheets, still disclose unknown issues, some of which were analysed and discussed in this thesis. This was duly taken into account for this work, particularly given that the prevailing standards for this test are not satisfactory. The apparent lack of timeliness of the subject, given its so great longevity, is also contradicted by the recent effort provided for the proper identification of the constitutive laws parameters, in which the bulge test persists in playing a key role.

This work aims to contribute for the understanding of the hydraulic bulge test, attempting to establish relationships between variables of the test, in order to improve the accuracy of the traditional experimental procedure for determining the stress *vs*. strain curve, but also to the development of new direct and inverse methodologies for simplifying its evaluation. It is supported by finite element simulations and experimental results were used for validation of methodologies. The main conclusions of this thesis are described next.

Firstly, a comprehensive analysis of the geometry and variables of test, with particular emphasis on anisotropic materials, was performed. This study contemplates materials with different anisotropy and hardening coefficient. It was concluded that the geometry of the cap is identical for all directions on the sheet plane, whatever the material anisotropy. This allows simplifying the use of the general membrane theory equation, since the radius of curvature is equal for both orthotropic axis. In contrast, the principal stresses (and strains) at the pole of the cap, although equal for both axes in the case of planar isotropy, are different in case of planar anisotropy with $r_0 \neq r_{90}$. The errors associated with the traditionally used approach, which considers the principal stresses (and strains) at the pole cap equal for both orthotropic axes, were quantified according to the anisotropy of the sheet. Moreover, an equation specific of the circular bulge test, that relates the stress path with the strain path at the pole, was proposed regardless of the yield criterion describing the anisotropic behaviour of the material: $(\sigma_2/\sigma_1 = (\varepsilon_2/\varepsilon_1)^{-2})$. This allows to determine the stress path since the strain path is known, which can be assessed by digital image correlation. In this context, the generally used simplified equation of membrane theory, which consists in assuming equibiaxial stress

and strain path, can be overcome and the accuracy of the stress *vs*. strain curve is greatly improved, mainly in case of materials with strong anisotropy.

Secondly, analytical models are proposed relating the radius of curvature and the sheet thickness with the pole bulge height. These models are based in an extensive analysis of different material behaviours, as well as different geometries of the bulge test. The analysed geometric variables are the bulge die radius and the fillet radius located at the entrance of the die. The equations of the models include the geometrical and material variables associated with the hardening behaviour and the sheet anisotropy. The evolution of the radius of curvature normalised by the die radius depends on the hardening coefficient of the material and the die geometry, but it is independent of the yield stress, initial sheet thickness and anisotropy of the material. The evolution of the sheet thickness normalized by initial sheet thickness is also dependent on the hardening coefficient and the die geometry, but still depends on the material anisotropy, while remaining independent of the yield stress and initial sheet thickness. The validation of the equations was firstly performed using numerical generated results, which shows that the error in the stress *vs.* strain curves is similar to that obtained by traditional procedure by measuring the radius of curvature and principal strain values at the pole, which requires the use of specific devices and involve more complex analysis. Moreover, experimental validation was performed using results from literature, with different bulge geometries, and those obtained in the framework of this thesis, with a specific die geometry.

Finally, an inverse methodology is proposed for determining the hardening law of metal sheets, from the results of pressure *vs.* pole height obtained in the bulge test. This involves the identification of the parameters of the Swift law, and complements the above mentioned work. The starting point of this analysis was to realize that it is possible to achieve a unified description of the evolution of the pressure with the pole height, for a given value of the hardening parameter of the Swift law, regardless of the yield stress and anisotropy of the material, and sheet thickness. To achieve this, i.e. the overlapping of such curves, appropriate multiplying factors must be used for the values of pressure and pole height, depending on the yield stresses and thicknesses ratios of the sheets, and also on their anisotropy. Thereafter, a forward analysis study on the influence and sensitivity of these parameters on the results of pressure with pole height allowed developing the inverse analysis methodology. This consists on the search for the best coincidence between pressure *vs*. pole

height experimental and reference curves, the latter being obtained by numerical simulation assuming isotropic material behaviour with various values of the hardening parameter in the range of the material under study. This methodology, when compared with the classical strategy, proves to be an efficient alternative avoiding the use of complex devices for measuring the radius of curvature and strain at the pole of the cap, during the bulge test. Moreover, it is easy to implement and it is more efficient than classical approach, since it is not exposed to experimental errors related to the evaluation of the strain at the pole of the bulge and the use of membrane theory approach for assessment of the stress from the radius of curvature, which is usually the major source of errors.

4.2. Future Perspectives

The work contributes to a better definition of issues of the hydraulic bulge test that deserve to be further studied, in view of experimental practices and understanding of this subject. Some few issues that deserve further research are now suggested.

The first refers to identically oriented studies, but now relative to elliptical dies, which is worth being accomplished, since the low frequency use of these bulge tests is linked to its experimental complexity and corresponding analysis. The enhanced complexity of this test comes from the fact that radius of curvature differs according to the direction in the plane, and the strain and stress paths are not close to symmetrical biaxial, not even in case of isotropic materials.

Secondly, the inverse analysis methodology herein proposed to evaluate the hardening law requires to be extended to other hardening laws, besides Swift. The current analysis is certainly an important step towards this objective.

Lastly, the inverse analysis methodology proposed to evaluate the hardening law justifies to be assessed in the framework of the latest methodologies for simultaneous identification of parameters of constitutive laws, including isotropic and kinematic hardening and anisotropic yield criterion.

[Page intentionally left blank]